# An interplay of various particle acceleration processes in turbulent astrophysical plasma

**Ph.D. Thesis**

by

**Sayan Kundu**

**Department of Astronomy, Astrophysics and Space Engineering**

**Indian Institute of Technology Indore**

**Khandwa Road, Simrol, Indore - 453552, India**

**August, 2023**

# An interplay of various particle acceleration processes in turbulent astrophysical plasma

**A THESIS**

*Submitted in partial fulfillment of the requirements for the award of the degree*

**of**

**DOCTOR OF PHILOSOPHY**

**by**

**Sayan Kundu**

**Department of Astronomy, Astrophysics and Space Engineering**

**Indian Institute of Technology Indore**

**Khandwa Road, Simrol, Indore - 453552, India**

**August, 2023**

# INDIAN INSTITUTE OF TECHNOLOGY INDORE

I hereby certify that the work which is being presented in the thesis entitled **An interplay of various particle acceleration processes in turbulent astrophysical plasma** in the partial fulfillment of the requirements for the award of the degree of **DOCTOR OF PHILOSOPHY** and submitted in the **DEPARTMENT/SCHOOL OF Astronomy, Astrophysics and Space Engineering, Indian Institute of Technology Indore**, is an authentic record of my own work carried out during the time period from July, 2018 to August, 2023 under the supervision of Dr. Bhargav Vaidya, Associate Professor, Indian Institute of Technology, Indore.

The matter presented in this thesis has not been submitted by me for the award of any other degree of this or any other institute.

Sayan Kundu

18/08/2023

**signature of the student with date**
**(Sayan Kundu)**

---

This is to certify that the above statement made by the candidate is correct to the best of my/our knowledge.

Dr. Bhargav Vaidya (18/08/2023)

Signature of Thesis Supervisor #1 with date — Signature of Thesis Supervisor #2 with date

**(NAME OF THESIS SUPERVISOR)** — **(NAME OF THESIS SUPERVISOR)**

---

**Sayan Kundu** has successfully given his/~~her~~ Ph.D. Oral Examination held on **16/08/2023**.

Dr. Bhargav Vaidya (18/08/2023)

Signature of Thesis Supervisor #1 with date — Signature of Thesis Supervisor #2 with date

**(NAME OF THESIS SUPERVISOR)** — **(NAME OF THESIS SUPERVISOR)**

---

**Dedicated**

**to**

**Maa, Baba, Didan, Bunu**

**and Suchi**

# Acknowledgements

I am deeply thankful to all the people I have encountered on my journey thus far. Their presence has played a critical role in shaping me into who I am today.

First and foremost, I owe a huge thank you to my dear Maa (mother). She's been my biggest supporter, believing in my dreams and giving me the courage to study physics. She's not just my mom but also a wonderful friend I can talk to about anything. Even when she doesn't have all the answers, her support means the world to me.

Then there's my Baba (father), who's like my go-to problem solver. His words of encouragement, like "chinta kiser Ami to acchi" (don't worry, I've got your back) and "venge jak tori dube jak pran lorai chaliye jetei hobe" (no matter what happens, keep fighting) have always given me the strength to keep moving forward.

And let's not forget my wonderful Didan (maternal grandmother), who's been by my side since I was a kid. Her constant support played a huge role in helping me finish my BSc degree. Her belief in me has been a guiding light.

My Bunu (sister) and I used to fight a lot when we were young, but over time our bond has become unbreakable. I miss her tea whenever I'm away from home. She's like my anchor, always knowing how to handle different situations.

Then comes my partner in crime, Suchi, my girlfriend. From the first day of my PhD, she was there to share my depression and frustrations. She can make me happy anytime with her unique style of motivation. She helped me whenever I needed it. In this thesis as well, the majority of the mathematical equations were LaTex-ed by her. Without her constant support and motivation, I doubt I would have reached where I am. I can not thank them enough for being there whenever I needed them.

I also want to extend my gratitude to IIT Indore for giving me the chance to be a part of their community.

My sincere gratitude goes out to my PhD supervisor, Dr. Bhargav Vaidya, for his constant guidance, support, and belief in my potential during my doctoral journey. His continuous motivation and encouragement have consistently provided me with the confidence that solutions are attainable even in the face of challenges.

My acknowledgement extends to Dr. Nishant Singh, my collaborator, for encouraging me to tackle theoretical problems. His support for my visit to IUCAA has proven to be immensely advantageous.

I want to thank Prof. Andrea Mignone for patiently reading and correcting my manuscripts. Due to his and my supervisor's encouragement and support, I could develop an entire code from scratch in a few days for my first paper.

Also, I would like to thank Dr. Dhrubaditya Mitra (Dhruba da), with whom I embarked on a collaborative journey to comprehend MHD turbulence. During this time, I learned about weak MHD turbulence and renormalization group theory.

I want to thank the Max Planck Partner Group grant for supporting my PhD. Without their computational facilities, my work on radio-lobe would not have been published at this time. I also wish to thank my PSPC members, Dr. Manoneeta Chakraborty, Dr. Suman Majumder, and Dr. Rupesh Devan, for their thought-provoking comments during my CERPs.

My journey would be incomplete without acknowledging the friends that I have made during my time at IITI. Back in the early days of my PhD, Sarvesh, Kamran, and I shared a flat at Silver Springs. During that stay, we had the privilege (as others used to call it) of having Kamran as our cook. I still miss the delicious Mughlai foods that he used to make. With Sarvesh, it took a bit of time to get used to each other, but once we did, our friendship became even stronger. Sarvesh was also one of my flatmates in the IIT hostel, and whenever I felt bored, I used to disturb him. He is one of those persons with whom I used to discuss serious science stuff apart from my research. I want to thank Sarvesh, along with my other IITI flatmates Yoshi and Sayan, for tolerating me and my singing.

I would like to give a special thanks to Sriya, with whom I used to share the lab. She took care of most of the issues that I faced during my early times at IIT, be they academic or non-academic. I am thankful to her for her support. Then I would like to thank Parul, Akriti and Unnati (my Rakhi sister) for their help and support during my PhD. I would also like to thank Gourab, Arghyadeep and Prateek, for bringing up all the discussions and conversations be they academic or non-academic. I want to express my deep appreciation for all these remarkable individuals who have shaped my journey in ways I can't fully put into words. Their support and influence have made me who I am today, and I'm incredibly thankful for that.

Finally, I am grateful to the entire DAASE family for making my time memorable and eventful.

# Abstract

Magneto-hydrodynamic (MHD) turbulence is ubiquitous in astrophysical systems, and it is typically attributed to governing various micro-physical activities in these systems. One of the important manifestations of this astrophysical turbulence is the origin and transport of non-thermal particles, often called cosmic rays (CR). These high-energy CRs, though small in number, play a significant and unique role in various astronomical phenomena. While propagating through a turbulent system, CRs acquire energy via Fermi acceleration processes and lose energy due to various loss processes. Among those acceleration mechanisms, diffusive shock acceleration (DSA) and stochastic turbulent acceleration (STA) are considered to be operative, particularly in weakly magnetised regions. While DSA is a systematic acceleration process that energises particles in the vicinity of shocks, stochastic turbulent acceleration (STA) is a random energising process where the interaction between cosmic ray particles and electromagnetic fluctuations results in particle acceleration. This process is usually interpreted as a biased random walk in energy space. The primary energy loss processes that these non-thermal high-energy CRs undergo are synchrotron and inverse compton (IC) losses. This interplay of particle acceleration processes and radiative losses subsequently shapes the emission features of different astrophysical sources.

In this thesis, we develop a novel Eulerian algorithm adopted to incorporate turbulent acceleration in the presence of DSA and radiative processes like synchrotron and inverse-Compton emission. The developed framework extends the hybrid Eulerian-Lagrangian module of a full-fledged relativistic magnetohydrodynamic (RMHD) code, PLUTO. Through various benchmark tests, we validated the developed framework and studied the competing and complementary nature of both acceleration

processes through various numerical test problems.

We subsequently focus on studying the interplay of particle acceleration and loss processes in different components of radio-loud AGNs. Such systems are thought to possess various sites of particle acceleration, which give rise to the observed non-thermal spectra. We explore a phenomenologically motivated numerical model for STA in order to investigate the interplay of different acceleration processes on the emission characteristics of the radio lobes of these extragalactic sources. The study demonstrates that STA produces curved particle spectra that differ morphologically from the standard shock-accelerated spectrum. As a consequence of this structural difference in the underlying particle energy spectrum, various multi-wavelength features arise in the spectral energy distribution of the radio lobe. Further analysis of these newly-emerged features and their comparison with realistic observations reveals the complemantary nature of STA and DSA in producing the diffuse X-ray emission in the radio lobes of FR-II radio galaxies.

Finally, we consider investigating the effects of STA caused by small-scale turbulence. Such a turbulent condition can arise in the vicinity of the relativistic shocks that these radio loud AGN possess. Under quasilinear approximation, and by assuming a turbulent spectrum with single scale injection at sub-gyroscale, we find that the Fokker-Planck diffusion coefficients $D_{\gamma\gamma}$ and $D_{\mu\mu}$ scale with the Lorentz factor $\gamma$ as: $D_{\gamma\gamma} \propto \gamma^{-2/3}$ and $D_{\mu\mu} \propto \gamma^{-8/3}$. Furthermore, with the calculated transport coefficients, we numerically solve the advection-diffusion type transport equation for the non-thermal particles. We demonstrate the interplay of various microphysical processes such as STA, synchrotron loss, and particle escape on the particle distribution by systematically varying the parameters.

# List of Publications

A. Published journal articles:

1. **Kundu, S.**, Vaidya, B., and Mignone, A. (2021) Numerical Modeling and Physical Interplay of Stochastic Turbulent Acceleration for Nonthermal Emission Processes, The Astrophysical Journal, vol. 921, no. 1. doi:10.3847/1538-4357/ac1ba5.

2. **Kundu, S.**, Vaidya, B., Mignone A. and Hardcastle M. J. (2022) A numerical study of the interplay between Fermi acceleration mechanisms in radio lobes of FR-II radio galaxies, Astronomy & Astrophysics, vol. 667, 2022, https://doi.org/10.1051/0004-6361/202244251

3. **Kundu, S.**, Singh, N. K., & Vaidya, B. (2023). Acceleration of cosmic rays in presence of magnetohydrodynamic fluctuations at small scales. MNRAS, 524(4), 4950-4972, doi:10.1093/mnras/stad2098

B. Published conference proceeding:

1. **Kundu, S.**, Vaidya, B., 2023. Interplay of various particle acceleration processes in astrophysical environment, IAU Symposium 362, 365372, doi:10.1017/S174392132200165X

**N.B**: Entries A1, A2, A3 are parts of this thesis.

# Table of Contents

# List of Figures

# List of Tables

# Chapter 1

# Introduction

*The majority of the astrophysical systems comprise plasma, which is a state of matter where the thermodynamic properties are maintained by the collective effects of charged particles. These collective effects infuse the system with nonlinearity, making it challenging to study the behaviour of astrophysical systems. Turbulence is one of the manifestations of such non-linear behaviour in the plasma medium. It is therefore expected to be present in astrophysical systems, where it plays a crucial role in governing their dynamics and energetics. This chapter introduces turbulent astrophysical plasma by gradually introducing hydrodynamic and magneto-hydrodynamic turbulence. This chapter also introduces the jet and related structures of the radio-loud AGN system. It further provides an outline of the work presented in this thesis.*

---

## 1.1 Turbulence in astrophysical systems

Turbulence is ubiquitous in nature. From mixing the coffee in a cup of milk to enhancing the diffusion of the scent of a perfume in the air, from interfering with the radio waves in the ionosphere to governing global weather patterns, the effect of turbulence can be found everywhere. In a simple way, turbulence can be described as a process by which energy transfer happens from large scales to smaller scales in a fluid. For example, while making a perfect caramel macchiato, the barista mixes the espresso with caramelised milk, and in doing so, he spends some of his mechanical energy stirring the system. The stirring happens at a scale of the diameter of the cup, but mixing happens at a scale where coffee molecules interact with the milk molecules, which is very small compared to the diameter of the cup. The mechanical energy given by the barista cascades through different scales and gets transferred to the scale where the interactions between the molecules take place. Such an energy transfer occurs due to turbulence.

In physics, turbulence is a century-old phenomenon, and it is often referred to as one of the unsolved problems of classical physics till now. From the canvases of Leonardo da Vinci at the beginning of the sixteenth century to today's era of multi-scale numerical simulations, the study of turbulence has evolved, and various novel analyses have been performed that have consequently improved the understanding of such phenomena. As a result of such a huge period of time, the study of turbulence has witnessed various breakthroughs, and a vast literature has emerged out of such studies. Here we briefly introduce the turbulence phenomena observed in hydrodynamics and magnetohydrodynamics before discussing the turbulence observed in astrophysical systems and their manifestations. For a general pedagogical introduction to the subject of turbulence, readers are advised to see Frisch (1995); Pope & Pope (2000); Verma (2019).

We begin the discussion by briefly introducing some basic mathematical features for a simpler case of hydrodynamic turbulence, below, even though the work presented in this thesis is primarily concerned with plasma turbulence, and in particular magnetohydrodynamic (MHD) turbulence. As a result of this discussion, it will be easier to comprehend turbulence-related concepts like turbulent cascade, Reynolds numbers, and others, which will prepare the reader for the introduction of the more complex

MHD turbulence scenario. We focus on the even simpler case of incompressible turbulence here for the sake of simplicity. The evolutionary dynamics of a fluid system is governed by the following equations,

$$\frac{\partial \rho}{\partial t} + \nabla \cdot (\rho \boldsymbol{v}) = 0 \tag{1.1}$$

$$\rho \left( \frac{\partial \boldsymbol{v}}{\partial t} + (\boldsymbol{v} \cdot \nabla) \boldsymbol{v} \right) = -\nabla P + \mu \nabla^2 \boldsymbol{v} \tag{1.2}$$

where $\rho$, $\boldsymbol{v}$, $P$ and $\mu$ are the density, velocity, thermal pressure and viscocity of the fluid. Eq. (1.2) is known as the Navier-Stokes equation. Due to incompressibility condition, Eq. (1.1) takes the following form,

$$\nabla \cdot \boldsymbol{v} = 0 \tag{1.3}$$

Following such condition the thermal pressure can be found to be dependent on the velocity through the following Poisson equation (see for example Eq. (2.6) of Frisch, 1995),

$$\partial_i \partial_i P = -\partial_{kl} \left( v_k v_l \right). \tag{1.4}$$

In the above equation $\{i, k, l\} \in [1, 3]$ where different values correspond to different spatial components; $v^k$ and $v^l$ are the $k^{th}$ and $l^{th}$ component of the velocity respectively; $\partial_{kl} \equiv \partial_k \partial_l$. Further note that while writing the equation Einstein's summation convention is used. Such a dependency of the thermal pressure leads Eq. (1.2) to take the following form (see Eq. (2.13) of Frisch, 1995),

$$\partial_t v_i + \left( \delta_{il} - \partial_{il} \nabla^{-2} \right) \partial_j \left( v_j v_l \right) = \nu \nabla^2 v_i \tag{1.5}$$

where $\partial_t$ denotes temporal derivative, $\nabla^{-2}$ denotes inverse of the Laplacian operator and $\nu = \mu/\rho$. Note that, for incompressible hydrodynamic turbulence, Eq. (1.5) describes the temporal behaviour of fluid velocity in terms of two quantities $\partial_j \left( v_j v_l \right)$ and $\nabla^2 v_i$. Such an evolving velocity behaviour will be used in the future to define the

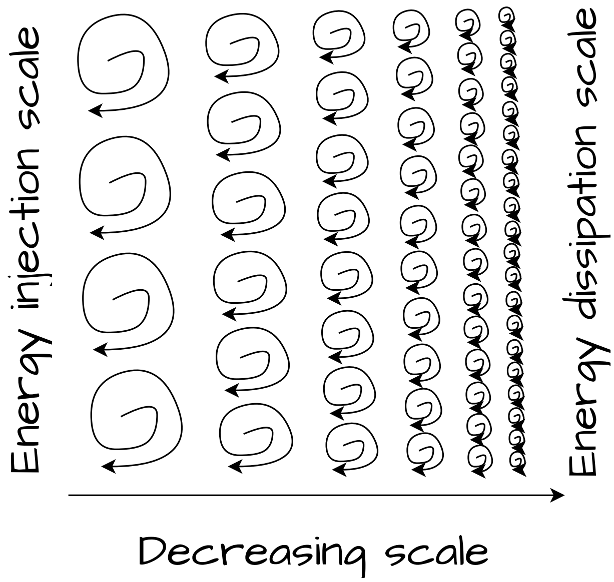


Figure 1.1: A schematic diagram of Richardson cascade where big whirls break into smaller whirls which breaks into even smaller whirls.

Reynolds number for turbulent systems, but for the time being, we will concentrate on the energy cascading behaviour of turbulence phenomena.

As stated earlier, turbulence makes the injected energy cascade from scale to scale. Such scale-to-scale energy transfer can be physically visualised through the Richardson cascade process (Richardson & Lynch, 2007). In such a case, energy is injected into the fluid via a large whirl-like structure that breaks into smaller whirls, and the energy of the large whirl is evenly distributed to the smaller whirls. These smaller whirls eventually fragment into even more smaller whirls, and so on. This breaking of whirls continues until the smallest scale, where energy is dissipated through viscosity rather than being distributed to smaller scales. A cartoon illustration of the Richardson cascade is shown in Fig. 1.1, where the process of breaking bigger whirls into smaller whirls is demonstrated.

To mathematically comprehend such cascade behaviour, it is instructive to conduct the study in the Fourier domain, where one can analyse the simultaneous action of multiple scales on a particular scale of interest (Verma, 2019). In the Fourier domain, the scale-by-scale energy transfer in the fluid due to turbulence is explained by the following energy budget equation (see Eq. (2.48) and section 2.4 of Frisch, 1995, for a derivation from Eq. (1.2)),

$$\partial_t \mathcal{E}_K = \mathcal{F}_K - 2\nu\Omega_K - \Pi_K. \tag{1.6}$$

The above equation has four different terms which are explained below,

$$\mathcal{E}_K = \frac{1}{2}\sum_{i\leq K} |\hat{\boldsymbol{v}}_i|^2 \qquad \Omega_K = \frac{1}{2}\sum_{i\leq K} i^2 |\hat{\boldsymbol{v}}_i|^2$$
$$\mathcal{F}_K = \sum_{i\leq K} i^2 \hat{\boldsymbol{f}}_i \cdot \hat{\boldsymbol{v}}_{-i} \qquad \Pi_K = \langle \boldsymbol{v}_K^< \cdot \nabla \boldsymbol{v}_K^< \cdot (\boldsymbol{v}_K^< \cdot \nabla \boldsymbol{v}_K^>)\rangle + \langle \boldsymbol{v}_K^< \cdot \nabla \boldsymbol{v}_K^< \cdot (\boldsymbol{v}_K^> \cdot \nabla \boldsymbol{v}_K^>)\rangle \tag{1.7}$$

with $\hat{\boldsymbol{v}}_i$ and $\hat{\boldsymbol{f}}_i$ being the $i^{th}$ Fourier component of velocity and force applied to the Navier Stokes equation as a source of energy injection; $\boldsymbol{v}_K^>$ and $\boldsymbol{v}_K^<$ being the inverse Fourier transform of the velocity only including Fourier scales greater than and less than $K$ respectively. Eq. (1.6) can be interpreted in the following way: the rate of change of energy ($E_K$) at a scale above $l = K^{-1}$ occurs due to energy input from outside at those scales ($\mathcal{F}_K$), dissipation of energy occurring at those scales ($2\nu\Omega_K$), and the flux of energy transferred to scales below $l$ ($\Pi_K$). Fig. 1.2 presents a representative illustration of such energy cascade due to turbulence in Fourier space. In the figure, energy injection occurs at $k = k_{min}$; at subsequently higher $k$ modes, the energy cascades from scale to scale and ultimately dissipating at $k = k_{max}$. The range of $k'$ values where energy cascade takes place is known as the **inertial range**. One interesting thing to note is the behaviour of the $E(k)$ in the inertial range, where $E(k)$ follows a power-law trend with the corresponding wave number ($k$), $E(k) \propto k^{-p}$. Due to the inherent nonlinearity and subsequent moment hierarchy of the Navier-Stokes equation, determining the exact value of $p$ using analytical methods is challenging. However, a value of $p$ for incompress-

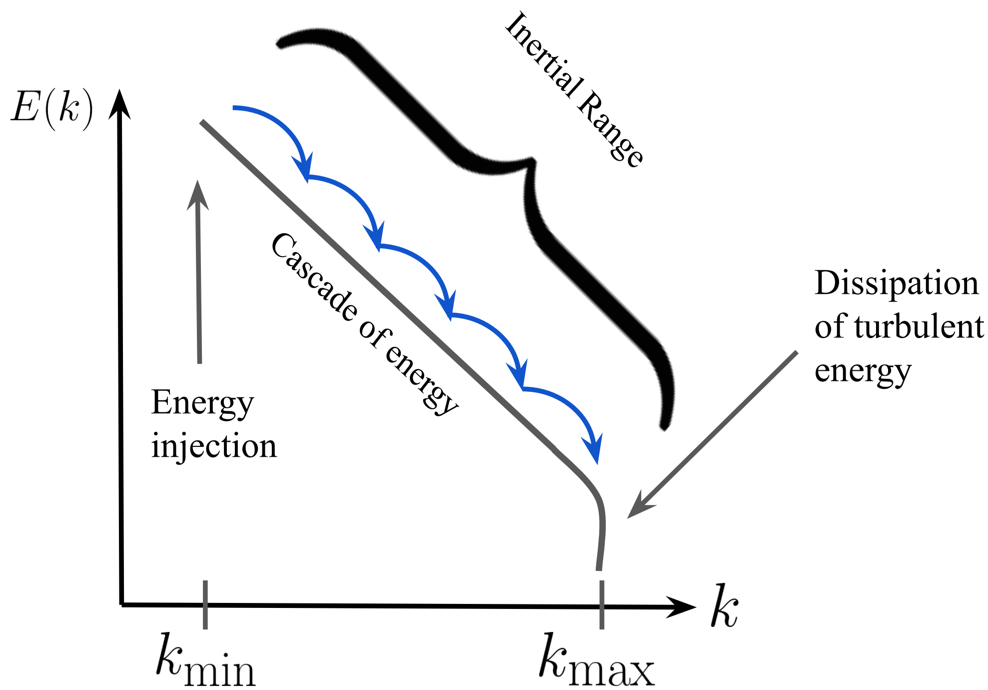


Figure 1.2: Schematic illustration of turbulence energy cascade.

ible steady hydrodynamic turbulence was empirically established by Kolmogorov (1941) as $E(k) \propto k^{-5/3}$ through a phenomenological approach (see section 1.1.2 of Rogachevskii, 2021, for a pedagogical derivation).

An interesting quantity related to turbulence is the **Reynolds number ($\mathcal{R}$e)**, whose value indicates whether a fluid system is turbulent or not. The quantity is defined in the following way: From Eq. (1.5), we found that the change in velocity is governed by two different terms, one related to the cascade of energy and the other related to dissipation. Although both of these processes occur concurrently, their dominance over one another at a given scale determines the behaviour of the velocity evolution. For example, when the term on the right-hand side gets larger than the second term on the left-hand side, the velocity evolution becomes dominated by diffusive decay. In contrast, when the relative proportion of those two terms becomes inverted, the behavioural dynamics of velocity is governed by non-linear scale-to-scale energy transfer. Therefore, at a particular scale, the ratio of these two terms dictates whether the energy cascades or decays. Through such motivation, $\mathcal{R}\mathbf{e}$ is phenomenologically defined by the ratio of the dimensions of those two terms at a scale $L$ as follows,

$$\mathcal{R}\mathbf{e} \approx \frac{v/(L/v)}{v/(L^2/\nu)} = \frac{Lv}{\nu} \tag{1.8}$$

Therefore, from the above formula, it is clear that to have turbulence, or $\mathcal{R}e \gg 1$, one needs to inject energy at very large scales, and the dissipation has to be very small.

In astrophysical sources, due to their enormous size, the length scales at which energy injection happens and the length scales at which energy dissipates stay far from each other; hence, these systems are usually considered turbulent. However, the behaviour of astrophysical turbulence is not governed by Eq. (1.2), but by MHD equations. Astrophysical turbulence is fundamentally compressible, and the work shown in the thesis also considers compressible plasma; however, to introduce the basic concepts of MHD turbulence, we consider here the incompressible MHD equation for simplicity. The evolutionary behaviour of plasma in ideal MHD conditions is governed by the following equations (Verma, 2004),

$$\partial_t \boldsymbol{v} + (\boldsymbol{v} \cdot \nabla)\, \boldsymbol{v} = -\nabla P_{tot} + (\boldsymbol{B} \cdot \nabla)\, \boldsymbol{B} + \nu \nabla^2 \boldsymbol{v} \tag{1.9}$$

$$\partial_t \boldsymbol{B} + (\boldsymbol{v} \cdot \nabla)\, \boldsymbol{B} = (\boldsymbol{B} \cdot \nabla)\, \boldsymbol{v} + \eta \nabla^2 \boldsymbol{B} \tag{1.10}$$

where $\boldsymbol{B}$ is the magnetic field; $P_{tot}$ is the total pressure and defined as $(P + B^2/8\pi)$; $\eta$ is the magnetic diffusivity. Eqs.(1.9) and (1.10), coupled with the incompressibility condition, $\nabla \cdot \boldsymbol{v} = 0$ and no-magnetic monopole condition, $\nabla \cdot \boldsymbol{B} = 0$ descibe the dynamics of incompressible MHD. Similar to the hydrodynamical case, here also the total pressure $P_{tot}$ can be evaluated by solving a Poisson equation of the following kind,

$$-\nabla^2 P_{tot} = \nabla \cdot [(\boldsymbol{v} \cdot \nabla)\, \boldsymbol{v} - (\boldsymbol{B} \cdot \nabla)\, \boldsymbol{B}] \tag{1.11}$$

An interesting property of incompressible MHD equations is that they give rise to Alfvèn waves (Alfvén, 1942; Alfven, 1950), which play a fundamental role in mediating turbulence in incompressible MHD. To understand the behaviour of Alfvèn waves in MHD turbulence, we cast the evolution equations of incompressible MHD via Elsässer variables, with $\nu = 0$ and $\eta = 0$, in the following way (see Eq. (11) of Galtier et al., 2000),

$$\left(\partial_t + \boldsymbol{z}^{-s} \cdot \nabla\right) \boldsymbol{z}^s = -\nabla P_{tot} \tag{1.12}$$

where $\boldsymbol{z}^s = \boldsymbol{v} + s\boldsymbol{b}$ are the Elsässer Variables with $s = \pm$ and $\boldsymbol{b} = \boldsymbol{B}/\sqrt{4\pi}$. In terms of Elsässer variables, the incompressibility and no-magnetic mono-pole equations can be written as $\nabla \cdot \boldsymbol{z}^s = 0$. Further, Eq. (1.11) takes the following form in terms of Elsässer variables,

$$\partial_i \partial_i P_{tot} = -\partial_j \partial_k z_k^{-s} z_j^s. \tag{1.13}$$

The emergence of Alfvèn wave can be observed by perturbing Eq. (1.12) with the following,

$$\boldsymbol{z}^s = \boldsymbol{u} + s\boldsymbol{b}_0 + \delta\boldsymbol{v} + s\delta\boldsymbol{b} \tag{1.14}$$

where $\boldsymbol{u}$ and $\boldsymbol{b}_0$ are the mean velocity and magnetic field, while $\delta\boldsymbol{v}$ and $\delta\boldsymbol{b}$ are the velocity and magnetic field perturbations, respectively. Considering $\boldsymbol{u} = 0$ for simplicity, Eq. (1.12) becomes(see section 7.2 of Galtier, 2022),

$$\left(\partial_t - s\boldsymbol{b}_0 \cdot \nabla\right) \delta \boldsymbol{z}^s = -\nabla P_{tot} - \left(\delta \boldsymbol{z}^{-s}.\nabla\right) \delta \boldsymbol{z}^s \tag{1.15}$$

where $\delta \boldsymbol{z}^s = \delta \boldsymbol{v} + s\delta \boldsymbol{b}$. An interesting property of Eq. (1.15) is its linearization (neglecting the non-linear right-hand side) gives the dispersion relation for the Alfvèn waves, $\omega_k^2 = (\boldsymbol{k} \cdot \boldsymbol{b}_0)^2$ with $\boldsymbol{k}$ being the wave vector and $\omega_k$ being the $k$-dependent circular frequency of the wave. Consequently, Eq. (1.15) is sometimes referred to as the non-linear evolution equation for the Alfvèn waves. Another property of Eq. (1.15) can be realized by noting that if $\delta \boldsymbol{z}^+ = 0$, the evolution of $\delta \boldsymbol{z}^-$ will follow the following equation,

$$\left(\partial_t + \boldsymbol{b}_0 \cdot \nabla\right) \delta \boldsymbol{z}^- = 0 \tag{1.16}$$

Such an equation can be interpreted as $\delta \boldsymbol{z}^-$ is propagating without deformation along the uniform magnetic field $\boldsymbol{b}_0$, with a speed $b_0$. The same reasoning will be applied when $\delta \boldsymbol{z}^- = 0$, and in that case, $\delta \boldsymbol{z}^+$ will propagate in the opposite direction to the mean magnetic field. As a result, $\delta \boldsymbol{z}^s$ can be interpreted as two oppositely propagating entities (often called Alfvèn wave packets) which deform non-linearly when they interact and the interaction is characterised by the right-hand side terms of Eq. (1.15).

In Fig. 1.3 we show a cartoon illustration of the interaction and subsequent deformation of two oppositely propagating Alfvèn wave packets threaded by a mean magnetic field. This non-linear interaction and the subsequent deformation of the Alfvèn waves are responsible for the energy cascade in incompressible MHD turbulence. Proceeding along the same line of argument, Iroshnikov (1964), and Kraichnan (1965) independently realised that, due to the presence of Alfvèn waves, the energy cascade would significantly differ from the Kolmogorov-like hydrodynamic turbu-

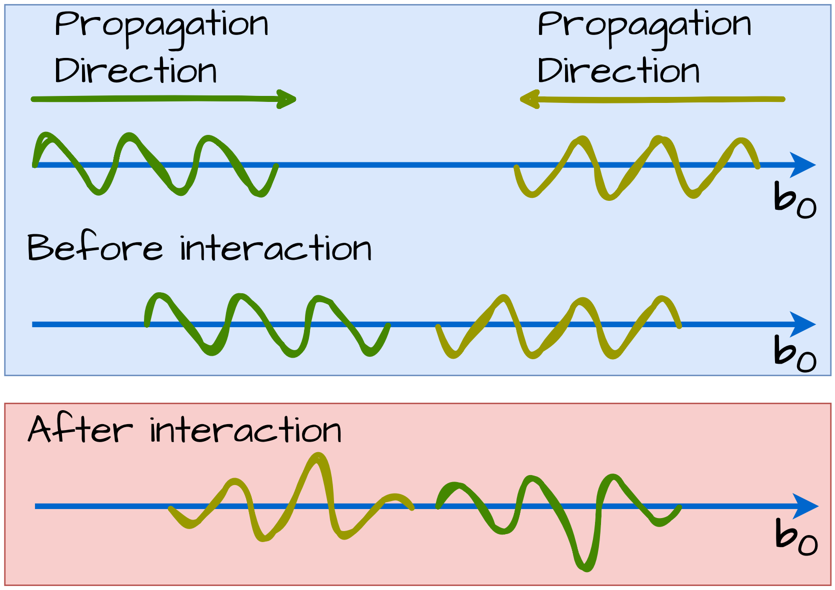


Figure 1.3: Cartoon showing the interaction between two oppositely propagating Alfvèn wave packets.

lence. They calculate the spectrum for the inertial range following $E(k) \propto k^{-3/2}$ for incompressible MHD turbulence. Galtier et al. (2000) following a perturbative approach found that for weak incompressible MHD turbulence ($|\boldsymbol{b}_0|/|\delta \boldsymbol{b}| > 1$), the turbulence spectrum becomes anisotropic and follows $E(k) \propto k_\perp^{-2}$. However, for strong MHD turbulence, the form is still debatable. For an extensive review of MHD turbulence and its current status, readers are encouraged to see Schekochihin (2022); Verma (2004).

As stated earlier, astrophysical plasma is compressible, which makes its study more challenging. Compared to the incompressible MHD case, compressible MHD is capable of generating compressive modes or waves in addition to the Alfvén wave, which can give rise to different types of non-linear interactions and thereby change the turbulence behaviour significantly. With the advent of numerical simulations, the behaviour of compressive MHD turbulence has been extensively studied (Beresnyak & Lazarian, 2019).

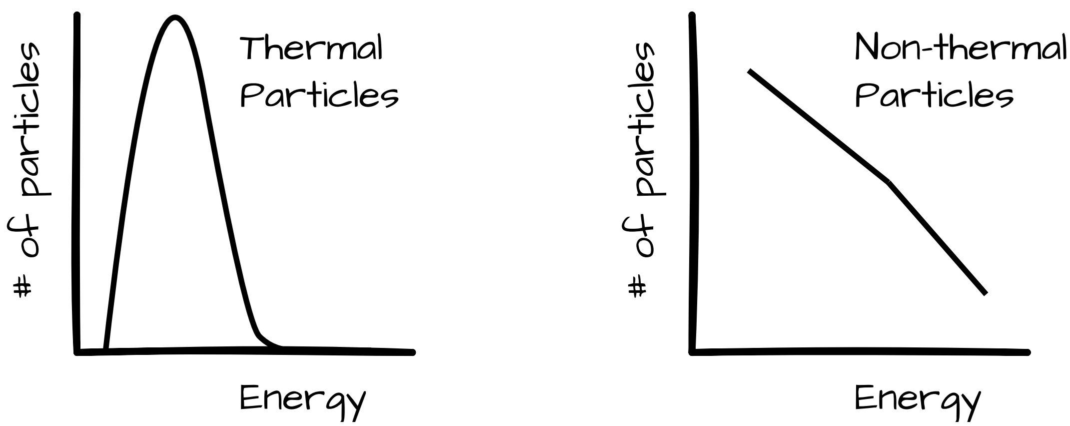


Figure 1.4: Schematic depiction of the typical particle energy distributions observed in turbulent astrophysical plasma. *Left:* Energy distribution of thermal particles following Maxwellian. *Right:* Broken power-law-like energy distribution typically observed for non-thermal particle population.

Moreover, in a typical astrophysical plasma, the collisional timescale is observed to be greater than the majority of plasma behaviour timescales, indicating that collisions between constituent particles in such systems are highly improbable. The absence of collisions within astrophysical turbulence has a significant impact on the turbulence dissipation mechanisms. In hydrodynamic turbulence, the dissipation of turbulence energy happens due to viscosity which is a quantity results from the collision of fluid molecules. However, due to the absence of collisions, such viscous dissipation does not occur in the majority of astrophysical sources; instead, alternative energy dissipation mechanisms operate in these systems. One such mechanism for energy dissipation is wave-particle interactions, through which turbulent waves can transfer their energy to the charged particles in the plasma. Due to such a mechanism, acceleration of charged particles occurs in turbulent astrophysical medium (see section 2.1.1 for more details).

Further, the emission of radiation from the majority of astrophysical systems is typically speculated to arise from two different particle populations. Among them, one population comprises the particles that follow a Maxwell-Boltzman (MB) like energy distribution resulting from the thermal equilibrium that these particles experience with their surroundings and are typically referred to as **thermal particles**. The other population exhibits an energy distribution that significantly differs from the previously known MB case and is referred to as **non-thermal particles**. A schematic representation of the distributions typically observed for these two particle populations is shown in Fig. 1.4. The distribution in the left panel of the figure exhibits a Maxwellian-like morphology, which is expected to be followed by the thermal population. The non-thermal populations are known to follow multiple kinds of distributions, for example, power-law or Kappa-like. In the right panel of the figure, we show a representative energy distribution for the non-thermal particles of the broken power-law type, which is usually considered to investigate the particle distribution in different astrophysical sources. The origin of these non-thermal particles is still debatable; however, according to the currently accepted model, they are considered to originate due to the collisionless turbulent behaviour of the plasma and subsequent particle acceleration (see Comisso & Sironi, 2018, for realization through first principle PIC simulation).

In this thesis, we focus on studying the simultaneous action of various acceleration and energy loss processes charged particles experience in turbulent plasma. To perform the study, we consider two different components of radio-loud AGNs, which are (1) radio lobes and (2) relativistic shocks. Typically radio-loud AGNs are considered highly turbulent, which is further speculated to have a noticeable impact on the emission properties of these sources. In the next section, we introduce radio-loud AGNs along with their various components.

## 1.2 Introduction to radio-loud AGN

Active galaxies (AGN) are considered to be one of the most interesting systems in astrophysics. Compared to a normal galaxy, these galaxies possess a luminous core or nucleus, which outshines the entire galaxy in the majority of cases. Such a phenomenon is often considered to be related to the ongoing black hole (BH) activities that these systems exhibit in their central region. The central BH activities originated from the ongoing accretion process, with which this BH feeds on their surrounding materials. One of the most widely accepted models for the morphology of this central nuclear region considers a gigantic donut-shaped structure of cold gas and dust, with the BH and accretion disc nestled inside the donut's hole.

One out of ten active galaxies shows signs of a jet emanating out of its nuclear region, transporting energy and particles to kpc or even Mpc scales. Such active galaxies are typically referred to as **radio galaxy** or **Quasar** or **Blazar** depending on the viewing angle with which these sources are observed (Peterson, 1997). Radio galaxies are usually categorised into two distinct populations of sources based on their radio power at 1.4 GHz. Such a classification was first realised by Fanaroff and Riley (Fanaroff & Riley, 1974), and the classes were subsequently termed Fanaroff-Riley type I (FR-I) and type II (FR-II). The power output of FR-I-type galaxies is less than that of FR-II types.

Due to such disparity in output power, these sources show different morphological structures. In Fig. 1.5, examples of sources falling into these two different categories are shown, indicating the various components of these systems. Both sources can be observed to have an oppositely directed dual jet-like structure. For the FR-I class, as shown in the left panel of the figure, a plume-like morphology of the jet can additionally be observed, while for the FR-II class, the jet can be seen to maintain a highly collimated structure for a large distance. Often the counter-jet of FR-II radio-loud AGNs is observed to be absent; however, it is expected to be present and of nearly the same intrinsic brightness as the visible jet. Such a phenomenon can be seen in the FR-II radio-loud AGN shown in the right panel of the figure, and the reason behind this is attributed to Doppler boosting, which enhances the

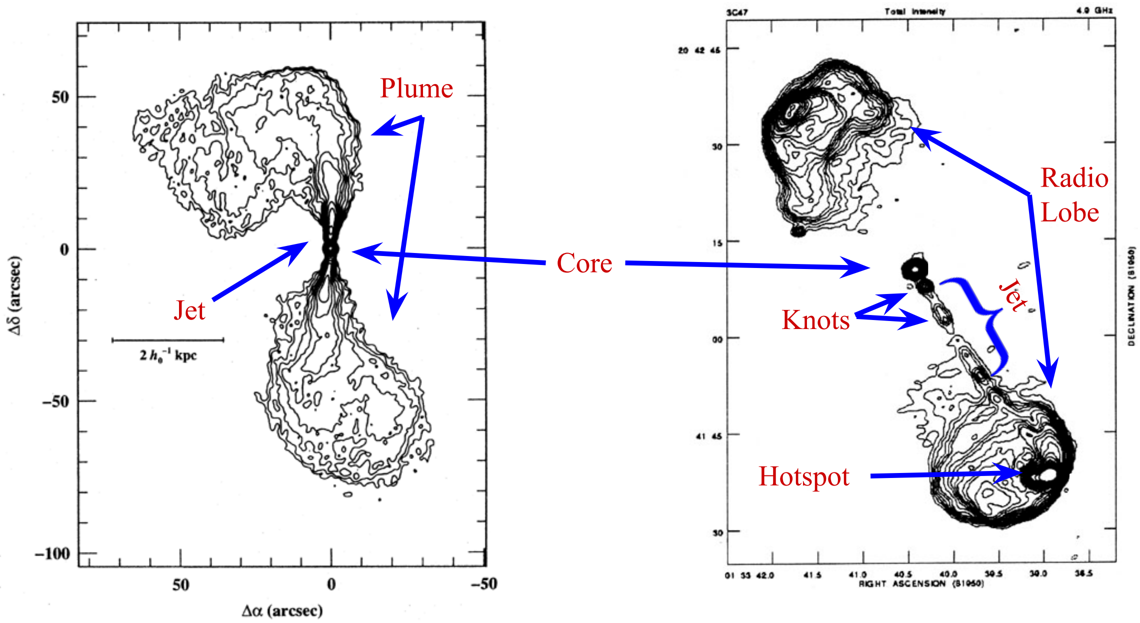


Figure 1.5: Example of Fanaroff-Riley classification. *Left:* Radio 4.9 GHz VLA image of FR-I type radio galaxy, M84 (Laing & Bridle, 1987). *Right:* Radio 4.9 GHz VLA image of FR-II quasar 3C 47 (Bridle et al., 1994).

brightness of the jet approaching the observer and decreases the brightness of the receding counter-jet (Urry & Padovani, 1995). The collimated jet structure of FR-II often shows evidence of knot-like structures embedded in it. These knots are associated with multiple re-collimation shocks (Hervet et al., 2017). Such re-collimation shocks result from the mechanical equilibrium between the under-pressured relativistic jet and its surrounding external medium. Typically, these shocks are considered relativistic (Baring et al., 2016; Crumley et al., 2019).

A **hotspot** region is typically seen at the jet termination point of the FR-II radio galaxy, which is distinguishable due to its high luminosity in comparison to its surroundings and is typically connected with head shock. Such a high-luminosity region is often found embedded inside a lobe-like structure called **radio lobe**. Such a structure results from the **backflow** of AGN jet materials in a direction opposite to

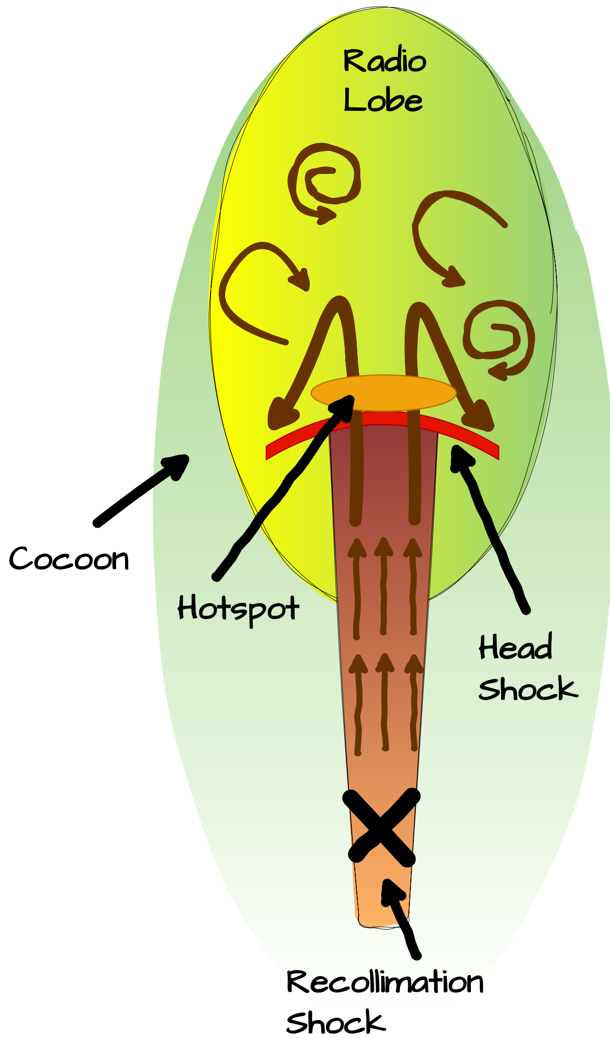


Figure 1.6: Cartoon representation of various components of FR-II type AGN jet.

the jet, which did not get converted to radiation at the hotspot (Longair et al., 1973). Due to the chaotic nature of these backflow plasma materials, radio lobes are often considered turbulent systems (Matthews et al., 2019). In Fig. 1.6 we schematically show various components of the FR-II type AGN jets.

In addition to such an interesting morphology, radio galaxies are observed to emit radiation over a vast range of frequencies. Different components of radio-loud AGNs are observed to emit differently, and the measure of the emission from various com-

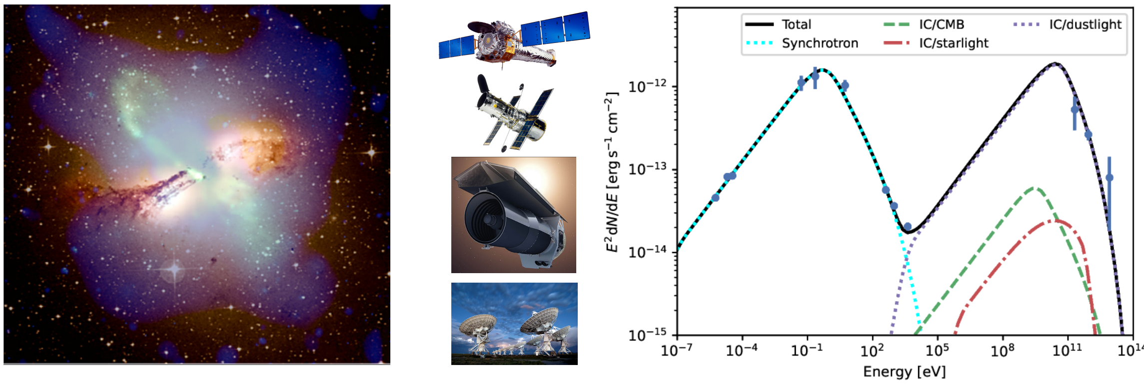


Figure 1.7: *Left:* Composite image of Centaurus A (adopted from Chandra Photo Album). *Middle:* Various observational facilities that were involved in producing the observational data. From top to bottom: Chandra X-ray telescope, Hubble space telescope, Spitzer Infrared telescope and VLA radio facility. *Left:* Spectral energy distribution of Centaurus A (Wang et al., 2021).

ponents contains the clue to deciphering the multi-scaled micro-physical plasma processes that are taking place inside them. Typically, the spectral energy distribution (SED) of these components exhibits a double-hump-like morphology. An example of SED is shown in the right panel of Fig. 1.7. The SED is computed for the jet of an FR-I type radio-loud AGN, Centaurus A (left panel of the figure), through various observational facilities (middle panel). The low-frequency emission for each component is usually attributed to synchrotron radiation from relativistic charged particles gyrating around the local magnetic field. A typical characteristic of such a radiation process is that the radiation flux follows an inverse power-law trend with the frequency, $S \propto \nu^{-\kappa}$ where $\kappa$ is referred to as the spectral index. For the high-energy part, different components emit through different radiative processes. Below, we categorically describe the origin of the emission from different components of the radio-loud AGN source (Harris & Krawczynski, 2006).

- The jet component of FR-I type radio galaxy strongly supports synchrotron origin of the emission from radio frequencies to X-rays. For these kinds of jets, $\kappa_x > \kappa_{xo} > \kappa_r$, where $\kappa_x, \kappa_{xo}$ and $\kappa_r$ is the spectral index at X-ray, X-ray to optical and radio frequencies. Such a model suffers from a problem. Synchrotron X-ray requires non-thermal leptons of very high energy, but due to the magnetic field, such particles cannot hold their energy for enough time to give off X-ray emission at a distance far from the core. Therefore, the in-situ reacceleration of those non-thermal particles through turbulence is often considered in such high-energy synchrotron models (Kataoka et al., 2006).

- The emission from FR-II jet is typically attributed to the inverse Compton mechanism, whereby photons from the surrounding cosmic ray microwave background get upscattered by high-energy non-thermal particles (IC-CMB) (Celotti et al., 2001; Ghisellini, G. et al., 2005; Tavecchio et al., 2000). For such a jet, the synchrotron origin of the emission would require multiple populations of non-thermal radiating particles, and the upscattering of the photons originating through the synchrotron process via inverse Compton (also called as **sychrotron self Compton**, SSC) would require an order of magnitude higher magnetic field than the equipartition one.

- Emission from the knots present in the FR-II jets is usually considered of synchrotron origin and associated with shocks.

- Emission from the radio lobe in X-ray is observed to explain via an IC-CMB process (Croston et al., 2005; Gill et al., 2021).

- X-ray emission from the hotspot is still debatable. For some hotspots, it is better explained through SSC (Hardcastle et al., 2004) while for others, synchrotron radiation provides better explanations (Hardcastle et al., 2007a). Similar to earlier considerations on the synchrotron origin of jet X-ray emission for FR-I radio galaxies, turbulent acceleration is often considered a possible mechanism for re-accelerating the particles for a sustained X-ray emission (Fan et al., 2008). Further, some FR-II radio galaxies show evidence of diffuse optical emission on the kpc scale surrounding the hotspot region. Such emission is observed to have a synchrotron origin, and distributed particle acceleration through turbulence has also been invoked there to maintain the optical emission up to the kpc scale (Cheung et al., 2005; Lähteenmäki & Valtaoja, 1999; Orienti et al., 2012; Prieto et al., 2002; Prieto & Kotilainen, 1997; Thomson et al., 1995).

Following the above discussion of employing a turbulent acceleration mechanism to address certain observational features in the radio-loud AGN system, in this thesis we try to understand the interplay of turbulence and shocks on the emission from the radio lobe component. Additionally, we study the turbulent acceleration that is typically expected to happen downstream of the relativistic shocks, which are typically observed in these radio-loud AGN sources. In the following two sections, we discuss the motivations for choosing these two components as candidates for our study.

### 1.2.1 Radio lobes

Radio lobes are known to be highly turbulent. The underlying turbulence is also found to contribute to accelerating the non-thermal particles residing there via a stochastic acceleration mechanism (Fan et al., 2008; Massaro & Ajello, 2011; O'Sullivan et al., 2009). Further, the presence of shocks due to the turbulent density compression at random locations in such a system has been observed through numerical simulations and speculated to act as an agent for accelerating charged particles present there (Matthews et al., 2019).

Radio lobes are also observed to emit in different frequency bands, from radio to X-ray. Such frequency-dependent emission is a manifestation of the particular microphysical processes that are taking place inside the radio lobes. Therefore, to gain

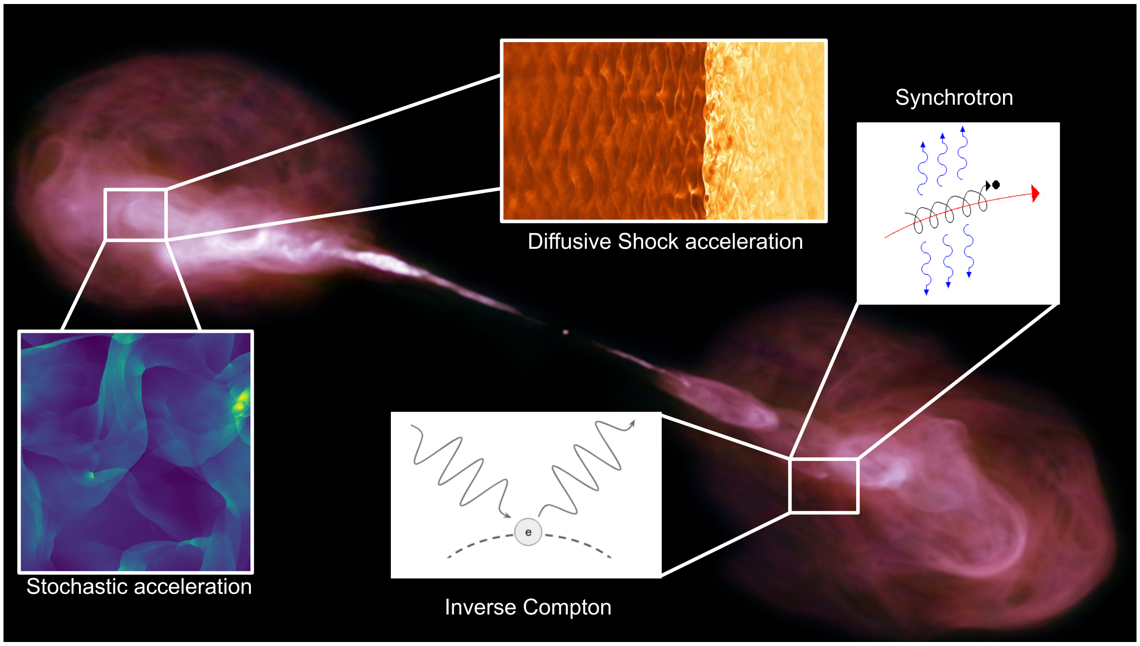


Figure 1.8: Picture of a radio lobe of FR-II radio loud AGN, indicating the micro-physical processes that has been used to compute the emission for this work. **Image descriptions:** *Background:* VLA radio composite image of Hercules A (Credit: Credit: B. Saxton, W. Cotton and R. Perley (NRAO/AUI/NSF)); *Stochastic acceleration:* Supersonic turbulent density field; *Diffusive shock acceleration: Collisionless shock observed through PIC simulations (Mignone et al., 2018)*; *Synchrotron:* Spiraling charged particle around magnetic field emitting radiation (Source: James Schombert/University of Oregon); *Inverse Compton:* Incoming photon getting scatted through an electron.

an understanding about the actual micro-physical processes, here we undertake the task of modelling the behaviour of the non-thermal particles in radio lobes, considering different acceleration and loss mechanisms working together in tandem. In Fig. 1.8, we show a representative picture of the work we undertake here, showing the locations of different acceleration and loss processes.

### 1.2.2 Relativistic shocks

Radio loud AGN systems exhibit shock-related features, such as knots, hotspots, etc. Due to the relativistic nature of the plasma flow in such systems, these shocks are often speculated to be relativistic in nature. Typically, relativistic shocks are mediated by small-scale turbulence in which the Larmour radius of the gyrating particles exceeds the correlation length of the turbulence (Lemoine et al., 2006). Various work has been devoted to comprehend the acceleration phenomena that these shocks can cause by focusing on the importance of spatial diffusion of charged particles in making them undergo sufficient numbers of Fermi cycles (upstream to downstream to upstream) (Plotnikov et al., 2011). Here, our aim is to understand the effect that this small-scale turbulence drives on particle acceleration via turbulence. Such a scenario is typically obtained in the downstream of relativistic shock waves once the particle escapes the shock region.

## 1.3 Objectives of the thesis

The primary aim of this thesis is to understand the manifestations of the interplay of different particle acceleration processes and radiative losses on the emission of turbulent astrophysical sources. The study is predicated mainly on the development and execution of cutting-edge numerical simulations of astrophysical sources employing sub-grid-scale (SGS) level physical models for particle acceleration processes. Due to the resolution constraints of numerical simulations, resolving all the necessary scales becomes impossible. To account for the influence of unresolved-scale activities on a large-scale simulation, one employs SGS-level modelling to model the micro-physical processes. In this work, we only restrict ourselves to the weakly magnetised regime. The principal objectives of this thesis can be stated as follows:

1. Developing a numerical framework for studying the effect of stochastic turbulent acceleration in large-scale astrophysical simulations.

2. Studying the interplay of various micro-physical acceleration and loss processes on the emission of the turbulent radio lobes of FR-II radio galaxies via the developed framework.

3. Developing an SGS-level model for particle acceleration in a scenario where the correlation length-scale of the turbulence is less than the particle's gyro-radius and studying its interplay with different loss processes. Such a scenario can be realised in the vicinity of collisionless shocks.

## 1.4 Outline of the chapters

The thesis is structured as follows: In **chapter 2**, we introduce the relevant plasma processes considered in this work. We also describe the numerical framework that has been utilised to achieve the above-mentioned objectives. In **chapter 3**, we showcase the numerical algorithm we developed to study the effect of stochastic acceleration. We validated the algorithm by performing various tests and comparing it with other existing algorithms. We then study the interplay of different acceleration processes through controlled test problems. We demonstrate the application of the developed module on an astrophysical source in **chapter 4**. We consider the radio lobe of the FR-II radio galaxy to study the interplay of particle acceleration processes and understand their subsequent emission behaviour. A phenomenologically motivated SGS model is employed for the stochastic acceleration process. We show the impact of such an SGS model on the multi-frequency emission of the simulated source. **chapter 5** considers the computation of the transport coefficients for the non-thermal charged particles in a situation of small-scale turbulence. We consider a turbulence spectrum that lacks power at the resonant scale and perform a quasi-linear calculation for the transport coefficients, focusing mainly on the particle acceleration through such turbulence. The turbulent acceleration of particles in a system consisting of relativistic shocks can be understood through the analysis we describe in this chapter. Our findings are summarised and discussed in **chapter 6**. We conclude the thesis by discussing future works that can be accomplished as a result of the developments made in this thesis, as well as the potential extension of the current developments. In the Appendix (A) we sketch out the derivations for the relevant equations used in this work.

# Chapter 2

# Microphysical processes

*This chapter introduces the theoretical and numerical framework utilized while carrying out the work presented in this thesis. After introducing the fundamental equations governing the behaviour of the plasma, this chapter discusses various particle acceleration processes in astrophysical plasma. This chapter also introduces various mechanisms by which plasma particles lose their energy. Subsequently, the novel Eulerian-Lagrangian numerical framework is introduced.*

---

Plasma is all pervaded in the universe and studying its behaviour plays a crucial role in understanding the present-day universe.

## 2.1 Introduction to plasma processes

By definition, plasma is a state of matter when its constituents get ionized; however, due to Coulomb attraction, such a state will only stay for a short amount of time unless some other thermodynamic quantities are involved, and one such parameter is temperature. Temperature plays a significant role in sustaining the electrostatic plasma state by giving a random component to the velocities of the constituents. For a more general plasma system, typically observed in astrophysical scenarios, the magnetic field also plays a fundamental role in sustaining the plasma. Due to the presence of charged particles whose evolution is governed collectively by Lorentz force law, Maxwell's equation, and temperature, the processes inside the plasma show a multi-scale nature, i.e., at different scales, the behaviour of plasma changes. Such multi-scaleness occurs not only on spatial scales but also on temporal scales. Such scales can be realized by proper statistical mechanical treatment of the plasma system. For example, due to the presence of temperature inside the medium of an overall neutral plasma, the long-range Coulomb interaction gets screened, and beyond a certain length, known as **Debye length**, the coulomb potential falls off exponentially due to other charges of opposite polarity. Mathematically, beyond such a length scale, the two-point spatial correlation of any function computed at two different positions in a system of charged particles experiencing Coulombic interactions at thermal equilibrium decays exponentially (Brydges & Federbush, 1981). A study of such a coulomb gas in the $d > 2$ dimension using renormalization group theory revealed the emergence of Debye length as an intrinsic length scale related to electrostatic plasma (Barkhudarov, 2014). Debye length, therefore, marks a spatial scale beyond which plasma can be treated as a state driven by the collective interactions of its constituents and the notion of a single charged particle becomes suppressed. A timescale associated with this Debye length also emerges due to the presence of temperature and the need to maintain overall neutrality, which govern the time up to which a single charge potential can be felt before it gets screened. An inverse of such timescale is known as **plasma frequency**. There are many such spatiotemporal scales that exist and can be found through proper statistical and mechanical treatments.

Below we briefly introduce the evolutionary equation of plasma kinetics for completeness.

Typically, plasma can be treated as a collection of charged particles, and for such a system, the phase-space density function considering the position and velocity of the individual particles can be written in the following way,

$$F_s(\boldsymbol{r}, \boldsymbol{v}, t) = \sum_{i=1}^{n_s} \delta(\boldsymbol{r} - \boldsymbol{R}_i(t))\, \delta(\boldsymbol{v} - \boldsymbol{V}_i(t)) \tag{2.1}$$

where $s$ specifies the particle species, $n_s$ is the number of particles in that species, $\delta(r - r_0)$ is the delta function peaking at $r = r_0$ and $(\boldsymbol{R}_i(t), \boldsymbol{V}_i(t))$ is the coordinate of $i^{th}$ particle in the phase space at time $t$. The evolutionary dynamics of such a density function is given by the following equation (see section 2.1.3 Swanson, 2008, for derivation)

$$\partial_t F_s + \boldsymbol{v} \cdot \nabla F_s + q_s (\boldsymbol{E}^m + \boldsymbol{v} \times \boldsymbol{B}^m) \cdot \frac{\partial F_s}{\partial \boldsymbol{p}} = 0 \tag{2.2}$$

where the subscript $m$ denotes that the electric and magnetic fields, $\boldsymbol{E}^m$ and $\boldsymbol{B}^m$ respectively, are a combination of external and the self-consistent field that the particles produce through Maxwell's equation; $\boldsymbol{p}$ denotes the momentum of the particles. Eq. (2.2) is known as **Klimontovich equation**, and it considers individual particle dynamics. The solution of such an equation is very difficult and not very illuminating, as this equation contains information that is unnecessarily huge for describing the evolution of the system at the spatial and temporal scales of investigation. Therefore, averaging over a small volume in phase space is typically performed on Eq. (2.2) to compute an equation with reduced information, which is necessary to understand the plasma behaviour. Additionally, by averaging the equation, one obtains a smoothed-out distribution function that does not contain any singularities arising from the discreteness of the charged particles. The volume over which the averaging is done plays an important role in the averaged behaviour of the plasma; for example, if it is too large, we lose the resolution for studying the variation in the plasma properties, or if it is too small, then the density at two adjacent locations might get very large. Typically, the volume is constructed by considering the spatial volume of the order of the Debye sphere, and the velocity range is considered such that the sphere could include many particles (Swanson, 2008). Upon performing such averaging, one gets an equation capable of modelling the evolutionary dynamics of plasma beyond the Debye length. Such an equation is known as **Vlasov equation**, which in cgs or gaussian units takes the following form,

$$\frac{\partial f}{\partial t} + (\boldsymbol{v}.\nabla) f + q\left(\boldsymbol{E} + \frac{\boldsymbol{v}}{c} \times \boldsymbol{B}\right).\frac{\partial f}{\partial \boldsymbol{p}} = 0 \tag{2.3}$$

where $f$ is the average distribution function. Note that we have omitted the subscript $s$, as the following discussion will consider only a single species of particles. Eq. (2.3) coupled with the following Maxwell's equations constitute a closed set of equations describing self-consistent plasma behaviour.

$$\begin{aligned}
\nabla \times \boldsymbol{B} &= \frac{1}{c}\frac{\partial \boldsymbol{E}}{\partial t} + \frac{4\pi}{c} q \int_{-\infty}^{\infty} d^3\boldsymbol{v}\boldsymbol{v} f(\boldsymbol{r}, \boldsymbol{v}, t) + \frac{4\pi}{c}\boldsymbol{J}_{ext} \\
\nabla \cdot \boldsymbol{E} &= 4\pi q \int_{-\infty}^{\infty} d^3 v f(\boldsymbol{r}, t) + 4\pi\rho_{ext} \\
\nabla \cdot \boldsymbol{B} &= 0 \\
\nabla \times \boldsymbol{E} &= -\frac{1}{c}\frac{\partial \boldsymbol{B}}{\partial t}
\end{aligned} \tag{2.4}$$

where $\boldsymbol{J}_{ext}$ and $\rho_{ext}$ defines the external current density and charge density.

The presence of Eq. (2.4) makes Eq. (2.3) non-linear and challenging to solve for a generic situation. Therefore, one needs to make additional analytical assumptions to extract information from Eq. (2.3). One such assumption, also known as **test particle** approach, considers computing the evolution of the distribution function due to the specified background electric and magnetic field. In this thesis, we will concentrate on the quasi-linear evolution of homogeneous plasma derived from the test particle approach. In the following section, we sketch out the derivation of the evolution equation that the distribution function will follow when the background electric and magnetic fields are weakly perturbed. The evolution equation for the distribution function in such a scenario will be helpful in understanding the particle acceleration process and is also essential for the work presented in the following chapters.

### 2.1.1 Quasi-linear evolution of plasma and particle acceleration

To derive the quasi-linear evolution of the distribution function, we perform a multi-scale analysis on Eq. (2.3) through the following kinds of perturbations,

$$\begin{aligned}
\frac{\partial}{\partial t} &= \frac{\partial}{\partial T_0} + \epsilon^1 \frac{\partial}{\partial T_1} + \epsilon^2 \frac{\partial}{\partial T_2} + \mathcal{O}(\epsilon^3) \\
f &= f_0 + \epsilon^1 f_1 + \epsilon^2 f_2 + \mathcal{O}(\epsilon^3) \\
\boldsymbol{E} &= \epsilon^1 \boldsymbol{E_1} + \epsilon^2 \boldsymbol{E_2} + \mathcal{O}(\epsilon^3) \\
\boldsymbol{B} &= B_0 + \epsilon^1 \boldsymbol{B_1} + \epsilon^2 \boldsymbol{B_2} + \mathcal{O}(\epsilon^3).
\end{aligned} \tag{2.5}$$

Upon substituting the perturbed fields in the homogeneous (zero spatial gradient) version of Eq. (2.3) and noting the randomness of the perturbation components, the evolution equation for $f_0$ takes the following form (see appendix A.1 for the derivation),

$$\frac{\partial f_0}{\partial T_2} + q \left\langle \left( \boldsymbol{E_1} + \frac{\boldsymbol{v}}{c} \times \boldsymbol{B_1} \right) . \nabla_p f_1 \right\rangle = 0. \tag{2.6}$$

The above equation describes the evolution of the zeroth order distribution function due to linear perturbations (or first-order perturbations) of the $\boldsymbol{E}$, $\boldsymbol{B}$ and $f$ fields. Note the timescale, $T_2$, on which such an evolution is realized. This indicates the temporal hierarchy of the processes that are taking place inside the plasma system. For example, while deriving Eq. (2.6) we consider $f_0$ to be steady over the timescale $T_0$ which gave rise to the evolution of the perturbation $f_1$ on a timescale $T_1 > T_0$. Those perturbation starts to affect the evolution of the zeroth order distribution function on a timescale of $T_2 > T_1$. This is an advantage of the multi-scale analysis, where the individual evolution processes happening at different timescales can be decoupled from the main equation and studied separately.

Upon substituting the form for $f_1$, Eq. (2.6) gives rise to a diffusion-like equation for $f_0$ of the following form(refer appendix A.1 for the derivation),

$$\frac{\partial f_0}{\partial T_2} = -q^2 \sum_{m=-\infty}^{\infty} \int d^3k \left\langle \left[ L_{||}^* \left( \tilde{E_{||}}^k \right)^* J_m(\beta) + \left( L_\perp^* - \frac{1}{p_\perp} \left( \frac{k_{||} v_{||}}{(\omega^k)^*} - 1 \right) \right) \left( \tilde{E_\perp}^k \right)^* \right] \right.$$
$$\left. \iota \frac{1}{m\Omega + k_{||} v_{||} - \omega^k} \left( L_{||} \tilde{E_{||}}^k J_m(\beta) + L_\perp \tilde{E_\perp}^k \right) f_0 \right\rangle \tag{2.7}$$

The above equation contains various terms, which are explained in appendix A.1. An interesting property of the above equation is the presence of a term, $m\Omega + k_{||} v_{||} - \omega^k$, relating quantities of the particles (such as $\Omega$ and $v_{||}$), which constitutes the distribution function, with the waves (such as $k_{||}$ and $\omega^k$) which arises due to the linear perturbations of the background electric and magnetic field. Such a term is capable of driving resonance, and when this resonance condition is satisfied between the particles and waves, the distribution function evolves. Such a resonance scenario is typical for quasi-linear theory, and it is often attributed to the fact that the quasi-linear approach in the physical space considers only the zeroth order orbit (Helical orbit due to mean magnetic field) to evaluate the diffusion coefficient. Eq. (2.7) can further be represented as a diffusion equation for $f_0$ (see Eqs. 14 and 15 of Lerche, 1968), which upon averaging over pitch-angle becomes,

$$\begin{aligned} \frac{\partial f_0}{\partial T_2} &= \frac{1}{p^2} \frac{\partial}{\partial p} \left( p^2 D_{pp} \frac{\partial f_0}{\partial p} \right) \\ &= \frac{\partial}{\partial p} \left( D_{pp} \frac{\partial f_0}{\partial p} \right) + \frac{2 D_{pp}}{p} \frac{\partial f_0}{\partial p}, \end{aligned} \tag{2.8}$$

where the form of the diffusion coefficient, $D_{pp}$, is a complicated function of a series of Bessel functions of the first kind and for a generic wave, the computation of $D_{pp}$ becomes very challenging.

The whole exercise of deriving the evolution of the zeroth order distribution function can be interpreted as follows, When the background electric and magnetic fields of Eq. (2.3) are perturbed weakly, they generate waves that interact with the particles constituting the zeroth order distribution function through a resonance condition. This means not all the waves will interact with all the particles residing inside the plasma; there will be certain waves (characterized by their frequency and wave vector) which will interact with particles having specific values of the gyrofrequency ($\Omega$), and the velocity. Through such resonant interactions, the distribution function subsequently evolves following a diffusion- and advection-like behaviour (the first term and the second term of the right-hand side of Eq. 2.8, respectively). The advection part of Eq. (2.8) describes the acceleration of the particles that constitute the distribution function $f_0$. Such acceleration occurs due to the interaction between the charged particles and the waves from the background field, through which the waves transfer their energy to the particles and get dampened. Moreover, this energization process is random in nature which implies that there could arise a situation whereby the particles transfer their energy to the waves, making them amplified. The former situation is more likely to occur than the latter one, making the entire process an overall acceleration process. However, the random behaviour of the energization process is taken care of by the presence of the diffusion term in Eq. (2.8). Such kind of acceleration of the charged particles is known as **stochastic turbulent acceleration** (STA) or **Fermi II$^{nd}$ order acceleration** process.

Another kind of acceleration of these charged particles is possible considering the shocks, which is known as **diffusive shock acceleration** (DSA) or **Fermi I$^{st}$ order acceleration** process. In this scenario, the charged particles get accelerated by interacting with the waves as before, but due to the shock conditions, the impact of such interactions on the particles results only in acceleration. The random energization does not occur here, making this acceleration more efficient than STA. The process of DSA is also defined through an advection-diffusion-like evolution of the distribution function; however, in this case, the advection and diffusion happen in the spatial domain, not in the momentum domain (see Chapter 5 of Zank, 2013, for details).

The work presented in this thesis aims to study the interplay of these two acceleration processes in turbulent astrophysical plasma. In the next section, we describe the development of the MHD equations, which play a fundamental role in our study, from the Vlasov equation.

### 2.1.2 Magneto-hydrodynamical evolution of plasma

From the Vlasov equation, one can calculate a coarse-grained spatio-temporal scale where, instead of considering velocity fluctuations separately, one utilises the moments of these fluctuations. By taking such a velocity moment of the Vlasov equation, one gets fluid-like equations for describing the plasma behaviour. These fluid-like equations combined with Maxwell's equations are termed as **magneto-hydrodynamic (MHD)** equations. For ideal plasma, the MHD equations can be written in the following way,

$$\frac{\partial \rho}{\partial t} + \nabla \cdot (\rho \boldsymbol{v}) = 0\,, \tag{2.9}$$

$$\frac{\partial \boldsymbol{v}}{\partial t} + (\boldsymbol{v} \cdot \nabla)\boldsymbol{v} = -\frac{1}{\rho}\nabla P + \frac{1}{\rho}(\nabla \times \boldsymbol{B}) \times \boldsymbol{B}\,, \tag{2.10}$$

$$\frac{\partial P}{\partial t} + \boldsymbol{v} \cdot \nabla P + \Gamma P \nabla \cdot \boldsymbol{v} = 0\,, \tag{2.11}$$

$$\frac{\partial \boldsymbol{B}}{\partial t} = \nabla \times (\boldsymbol{v} \times \boldsymbol{B})\,, \tag{2.12}$$

where the quantities $\rho$, $P$, $\boldsymbol{v}$, and $\boldsymbol{B}$ represent density, pressure, velocity, and magnetic field, respectively; the magnetic field $\boldsymbol{B}$ further satisfies the constraint $\nabla \cdot \boldsymbol{B} = 0$; and $\Gamma$ represents the ratio of specific heats. Similar to the hydrodynamic waves, the MHD equations give rise to different kinds of linear waves (originating from linear perturbations to the MHD equations). For a typical ideal compressible MHD system, three kinds of waves can be observed, which are known as Alfvèn wave, fast wave, and slow wave. The last two waves are compressive and can not be found for incompressible MHD. For our purpose of study, the fluctuations due to these waves are considered the source of fluctuations in the turbulent particle acceleration process.

## 2.2 Introduction to radiation processes

The primary mode of information transfer from distant astrophysical sources to us is through the emission of radiation. However, in the era of multi-messenger astronomy, other modes, such as gravitational waves, are also becoming tools for investigating the processes that occur in these sources. In this thesis, our primary concern would be the former mode of information transfer. Astrophysical sources are observed to emit radiation spanning a huge range of frequencies. Analysis of the emission for such a range of frequencies helps decipher the actual micro-physical processes happening in those systems. For the majority of astrophysical sources, the emitted radiation is typically classified into the following three different categories,

- **Thermal radiation:** The radiation emitted by the particles follows a Maxwellian energy distribution.
- **Non-thermal radiation:** The radiation emitted by the non-thermal particle population residing in the turbulent plasma.
- **Line emission:** The radiation originates from the energy level transitions of the atoms and molecules present in the astrophysical sources.

Through all the kinds of radiation described above, the radiating particles lose a portion of their energy by emitting it through radiation. In this work, we primarily

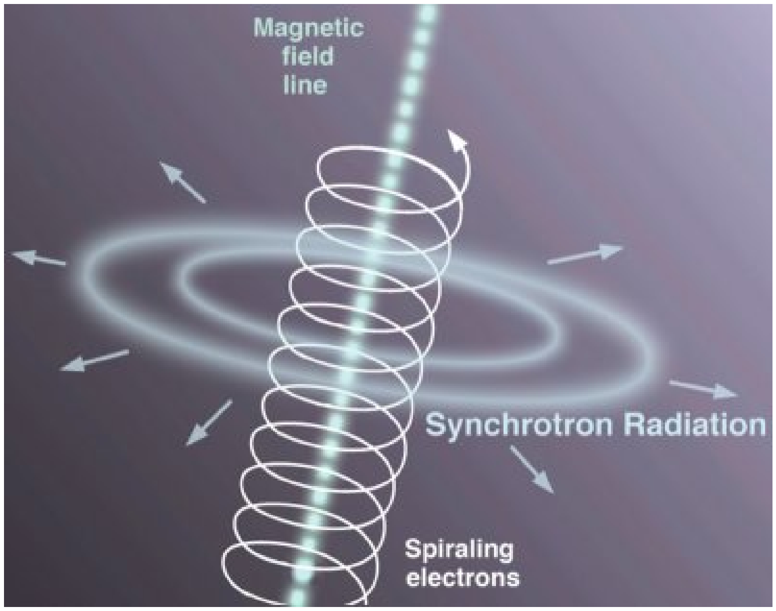


Figure 2.1: Schematic representation of the synchrotron process
(Source: Jon Lomberg/Gemini Observatory).

focus on two radiation loss processes, along with the adiabatic loss/gain, that the non-thermal particles suffer in turbulent astrophysical systems. In the following sections, we describe these three processes in detail.

### 2.2.1 Synchrotron radiation

Charged particles can radiate their energy when they undergo any mechanical acceleration or deceleration. Note that the kind of acceleration we refer to here differs from the acceleration considered in the previous section. In the previous section, by acceleration, we meant "energization of the charged particles at a compensation of the energy from the underlying turbulent field," but here, "acceleration" means "the change in the velocity of the charged particles through mechanical processes," as will be discussed below. The analytical model of such radiation arising due to the mechanical acceleration or deceleration process of the charged particles is given by the following electromagnetic potential function, known as **LiènardWiechert potential**

(Bartelmann, 2013; Englert, 2014; Sengupta, 2007),

$$\phi(\boldsymbol{r}, t) = \left(\frac{q}{R(1 - \boldsymbol{e}\cdot\boldsymbol{\beta}{-}\boldsymbol{s})}\right)_{t_r}, \qquad \boldsymbol{A}(\boldsymbol{r}, t) = \frac{\boldsymbol{\beta}_s(t_r)}{c}\phi(\boldsymbol{r}, t) \tag{2.13}$$

where $\phi$ and $\boldsymbol{A}$ are the scalar and vector electromagnetic potentials respectively measured at a spatial position $\boldsymbol{r}$ and at time $t$ due to a charged particle moving with velocity $\boldsymbol{\beta} = \boldsymbol{v}/c$ at an earlier time $t_r = t - R/c$, with $R = |\boldsymbol{r} - \boldsymbol{r}_0\,(t_r)\,|$ being the distance between the position of the charged particle at a time $t_r$ and the point of observation; $\boldsymbol{e}$ is the unit vector directing from the charged particle to the point of observation, $\boldsymbol{e} = \boldsymbol{R}/R$. The corresponding electric, $\boldsymbol{E}$, and magnetic, $\boldsymbol{B}$, fields at the point of observation can be computed by properly differentiating the above potentials and are described as follows,

$$\begin{aligned} \boldsymbol{E}(\boldsymbol{r}, t) &= \frac{q}{(R - \boldsymbol{\beta}\cdot\boldsymbol{R})^3}\left[(\boldsymbol{R} - \boldsymbol{\beta}R)\left(1 - \beta^2\right) + \left(\boldsymbol{R}\times\left\{(\boldsymbol{R} - \boldsymbol{\beta}R)\times\frac{\dot{\boldsymbol{\beta}}}{c}\right\}\right)\right], \\ \boldsymbol{B}(\boldsymbol{r}, t) &= \frac{\boldsymbol{R}\times\boldsymbol{E}(\boldsymbol{r}, t)}{R}. \end{aligned} \tag{2.14}$$

The first term in the right-hand side of the electric field corresponds to a generalised Coulombic field originating due to the moving charged particle, while the second term corresponds to the radiation that the particle emits due to its acceleration $\dot{\boldsymbol{\beta}} = \dot{\boldsymbol{v}}/c$. The corresponding radiation power, which can be calculated by computing the Poynting vector for the radiation terms present in the electric and magnetic fields, takes the following form (see Eqs. 1.129-1.132 of Bartelmann, 2013):

$$\frac{dL}{d\Omega_s} = \frac{dE}{dtd\Omega_s} = \frac{q^2}{4\pi c\,(1 - \boldsymbol{e}\cdot\boldsymbol{\beta})^5}\left|\boldsymbol{e}\times\left[(\boldsymbol{e} - \boldsymbol{\beta})\times\dot{\boldsymbol{\beta}}\right]\right|^2 \tag{2.15}$$

where $\Omega_s$ is the solid angle. Upon integrating Eq. (2.15) over the entire solid angle, the total power is described by the following form (see Eq. 1.135 of Bartelmann, 2013):

$$L_{tot} = \frac{dE_{tot}}{dt} = \frac{2q^2}{3c}\gamma^6 \left[\dot{\boldsymbol{\beta}}^2 - \left(\boldsymbol{\beta} \times \dot{\boldsymbol{\beta}}\right)^2\right] \tag{2.16}$$

where $\gamma$ is the Lorentz factor of the charged particle. Eq. (2.16) gives a quantitative measure of the total power emitted by the charged particle at different acceleration situations.

Relativistic charged particles residing in magnetized astrophysical systems are known to follow a helical path around the local magnetic field, and in the course of such a movement, they suffer centrifugal acceleration. The radiation that those particles emit in such a situation is known as **synchrotron radiation**, and the total radiated power by a single charged particle can be written as follows,

$$L_{syn} = \frac{dE_{syn}}{dt} = c\gamma^2\sigma_T U_B \tag{2.17}$$

where $\sigma_T$ is the Thomson cross-section of the charged particle and $U_B = B^2/4\pi$ is the local magnetic energy density. In Fig. 2.1, we show a schematic representation of the synchrotron process, where a charged particle can be seen to gyrate around the magnetic field and consequently emit radiation.

The emission of radiation from a single particle does not happen uniformly over all the frequencies. The spectrum of the radiation (power emitted per unit frequency) is obtained by using the Parseval's theorem (see section 2.2 and Eq. 2.35 of Bartelmann, 2013) which take the following form for synchrotron radiation,

$$L_{syn}(\nu, \gamma) = \sqrt{3}\frac{e^3 B \sin\theta}{m_q c^2}\mathcal{F}\left(\frac{\nu}{\nu_c}\right), \tag{2.18}$$

where $\mathcal{F}(x) \coloneqq x\int_x^\infty K_{5/3}(x')\,dx'$, $\nu_c = 3\gamma^2\Omega_0 \sin\theta/4\pi$ and $m_q$ is the mass of the charge particle. Typically in astrophysical systems, multiple particles radiate simul-

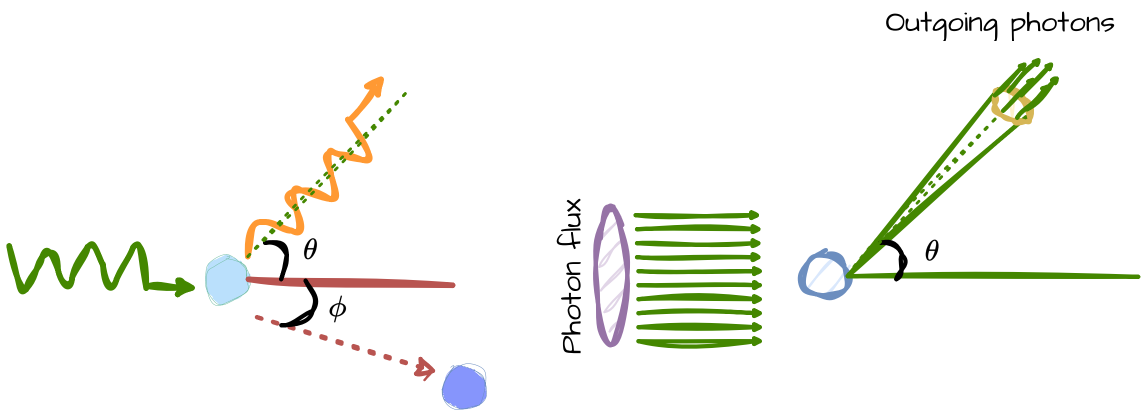


Figure 2.2: Cartoon representation of *left:* the Compton process, *right:* the differential cross-section.

taneously and give rise to the observed radiation. In such a case, the frequency, $\nu$, dependent synchrotron emissivity of a particle distribution can be described in the following way,

$$J(\nu, \boldsymbol{n}_{los}) = \int L_{syn}(\nu, E')N(E', \boldsymbol{n}_{los})\, dE' d\Omega_{\boldsymbol{n}_{los}} \tag{2.19}$$

where $L_{syn}(\nu, E')$ is the spectral power per unit frequency and unit solid angle emitted by a single relativistic particle, with energy $E'$, $\boldsymbol{n}_{los}$ is the unit vector along the direction of observation; and $N(E', \boldsymbol{n}_{los})\, dE' d\Omega_{\boldsymbol{n}_{los}}$ is the number of particles with energy between $E'$ and $E' + dE'$ and whose velocity is inside the solid angle $d\Omega_{\boldsymbol{n}_{los}}$ around the direction $\boldsymbol{n}_{los}$. Here we conclude our discussion of synchrotron radiation, and in the next section, we introduce another radiation process that has been used in this work.

### 2.2.2 Inverse Compton radiation

Compton scattering is a well-known phenomenon where a photon transfers its energy to static particles. Such a scattering phenomenon is theoretically modelled through quantum mechanics, and the change in the energy of the photon is described by the following equation,

$$h\nu_s = \frac{h\nu_i}{1 + \frac{h\nu_i}{m_q c^2}(1 - \cos\theta)} \tag{2.20}$$

where $h$ is the Planck constant, $\nu_s$ is the frequency of the scattered photon, $\nu_i$ is the frequency of the incident photon, and $\theta$ is the angle between the direction of the incoming photon and the scattered photon. In the left diagram of Fig. 2.2, we show a cartoon representation of the Compton scattering process, in which a green-coloured incoming photon interacts with a particle and is scattered at an angle $\theta$ with the initial propagation direction and with lower energy (orange-coloured). Furthermore, as a result of this scattering process, the particle scattered at an angle $\phi$ with the incoming direction of the photon.

Eq. (2.20) has two input variables, $\nu_i$ and $m_q$ and one output $\nu_s$. Therefore, for the above equation to have a solution, the value of $\theta$, the angle between the direction of the incoming photon and the scattered photon, has to be provided from outside. It is typically computed from the differential cross-section of such a scattering process, which is defined as the ratio of the number of photons scattered into a solid angle per unit time to the flux of incident photons. In the right diagram of In the right diagram of Fig. 2.2, we show a cartoon representation for calculating the differential cross-section.

For the Compton process, when $h\nu_i \ll m_q c^2$, this differential cross-section is given by the Thompson cross-section $\sigma_T$, while when $h\nu_i \gg m_q c^2$ a quantum electrodynamic treatment has to be adopted, which subsequently leads to the following Klein-Nishina cross-section formula,

$$\frac{d\sigma_{KN}}{d\Omega_{solid}} = \frac{r_0^2}{2}\left(\frac{\nu_s}{\nu_i}\right)\left(\frac{\nu_i}{\nu_s} + \frac{\nu_s}{\nu i} - \sin^2\theta\right) \tag{2.21}$$

where $r_0$ is the classical radius of a charged particle of mass $m_q$ and charge $q$. In the low energy limit $h\nu_i \ll m_q c^2$, Eq. (2.21) reduces to the following Thompson differential cross-section formula,

$$\frac{d\sigma_t}{d\Omega} = r_0^2 \frac{1 + \cos^2\theta}{2} \tag{2.22}$$

When this Compton process occurs on a moving particle rather than a static particle, it may also energise the photons at a compensation of the particle's energy. Such a process where photons get energised through the Compton mechanism is known as **inverse Compton process (IC)**, and it is typically attributed to being one of the primary high-energy radiation emission mechanisms for turbulent astrophysical systems. The energy loss of a charged particle via the IC process in the Thompson limit can be quantified through the following equation (Eq. 4.12 in Kembhavi & Narlikar, 1999),

$$\frac{dE_{IC}}{dt} = \frac{4}{3} c\gamma^2\beta^2\sigma_T U_{ph} \tag{2.23}$$

with $U_{ph}$ being the total energy density of the photon field. The work presented here considers cosmic microwave background (CMB) radiation as the source of the photon field. The energy density of the CMB radiation can be written in the following way,

$$u_{CMB} = 4\frac{\sigma_B}{c}\left[T_{CMB}(1+z)\right]^4 \tag{2.24}$$

where $\sigma_B$ is the Stepfan Boltzmann constant,$T_{CMB}$ is the temperature of the CMB photons, $T_{CMB} = 2.728\,\mathrm{K}$ and $z$ is the red-shift of the source of interest. The IC emissivity for such a photon source can be written in the following way (Vaidya et al., 2018),

$$
\begin{aligned}
j_{IC}/h\nu = \int_0^\infty d\varepsilon'_{ph} \int d\Omega'_{ph} \int dE' \int d\Omega'_\tau \\
\left[N(E',\tau)\, c(1-\beta_e \cdot l')\, n'_{ph}(\varepsilon'_{ph}, l')\, \sigma_{Th}(\varepsilon'_{ph}, l', \nu', \hat{n}')\right],
\end{aligned}
\tag{2.25}
$$

where $n'_{\rm ph}(\varepsilon'_{ph}, \boldsymbol{l}')d\varepsilon'_{ph}$ and $N'(E', \boldsymbol{\tau})dE'$ are, respectively, the number of photons between the energy range $\varepsilon'_{ph}$ and $\varepsilon'_{ph} + d\varepsilon'_{ph}$ along a direction $\boldsymbol{l}'$ and the number of particles within the energy range $E'$ and $E' + dE'$ and direction $\boldsymbol{\tau}$. The factor $c(1-\boldsymbol{\beta_e}\cdot\boldsymbol{l}')$ arises from the differential velocity between the photon and the electron, and $\boldsymbol{\beta}_e$ is the scattering electron velocity vector in units of $c$. The scattering cross-section, $\sigma$, depends, in principle, on the directions and energies of the incident and outgoing photons.

### 2.2.3 Adiabatic loss/gain process

Along with the radiative losses, the charged particles residing in astrophysical plasma also suffer adiabatic loss (gain) if the particles are confined within an expanding (Compressing) volume. Such a loss process is typically observed to happen in the vicinity of shocks. The adiabatic loss/gain can be described through the first law of thermodynamics, which says,

$$
\text{đ}Q = dU + PdV \tag{2.26}
$$

where $Q$ is the heat given to the system, đ implies the inexact differential, $U$ is the internal energy of the system, and $PdV$ is the work done by the system. For the adiabatic process, heat exchange is forbidden; consequently, $\text{đ}Q = 0$. Further, if we consider only non-relativistic particles constitute the system, then through statistical mechanics, we can get a relation between the internal energy of the system and the pressure $P$ as follows (see Eqs. 8.71 and 8.73 of Fitzpatrick, 2020),

$$
P = \frac{2U}{3V}. \tag{2.27}
$$

Substituting it in Eq. (2.26) and considering the adiabatic condition, the temporal evolution of the internal energy can be written as the following,

$$\frac{dU}{dt} = -\frac{2U}{3V}\frac{dV}{dt} \tag{2.28}$$

where $dV/dt$ describes the change in volume, which can be related to the divergence of the fluid velocity in the following way (see Eq. 11.24 of Longair, 1992),

$$\frac{dV}{dt} = (\nabla \cdot \boldsymbol{v})\, V \tag{2.29}$$

which, upon substitution in Eq. (2.28) gives an expression for the momentum evolution of these charged particles due to the adiabatic process in the following way,

$$\frac{dp}{dt} = -\,(\nabla \cdot \boldsymbol{v})\, p \tag{2.30}$$

Such an equation remains valid even for relativistic particles, which we consider in this thesis. With this, we conclude our discussion on the adiabatic loss/gain process. In the following section, we introduce the transport equation for the particles residing in the plasma, through which one can obtain the evolution of the particle energy spectrum considering all of the above-discussed processes.

### 2.2.4 Particle transport equation

In typical astrophysical sources, all the above processes do not happen in isolation but rather in tandem with each other. Such a simultaneous action of all the microphysical processes that these charged particles undergo can be described through a transport equation. Here, to give an idea of how all such processes arise in the transport equation below, we briefly describe the derivation of a simple transport equation. The derivation considers a system of charged particles that are either accelerating or losing their energy through some means, and the evolution of the entire system is governed solely by these micro-physical acceleration and loss processes. The energy of such a system, in that case, can be described through an energy distribution function $f(E)\,dE$, which quantifies the number of particles in the energy range $E$ and $E + dE$ and follows the equality,

$$\mathcal{N} = \int_{E_i}^{E_f} f(E')\,dE' \tag{2.31}$$

where $\mathcal{N}$ is the number of particles inside the system, $E_i$ and $E_f$ are the minimum and maximum energies that the particles have at a particular time. Note that due to the loss process, as the energy of the constituent particles decreases, the limit also moves towards lower energies, while due to the presence of the acceleration process, the opposite situation happens. Therefore, with time, these bounds will evolve as well and will be governed by the loss and acceleration processes; however, during such evolution, the particle number inside the system should remain constant. The above statement can mathematically be described as follows,

$$\frac{d\mathcal{N}}{dt} = \frac{d}{dt}\left(\int_{E_i}^{E_f} f(E')\,dE'\right) = 0 \tag{2.32}$$

By applying Leibniz rule of integration we get the following,

$$\begin{aligned}\frac{d}{dt}\left(\int_{E_i}^{E_f} f(E')\,dE'\right) &= \int_{E_i}^{E_f} \frac{\partial f(E')}{\partial t}\,dE' + f(E_f)\frac{dE_f}{dt} - f(E_i)\frac{dE_i}{dt} \\ &= \int_{E_i}^{E_f} \left\{\frac{\partial f(E')}{\partial t} + \frac{\partial}{\partial E'}\left(\frac{dE'}{dt} f(E')\right)\right\} dE'\end{aligned} \tag{2.33}$$

Therefore, we can write Eq. (2.32) in the following way,

$$\frac{\partial f(E)}{\partial t} + \frac{\partial}{\partial E}\left(\frac{dE}{dt} f(E)\right) = 0 \tag{2.34}$$

where we dropped the $'$ for clarity. Eq. (2.34) is a simple representation of the transport equation which describes the evolution of the energy distribution function of the system due to the loss and acceleration processes, $dE/dt$, that the particles undergo.

Further, the term $dE/dt$ can be written as a combination of all the energy loss and acceleration processes, and for our case, it can be written in the following way,

$$\frac{dE}{dt} = \frac{dE}{dt}\Big|_{sync} + \frac{dE}{dt}\Big|_{IC-CMB} + \frac{dE}{dt}\Big|_{adiab} \tag{2.35}$$

where the first term on the right-hand side is due to synchrotron loss, which takes the form specified in Eq. (2.17), the second term corresponds to IC-CMB loss, and the last term corresponds to adiabatic loss/gain (see Eq. 2.30).

Further, the acceleration due to turbulence that we discussed in section 2.1.1 can be incorporated to Eq. (2.34) as follows,

$$\frac{\partial f(\gamma)}{\partial t} + \frac{\partial}{\partial \gamma}\left(\frac{d\gamma}{dt} f(\gamma)\right) + \frac{\partial}{\partial \gamma}\left(\frac{2D_{\gamma\gamma}}{\gamma} f(\gamma)\right) = \frac{\partial}{\partial \gamma}\left(D_{\gamma\gamma}\frac{\partial f(\gamma)}{\partial \gamma}\right) \tag{2.36}$$

where we have substituted Eq. (2.8) in the right-hand side of the Eq. (2.34) and written the whole equation in terms of the particle Lorentz factor, $\gamma$. In addition, while substituting Eq. (2.8), we consider a transformation of the distribution function from $f_0$ to $f$ in the following way $f = 4\pi p^2 f_0$. Such a transformation is required to maintain the similarity between the definition of the distribution function, as from Eq. (2.8) the particle number is calculated through the following expression,

$$\mathcal{N} = \int_{p_i}^{pf} 4\pi p^2 f_0 \, dp \tag{2.37}$$

while for Eq. (2.34) the definition of the number of particles is given by Eq. (2.31), which is different from the above definition. This transport equation changes significantly for realistic astrophysical flows, and one such transport equation is considered in chapter 3. In the next section, we discuss the numerical framework used to perform the works in this thesis.

## 2.3 Numerical framework

Most of the work presented in this thesis is carried out using a massively parallel relativistic magnetohydrodynamic (RMHD) code called PLUTO (Mignone et al., 2007). This code is primarily used to numerically solve non-linear mixed hyperbolic/parabolic systems of partial differential equations in the conservative form of the following type,

$$\frac{\partial \mathcal{U}}{\partial t} + \nabla \cdot \mathcal{A}(\mathcal{U}) = \nabla \cdot \mathcal{D}(\mathcal{U}) + \mathcal{S}(\mathcal{U}) \tag{2.38}$$

where $\mathcal{U}$ represents the set of dynamical quantities whose evolution has to be calculated, $\mathcal{A}$ represents the non-linear advection flux, and $\mathcal{D}$ represents the diffusion flux of those quantities. $\mathcal{S}$ defines the source term. The form of these quantities depends on the type of physical scenario used for the simulations. Currently, the code is capable of solving dynamical equations for hydrodynamics (HD), ideal magneto-hydrodynamics (MHD), relativistic hydrodynamics (RHD), relativistic ideal magneto-hydrodynamics (RMHD) and resistive magneto-hydrodynamics (ResMHD). PLUTO can work in static and adaptive grids (Mignone et al., 2012). It also provides a hybrid framework whereby particles and grid-based dynamics can be coupled. Such a framework reduces the large-scale gap between physics at micro and macro scales.

As a part of this hybrid framework, a novel Eulerian-Lagrangian particle module was developed by Vaidya et al. (2018), which employs passively evolving Lagrangian (or macro-) particles for simulating the emission of different astrophysical systems. The dynamics of such macro-particles is governed by the underlying thermal fluid. The concept of this module is described in Fig. 2.3 where a background is taken as a representation of the density, which is calculated by solving the MHD equations

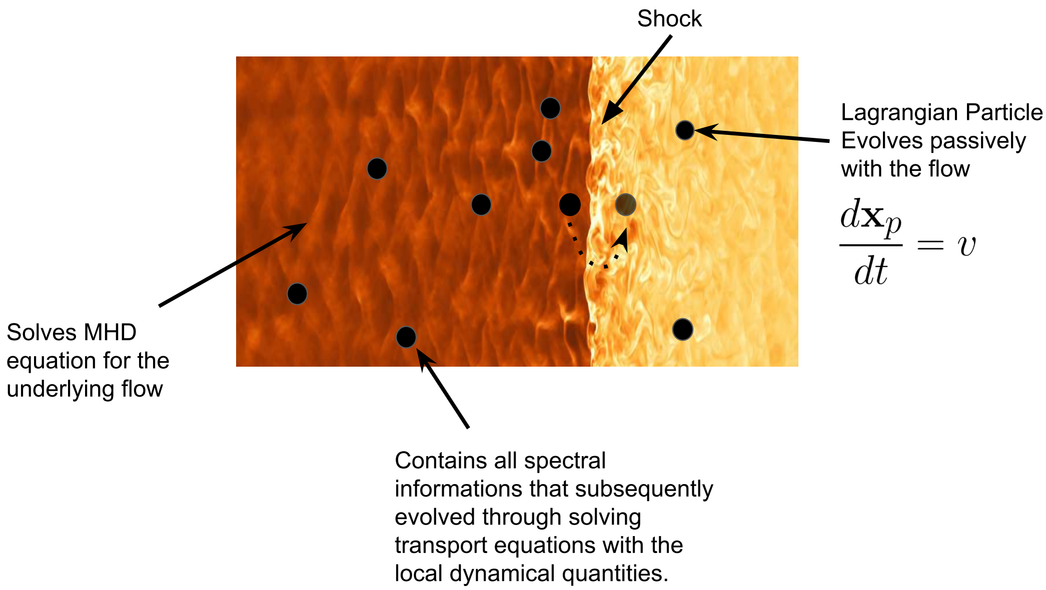


Figure 2.3: Schematic representation of the working of Lagrangian macro-particles. The background of the figure is adopted from Mignone et al. (2018). The black dots are representative of the macro-particles.

and inside which the macro-particles (depicted by black dots) move passively. Each of these particles constitutes an ensemble of non-thermal micro-particles (usually leptons) existing in close proximity in physical space with a finite energy distribution. The energy distribution for each of the macro-particles is evolved following a pre-specified transport equation, and such evolution happens concurrently with the fluid evolution, considering the dynamical quantities interpolated from the nearest grid points at the position of the macro-particles. Further, to compute the emissivity, the instantaneous energy distribution of each macroparticle is convolved with the corresponding single-particle radiative power and extrapolated to the nearest grid cells.

In addition, to calculate the effect of shock acceleration, PLUTO employs a shock-capturing technique that identifies the shock zone when the following conditions are met:

1. $\nabla \cdot \boldsymbol{v} < 0$, with $\boldsymbol{v}$ being the fluid velocity,
2. $\Delta P/P_1 > \epsilon_P$, with $\epsilon_P$ being an pre-imposed threshold and $P_1$ is the upstream pressure.

When a Lagrangian particle crosses such a flagged region, its energy distribution is evolved following a subgrid prescription.

Our concern in the current work is to understand the effect of such an interplay of different micro-physical processes on the emission of astrophysical sources. To perform the study, we extend the above-mentioned numerical framework to include the stochastic turbulent acceleration mechanism. We then apply the extended framework to study the emission properties of the radio lobes of FR-II radio-loud AGN systems due to the interplay of DSA and STA. Subsequently, we study the STA process in small-scale turbulence by computing the momentum diffusion coefficients through quasi-linear theory. Such a turbulent scenario is typically observed in relativistic shocks. In the following chapters, we describe in detail the methods used to complete these objectives and the results obtained from it.

# Chapter 3

# Numerical modeling of Fermi II $^{nd}$ order acceleration process

*This chapter has been adopted from Kundu et al. (2021)[0] and it describes the numerical algorithm that has been developed to study the effect of stochastic turbulent acceleration process in turbulent astrophysical plasma and its manifestations on the spectral evolution of highly energetic non-thermal particles. This chapter further discusses about the interplay of diffusive shock acceleration and stochastic turbulent acceleration processes through pilot case studies.*

---

## 3.1 Introduction

From giving a universal power-law trend to the cosmic ray spectrum to explaining the observed emission features of various astrophysical sources, particle acceleration process plays a crucial role in shaping our understanding of the nature of various space and astrophysical phenomena. Several observations require particles to be accelerated to very high energies in order to explain the energetics in different astrophysical sources. Due to high electrical conductivity, astrophysical plasma is incapable of sustaining a global electric field, making it challenging to energize par-

[0]Kundu, S., Vaidya, B., and Mignone, A. (2021) Numerical Modeling and Physical Interplay of Stochastic Turbulent Acceleration for Nonthermal Emission Processes, The Astrophysical Journal, vol. 921, no. 1. doi:10.3847/1538-4357/ac1ba5.

ticles in this scenario. Particle acceleration processes provide an alternative way to accelerate particles in the absence of a global electric field. The existing literature (Blandford, 1994; Kirk et al., 1994; Melrose, 1996) suggests three main approaches to accelerate charged particles in an astrophysical plasma environment: shock acceleration (DSA), coherent electric field acceleration, and stochastic acceleration (STA).

In Fermi (1949), Fermi first gave a proper mechanism for accelerating charged particles to explain the cosmic ray spectrum and the possible origin of high-energy cosmic ray particles. The mechanism considers relativistic particles getting scattered by moving inhomogeneities, mainly various plasma waves (MHD waves for highly relativistic cosmic ray particles (Kulsrud & Ferrari, 1971; Parker, 1955; Sturrock, 1966)), and gaining energy (accelerate) in a randomized manner. This process is known as stochastic turbulent acceleration (STA) process. The randomness in the acceleration makes this process inefficient to energize particles, as suggested by the emission timescales observed in various astrophysical sources. Nevertheless, STA is considered to be an important source of turbulence damping in plasma and because of the omnipresence of turbulence in various astrophysical sources, STA has been invoked in order to explain the particle acceleration process in solar flares (Petrosian, 2012), corona above accretion disk of compact object (Belmont et al., 2008; Dermer et al., 1996; Liu et al., 2004; Vurm & Poutanen, 2009), supernova remnant (Bykov & Fleishman, 1992; Ferrand & Marcowith, 2010; Kirk et al., 1996; Marcowith & Casse, 2010), gamma-ray burst (Schlickeiser & Dermer, 2000), emission from blazars(see Asano & Hayashida (2018) and references therein), radio lobes of AGN Jets (O'Sullivan et al., 2009), the diffuse X-ray emission from AGN jets (Fan et al., 2008) along with fermi bubbles of galaxies (Mertsch & Petrosian, 2019), galaxy clusters (Brunetti & Lazarian, 2007; Donnert & Brunetti, 2014). Recently STA has also been suggested as a candidate for the spectral gradient observed in galaxy clusters (Rajpurohit et al., 2020).

On the other hand, DSA gives a proper framework where particles can interact with the magnetic inhomogeneities in a way that could only increase the particles energy (Bell, 1978; Blandford & Eichler, 1987; Drury, 1983; Malkov & Drury, 2001). Due to it's efficiency, DSA has been used to describe the particle acceleration process in various astrophysical systems, for example interplanetary helio-spheric shocks (Jokipii et al., 2007; Perri & Zimbardo, 2015), shock wave of supernova remnant (Bell, 2014), stellar bow shock (Rangelov et al., 2019), oblique shock in AGN jets (Meli, A. & Biermann, P. L., 2013), radio relics of galaxy clusters (Kang et al., 2017; van Weeren et al., 2017; Zimbardo & Perri, 2017). Though DSA is more efficient compared to STA mechanism, it is believed to only give rise to localized emission where STA is thought to produce large scale diffusive emission (Fan et al., 2008).

To study these particle acceleration processes in various astrophysical systems, a numerical approach is imperative because of the multi-scale nature of the astrophysical plasma. Numerical study for plasma systems can broadly be categorized into different classes. Direct computation, mainly known as Particle in Cell (PIC) method, where Newton-Lorenz force law is solved along with Maxwells equation describing the dynamical evolution of the electric and magnetic field (Giacalone & Ellison, 2000; Nishikawa et al., 2007; Sironi & Spitkovsky, 2011; Spitkovsky, 2008). This first principle approach has been taken by various researchers to study the particle acceleration processes (Comisso & Sironi, 2018; Marcowith et al., 2020; Wong et al., 2019). The next numerical scheme studies the plasma by solving the Vlasov equation for particle distribution evolution along with Maxwells equations (Palmroth et al., 2018). This scheme provides the advantage to study various plasma behaviour distinctively. This approach also enables us to study particle acceleration processes in different physical settings. Similar to this approach, another approach is often taken to study particle acceleration process in the quasi-linear approximation where a Fokker-Plank equation is solved in order to evolve the cosmic ray spectrum due to interaction with MHD waves (Donnert & Brunetti, 2014; Miniati, 2001; Vazza et al., 2021; Winner et al., 2019).

Another numerical procedure studies the plasma in the fluid regime, also known as magneto-hydrodynamic (MHD) regime. This numerical procedure assumes plasma to be sufficiently collisional. That is why this procedure is incapable of capturing the physics of particle acceleration because collisions would make them to follow a Maxwellian which is in contrast to the observed power-law trend for the distribution of the accelerated particles. Though fluid approach fails to capture the particle acceleration process, it provides the background for the particles to interact with various MHD waves and accelerate. Recently some research has been devoted to combine the fluid and the PIC approaches (Bai et al., 2015) to study the DSA (Mignone et al., 2018). The final numerical method uses Monte-Carlo technique to study particle acceleration by shock wave (Achterberg & Krulls, 1992; Baring et al., 1994; Marcowith & Kirk, 1999; Wolff & Tautz, 2015) and turbulence (Giacalone & Jokipii, 1999; Teraki & Asano, 2019). Among all the numerical techniques available the Particle in Cell method has an advantage (Baring, 2004; Ellison & Double, 2002; Ellison et al., 1990; Lemoine & Pelletier, 2003; Niemiec & Ostrowski, 2006; Ostrowski, 1988) over all other techniques because PIC not only can model the particle acceleration process, it also determine the self-generated magnetic turbulence, and treat them self-consistently with the cosmic ray particles. But the disadvantage of the PIC technique is, it is computationally very expensive (Ellison et al., 2013). And in order to bypass this problem other numerical techniques are used. Among them the kinetic test particle approach is one of the most efficient one because it could easily be incorporated with multi-scale simulations.

As most of the sources of particle acceleration act simultaneously in different regions of astrophysical sources, it is imperative to develop a framework that can study such region to understand role of individual acceleration process. In this work, we use the kinetic test particle approach to study the competing and complimentary actions of DSA and STA. Other complimentary approaches have focused on studying the role either of the acceleration processes individually, for example, Donnert & Brunetti (2014); Miniati (2003); Miniati et al. (2001) have demonstrated the role of STA in large scale galaxy clusters.

Recently, the existing Lagrangian particle module developed by Vaidya et al. (2018) in the PLUTO Code (Mignone et al., 2007) has been applied to AGN jets at kpc scales to study the impact of instabilities and subsequent shocks on particle acceleration and non-thermal emission (Borse, Nikhil et al., 2021; Mukherjee et al., 2021). In the present work, we extend this Lagrangian framework by incorporating the STA process, to study the effect of both DSA and STA along with their roles in shaping the emission structure in astrophysical sources. In this context, a macro-particle is a Lagrangian entity that moves along with the fluid and collects an ensemble of real particles (e.g. leptons) that are distributed in 1D momentum space.

The chapter is organised as follows; in section 3.2, we discuss the fundamental theory and necessary equations to describe the STA process. In section 3.3, we propose and describe a numerical algorithm to solve the cosmic ray transport equation. We validate our algorithm and discuss it's accuracy in section 3.4. We analyze STA process in presence and absence of shocks in section 3.5 and also discuss the role of several STA parameters through applications to test situations. Section 3.6 discusses our findings and summarizes this work.

## 3.2 Turbulent Particle Acceleration : Theory

In this chapter, we aim to study the effect of MHD turbulence and shocks on cosmic ray transport and their effect on the spectral signature of various astrophysical systems. The process of interaction between cosmic ray particles and turbulent plasma is stochastic in nature. Due to the random nature of the interaction, the energy of a cosmic ray particle follows a biased random walk, which leads the particle distribution to follow a diffusion equation (Tverskoĭ, 1967):

$$\frac{\partial f_0}{\partial t} = \frac{1}{p^2}\frac{\partial}{\partial p}\left(p^2 D_{pp}\frac{\partial f_0}{\partial p}\right) = \frac{\partial}{\partial p}\left(D_{pp}\frac{\partial f_0}{\partial p}\right) + \frac{2D_{pp}}{p}\frac{\partial f_0}{\partial p}, \tag{3.1}$$

where, $f_0$ is the particle distribution function that depends on time $t$ and momentum $p$. $D_{pp}$ is the diffusion coefficient in momentum space. The above equation resembles a Fokker-Planck equation (Blandford & Eichler, 1987). In a magnetized medium charged cosmic rays are also prone to loose their energy via various radiative and adiabatic losses. Inclusion of these loss effects along with the random interactions with turbulent magnetic fields results in the evolution of the distribution of relativistic cosmic ray particles as follows (Webb, 1989),

$$\nabla_\mu(u^\mu f_0 + q^\mu) + \frac{1}{p^2}\frac{\partial}{\partial p}\left[-\frac{p^3}{3} f_0 \nabla_\mu u^\mu + \langle\dot{p}\rangle_L f_0 - \Gamma_{visc} p^4 \tau \frac{\partial f_0}{\partial p} - p^2 D_{pp}\frac{\partial f_0}{\partial p} - p(p^0)^2 \dot{u}_\mu q^\mu\right] = 0. \tag{3.2}$$

The various terms of the equation are described below:

1. $\nabla_\mu(u^\mu f_0 + q^\mu)$ represents the change in $f_0$, due to the spatial transport. $q^\mu$ is the spatial diffusion flux, $u^\mu$ is the bulk four-velocity;

2. $\frac{p^3}{3} f_0 \nabla_\mu u^\mu$ defines the energy loss/gain due to adiabatic expansion;

3. $\langle\dot{p}\rangle_L f_0$ describes the radiative losses, such as synchrotron and various Inverse Compton (IC) processes;

4. $\Gamma_{\rm visc} p^4 \tau \frac{\partial f_0}{\partial p}$ is the particle acceleration term due to fluid shear (Rieger & Duffy, 2019);

5. $p^2 D_{pp}\frac{\partial f_0}{\partial p}$ represents the Fermi II order particle acceleration or STA process (see Eq. (3.1));

6. $p(p^0)^2\dot{u}_\mu q^\mu$ originates because of the frame transformation.

Following Vaidya et al. (2018), we neglect the spatial diffusion flux $q^\mu$ as well as the acceleration due to frame transformation (i.e., terms 1 and 6). Also, acceleration due to shear flow ($\Gamma_{\rm visc} = 0$) is not considered in the present study. Furthermore, the omission of the spatial diffusion term is compromised by an inclusion of a momentum independent escape term in Eq. (3.2) (Achterberg & Krulls, 1992), so that Eq. (3.2) takes the form,

$$\nabla_\mu(u^\mu f_0) + \frac{1}{p^2}\frac{\partial}{\partial p}\Big[ -\frac{p^3}{3}f_0\nabla_\mu u^\mu + \langle \dot{p}\rangle_L f_0 - p^2 D_{pp}\frac{\partial f_0}{\partial p}\Big] = -\frac{f_0}{T_{\rm esc}}, \tag{3.3}$$

where $T_{\rm esc}$ is the escape timescale. The above equation is same one used in Vaidya et al. (2018) to update the spectral distribution of a single macro-particle with the additional contributions related to Fermi II order acceleration and the escape term.

Note that, for relativistic flows, the convective derivative can be expressed as,

$$u^\mu\nabla_\mu \equiv \gamma\left[\frac{\partial}{\partial t} + v^i\frac{\partial}{\partial x^i}\right] = \frac{d}{d\tau}, \tag{3.4}$$

where $\tau$ is the proper time. Assuming pitch angle isotropy in momentum space ($p$), the distribution function can be written in terms of the number density of the relativistic particles as $N(p,\tau)dp = 4\pi p^2 f_0 dp$ with $N(p,\tau)$ being the number density of non-thermal particles with momentum between $p$ and $p{+}dp$. Accordingly Eq. (3.3) can be written as,

$$\begin{aligned}\frac{dN}{d\tau} + \frac{\partial}{\partial p}\Bigg[ -N\nabla^\mu u_\mu\frac{p}{3} + \frac{\langle\dot{p}\rangle_l}{p^2}N - D_{pp}\frac{\partial N}{\partial p} \\ + \frac{2ND_{pp}}{p}\Bigg] = -N\nabla^\mu u_\mu - \frac{N}{T_{\rm esc}}\end{aligned} \tag{3.5}$$

Transforming the independent variable from momentum ($p$) to Lorentz factor ($\gamma$) following $p \approx \gamma m_0 c$, with $c$ being the speed of light in vacuum and $m_0$ being the mass of the ultra relativistic cosmic ray particles, Eq. (3.5) can be expressed as (see Eq. 11 of Tramacere et al., 2011):

$$\begin{aligned}\frac{\partial \chi_p}{\partial \tau} + \frac{\partial}{\partial \gamma}\left[(S + D_A)\chi_p\right] \;&=\; \frac{\partial}{\partial \gamma}\left(D\frac{\partial \chi_p}{\partial \gamma}\right) - \frac{\chi_p}{T_{\mathrm{esc}}} \\ &\quad + Q(\gamma, \tau)\,,\end{aligned} \tag{3.6}$$

where $\chi_p = N/n$, with $n$ being the number density of the fluid at the position of macro-particle, $S$ corresponds to radiative losses and adiabatic loss/gain process and $D_A = 2D/\gamma^2$ corresponds to the acceleration due to Fermi II order with $D = D_{pp}/m_0^2c^2$. We also include $Q(\gamma, \tau)$ as a source term in Eq. (3.6), which accounts for particle injection process from external sources.

A numerical approach to solve Eq. (3.6) without the terms on the right hand side and $D_A$ has been discussed in an earlier work (Vaidya et al., 2018), along with the particle energization through 1$^{\mathrm{st}}$-order Fermi acceleration at shocks. The numerical method for DSA has then recently been improved to account for the history of particle spectra by Mukherjee et al. (2021) and will be repeated here for completeness.

The improved version of the DSA routine includes a convolution of the upstream spectra to the downstream region of the shock in an instantaneous steady state manner. In particular, as the macro-particle crosses the shock, its downstream spectra is updated as follows:

$$\chi_p^{\mathrm{down}}(\gamma) \propto \int_{\gamma_{\mathrm{min}}}^{\gamma} \chi_p^{\mathrm{up}}(\gamma')G(\gamma, \gamma')\frac{d\gamma}{\gamma} \tag{3.7}$$

where, $\chi_p^{\mathrm{up}}(\gamma)$ is the distribution function far upstream and $\chi_p^{\mathrm{down}}(\gamma)$ is the steady state downstream distribution function, $G(\gamma, \gamma') = (\gamma/\gamma')^{-m+2}$, with $m = 3r/(r-1)$ and $r$ is the compression ratio. Here, $\gamma_{\mathrm{min}}$ is the minimum value of Lorentz factor obtained from the upstream spectrum. The value of $\gamma_{\mathrm{max}}$, the upper-limit of the convolution, is evaluated by equating timescales due to radiative losses and various acceleration processes (i.e., DSA and STA) (Böttcher & Dermer, 2010; Mimica & Aloy, 2012; Vaidya et al., 2018). Further, it is also ensured that the Larmor radius of the highest energetic lepton within a macro-particle has a radius equal to or less than one grid cell width. Further details are explicitly mentioned in (Mukherjee et al., 2021; Vaidya et al., 2018).

### 3.2.1 Momentum diffusion coefficient ($D$)

The micro-physical processes of the turbulent interaction are encapsulated in the transport coefficients of Eq. (3.6). The mathematical form of these transport coefficients due to different interactions of cosmic ray and turbulent magnetized medium have been derived for Alfvènic turbulence (see, for instance, Brunetti & Lazarian, 2007; O'Sullivan et al., 2009; Schlickeiser, 2002a).

In this work, we will consider STA following a 1D energy spectrum expressed as a power-law in terms of wave vector norm $|\boldsymbol{k}| = k$ with exponent $-q$,

$$W(k) \sim k^{-q}, \tag{3.8}$$

where, $W(k)$ is the turbulent energy spectrum in Fourier space. The momentum diffusion coefficient can therefore be expressed as (O'Sullivan et al., 2009; Schlickeiser, 1989),

$$D_{pp} \approx \beta_A^2 \frac{\delta B^2}{B^2} \left(\frac{r_g}{\lambda_{\max}}\right)^{q-1} \frac{p^2 c^2}{r_g c} \propto p^q, \tag{3.9}$$

where $p$ is the momentum of the cosmic ray particles, $D_{pp}$ is the momentum diffusion coefficient, $\beta_A$ is the Alfv́en velocity normalized to the speed of light, $B$ is the mean magnetic field, $\delta B$ its fluctuations, $r_g$ is the particle gyroradius and $\lambda_{\max}$ is the maximum correlation length of the turbulent medium.

With the definitions above, the systematic acceleration timescale ($t_A$) for STA can be written as

$$t_A \approx \beta_A^{-2} \frac{l}{c}. \tag{3.10}$$

where $l$ (the mean free path of the cosmic ray particle) can be expressed as

$$l \approx \frac{B^2}{\delta B^2} \left(\frac{r_g}{\lambda_{\max}}\right)^{1-q} r_g. \tag{3.11}$$

Therefore, the acceleration timescale (Eq. (3.10)) in terms of $\gamma$ could be expressed as,

$$t_A \approx \frac{A^2}{2}\rho c(m_0\gamma c^2)^{2-q}B^{q-4}\lambda_{\max}^{q-1}, \tag{3.12}$$

where, $A = B/\delta B$ defines the turbulence level whose value is set to unity for the present study (O'Sullivan et al., 2009).

### 3.2.2 Timescales

The processes described in Eq. (3.6) involve separate timescales due to different radiative losses and STA process. These timescales can be expressed in terms of the particle Lorentz factor $\gamma$ as follows:

1. Radiative losses time due to Inverse Compton (IC) in Thompson limit and synchrotron radiation, $t_L \propto 1/\gamma$;

2. Diffusion time due to Fermi II order momentum diffusion $t_D \propto (\frac{\gamma}{\gamma_s})^{2-q}$, for the chosen diffusion coefficient $D \propto \left(\frac{\gamma}{\gamma_s}\right)^q$. The value of $t_D$ therefore becomes a constant, $t_D = 1/D_0$ with a choice of $q = 2$, where $D_0$ is the proportionality constant. Here, $\gamma_s$ defines scale Lorentz factor which we have taken it to be unity for all the cases considered in this work;

3. The acceleration timescale $t_A = t_D/2$, estimated from Eq. (3.6) with the acceleration coefficient $D_A = 2D/\gamma$.

These considerations are of crucial importance in devising a numerical scheme for the solution of Eq. (3.6), since an explicit method would demand $\Delta t < \min\{t_L,\, t_D,\, t_A\}$ for stability reason.

## 3.3 Turbulent Particle Acceleration : Algorithm

### 3.3.1 Numerical Method

Eq. (3.6) is a non-homogeneous, convection-diffusion like partial differential equation (PDE) with variable coefficients. This equation combines both hyperbolic and parabolic terms. The non-homogeneous character of the equation is attributed to the presence of the source and sink terms.

While various numerical methods for the numerical solution of Eq. (3.6) have been proposed (see, for instance Chang & Cooper, 1970; Winner et al., 2019), here we take a more up-to-date and refined approach based on the employment of Runge-Kutta IMplicit-EXplicit (RK-IMEX) schemes whereby the hyperbolic term of the PDE are treated using an upwind Godunov-type explicit formalism while the parabolic (diffusion) term is handled implicitly.

Also, in order to account for the large range of values taken by the particle Lorentz factor $\gamma$, we employ a logarithmically spaced grid to provide equal resolution per decade.

To this end, we first introduce a coordinate transformation for the independent coordinate $\gamma \in [\gamma_{\min}, \gamma_{\max}]$ in the following way,

$$\xi(\gamma) = \frac{\log(\gamma/\gamma_{\min})}{\log(\gamma_{\max}/\gamma_{\min})}, \tag{3.13}$$

where, $\xi \in [0, 1]$ is the transformed (logical) coordinate. Eq. (3.6) is then rewritten as,

$$\frac{\partial\chi}{\partial\tau} + \xi'\frac{\partial}{\partial\xi}(H\chi) = \xi'\frac{\partial}{\partial\xi}\left[D\xi'\frac{\partial\chi}{\partial\xi}\right] - \frac{\chi}{T_{esc}} + Q \tag{3.14}$$

where we have dropped the subscript $p$ for ease of notation, while $\xi'$ is the Jacobian of this transformation given by Eq. (3.13),

$$\xi' = \frac{d\xi}{d\gamma} = \frac{1}{\gamma\log(\gamma_{\max}/\gamma_{\min})}\,, \tag{3.15}$$

while $H = S + D_A$, from Eq. (3.6).

In order to apply the RK-IMEX scheme, we discretize Eq. (3.14) on a one-dimensional mesh of $N$ points using the method of lines,

$$\frac{d\chi_i}{dt} = \mathcal{A}_i + \mathcal{D}_i + \mathcal{S}_i, \tag{3.16}$$

so that the original PDE becomes a system of ordinary differential equations at the nodal points $i = i_b$, ..., $i_e$, with $N = i_e - i_b + 1$. In Eq. (3.16), $\mathcal{A}_i$ is the advection term, $\mathcal{D}_i$ is the diffusion term and $\mathcal{S}_i$ accounts for accounts for source and sink terms.

The advection term $\mathcal{A}_i$ is discretized in conservative fashion using the nonlinear Van Leer flux limiter scheme (Van Leer, 1977),

$$\mathcal{A}_i = -\xi_i' \frac{\mathcal{F}^{\rm adv}_{i+\frac{1}{2}} - \mathcal{F}^{\rm adv}_{i-\frac{1}{2}}}{\Delta\xi}, \tag{3.17}$$

where the advection flux follows an upwind selection rule,

$$\mathcal{F}^{\rm adv}_{i+\frac{1}{2}} = \begin{cases} H(\gamma_{i+\frac{1}{2}})\chi^L_{i+\frac{1}{2}} & H(\gamma_{i+\frac{1}{2}}) > 0 \\ H(\gamma_{i+\frac{1}{2}})\chi^R_{i+\frac{1}{2}} & H(\gamma_{i+\frac{1}{2}}) < 0\,. \end{cases} \tag{3.18}$$

The left and right states $\chi^L_{i+\frac{1}{2}}$ and $\chi^R_{i+\frac{1}{2}}$ are constructed up to 2$^{\rm nd}$-order accuracy in space using a slope limiter to prevent oscillations around extrema,

$$\begin{aligned} \chi^L_{i+\frac{1}{2}} &= \chi_i + \frac{\delta\chi_i}{2}, \\ \chi^R_{i+\frac{1}{2}} &= \chi_{i+1} - \frac{\delta\chi_{i+1}}{2}, \end{aligned} \tag{3.19}$$

with the $\Delta\chi_i$ is the harmonic mean slope limiter (Van Leer, 1977),

$$\delta\chi_i = \begin{cases} \dfrac{2\Delta\chi_{i+\frac{1}{2}}\Delta\chi_{i-\frac{1}{2}}}{\Delta\chi_{i+\frac{1}{2}} + \Delta\chi_{i-\frac{1}{2}}} & \text{if} \quad \Delta\chi_{i+\frac{1}{2}}\Delta\chi_{i-\frac{1}{2}} > 0 \\ 0 & \text{otherwise} \end{cases} \tag{3.20}$$

where, $\Delta\chi_{i\pm\frac{1}{2}} = \pm(\chi_{i\pm1} - \chi_i)$. Note that this scheme is 2$^{\rm nd}$-order accurate away from discontinuities and that the reconstruction step demands for 2 ghost zones beyond the active domain cells.

For the diffusion term $\mathcal{D}_i$, we also adopt a conservative formalim and choose a central differencing approach yielding 2$^{\rm nd}$-order accuracy in the uniform $\xi$ grid:

$$\mathcal{D}_i = \xi_i' \frac{\mathcal{F}^{\rm diff}_{i+\frac{1}{2}} - \mathcal{F}^{\rm diff}_{i-\frac{1}{2}}}{\Delta\xi}, \tag{3.21}$$

where,

$$\mathcal{F}^{\rm diff}_{i+\frac{1}{2}} = (\xi' D(\gamma, t))_{i+\frac{1}{2}} \left(\frac{\chi_{i+1} - \chi_i}{\Delta\xi}\right), \tag{3.22}$$

is the diffusion flux constructed following a central difference approach.

In the RK-IMEX approach, the advection is carried out explicitly while the diffusion operator and the source terms are handled implicitly. This allows to overcome the restrictive time step limitation $\Delta t \lesssim \Delta\xi^2/(\xi' D)$ imposed by a typical explicit discretization.

We have implemented two similar approaches for the temporal integration of Eq. (3.16) in the PLUTO code. The first one is the Strong Stability Preserving (SSP) scheme (2,2,2) of Pareschi & Russo (2005).

Omitting the subscript $i$ for simplicity,

$$\begin{aligned}
\chi^{(1)} &= \chi^{(n)} + \Delta t \alpha \mathcal{D}^{(1)} \\
\chi^{(2)} &= \chi^{(n)} + \Delta t \Big[\mathcal{A}^{(1)} + (1-2\alpha)\mathcal{D}^{(1)} + \alpha\mathcal{D}^{(2)}\Big] \\
\chi^{(n+1)} &= \chi^{(n)} + \frac{\Delta t}{2}\Big[\mathcal{A}^{(1)} + \mathcal{A}^{(2)} + \mathcal{D}^{(1)} + \mathcal{D}^{(2)}\Big],
\end{aligned} \tag{3.23}$$

where $\Delta t$ is the time-step, $\alpha = 1 - 1/\sqrt{2}$.

For the second approach we choose ARS(2,2,2) scheme due to Ascher et al. (1997):

$$\begin{aligned}
\chi^{(1)} &= \chi^{(n)} + \Delta t \Big[\alpha\mathcal{A}^{(n)} + \alpha\mathcal{D}^{(1)}\Big] \\
\chi^{(n+1)} &= \chi^{(n)} + \frac{\Delta t}{2}\Big[\delta\mathcal{A}^{(n)} + (1-\delta)\mathcal{A}^{(1)}\Big] \\
&\quad + \frac{\Delta t}{2}\Big[(1-\alpha)\mathcal{D}^{(1)} + \alpha\mathcal{D}^{(n+1)}\Big],
\end{aligned} \tag{3.24}$$

where, $\alpha = 1 - 1/\sqrt{2}$, $\delta = 1 - \frac{1}{2\alpha}$.

Both time-stepping methods require the inversion of two tri-diagonal matrices per step, which we perform following the Thomas algorithm (Press et al., 1992). In the present work, we will only show results from the SSP(2,2,2) scheme since results obtained with the ARS(2,2,2) are similar. Furthermore, for the sake of comparison, we have also implemented the standard Chang-Cooper algorithm (Chang & Cooper, 1970; Park & Petrosian, 1996) for solving the Fokker-Planck Equation.

#### 3.3.1.1 Boundary conditions

In order for our numerical method to operate correctly, boundary conditions (b.c.) must be specified in the guard (or ghost) zones for $i = i_b - 1, i_b - 2$ and likewise for $i = i_e + 1, i_e + 2$. Two common b.c. have been routinely employed (Marcowith et al., 2020). The first one (zero-particle) is a Dirichlet b.c. requiring the value of the distribution function $\chi$ to vanish in the ghost zones. This kind of boundary condition in solving the cosmic ray transport problem is used, for instance, by Winner et al. (2019). Another boundary condition is a Neumann-like condition requiring zero-flux across the boundary interface. This condition has been used, for instance, by Chang & Cooper (1970) to solve the Fokker-Planck equation. The zero-flux b.c. conserves the integral of $\int \chi d\gamma$ (the analogous of particle number conservation). For more discussion on the boundary conditions for cosmic ray transport see Park & Petrosian (1995). Unless otherwise states, we will employ the zero-flux b.c. to ensure that without the presence of source and sink terms in Eq. (3.6), the total number of particles remain conserved. At the implementation level, we enforce the zero-flux b.c. separately according to the implicit/explicit stage level in our RK-IMEX update:

- during the implicit diffusion step we impose zero-gradient b.c.:
$$\begin{cases} \chi_i^{\rm diff} = \chi_{i_b}^{\rm diff} & \text{for} \quad i < i_b \\ \chi_i^{\rm diff} = \chi_{i_e}^{\rm diff} & \text{for} \quad i > i_e \end{cases} . \tag{3.25}$$
where $\chi^{\rm diff}$ is the solution array immediately before the implicit step.

- during the explicit hyperbolic update we impose reflective condition
$$\begin{cases} \chi_i^{\rm adv} = -\chi_{2i_b-i-1}^{\rm adv} & \text{for} \quad i < i_b \\ \chi_i^{\rm adv} = -\chi_{2i_e-i+1}^{\rm adv} & \text{for} \quad i > i_e \end{cases} \tag{3.26}$$
together with
$$\mathcal{F}_{i_b-\frac{1}{2}}^{\rm adv} = \mathcal{F}_{i_e+\frac{1}{2}}^{\rm adv} = 0\,. \tag{3.27}$$

In Eq. (3.26) $\chi^{\text{adv}}$ represents the solution array immediately before the explicit advection step.

A third b.c. is used to assess the accuracy of our algorithm against a reference or analytical solution. In this case, the value of $\chi$ in the ghost zones is set to the corresponding analytical value in those zones, unless otherwise stated.

## 3.4 Results : Code Validation Tests

In this section we proceed to assess the accuracy of our newly proposed algorithm. For accuracy calculation, errors will be computed using the $L_1$ norm, defined as (Winner et al., 2019):

$$L_1(N) = \frac{\sum_{i=1}^{N} \left|\chi_i^{\text{ref}} - \chi_i^{\text{num}}\right| \Delta\gamma_i}{\sum_{i=1}^{N} \chi_i^{\text{ref}} \Delta\gamma_i}, \tag{3.28}$$

where, $N$ is the number of energy bins. To further ensure that the scheme accuracy is not get dominated by the spatial discretization, the increment in $N$ is compensated by the decrement in $\Delta t$ such that the ratio $N/\Delta t$ stays constant (Vaidya et al., 2017). In section 3.5 all the tests are performed following the zero-flux boundary prescription. Furthermore all the simulations in this work are performed using the SSP(2,2,2) scheme with Courant number 0.4, unless otherwise specified.

### 3.4.1 Simple Advection

We start by considering a simple advection benchmark by setting $S = k\gamma^2$, $D_A = D = 0$ in Eq. (3.6). Here we consider two cases, owing to two diffrent values of $k = \pm 1$. The analytical solution for the case of $k = -1$ is given by (Kardashev,

Figure 3.1: Evolution of the particle distribution function and their corresponding $L_1$ error for the simple advection following $S = \gamma^2$ (*Top panel*) and $S = -\gamma^2$ (*Bottom panel*) case with IMEX-SSP algorithm. *Left panel:* shows the numerical (solid lines) and analytical (black dotted lines) solutions at different times. *Right panel:* $L_1$ norm errors at different resolutions (blue dots) and 2$^{\text{nd}}$-order reference slope (dashed lines).

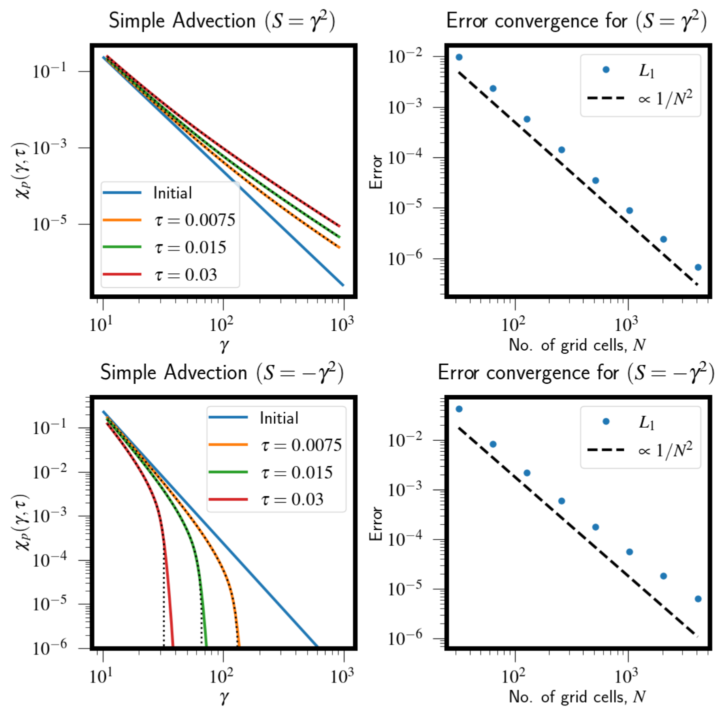


1962; Sarazin, 1999):

$$\chi_p = \begin{cases} N_0 \gamma^{-s}(1 - \gamma/\gamma_{\text{cut}})^{s-2}, & \gamma \geq \gamma_{\text{cut}} \\ 0, & \gamma \leq \gamma_{\text{cut}} \end{cases} \tag{3.29}$$

where, $\gamma_{\text{cut}} = 1/\tau$, while for $k = 1$ we do not encounter such discontinuity in the result,

$$\chi_p = N_0 \gamma^{-s}(1 + \gamma/\gamma_{\text{cut}})^{s-2}. \tag{3.30}$$

The initial condition consists of a power-law spectrum, $\chi_p(\gamma, 0) = N_0 \gamma^{-s}$ with $s = 3.3$. For the numerical calculations, we consider the range of $\gamma \in [10, 10^3]$ as our computational domain. We show the evolution of $\chi_p$ and the corresponding error for both values of $k$ in Fig. 3.1, using 128 bins and fixed time step $\Delta\tau = 0.00375$. The top left panel of Fig. 3.1 shows the evolution of $\chi_p$ for $k = 1$, while the bottom left panel depicts the same for $k = -1$. The solid curves represent the numerical solutions while the black dotted curves depict the analytical solution at the corresponding time. For $k = 1$, the distribution function follows the analytical results closely, while,

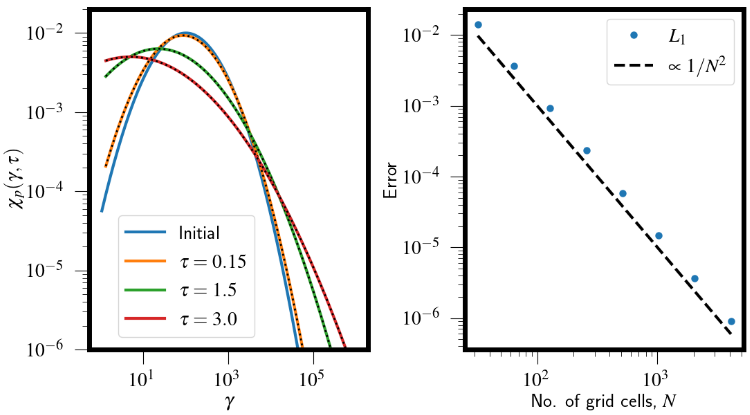


Figure 3.2: *Left:* Simple diffusion case for different times where solid lines show the numerically computed particle distribution function and black dotted curve depicts analytical solutions. *Right:* $L_1$ error convergence plot for the Simple diffusion case with IMEX-SSP algorithm.

for $k = -1$ some deviations are observed at a later stage ($\tau = 0.03$) between the analytic and numerical solution, owing to the steepening of the solution (Eq. 3.29). A convergence test is shown for both cases in the right panel of Fig. 3.1 where we plot the $L_1$ error as a function of the number of bins. Blue dots and the black dashed curve represent, respectively, the computed $L_1$ error and a reference for the $1/N^2$ slope. For $k = 1$ (top right) results converge with $2^{\mathrm{nd}}$-order accuracy for all resolutions, while for $k = -1$ (bottom right) a slight deviation from the $2^{\mathrm{nd}}$-order convergence can be observed. This discrepancy is attributed to the discontinuous nature of analytic solution presented in Eq. (3.29).

### 3.4.2 Simple Diffusion

Next, we solve Eq. (3.6) in the case of simple diffusion where, $S = D_A = 0$ and $D = \gamma^2$. The analytical solution for this case can be written as (Park & Petrosian, 1995),

$$\chi_p = \frac{1}{\gamma\sqrt{4\pi\tau}} \exp\left\{ -\frac{[\log(\gamma_0/\gamma) + \tau]^2}{4\tau} \right\} \tag{3.31}$$

We define the computational domain as $\gamma \in [1, 10^6]$ and employ 128 logarithmically spaced bins with a fixed time-step $\Delta\tau = 0.0375$. The initial condition is given by the analytical solution (Eq. 3.31) at $\tau = 1.0$ and $\gamma_0 = 100.0$. The results are

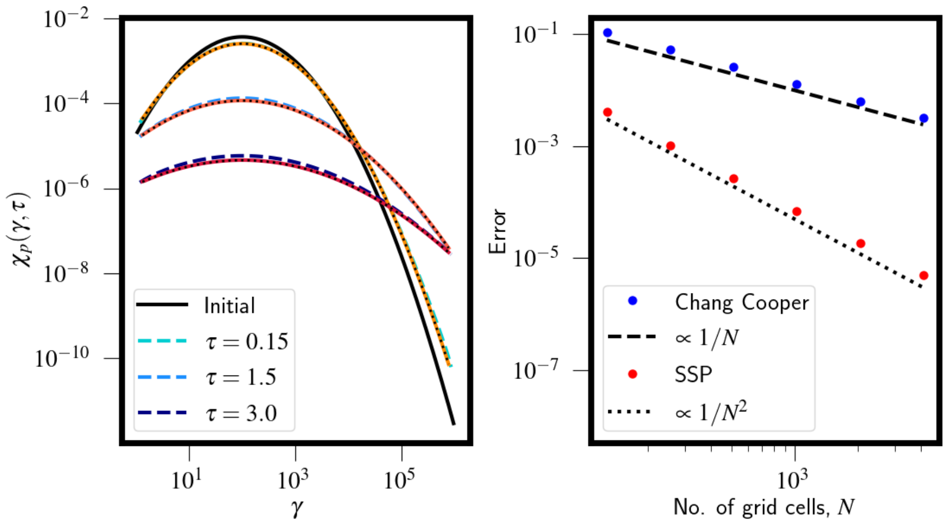


Figure 3.3: *Left:* Evolution of the particle distribution following Eq. (3.32) with $\theta = 1$. Dashed curves plot results obtained with the Chang-Cooper scheme, red curves correspond to the SSP(2,2,2) scheme. Different shades correspond to different times. Black dotted curve depicts the analytical solutions at the corresponding times. *Right:* $L_1$-norm error convergence for both Chang-Cooper (blue dots) and SSP(2,2,2) (red dots) schemes. Black curves shows the reference slopes for the corresponding schemes.

shown in Fig. 3.2. The left panel shows the evolution of the distribution function at different times with solid (black dotted) curve representing the numerical (analytical) solution. In the right panel of Fig. 3.2 the corresponding $L_1$ error is shown by varying the grid size from 32 to 4096 bins. Here 2$^{\mathrm{nd}}$-order convergence is observed uniformly at all resolutions.

### 3.4.3 Hard-sphere Equations

The next numerical benchmark is intended to verify the correctness of our implementation when source and sink terms are present in the Fokker-Planck equation. Additionally, we also compare our code with the standard Chang-Cooper algorithm (Chang & Cooper, 1970). For this purpose, we solve the following Fokker-Planck equation

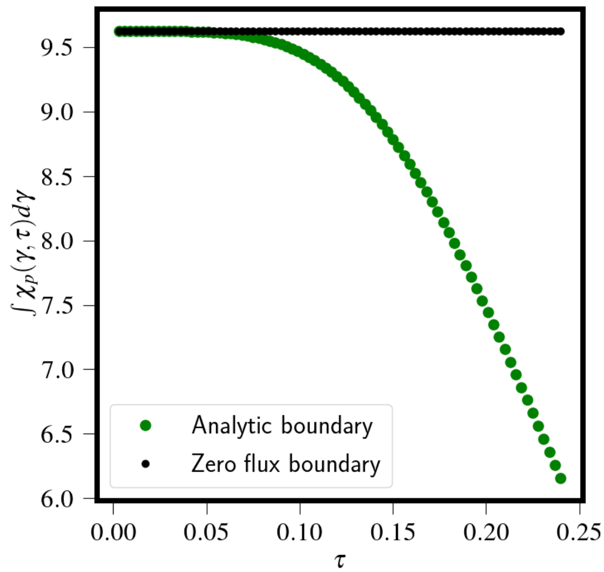


Figure 3.4: Time evolution of the integral $\int \chi_p(\gamma,\tau)d\gamma$ is shown for the proposed boundary condition (zero flux boundary) along with the boundary condition where the value of the distribution functions in the ghost zones are computed from the analytic expression (analytic boundary).

$$\frac{\partial \chi_p}{\partial \tau} = \frac{\partial}{\partial \gamma}\Big(\gamma^2 \frac{\partial \chi_p}{\partial \gamma} - \gamma \chi_p(\gamma,\tau)\Big) - \theta \chi_p \,. \tag{3.32}$$

The analytical solution of the previous equation can be written as (Park & Petrosian, 1995),

$$\chi_p = \frac{e^{-\theta\tau}}{\gamma\sqrt{4\pi\tau}} \exp\left\{ - \frac{[\log(\gamma_0/\gamma) + 2\tau]^2}{4\tau} \right\}. \tag{3.33}$$

For the present purpose, we take the inverse escape timescale $\theta = 1$ and the initial particle distribution is obtained by setting $\tau = 1.0$, $\gamma = \gamma_0 = 100.0$ in Eq. (3.33). The computational domain is taken as $\gamma \in [1, 10^6]$ using 128 (log-spaced) energy bins and a fixed time step $\Delta\tau = 0.0375$.

Numerical solutions obtained via the Chang-Cooper algorithm (dashed curves) and the SSP(2,2,2) algorithm (solid lines) are shown in the left panel of Fig. 3.3 at different time (colors). The analytical solution (dotted lines) is also superposed. The corresponding resolution study is reported in the right panel of the same figure using $L_1$ error. From the plots it clearly appears that the Chang-Cooper algorithm converges at 1$^{\text{st}}$-order rate while the SSP(2,2,2) scheme gives full 2$^{\text{nd}}$-order convergence, so that even at low resolutions the latter yields an error which is already one order of magnitude smaller than the former. At the resolution of $N = 4096$ the SSP method outperforms the Chang-Cooper scheme by more than 3 orders of magnitude.

Notice that, although we employ a conservative discretization, particle number is not strictly conserved for this test, owing to the chosen boundary condition which allows a non-zero net flux through the endpoints of the computational domain. In order to check particle conservation, we have therefore repeated the same test in absence of sink ($\theta = 0$) and by prescribing the zero-flux b.c. (see section 3.3.1.1). Results for the previous and current b.c. are shown in Fig. 3.4. It can be observed from the figure that while the integral due to the previous b.c (depicted by green dots), decreasing with time, the integral due to the zero-flux b.c. (depicted by black dots) remains constant. This validates the particle number conserving nature of the proposed boundary condition.

### 3.4.4 Log-Parabolic Nature of Particle Spectra

It has been shown (Massaro et al., 2006; Massaro, E. et al., 2004) that the hump structure in the spectral energy distribution (SED) of blazars could be described with a log-parabolic curve and this log-parabolicity is speculated to have originated from STA (Tramacere et al., 2011). Here we validate the log-parabolic nature of the particle distribution due to STA which consequently translates to log-parabolic nature of observed SED. In particular, we numerically solve the transport equation (3.6), in its conservative form (without source and sink terms) using the zero-flux boundary prescription, for STA including synchrotron losses. We choose our grid

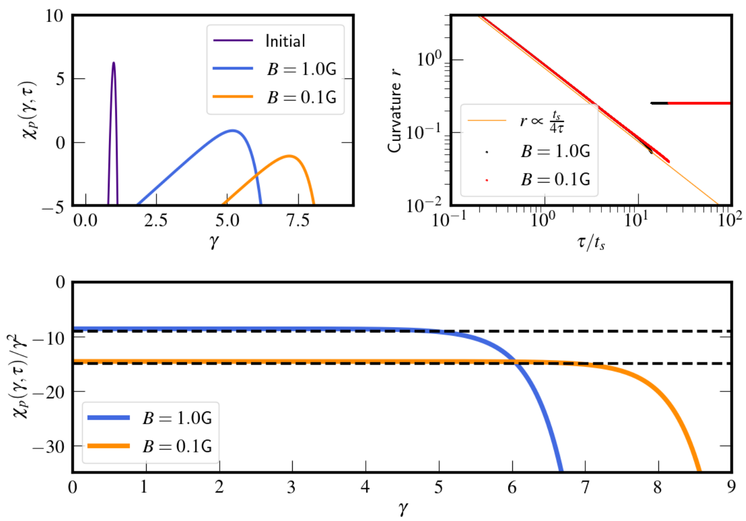


Figure 3.5: *Top left*: evolution of the particle distribution function with turbulent acceleration and synchrotron losses with two magnetic field values. *Top right*: evolution of the curvature of the distribution function fitted with a log-normal density profile (Eq. 4.17). Analytic solution is shown in solid orange line. *Bottom panel*: $\chi_p(\gamma,\tau)/\gamma^2$ as a function of $\gamma$ at steady state ($\tau = 30\, t_s$), in agreement with Eq. A.21. The plot shows the increase as $\gamma^2$ (black dashed lines) followed by an exponential cut-off.

as $1.0 \leq \gamma \leq 10^9$ with 5000 computational bins and $\Delta\tau = 0.003$ with the following transport coefficients,

$$S = -C_0 \gamma^2 B^2\,, \quad D = D_0 \gamma^2\,, \quad D_A = \frac{2D}{\gamma}\,, \tag{3.34}$$

where $C_0 = 1.28 \times 10^{-9}$, $D_0 = 10^{-4}$ sec$^{-1}$ is the diffusion constant. We employ $1/D_0$ as our unit time ($t_s$).

Here, we consider the one-zone model for the blazar emission (Tramacere et al., 2011) where the geometry of the acceleration region is taken as spherical with radius $R = 5 \times 10^{13}$ cm threaded by a magnetic field $B_{\rm mag}$. In this region, the acceleration is accompanied by the radiative losses. Moreover, in order to solve Eq. (3.6) we consider a mono-energetic initial distribution $\chi_p$ corresponding to a total power $L_{\rm inj} = 10^{39}$ erg/sec, where

$$L_{\rm inj} = N_{\rm part} \frac{4}{3}\pi R^3 \int \gamma m_e c^2 \delta(\gamma - \gamma_{\rm inj}) d\gamma, \tag{3.35}$$

where, $N_{part}$ is the total number of particles injected per unit volume and $\gamma_{\rm inj} = 10.0$.

The Dirac delta is approximated with a Gaussian distribution with $\sigma = 0.5$ and $\mu = 10$ and it is shown by the purple solid line in left panel of Fig 3.5. Furthermore, Eq. (3.6) is solved by adopting two different magnetic field values $B_{\rm mag} = 1$G, 0.1G and the corresponding distribution of $\chi_p$ for time $\tau = 30\, t_s$ is shown in the top left panel of Fig. 3.5.

The numerical solution is shown in the top left panel of Fig. 3.5 for different magnetic field strengths. We point out that the steady-state distribution is expected to have an ultra-relativistic Maxwellian form as described in Eq. (A.21) in Appendix A.2. This is confirmed in the bottom panel of Fig. 3.5 where we plot $\chi_p/\gamma^2$ as a function of $\gamma$, showing that our results correctly reproduce the $\gamma^2$-dependence of the spectrum.

Also, in order to quantify the effects of acceleration and radiative losses on the spectral evolution, we estimate the curvature of the distribution function. The curvature is measured by finding the peak value of the distribution function at each time-step which is also the point at which $t_L = t_A$ (Katarzyński et al., 2006, see also Sec. 3.2.2) and subsequently fitting a log-normal curve through 10 points centered around $\gamma_c$ (the energy at which the maximum occurs). The curvature is then taken as the inverse of the variance of the best fit. In particular, we adopt the fitting curve (Kardashev, 1962) as follows:

$$\chi_{\rm fit} = \frac{A}{\gamma\sigma} \exp\left\{ -\frac{(\log(\gamma) - \mu - \sigma^2)^2}{4\sigma^2} \right\}, \tag{3.36}$$

with curvature parameter defined as $r = 1/(4\sigma^2)$. The fitting curve is a solution to the Fermi II order transport equation (Eq. 3.6 with $S = 0, D = \gamma^2$ and $D_A = 2D/\gamma$ without sources and sinks) when $\sigma^2 = \tau$, therefore the evolution of the curvature $r$ goes as $\sim 1/(4\tau)$. In the top right panel of Fig. 3.5 we compare $r$ in the acceleration region (yellow solid line) with $r$ numerically calculated by fitting Eq. (4.17) with the particle distribution, at each time, for different $B_{\rm mag}$ values (red and black dotted lines) .

Our results show that the fitted curvature initially decays with time as $r \propto t_s/4\tau$, following a trend of curvature in the acceleration region, and then a sudden jump of the curvature to the steady value of $r = 0.25$ can be observed. The results therefore confirm that, during the earlier stages, STA dominates the evolution of the particle distribution function and, later, that steady state is reached much faster for stronger magnetic fields, as confirmed by the curvature evolution (black dots in the top right plot of Fig. 3.5).

Summarizing, the numerical benchmarks proposed in this section validate our implementation and demonstrate that the proposed SSP(2,2,2) scheme is fully conservative and it provides full $2^{\text{nd}}$-order accuracy, in contrast to its predecessors (i.e. Chang & Cooper, 1970; Winner et al., 2019) with typical $1^{\text{st}}$-order accuracy.

## 3.5 Effect of Turbulent acceleration in presence of Shocks

In this section, we describe the effect of STA on particle spectra in presence of shock. In particular, we consider several test situations where the equations of classical or relativistic MHD are solved using the PLUTO code (Mignone et al., 2007) along with Lagrangian particles to model the non-thermal emission (Mukherjee et al., 2021; Vaidya et al., 2018) in presence of DSA and radiative losses. To study the effects of STA, the newly developed algorithm (see section 3.3) has been incorporated into the Lagrangian framework. The effects of DSA and STA on particle spectra and subsequent non-thermal emission signatures are compared for various test situations and discussed in the following.

### 3.5.1 Non-relativistic MHD Planar shock

Here we perform a simulation of a non-relativistic MHD planar shock interacting with a single macro-particle in a turbulent medium. We solve the 2D ideal MHD equations with adiabatic equation of state on a Cartesian grid $x \in [0, 40]$ and $y \in [0, 2]$ using $1024 \times 128$ grid zones. Initially, we place a shock wave at $x = 1$ which moves towards the increasing $x$ direction. The upstream density and pressure, $\rho_u$ and $P_u$, are taken as 1 and $10^{-4}$, respectively, in dimensionless units. A random density perturbation is added to simulate a non-homogeneous upstream medium. The magnetic field is defined as $\boldsymbol{B} = B_0(\cos\theta, \sin\theta)$, where $\theta$ (the obliquity) is the angle between $\boldsymbol{B}$ and the direction of shock normal. For our purpose, we have considered $\theta = 30°$ while $B_0$ is computed from the plasma beta, $\beta = 10^2 = 2P_u/B_0^2$.

The physical units adopted for this test are: length $\hat{L}_0 = 100\,\mathrm{pc}$, density $\hat{\rho}_0 = 10^{-2}\,\mathrm{amu}$ while the unit velocity is taken to be the speed of light $c$. With this choice, pressure will be given in units of $\hat{P}_0 = 1.5 \times 10^{-5}\,\mathrm{dyne/cm^2}$, magnetic field in units of $\hat{B}_0 = 1.4 \times 10^{-2}\,\mathrm{G}$ and time in units of $\hat{\tau}_0 = 326.4\,\mathrm{yrs}$.

The particle is initially located at $(x, y) \equiv (1.5, 1.0)$ with an energy distribution following a steep decreasing power-law profile with index 9. The grid ranges in $10 \leq \gamma \leq 10^{10}$ using 128 (log-spaced) bins. The particle spectrum (Eq. 3.6) is evolved accounting for synchrotron, inverse-Compton losses and adiabatic loss/gain along with the diffusion effect, modelled following the STA timescale (Eq. 3.12). Additionally, the effect of shock is captured via the steady state update convolution, Eq. (3.7). We also vary the index $q$ for various turbulent spectra $W(k) \propto k^{-q}$ in three different scenarios: a) with only STA and no shock, b) both shock and STA and c) both shock and STA with the latter active only in the downstream region. The value of $\lambda_{\max}$ is taken to be $\hat{L}_0/10^5$ for all the simulations.

The result in the case of a turbulence spectrum following $W(k) \propto k^{-2}$ is shown in Fig. 3.6 where $t_A$ (see section 3.2.2) is independent of $\gamma$. The top panel shows the Lagrangian particle position on top of the background gas density distribution at $t = 56.13$. The evolution of the particle energy spectra with various radiative losses and different acceleration scenarios are shown in the bottom four panels using different colors (as indicated by the colorbar). The upper plot depicts the evolution of the particle spectra for the situation when only DSA is effective. As the shock

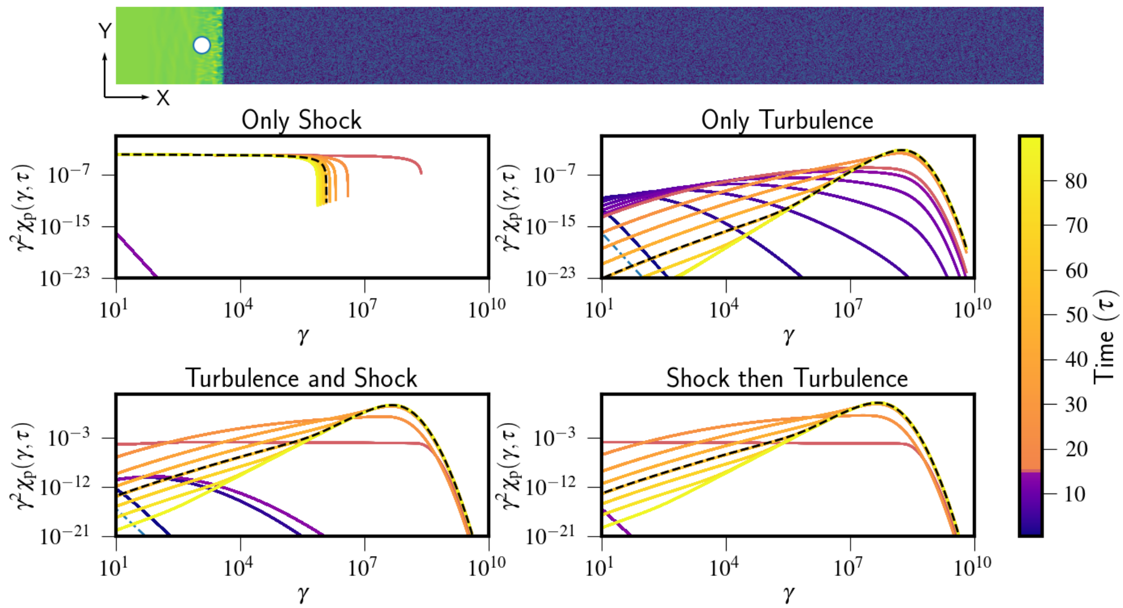


Figure 3.6: *Top section*: Density map of a fluid with a lagrangian particle (shown in white dot). The upstream region is shown in blue, and the downstream region is shown in green. *Bottom section*: Particle spectra in various scenarios with $q = 2$ turbulence spectrum. Particle spectra *Middle left*: For the case of only DSA with a compression ratio of 3.89 and various losses. *Middle right*: In a turbulent medium with various losses but no shock. *Bottom left*: With the both shock of same compression ratio, turbulence and various losses. *Bottom right*: For turbulence present only at the downstream region. The black dashed curve shows the particle energy spectrum for the time when the density map snapshot is taken.

hits the particle, the spectra becomes flatter and radiative and adiabatic losses give rise to a cut-off that gradually shifts from larger values of $\gamma$ to lower values.

The evolution of the particle spectra due to STA alone is shown in the corresponding right panel. The spectra is now considerably different when compared to the previous case since, owing to turbulence and losses, particle energization occurs continuously rather than just when crossing the shock. The spectra evolves towards the typical steady state of the ultra-relativistic Maxwellian, as observed in the section 3.4.4, with a peak value $\gamma_c \sim 10^8$ when $t_A = t_L$. We also notice that the high energy cut-

Figure 3.7: Steady-state particle distribution with shock and turbulence acceleration for various turbulence spectra. *Left*: For $q = 2$, *Middle*: for $q = 5/3$ and *Right*: for $q = 3/2$. The solid blue line depicts the case of turbulent acceleration without shock; the orange line describes the case of shock and turbulence acceleration considering both regions ahead and behind of shock are turbulent, and the green line also describes the shock and turbulence acceleration scenario where only the post-shock region is turbulent.

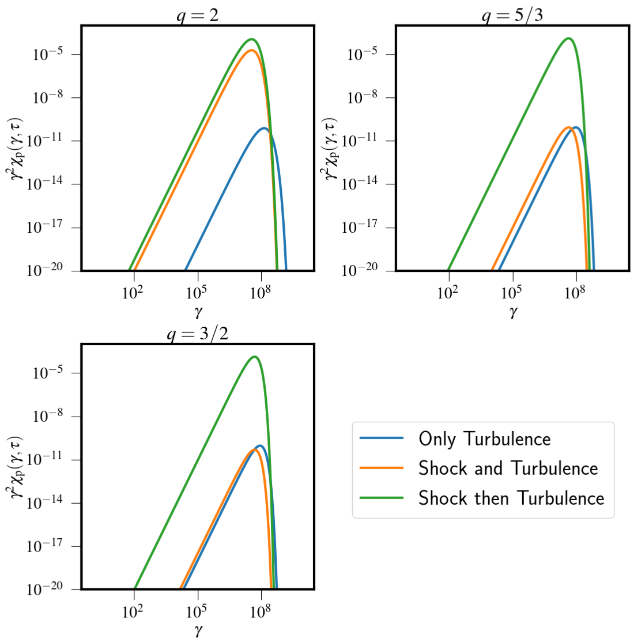


off does not ever decreases to lower values of $\gamma$ (as for the pure DSA) but, rather, it settles into a steady state as the result of mutual compensation between losses and STA.

In the bottom left plot, we show the evolution of the energy spectrum in the presence of both shock and STA. Both the upstream and the downstream are turbulent. In this scenario, the distribution function becomes harder than the initial one owing to the presence of upstream turbulence. The height of the spectrum now considerably increases if compared to the previous two cases. Such an increase is primarily due to the sub-grid modeling adopted at the shock front: the particle enters the shock with a pre-accelerated spectrum and eventually ends up in the downstream region with a different steady state (when compared to the STA alone case).

Finally, the particle energy evolution for the case in which STA is active only in the downstream region is shown in bottom right panel. As expected, the particle distribution does not significantly change until the particle crosses the shock and then enters in the downstream region where turbulence is active. Here steady state

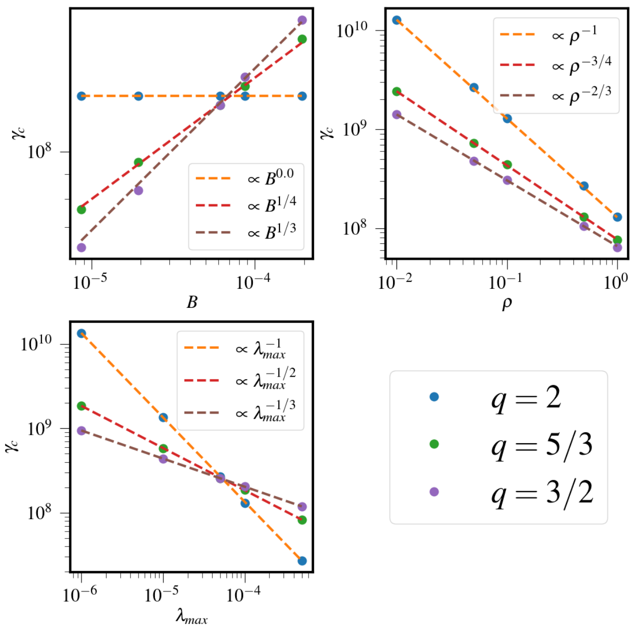


Figure 3.8: Dependence of $\gamma_c$ on various parameters for turbulent acceleration. *Left*: Dependence of $\gamma_c$ on various $B$ field, *Middle*: Dependence of $\gamma_c$ on various $\rho$ values and *Right*: Dependence of $\gamma_c$ on various values of $\lambda_{\max}$. Data point from corresponding simulations are shown as dots and the result from analytic calculations (see Eq. (3.37)) is shown with a dashed line for reference.

is attained due to STA. In this sense, the evolution resembles the previous case.

Further notice that, for all the cases but the pure DSA one, the particle distribution functions eventually seem to achieve steady states of similar kind. This is expected as the predicted steady state spectrum depends on the functional form of the transport coefficients which are not affected by the presence of the shock.

#### 3.5.1.1 Effect of turbulence on evolution of particle spectra

Additionally, in Fig. 3.7 we compare the particle steady-state distribution for turbulent spectra with $q = 5/3$ (middle), and with $q = 3/2$ (right) with that obtained for $q = 2$ (left).

The main difference between the acceleration scenario for turbulent spectrum with $q = 2$, on one side, and $q = 5/3$ or $q = 3/2$, on the other, is that the latter achieve steady state more rapidly because of the dependence of $t_A$ on $\gamma$.

Furthermore, the steady-state spectra for $q = 5/3, 3/2$ in the case of shock and STA are not significantly different from the ones computed with STA alone (see blue and orange solid line in the middle and right plot of Fig. 3.7). Owing to the smaller acceleration timescale, in fact, the spectra for $q = 5/3, 3/2$ approach the steady state only when the particle arrives in the upstream region making the shock injection less effective (see section 3.6) compared to the $q = 2$ case. However, for the case where turbulence is present only in the downstream region, shock injection can clearly be observed (solid green line in Fig. 3.7) as no significant turbulent energization took place in the upstream region.

Additionally, we analyze the behaviour of $\gamma_c$, with various values of $B_0$, $\rho_u$ and $\lambda_{\max}$. Analytically the value of $\gamma_c$ can be calculated by equating $t_A$ to $t_L$ and yielding

$$\gamma_c = \left\{ 2 \times 10^3 \times \frac{\left(\frac{eB\lambda_{\max}}{m_e c^2}\right)^{2-q}}{\rho\lambda_{\max}} \right\}^{\frac{1}{3-q}} \tag{3.37}$$

Plots of $\gamma_c$ computed from simulation data with different values of $B$ , $\rho$ and $\lambda_{\max}$ are compared in Fig. 3.8 toghether with the analytic form (Eq. 3.37). We observe a good correspondence between the results.

#### 3.5.1.2 Interplay of DSA and STA

In the previous section we found that the shock acceleration depends on the upstream spectrum. With this motivation here we try to analyze the impact of STA on particle shock energization by modulating the acceleration timescale $t_A$ and display its effect on the shock injection with different compression ratios. Moreover, we define the value of $t_A$ in terms of $t_L$ at $\gamma = 1.0$ and for each choice of $t_A$, we perform the simulation up to time $\tau = 100\,\hat{\tau}_0$. Owing to the conserving nature of the boundary condition, the number of micro-particles in a macro-particle remains same once the shock takes place, thus by calculating the number of micro-particles after shock we estimate the effect of shock injection when STA is in process. The variation of total number of particles after shock is shown with ratio $t_A/t_L$ at $\gamma = 1.0$ for different shock compression ratio in Fig. 3.9 with a fixed magnetic field calculated using

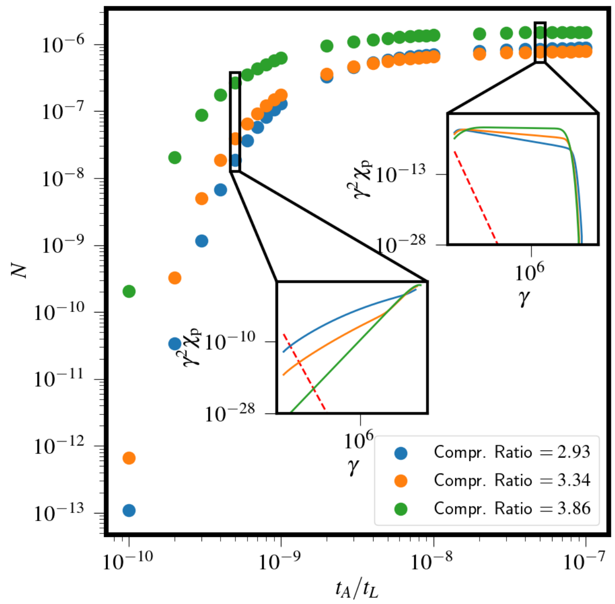


Figure 3.9: Dependence of shock injection on the upstream spectrum for various shock compression ratio with $\beta = 100.0$. The obliquity is made fixed at 30°. In the inset the downstream distribution function is shown for two different values of $t_A/t_L$.

$\beta = 100.0$. Further, the corresponding particle spectra at $\tau = 100\,\hat{\tau}_0$ is plotted for two values of the ratio and is shown in the inset of Fig. 3.9.

When $t_A$ is much less than $t_L$ at $\gamma = 1.0$ (or the ratio $t_A/t_L$ is small) the particle spectrum reaches the log-parabolic steady-state (see section. 3.5.1), before shock hits the particle. making the shock injection less effective. On the other hand when the ratio $t_A/t_L$ is comparatively high, one observe very minute effect of STA on the particle distribution in the upstream making the shock injection very effective for this case. Furthermore, notice that for any value of $t_A/t_L$ shock with higher compression ratio injects more number of particles than the lower ones. Also from the distribution functions shown in the inset, for two different values of $t_A/t_L$, it can be observed that the spectra that were hit by strong shock (high compression ratio) reach to the steady state much faster compared with the spectra hit by moderate shock (moderate compression ratio). Moreover, the decrement of the $\gamma_c$ (see section 3.5.1.1) with increasing $t_A/t_L$ could also be seen. Additionally, the number could be seen to achieve a steady state, around $N \sim 10^{-6}$, at the higher values of $t_A/t_L$ implies an upper bound of the particle injection at the shock for different compression ratios.

In summary, we observe that the effect of shock injection on the particle distribution function depends on the nature of the upstream particle distribution spectra. If the timescale of the STA in the upstream region is such that the particle distribution converges to steady-state spectra before the DSA could take place, the effect of shock injection becomes minimal. However, if in the upstream region the particle spectra do not reach the steady-state before the shock hits the particle, then a considerable effect of shock injection on particle spectra could be seen. This analysis spanning a wide parameter base, therefore showcases the interplay of these two particle acceleration processes.

### 3.5.2 Relativistic Blast Wave

Here we focus on the impact of a relativistic blast wave on the evolution of the spectral distribution in the presence of both shock and turbulence. Due to the underlying symmetry of the problem we choose a single quadrant with $512^2$ Cartesian computational zones with $x, y \in [0, 6]$. The initial condition consists of an over-pressurized central region of circular radius $0.8\hat{L}_0$ filled with pressure and density $\{P_c, \rho_c\} = \{1, 1\}$ surrounded by a uniform medium with $\{P_e, \rho_e\} = \{3\times10^{-5}, 10^{-2}\}$. The magnetic field is taken perpendicular to the $\{x, y\}$ plane, $\boldsymbol{B} = B_0\hat{z}$ as in Vaidya et al. (2018). The boundary condition is set to be reflecting at $x = y = 0$ and outflow elsewhere. We initially place 360 Lagrangian macro-particles uniformly over $0 < \phi < \pi/2$ at the radius of $\sqrt{x^2 + y^2} = 2$. Physical units are chosen such that $\hat{L}_0 = 10\,\mathrm{pc}$, $\hat{\rho}_0 = 0.01\,\mathrm{amu}$, $\hat{P}_0 = 1.5\times10^{-5}\,\mathrm{dyne/cm^2}$, $\hat{v}_0 = c$, $\hat{B}_0 = 1.37\times10^{-2}\,\mathrm{G}$ and $\hat{\tau}_0 = 32.64\,\mathrm{yrs}$. The initial distribution function for each macro-particle is taken

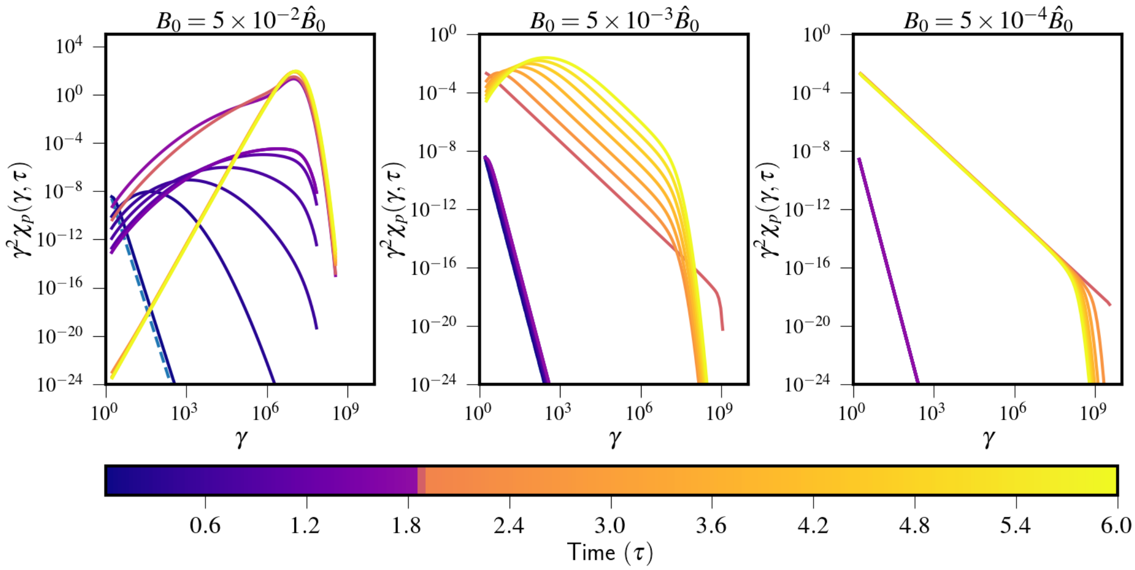


Figure 3.10: Temporal evolution of particle distribution of a Lagrangian particle in a turbulent medium for relativistic blast wave with different $B$ fields. The turbulent spectrum is taken as $\propto k^{-2}$, so the value of $q$ is 2 and the value of $\lambda_{\rm max} = \hat{L}_0/10$. *Left*: Corresponds to $B_0 = 5\times10^{-2}\hat{B}_0$, *Middle*: Depicts the evolution of the particle distribution for $B_0 = 5 \times 10^{-3}\hat{B}_0$ and *Right*: Corresponds to the evolution for $B_0 = 5 \times 10^{-4}\hat{B}_0$. Dashed blue line corresponds to the initial distribution function which is $\propto \gamma^{-9}$.

to be a steep decreasing power-law profile with index 9 covering a range in Lorentz factor $\gamma \in \{1, 10^8\}$ discretized using 128 bins. Similar to the MHD planar shock test (section 3.5.1), the diffusion coefficient is modelled following the acceleration timescale. The other microphysical processes considered are synchrotron, Inverse-Compton losses and adiabatic loss/gain.

The evolution of the particle distribution for a macro-particle initially placed at 65°, for $q = 2$, is shown in Fig. 3.10, where the particle evolution is shown for 3 different magnetic fields: $B_0 = 5 \times 10^{-2}$ (left panel), $B_0 = 5 \times 10^{-3}$ (middle panel) and $B_0 = 5\times10^{-4}$ (right panel). Furthermore, in all three cases the value of $\lambda_{\rm max} = \hat{L}_0/10$.

For the case with strongest magnetic field, the particle distribution initially evolves

Figure 3.11: Spectral slope distribution of particles initially placed at different angle ($\phi$) at the final time ($\tau = 6$) with $B_0 = 5 \times 10^{-4}\hat{B}_0$ for the relativistic blast wave test.

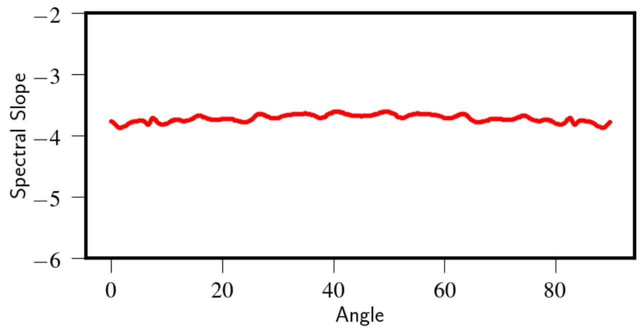


due to STA and, after crossing the shock, a steady-state ultra-relativistic Maxwellian-like spectral distribution can be seen to emerge eventually with a sharp cut-off beyond $\gamma_c \sim 10^8$. On the contrary, for the weakest magnetic field case, the spectral evolution shows distinct signatures of DSA only. Indeed, STA signature can hardly be observed as the timescale obeys $t_A \propto B^{-2}$ (see Eq. 3.12), thus very large for the simulation time. In this case, the initial steep spectra is accelerated and the spectral slope is flattened and cooling due to synchrotron and IC emission is evident from the cut-off. Moreover, it should be noted that the particle can be energized beyond $\gamma > 10^9$. For the intermediate case, we observe effects of both shock and STA in shaping the particle spectra.

Additionally, we quantified grid orientation effects by estimating the slope of the distribution functions for each macro-particle as a function of their initial angular positions. This is shown, at time $\tau = 6$ for $B_0 = 5 \times 10^{-4}\hat{B}_0$, in Fig. 3.11. The final slope for all the macro-particles approximately fall in the same range ($\approx -4$) with additional variations due to discretization error ($\sim 2\%$). Therefore all macro-particles will have similar spectral distribution as shown for the typical macro-particle in Fig. 3.10, apart from the minor variations due to discretization error.

### 3.5.3 Relativistic Magneto-hydrodynamic Jet

In this section, we describe a toy model of a relativistic magneto-hydrodynamic jet and analyze its emission signatures due to the DSA and STA of cosmic rays. In

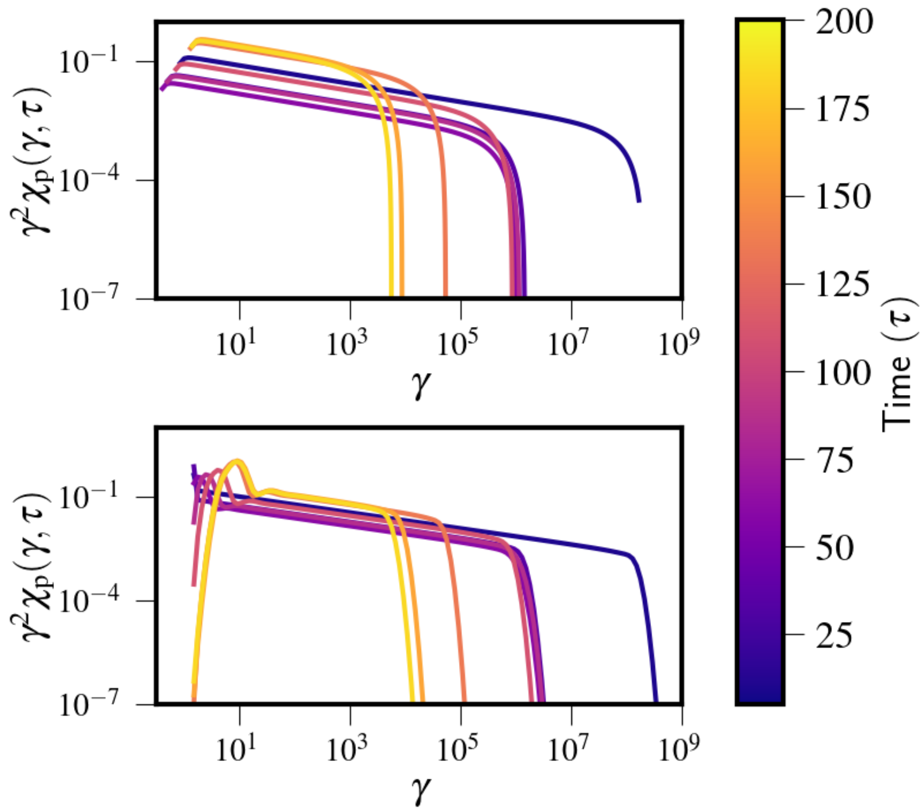


Figure 3.12: Temporal evolution of the spectrum of a Lagrangian particle which has gone through shock atleast once, in the RMHD Jet. *Top:* For the case of only DSA *Bottom:* For the case with STA along with DSA.

particular, we employ a $2D$ cylindrical grid $\{R, Z\} \in \{0, 0\}$ to $\{20, 50\}$ using $160 \times 400$ grid cells. The ambient medium is initially static ($\boldsymbol{V}_m = 0$) with constant density $\rho_m = 10^3\hat{\rho}_0$, where, $\hat{\rho}_0 = 1.67 \times 10^{-24}\,\mathrm{gr\,cm^{-3}}$. An under-dense beam with $\rho_j = \hat{\rho}_0$ is injected into the ambient medium with velocity $v_z$ along the vertical direction through a circular nozzle of unit radius, $R_j = \hat{L}_0$ from the lower $Z$ boundary. The value of $v_z$ is prescribed using the Lorentz factor $\gamma_j = 10$ and $\hat{L}_0 = 100\,\mathrm{pc}$ implying an unit timescale of $\hat{\tau}_0 = 326.4\,\mathrm{yrs}$. The magnetic field is purely poloidal, $\boldsymbol{B} = B_z\hat{\boldsymbol{e}}_z$ and is initially prescribed in jet nozzle and also in the ambient medium,

$$B_z = \sqrt{2\sigma_z P_j}. \tag{3.38}$$

where, $P_j$ is the jet pressure at $R = R_j$ estimated from the Mach number in the following way $M = v_j\sqrt{\rho_j/(\Gamma P_j) + 1/(\Gamma - 1)} = 6$ and adiabatic index $\Gamma = 5/3$. The values for $\sigma_z$ is taken to be $10^{-4}$ for the present simulation.

We further inject 25 Lagrangian macro-particles every two time steps with an initial power-law spectral distribution with index $-9$ on a initial $\gamma$ grid with $\{\gamma_{\min}, \gamma_{\max}\} \equiv \{1, 10^5\}$ discretized with 128 bins.

The energy spectrum of the macro-particles are calculated for two different scenarios: i) considering only DSA and different losses and ii) considering, in addition, also stochastic processes. For scenario (i) we follow the numerical algorithm developed in Mukherjee et al. (2021); Vaidya et al. (2018) to estimate the particle spectral distribution, while for scenario (ii) we solve Eq. (3.6) without the source and sink terms, along with the diffusion coefficient $D \propto \gamma^2$, where the proportionality constant is computed from the value of $t_A$ following Eq. (3.12) and with the value of $\lambda_{\max} = \hat{L}_0/100$. The advection term $S$ accounts for synchrotron, Inverse Compton losses and adiabatic loss/gain. Also, compared to the previous test problems here we take Courant number 0.8 when solving Eq. (3.6). Moreover, for both scenarios we compute the emissivity for each macro-particle based on their local spectral distribution and interpolated it on the underlying grid (Vaidya et al., 2018).

In Fig. 3.12, we show the spectral evolution of representative particles, that have been shocked at least once, for each of the scenarios. The top panel shows spectral evolution of a representative particle for the case where acceleration is due to shocks alone. The effect of DSA and radiative losses are clearly visible, respectively, from the spectral flattening and from high energy cut-offs. Here the cut-off can be observed clearly, as during DSA, the maximum energy get shifted according to

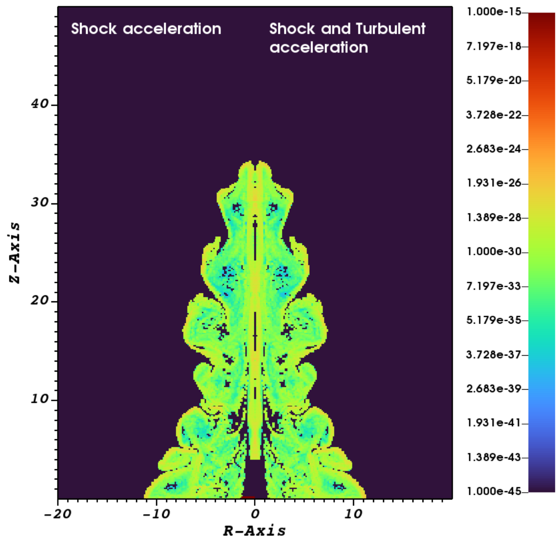


Figure 3.13: Comparison between the emission from turbulence and DSA and only DSA for radio frequency, $1.4\,GHz$ at time $\tau = 200$. Notice that the radial coordinate has been mirrored in the left plot.

the prescription described in Sec. 3.2. When the maximum $\gamma$ exceeds its initial value, cooling processes become effective so that the macro-particle quickly cools, accounting for a sharp spectral cut-off.

The bottom panel shows the spectral evolution of similar particles for the case where STA is also included (besides DSA). the distribution reveals a hump-like structure in the low-energy end of the spectrum that slowly shifts towards higher $\gamma$ values. With time, this eventually leads the distribution function to reach a steady state, as described by Eq. (A.21). Notice that our choice of parameters (Eq. 3.12) is such that the acceleration timescale $t_A$ is larger or comparable to the dynamical time, leading to feeble acceleration. We also point out that, during the initial stages, the particle spectrum exhibits a pile-up effect at low $\gamma$, because of the finite grid constraint, as discussed in section 3.4.3. This spurious effect dims with time as lower $\gamma$ particles start to accelerate toward higher $\gamma$. The impact of DSA (in addition to STA) can be

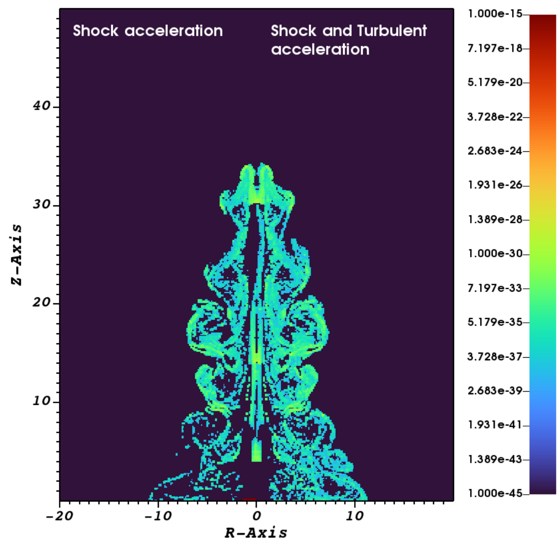


Figure 3.14: Same as Fig. 3.13 but for optical blue light frequency $6.59 \times 10^5\, GHz$ at time $\tau = 200$.

distinguished from the flattening of the spectral distribution. The more pronounced low-energy cutoff is attributed to the lower energy particles being accelerated by STA, eventually creating a deficiency in the number of particles at low $\gamma$.

From the instantaneous spectral distribution of Lagrangian macro-particles spread across the computational domain, we estimate the synchrotron emissivity by convolving the macro-particle spectra with single electron synchrotron spectra and interpolated it on the computational grid (see Eq. 36-37 in Vaidya et al., 2018). In Figs. 3.13, 3.14 and 3.15, the emissivity $J_\nu$ computed from the Lagrangian macro-particles is shown for different frequencies at time $\tau = 200\hat{\tau}_0$ for the two different scenarios (left and right halves, respectively).

In Fig. 3.13, with 1.4 GHz radio frequency, the emission due to turbulence and shock (right half) is very similar to the case with DSA only (left half). For the case with optical frequency ($\nu = 6.59 \times 10^5$ GHz) (Fig. 3.14), the emission becomes less than the radio frequency (Fig. 3.13) for both cases with and without STA. This is expected

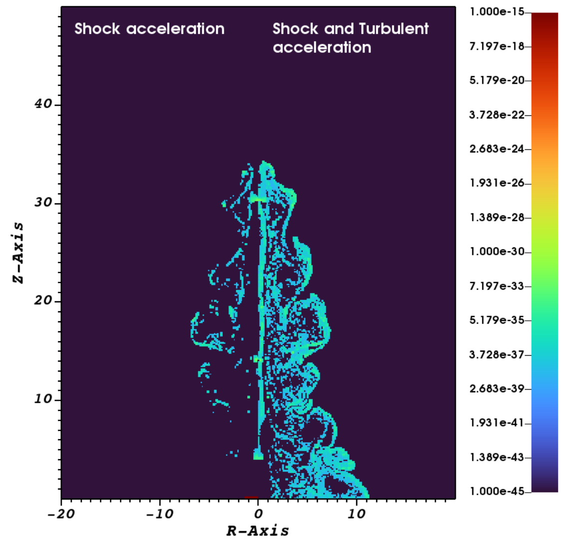


Figure 3.15: Same as Fig. 3.13 but for $0.4\,KeV$ X-Ray at time $\tau = 200$.

because of the faster cooling time with higher energy. However, a significantly larger emission can be seen in case ii) in the region $Z \lesssim 10$. The material in this region originates from the back-flow dynamics of the jet (Cielo et al., 2014; Matthews et al., 2019). If only shock energization is accounted for, the particle spectra become very steep in this region owing to radiative losses and the absence of strong shocks. However, if STA is also taken into account, the spectra remain hard because of the competing effects of STA and radiative losses. Similar high emission features are observed in X-ray ($\nu = 10^8$ GHz) as well (right panel of Fig. 3.15). On the contrary, in the presence of DSA only, a significant reduction in the X-ray emission can be seen (left half). Here most of the emission originates from the regions near jet head as well as isolated spots in the cocoon. In addition, smaller emission centers can be observed in the region around the re-collimation shocks along the beam. This differs from the case with DSA + STA, where the emission pattern was wider and more uniformly distributed throughout the jet and the backflow region.

## 3.6 Discussion and Summary

This chapter focuses on the numerical modeling of stochastic turbulent acceleration (STA) and its physical contribution to the spectral evolution of highly energetic particles. The numerical formulation is based on the fluid-particle hybrid framework of Mukherjee et al. (2021); Vaidya et al. (2018) developed for the PLUTO code, where the non-thermal plasma component is modeled by means of Lagrangian macro-particles embedded in a classical or relativistic magnetized thermal flow.

The particle distribution function is evolved by solving numerically a Fokker-Planck equation in which STA is modelled by two components: a hyperbolic term describing the systematic acceleration (Fermi II) and a parabolic contribution accounting for random resonant interaction between particles and plasma turbulent waves. While Vaidya et al. (2018) presented a Lagrangian method for the solution of the Fokker-Planck equation in the presence of hyperbolic terms only, here we have introduced a novel Eulerian algorithm to account also for an energy-dependent diffusion coefficient $D \sim \gamma^2$ which can become stiff in the high-energy limit. To overcome the explicit time step restriction, the new method takes advantage of $2^{\text{nd}}$-order Runge Kutta Implicit-Explicit (IMEX) methods, so that hyperbolic terms (e.g. adiabatic expansion or compression / radiative losses / Fermi II) are treated explicitly while parabolic terms (modelling turbulent diffusion) are handled implicitly.

Selected numerical benchmarks validated against analytical solutions and grid resolution studies demonstrate that our implementation has improved stability and accuracy properties when compared to previous solvers (see for example Chang & Cooper, 1970; Winner et al., 2019). In addition, due to the presence of boundary condition our algorithm respects physical constraints (for example, $\gamma \geq 1$) which are not always satisfied in the Lagrangian method (Mukherjee et al., 2021; Vaidya et al., 2018) with an evolving grid. STA modeling has also been validated against radiative synchrotron loss process by studying the evolution of curvature of particle spectrum (Tramacere et al., 2011).

With these motivations, we have studied the effect of STA as well as other energization processes, on the particle spectrum in the presence of shocks, using toy-model applications. Such an interplay is commonly believed to operate in supernova remnants, AGN radio lobes, galaxy clusters and radio relics.

As a first application example, we considered a simple planar shock in four different acceleration scenarios. We found that when STA and DSA both are considered, the former seems to affect the shock injection by changing the macro-particle distribution function. Further tests with different forms of the diffusion coefficient reveal a similar behavior. Additionally, we have also quantified the effect of STA time scale on the radiative losses and its influence on the interplay with DSA. In particular, we observe that the effect of shocks on particle distribution weakens with decreasing STA time scales. Similar interplay of DSA and STA was also evident in case of spherical shock formed in the test case of RMHD blast wave.

Finally, we have extended our algorithm to explore the emission properties of the axisymmetric RMHD jet using a toy model. We find a significant difference both in the evolution of the spectral distribution and the ensuing emission signatures due to the presence or absence of the STA process. In particular, inclusion of STA results in diffuse emission within the jet back-flow, particularly in the high-energy X-ray band. Consequences of such an important finding will be further explored in forthcoming works focusing on astrophysical systems along with comparison with observed signatures.

# Chapter 4

# Interplay of different Fermi acceleration processes in the radio lobe

*This chapter has been adopted from Kundu et al. (2022)*[0]*, and it discusses the effect of the interplay of shock and stochastic acceleration on the non-thermal emission from the radio lobes of the FR-II AGN jet systems. It considers a phenomenologically motivated ansatz for stochastic acceleration, and by comparing various acceleration scenarios, it demonstrates the complementary nature of the acceleration processes in producing X-ray emission.*

---

## 4.1 Introduction

Radio galaxies are thought to be among the most energetic systems in the Universe. These extragalactic objects are observed to possess a huge reservoir of relativistic nonthermal particles, which collectively shape their emission features (Blandford et al., 2019). Furthermore, due to the abundance of highly energetic particles, these galaxies are generally considered favorable sites to study various high-energy phenomena (Meisenheimer, 2003). In recent years, thanks to the advent of multi-

[0]Kundu, S., Vaidya, B., Mignone A. and Hardcastle M. J. (2022) A numerical study of the interplay between Fermi acceleration mechanisms in radio lobes of FR-II radio galaxies, Astronomy & Astrophysics, vol. 667, 2022, https://doi.org/10.1051/0004-6361/202244251

messenger astronomy, different observations have uncovered various features and are helping us understand the different microphysical processes occurring in these systems (Marcowith et al., 2020).

Low-frequency radio observations of these radio galaxies provide insights about their morphological structures (see Hardcastle & Croston, 2020, for more details), their magnetic field strength (Croston et al., 2005), and their age (Alexander & Leahy, 1987; Carilli et al., 1991; Mahatma et al., 2019). Based on the brightness of these sources at 178 MHz, they are classified as FanaroffRiley (FR) class I (low power) or II (high power) (Fanaroff & Riley, 1974). These two classes of radio galaxies are observed to manifest different morphological structures. While FR-II sources exhibit a one-sided smooth spine-like structure with a bright termination point, FR-I sources show a two-sided plume-like structure. Additionally, FR-II sources show prominent signs of turbulent cocoons that have an extent of a few hundred kiloparsecs, and are often partly visible as lobes (Hardcastle & Croston, 2020; Mullin et al., 2008). These lobes are believed to be highly magnetized cavities of rarefied plasma where most of the jet kinetic power is deposited. Radio lobes also have a hotspot region near the jet termination region, responsible for accelerating particles to high energies via diffusive shock acceleration (DSA) (Araudo et al., 2018; Brunetti et al., 2001; Prieto et al., 2002). These freshly shock-accelerated particles further mix with the older plasma particles already residing in the lobe, which makes the lobe a turbulent playground for various plasma waves to interact with the particles and then accelerate them via stochastic turbulent acceleration (STA). This mechanism has also been invoked to explain the particle acceleration in various astrophysical systems such as solar flares (Petrosian, 2012), the corona above the accretion disk of compact objects (Belmont et al., 2008; Dermer et al., 1996; Liu et al., 2004; Vurm & Poutanen, 2009), supernova remnants (Bykov & Fleishman, 1992; Ferrand & Marcowith, 2010; Kirk et al., 1996; Marcowith & Casse, 2010), gamma-ray bursts

(Schlickeiser & Dermer, 2000), emission from blazars (see Asano & Hayashida, 2018; Tavecchio et al., 2022, and references therein), Fermi bubbles (Mertsch & Petrosian, 2019), and galaxy clusters (Brunetti & Lazarian, 2007; Donnert & Brunetti, 2014; Vazza et al., 2021). STA has been invoked as a possible mechanism for producing ultra-high-energy cosmic rays (UHECRs) from the radio lobe of Pictor A (Fan et al., 2008) and Cen A (Hardcastle et al., 2009; O'Sullivan et al., 2009). Recently, it has also been invoked as a plausible candidate in explaining the spectral curvature usually observed in FR-II radio lobes (Harris et al., 2019).

In addition to the radio observations, X-ray observations of these radio-loud active galactic nuclei (AGNs) have become popular due to the minimal contamination of the X-ray radiation by non-AGN sources. Several components of these sources, such as radio lobes, hotspots, and collimated radio jet spines, are observed to radiate in the X-ray band (de Vries et al., 2018; Massaro et al., 2018). Additionally, these lobes are often observed to give rise to diffuse X-ray emission from the region between the host galaxy and the radio hotspot, which is usually ascribed to the inverse-Compton emission off the cosmic microwave background radiation (IC-CMB) (Blundell et al., 2006; Croston et al., 2005; Hardcastle et al., 2002). Recent observations reveal that the nonthermal X-ray emission from the radio lobe increases with redshift, further supporting the IC-CMB origin (Gill et al., 2021). Diffuse X-ray emission has also been reported in the jets of the FR-I class of radio galaxies and has been ascribed to a distributed particle acceleration mechanism (Hardcastle et al., 2007b; Worrall, 2009; Worrall et al., 2008). An IC-CMB model is sometimes invoked to explain X-ray emission from the jets of FR-II radio galaxies and quasars; however, such models require the jet to be highly relativistic and well aligned with the line of sight and consequently tend to imply very large physical jet lengths, sometimes in excess of several megaparsecs (Celotti et al., 2001; Ghisellini, G. et al., 2005; Tavecchio et al., 2000). Furthermore, recent polarimetric studies and high-energy gamma-ray constraints provide evidence supporting the synchrotron emission model as the origin of diffuse X-ray emission from AGN jets (see Perlman et al., 2020, for a recent review). This consequently requires particles with very high energies to be present in the jet and also favours a distributed particle acceleration mechanism due to the short synchrotron lifetime of the radiating particles.

The present work explores, for the first time, the interplay of vital particle acceleration mechanisms in a weakly magnetised plasma environment such as the radio lobes of FR-II radio galaxies and studies their effect on the emission properties of these systems. Due to the complicated evolution of the dynamical quantities as a result of a nonlinear plasma flow pattern inside these lobes, we adopt a numerical approach for this work. In particular, we employed magnetohydrodynamic (MHD) simulations to produce radio lobes and analyze the emission features caused by particle energization in the presence of shocks and underlying turbulence. We adopted our recently developed second-order accurate STA framework (Kundu et al., 2021) for this purpose. Owing to the increased computational complexity of the developed framework, this chapter focuses on a 2D axisymmetric MHD jet model only, while leaving the more computationally expensive 3D case to forthcoming works.

The chapter is organised in the following way. We describe our numerical setup for simulating a 2D axisymmetric AGN jet in section 4.2.1. Section 4.2.2 describes the numerical model to compute the emission properties. In section 4.3 we present the results of the simulations. In section 4.4 we summarize our findings and discuss the limitations of our model.

## 4.2 Numerical setup

In this section we describe the numerical setup adopted for the present work. The radio lobes are typically associated with the termination point of the AGN jet, where the velocity of the jet material reduces considerably such that relativistic effects become negligible (Huarte-Espinosa et al., 2011). Furthermore, as shown by Hardcastle & Krause (2013), numerical simulations of realistic radio lobes require high Mach number flows as well as very high-resolution meshes in order to have radio lobes in pressure equilibrium with the surrounding medium and to resolve the transverse radial equilibrium. Therefore, to investigate the emission profile of the radio lobes, we focus on a nonrelativistic scenario and perform a two-dimensional axisymmetric ideal MHD simulation using the PLUTO code (Mignone et al., 2007). In particular, we solve the following set of conservation equations

$$\frac{\partial \rho}{\partial t} + \nabla \cdot (\rho \boldsymbol{v}) = 0\,, \tag{4.1}$$

$$\frac{\partial \boldsymbol{v}}{\partial t} + (\boldsymbol{v} \cdot \nabla)\boldsymbol{v} = -\frac{1}{\rho}\nabla P + \frac{1}{\rho}(\nabla \times \boldsymbol{B}) \times \boldsymbol{B}\,, \tag{4.2}$$

$$\frac{\partial P}{\partial t} + \boldsymbol{v} \cdot \nabla P + \Gamma P \nabla \cdot \boldsymbol{v} = 0\,, \tag{4.3}$$

$$\frac{\partial \boldsymbol{B}}{\partial t} = \nabla \times (\boldsymbol{v} \times \boldsymbol{B})\,, \tag{4.4}$$

where the quantities $\rho$, $P$, $\boldsymbol{v}$, and $\boldsymbol{B}$ represents density, pressure, velocity, and magnetic field, respectively; the magnetic field $\boldsymbol{B}$ further satisfies the constraint $\nabla \cdot \boldsymbol{B} = 0$; and $\Gamma$ represents the ratio of specific heats and its value is taken to be 5/3, which is typically considered for supersonic nonrelativistic jets (Massaglia et al., 2016). Equations (4.1)-(4.4) are solved with the HartenLaxvan Leer contact (HLLC) Riemann solver using piece-wise linear reconstruction, the van Leer flux limiter (Van Leer, 1977) and second-order Runge-Kutta time-stepping. Additionally, we consider divergence cleaning (Dedner et al., 2002) to satisfy the solenoidal constraint of magnetic field.

### 4.2.1 Dynamical setup

The two-dimensional axisymmetric simulations are carried out in a cylindrical geometry $\{r, z\}$ such that the radial and vertical extents range from $\{0, 0\}$ to $\{65L_0, 195L_0\}$ with a resolution of $780 \times 2340$. The physical quantities defined in our simulations are appropriately scaled by defining length, velocity, and density scales. For the length we define the jet radius $r_j = L_0 = 2\,\mathrm{kpc}$ as the scale length. The core density is adopted as the scale for density such that $\rho_0 = 5 \times 10^{-26}\,\mathrm{gm/cc}$. Finally, for an ambient temperature $T_a = 2\,\mathrm{keV}$, we define the sound speed $c_a = v_0 = 730\,\mathrm{km/s}$ as the scale velocity.

The ambient medium density is initialized with an isothermal King profile (King, 1972)

$$\rho_a = \frac{\rho_0}{\left(1 + \left(\frac{R}{R_c}\right)^2\right)^{\frac{3\beta}{2}}}, \tag{4.5}$$

where $\rho_a$ is the ambient density that consists of a core with radius $R_c = 40L_0$, and $R/L_0 = \sqrt{r^2 + z^2}$ is the spherical radius. The value of the power-law index is kept constant at $\beta = 0.35$. Initially, the ambient medium is set to hydrostatic equilibrium using a gravitational potential ($\Phi_\mathrm{k}$) (Krause, 2005)

$$\Phi_\mathrm{k} = \frac{3\beta k_B T_a}{2\mu m_H} \log\left(1 + \left(\frac{R}{R_c}\right)^{\mathbf{2}}\right), \tag{4.6}$$

where $k_B$, $\mu$, and $m_H$ are the Boltzmann constant, mean molecular weight, and hydrogen atom mass, respectively. The ambient pressure ($P_a$) is computed as

$$P_a = \frac{\rho_a T_a k_B}{\mu}. \tag{4.7}$$

The ambient medium is set to be nonmagnetized initially, with the expectation that the magnetic field in the environment will have minimal impact on the nonthermal particle transport and the subsequent emission features within the lobe.

An underdense beam of density $\rho_j = \eta\rho_0$ with velocity $v_j$ is continuously injected in the medium from a circular nozzle of radius $r_j$, along the vertical direction ($\hat{z}$) at $t = 0$, with $\eta = 0.1$ being the density contrast. The nozzle is placed within the numerical domain with a height of $0.5L_0$. The adopted resolution samples the jet nozzle radius with 12 computational cells. The injection velocity ($v_j$) is obtained by choosing the sonic Mach number $M$ such that

$$v_j = Mc_a, \tag{4.8}$$

with $M = 25.0$. The injected beam includes a toroidal magnetic field ($B_j$) with the following radial profile (Lind et al., 1989)

$$B_{j,\phi} = \begin{cases} B_m \frac{r}{r_m} & \text{for } r \leq r_m \\ B_m \frac{r_m}{r} & \text{for } r_m \leq r \leq r_j \\ 0 & \text{otherwise} \end{cases}, \tag{4.9}$$

where the value of $B_m$ is governed by the plasma-beta parameter and $r_m$ is the magnetization radius. This magnetic field profile corresponds to a uniform current density within the radius $r_m$, the zero current density between $r_m$ and $r$, and a return current at $r$. Furthermore, this configuration also respects the symmetry condition on the $z$-axis ($B_j = 0$ at $r = 0$) (Komissarov et al., 2007). Additionally, a suitable gas pressure is provided inside the jet to ensure radial balance between the hoop stress and pressure gradient force

$$P_j = \begin{cases} \left(\delta + \frac{2}{\kappa}\left(1 - \frac{r^2}{r_m^2}\right)\right) P_e & \text{for } r < r_m \\ \delta P_e & \text{for } r_m \leq r < r_j \\ P_e & \text{at } r = r_j \end{cases}, \tag{4.10}$$

where $\delta = 1 - \frac{r_m^2}{\kappa r_j^2}$ and $\kappa = \frac{2P_e}{B_m^2}$, and $P_e$ is the pressure in units of $\rho_0 v_0^2$ at the nozzle radius computed from the ambient medium ($P_e = P_a$ at $r = r_j$). Owing to the constraint imposed by the 2D axisymmetric geometry, the induction equation (Eq. 4.4) does not enable conversion of the toroidal magnetic field ($B_\phi$) to a poloidal one. As a result, we consider a minimum value of $B_m \sim 100\,\mu$G to avoid significant amplification of the $B_\phi$ due to its continuous injection into the computational domain over time. Furthermore, the initial kinetic power of the jet is calculated from the quantities defined at the jet nozzle (Massaglia et al., 2016)

$$W = \frac{\pi}{2}\left(\frac{\Gamma k_B N_A}{\mu}\right)^{\frac{3}{2}} \eta \rho_0 r_j^2 M^3 T_a^{\frac{3}{2}}, \tag{4.11}$$

where $N_A$ is Avogadro's number. For the choices adopted in the present work, we obtain $W \simeq 10^{45}$ erg/s corresponding to the FR-II class of radio galaxies (Fanaroff & Riley, 1974).

For the boundaries we employ axisymmetric boundary conditions about the axis for the inner $r$ boundary and free flow boundary conditions for all the other boundaries in the computational domain.

### 4.2.2 Numerical setup to compute emission

The nonthermal emission from the radio lobe is modeled using the Eulerian-Lagrangian hybrid framework of the PLUTO code (Mukherjee et al., 2021; Vaidya et al., 2018). It employs passive Lagrangian (or macro-) particles whose dynamics is governed by the underlying fluid motion. Physically, these macro-particles represent an ensemble of nonthermal particles (typically leptons) residing very closely together in physical space with a finite energy distribution.

The energy distribution of these macro-particles is evolved by solving the transport equation

$$\frac{\partial \chi_p}{\partial \tau} + \frac{\partial}{\partial \gamma}\left[(S + D_A)\chi_p\right] = \frac{\partial}{\partial \gamma}\left(D\frac{\partial \chi_p}{\partial \gamma}\right), \tag{4.12}$$

where $\tau$ is the proper time; $\gamma \approx p/m_0 c$ is the Lorentz factor of the electrons, with $m_0$ being the rest mass of the electron; and $c$ is the speed of light in vacuum. The dimensionless quantity $\chi_p = N/n$, with $N(p, \tau)$ being the number density of the nonthermal particles with momentum between $p$ and $p + dp$ and $n$ being the number density of the fluid at the position of the macro-particle. The quantity $S$ represents various radiative losses and adiabatic loss/gain. The acceleration due to the Fermi second-order mechanism is given as $D_A = 2D/\gamma$, with $D$ being the momentum diffusion coefficient. For simplicity, we neglect the source and sink terms in the transport equation.

Equation (4.12) is solved using a second-order accurate finite-volume conservative implicit-explicit (IMEX) scheme (Kundu et al., 2021). The radiative losses considered include synchrotron, IC-CMB, and adiabatic expansion to model the cooling processes of relativistic electrons. Additionally, as the particle spectra in the high-energy region falls off rapidly due to various cooling processes, we follow Winner et al. (2019) and set the values of $\chi_p = 0$ beyond a threshold $\chi_{\rm cut} = 10^{-21}$ . We note that Eq. (4.12) does not include shock acceleration; instead, a separate sub-grid prescription is employed to account for DSA (Mukherjee et al., 2021; Vaidya et al., 2018).

The microphysics of turbulent acceleration is encapsulated in the diffusion coefficient $D$. Typically, the empirical form of $D$ is given as an input in numerical simulations (Donnert & Brunetti, 2014; Vazza et al., 2021) as its quantification from first principles is complex, particularly when applied to study large-scale astrophysical environments. In this work we opt for a phenomenologically motivated ansatz of exponentially decaying hard-sphere turbulence as a model of STA inside the radio lobe. We consider the acceleration timescale ($t_A$) as (Kundu & Vaidya, 2022)

$$t_A = \tau_A \exp\{(t - \tau_t)/\tau_d\}, \tag{4.13}$$

where $\tau_d$ is the turbulence decay timescale, $\tau_A$ represents the acceleration timescale when turbulence decay is absent (or $\tau_d \rightarrow \infty$), $t$ is the simulation time, and $\tau_t$ is the injection time of the macro-particle in a turbulent region. For a macro-particle that encounters a shock, its value is set to the time at which the last shock is encountered, while for those macro-particles that never undergo a shock the value of $\tau_t$ is set to the initial injection time in the computational domain.

This acceleration timescale has the capability to mimic the decay of turbulence, generally observed in various astrophysical sources. The decay is a consequence of the finite lifetime of the turbulence and prevents particles from being continuously accelerated. For this work we model $\tau_A$ and $\tau_d$ as

$$\begin{aligned}\tau_A &= \frac{\tau_c(\gamma_{\max} \to \gamma_{\min})}{\alpha}, \\ \tau_d &= \tau_A,\end{aligned} \tag{4.14}$$

where $\tau_c(\gamma_{\max} \to \gamma_{\min})$ represents the radiative loss time for a particle to cool from $\gamma_{\max}$ to $\gamma_{\min}$, and $\alpha$ is the ratio of synchrotron cooling time to acceleration time, which also controls the efficiency of STA. A higher value of $\alpha$ corresponds to smaller $\tau_A$ (STA timescale) and $\tau_d$ (turbulence damping timescale). Hence higher $\alpha$ indicates faster stochastic acceleration and faster damping. In addition, with lower values of $\alpha$ the effect of STA asymptotically diminishes. It is a parametric representation that models the turbulence that actually occurs in realistic radio lobes of FR-II radio galaxies, which is unresolved in our simulation. In this work we vary its value and study how this affects the emission signatures. The diffusion coefficient can subsequently be written as

$$D = \frac{\gamma^2 \exp\{-(t - \tau_t)/\tau_d\}}{\tau_A}. \tag{4.15}$$

The $\gamma^2$ dependency of the diffusion coefficient is a characteristic of the hard-sphere turbulence. Furthermore, instead of a $\gamma^2$ dependent diffusion coefficient, alternative diffusion models can also be explored. For example, adopting Bohm diffusion ($\propto \gamma$) could influence the results; however, a study of varying dependence of the diffusion coefficient on $\gamma$ is beyond the scope of the scope of the work presented here. To explore the ramifications of STA with varying efficiency on the emission of the simulated radio lobe structure, we use two alternative values for $\alpha = 10^4$ and $10^5$ in this study. Furthermore, to sample the jet cocoon uniformly, we inject enough ($\sim 20$) macro-particles at every time step in the computational domain. Initially, the normalized particle spectrum for each macro-particle is assumed to be a power law, defined as $\chi_p(\gamma) = \chi_0 \gamma^{-9}$, ranging from $\gamma_{\min} = 1$ to $\gamma_{\max} = 10^5$. The value of $\chi_0$ is set by prescribing the energy density of the macro-particles to be a fraction ($\approx 10^{-4}$) of the initial magnetic energy density. We note that the initial spectral index has a negligible effect on the emission of the system at later times as long as we consider a steep power law.

To compute the emissivity, we convolve the instantaneous energy spectrum of each macro-particle with the corresponding single-particle radiative power and extrapolate it to the nearest grid cells. In particular we solve the following integral to compute the emissivity

$$j(\nu', n', \tau) = \int_1^\infty \mathcal{P}(\nu', \gamma', \psi') N'(\gamma', \tau) d\gamma' d\Omega', \tag{4.16}$$

where $\mathcal{P}(\nu', \gamma', \psi')$ is the power emitted by a nonthermal particle per unit frequency ($\nu'$) and unit solid angle ($\Omega'$) with Lorentz factor $\gamma'$, and whose velocity makes an angle of $\psi'$ with the direction $n'$, and $N'(\gamma', \tau)$ is the number of micro-particles between Lorentz factor $\gamma'$ and $\gamma' + d\gamma'$ at time $\tau'$. In the case of an axisymmetric simulation, the magnetic field becomes independent of the polar angle, and therefore to consider the line-of-sight (LOS) effect in the synchrotron emissivity, an appropriate coordinate transformation is required (Meyer et al., 2021). We transform the magnetic field from cylindrical to Cartesian coordinates and compute the LOS effect by rotating the simulated structure explicitly. The entire rotation (of 360°) is performed with an interval of 5°. Subsequently, the intensity maps of the structure are computed by doing a LOS integration of the calculated emissivity. We note that all the emissivity calculations are performed by considering a viewing angle of $\theta = 90°$ (i.e., along the $z = 0$ plane in Cartesian coordinates).

## 4.3 Results

We categorize the major results from our simulations in two parts. The first part gives an overview of dynamical aspects of radio lobes and the second part provides a detailed analysis of multiwavelength emission signatures and particle acceleration processes within these lobes.

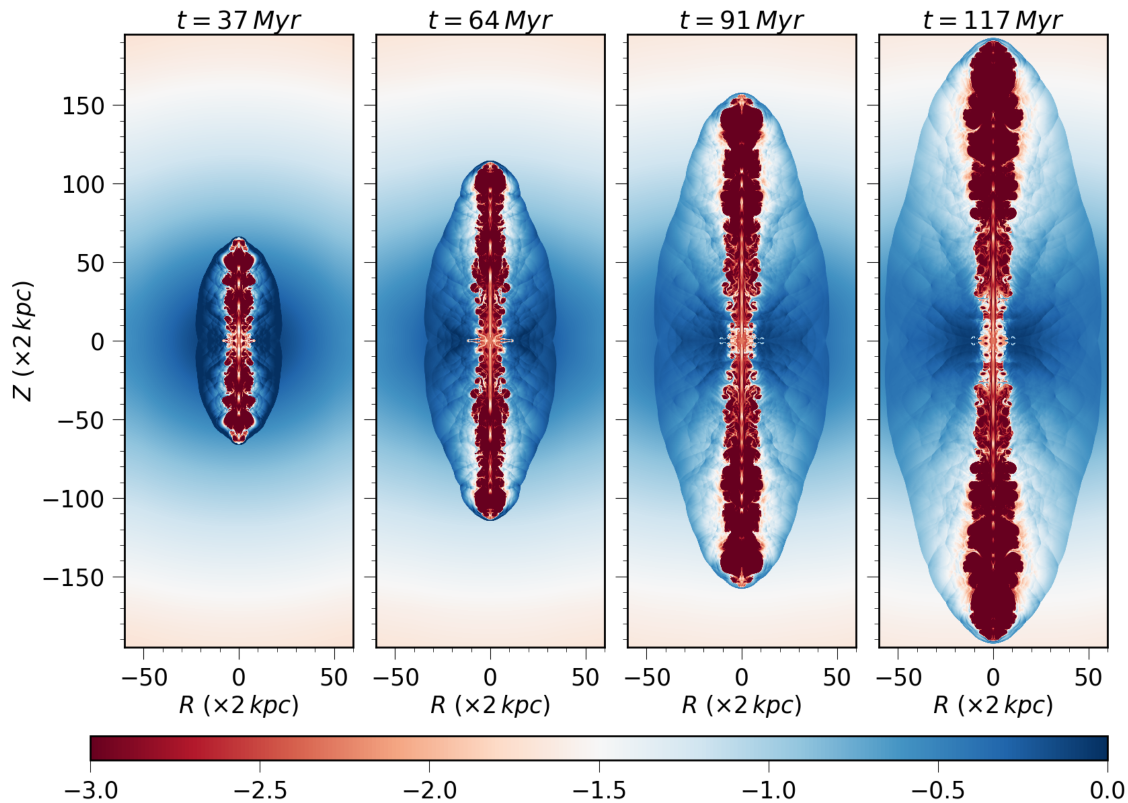


Figure 4.1: Normalized density $\rho/\rho_0$ evolution of the simulated radio lobe structure. The images depict a slice through the mid-plane of the notional 3D volume; all images are reflection-symmetric around the jet axis and the $z = 0$ plane since the simulations are axisymmetric. The color bar shows a logarithmic scale of density.

### 4.3.1 Dynamics

We carried out axisymmetric MHD simulations following the initial conditions described in Section 4.2 using the relevant jet and ambient medium parameters. The simulation was carried out up to a physical time of $\sim$ 120 Myr. In Fig. 4.1 we show the density evolution of the injected jets at different times: t = 37, 64, 91, and 117 Myr. The density structure at every time snapshot shows an expanding bi-directional underdense region, which at a later time ($t$ = 117 Myr) can be identified as lobes (English et al., 2016). Similarly to Hardcastle & Krause (2013), we found the formation of a long, thin lobe initially and a transverse expansion after-

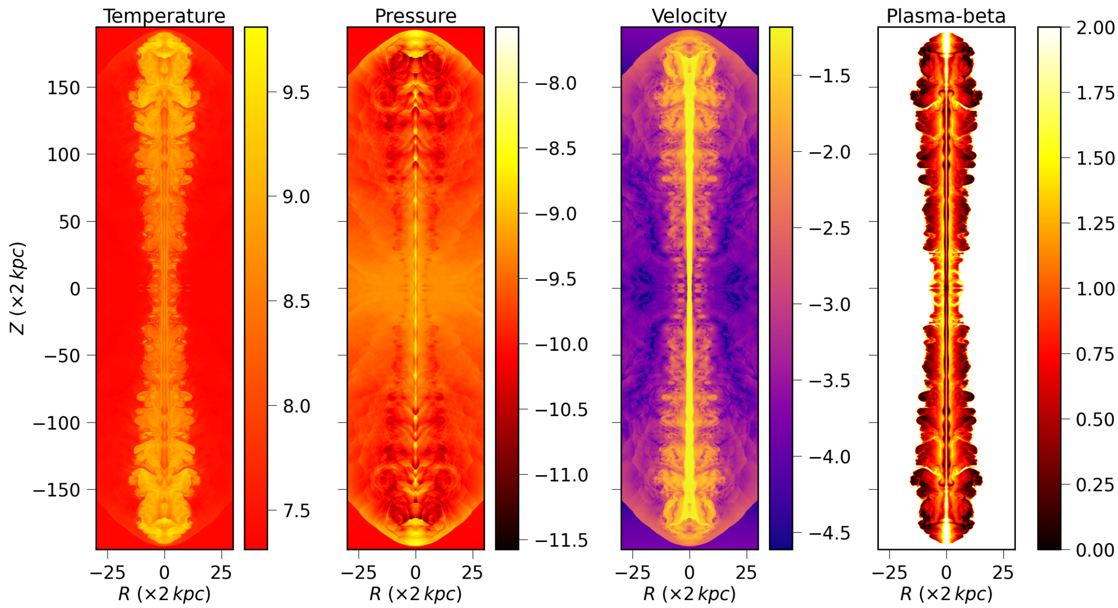


Figure 4.2: Temperature, pressure, absolute velocity, and plasma-beta maps of the simulated jet structure for time $t = 117\,\mathrm{Myr}$. Temperature and pressure are shown in physical units, velocity is shown in units of $c$, and the color bars are shown in logarithmic scale. The average temperature of the radio lobe is on the order of $\sim 70\,\mathrm{keV}$, average plasma-beta is $\sim 32$, and average velocity is $\sim 0.02c$.

ward. This subsequent expansion in the transverse direction is attributed to the thermalization of the jet material by the shocks present in the lobe. Furthermore, we observe the formation of vortices at the lobe boundary, which are typically attributed to Kelvin-Helmholtz instabilities originated from the velocity shear between the lobe material and shocked ambient material. Moreover, the entire structure is encapsulated within a forward-moving shock that can be seen to propagate through the ambient medium. This shock remains in the computational domain throughout the simulation time, preventing any mass, energy, and momentum from escaping the domain.

In Fig. 4.2 we show the temperature (left panel), thermal pressure (second panel), absolute velocity $|\boldsymbol{v}|$ (third panel), and plasma-beta (right panel) maps of the bi-directional jet at time $t = 117\,\mathrm{Myr}$. The temperature of the lobe (average value of

$\sim 70\,\mathrm{keV}$) is higher than the ambient medium ($T_a = 2\,\mathrm{keV}$). This is expected given the presence of a strong shock at the jet termination region, which is responsible for heating the jet material in the cocoon. The existence of the strong shock can be seen from the pressure map, as shown in the second panel of the figure. The pressure map also provides evidence of multiple re-collimation shocks along the jet axis. These shocks are expected to be favorable sites for accelerating particles via shock acceleration, and are known to be a source of localised high-energy emissions. Furthermore, we observe that the velocity of the jet is within the nonrelativistic limit, with an average value of $\sim 0.02c$. The plasma-beta map, as depicted in the right panel of the figure, shows that the lobes are thermally dominated with an average lobe plasma-beta value of $\sim 32$.

The underdense lobes observed in 2D simulations resemble the radio galaxies in a more consistent manner at later times (Hardcastle & Krause, 2013), in particular when the expansion results in the length of the underdense region being comparable to the core radius of the galaxy. Therefore, in this work, for the emission studies, we adopt the dynamical results at time $t = 117\,\mathrm{Myr}$.

### 4.3.2 Emission

We now look at the emission signatures of our model. The discussion is based on the comparison of synthetic emission signatures from different runs considered in our study. The parametric study focuses mainly on the properties of the stochastic turbulent acceleration mechanism. The details of these simulation runs are listed in Table 4.1; various acceleration scenarios are considered, corresponding to different turbulent acceleration timescales $t_A$, while the background thermal fluid evolution remains exactly the same.

The results obtained from cases (a) and (b) are useful in comprehending the impact of STA and its interplay with DSA. Cases (b) and (c) highlight the implications of

| Run ID | DSA | STA | Turbulent decay | $\alpha$ | Remarks |
|---|---|---|---|---|---|
| Case (a) | YES | NO | NO | 0 | Energy spectrum exhibits power law with exponential cutoff; PDF of $\gamma_{\rm avg}$ shows power law; SED shows transient peaks. |
| Case (b) | YES | YES | YES | $10^4$ | Individual macro-particle energy spectrum exhibits curvature; $\gamma_{\rm max}$ PDF indicates accumulation of particles around $10^4$; $\gamma_{\rm avg}$ PDF exhibits low-energy cutoff. Peak radiation from synthetic SED is $10^{10}$ Hz through synchrotron and $10^{19}$ Hz via IC-CMB. |
| Case (c) | YES | YES | YES | $10^5$ | Individual macro-particle energy spectrum exhibits curvature. $\gamma_{\rm max}$ PDF shows particle accumulation around $10^5$; $\gamma_{\rm avg}$ PDF provides evidence of low-energy cutoff. Synthetic SED peak at $10^{13}$ Hz through syncrotron and $10^{21}$ Hz via IC-CMB. |
| Case (d) | YES | YES | NO | $10^4$ | Individual macro-particle energy spectrum exhibits steady ultra-relativistic Maxwellian structure peaking at $\gamma \approx 10^4$. |
| Case (e) | YES | YES | NO | $10^5$ | Individual macro-particle energy spectrum exhibits steady ultra-relativistic Maxwellian structure peaking at $\gamma \approx 10^5$. |

Table 4.1: Properties of the different cases considered in the present study for calculating emission from the radio lobe. Column 1 gives the case labels for further reference. Columns 2, 3, and 4 represent the presence or absence of DSA, STA, and turbulent decay effects on the emission runs. Column 5 gives the value of the free parameter $\alpha$ (Eq. 4.14) chosen for different runs. The last column describes the results for each of the cases.

having different turbulent decay timescales (see Eqs. 4.13, 4.14). For cases (d) and (e), the turbulent decay is turned off by setting $\tau_d \to \infty$ in Eq. (4.13). Comparing results from these cases demonstrate the effect of the turbulent decay process in our simulations. In realistic astrophysical environments, we expect the turbulence to decay on a timescale that is governed by the micro-physical properties of the wave–particle interaction in that system. As the current work incorporates turbulence via a sub-grid model, we explored the implications of different parameters through these five cases. All the results presented in this section are for a dynamical time of 117 Myr, unless specified otherwise. Logarithmic binning has been adopted for all the histograms.

#### 4.3.2.1 Effect of turbulent acceleration on individual macro-particle energy spectra

In Fig. 4.3 we show the evolution of the energy spectra for all the cases listed in Table 4.1 for a randomly chosen macro-particle that encountered final shock at a dynamical time $t = 25$ Myr. In the simulations presented in this work the majority of the Lagrangian macro-particles are observed to encounter more than one shock. We selected one particular particle that had experienced multiple shocks only at earlier times as a representative candidate to demonstrate the effects of turbulent acceleration on the particle energy distribution in the downstream of the shock for all the case scenarios. The effect of multiple shocks on the energy spectrum of a Lagrangian macro-particle without STA has already been investigated in the context of AGN jet simulation (see, e.g., Giri et al., 2022; Mukherjee et al., 2021).

The spectral evolution of the macro-particle of case (a) is shown in the top left panel. The spectrum exhibits a power law with a high-energy cutoff which gradually shifts to lower energy with time owing to various energy losses. Additionally, a small hump can be seen in the low-energy part of the spectrum, caused by an excess of lower energy electrons arising from their higher energy counterparts due to radiative

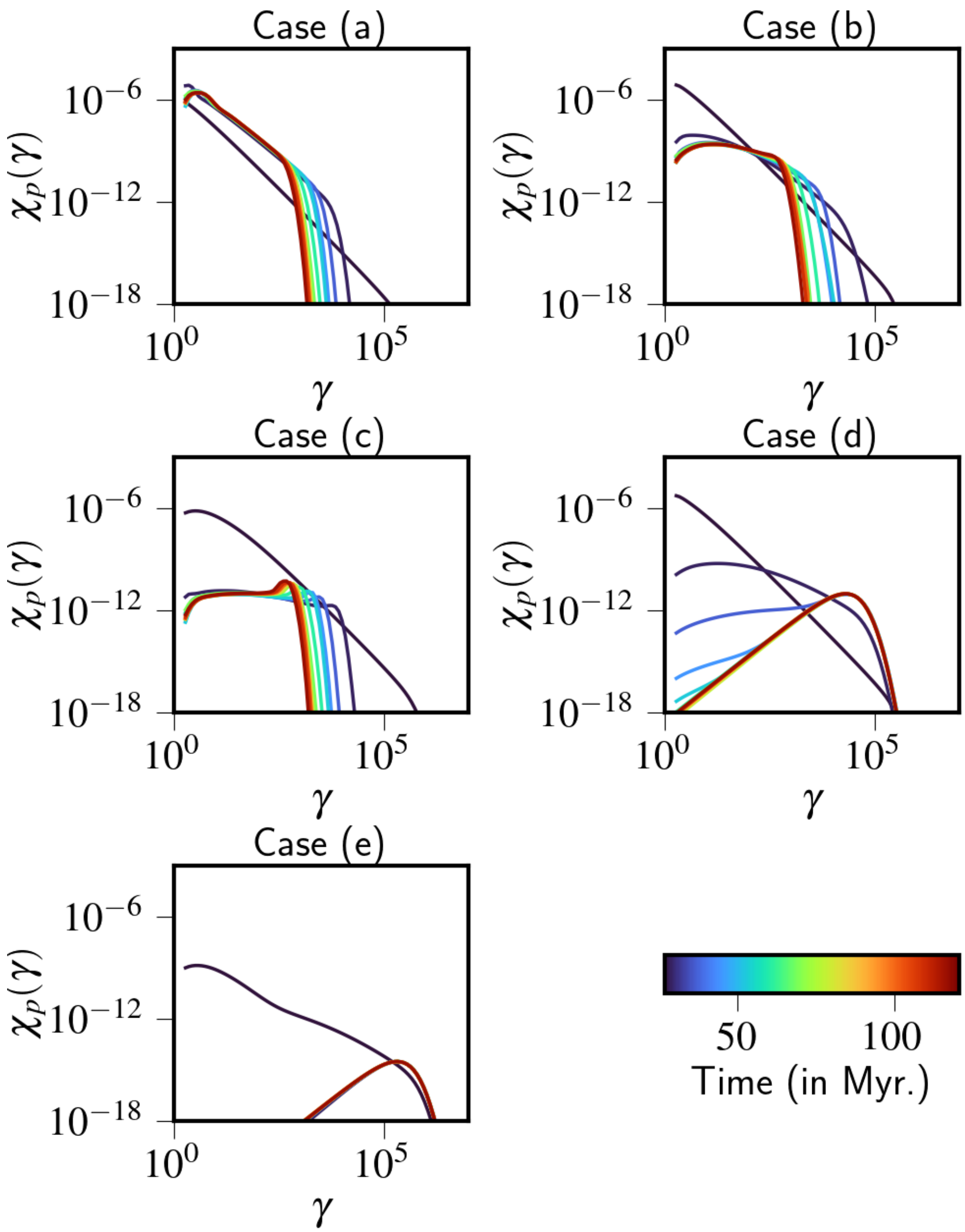


Figure 4.3: Evolution of the energy spectrum for a randomly chosen macro-particle for all the cases described in Table 4.1. The macro-particle encountered shock at a dynamical time of $t = 25\,\mathrm{Myr}$. The color bar shows how much time has elapsed since the simulation began. The value of the lower end of the color bar is set to the time when the macro-particle encountered the final shock.

cooling.

The shape of the spectrum changes considerably when STA is considered in addition to DSA. For cases (d) and (e) (right plot of the middle panel and left plot of the bottom panel, respectively) the spectrum exhibits an ultra-relativistic Maxwellian distribution at later times. This is a consequence of a steady competition between stochastic acceleration and radiative losses resulting in the acceleration of low-energy electrons toward higher energies (Kundu et al., 2021). Moreover, the peak of the distribution corresponds to the value of $\gamma$ at which acceleration and loss timescales match (i.e., $\tau_c = t_A$). We find that the peak corresponds to $\gamma \approx \alpha$ and depends on the choice of the turbulent acceleration timescale (see Eq. 4.13).

When turbulent decay is included (cases b and c) we observe flatness of the spectrum in the lower energy regime, compared to the power-law behavior observed in case (a), along with a high-energy cutoff. The flattening of the lower energy component of the spectrum is a consequence of the fact that STA provides a continuous acceleration to all the micro-particles, resulting in their acceleration to higher energies, depopulating the low-energy regime.

We also note that for the macro-particles that have encountered a shock, STA starts acting in the downstream and modifies the energy spectra on a timescale that depends on $t_A$ (Eq. 4.13), which in turn is regulated by the turbulent decay timescale $\tau_d$, and consequently develops a cutoff that moves toward lower energies.

In summary, the spectral evolution of a macro-particle, presented in Fig. 4.3 for different cases, clearly indicates that the presence of turbulent acceleration significantly affects the spectral energy distribution and its evolution. Our results indicate, in the absence of turbulent decay, that spectral evolution eventually relaxes toward a steady-state configuration in which energy losses are balanced by turbulent acceleration, while, when accounting for the decay of turbulence, the energy spectrum

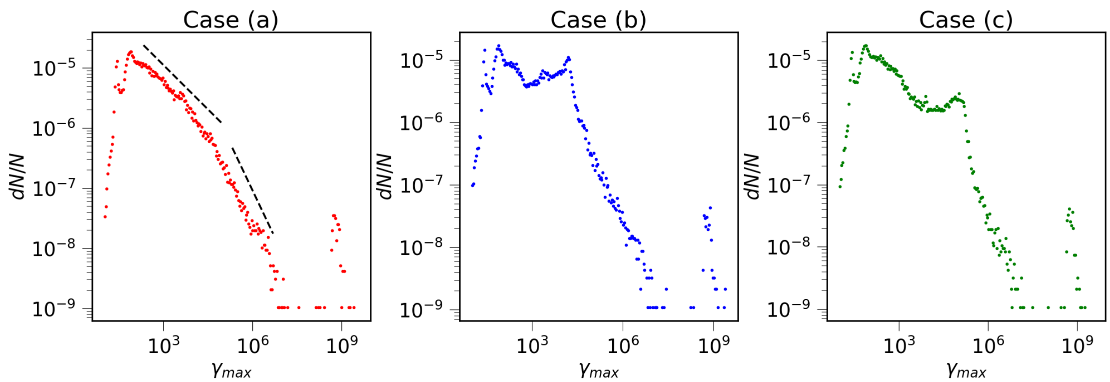


Figure 4.4: Probability distribution function of the cutoff energy for the entire macro-particle population. The **left, middle,** and **right panel** shows the PDF for case (a), (b), and (c), respectively.

exhibits a nonstationary behavior in time and the cutoff is governed by the radiative loss timescale subsequent to the decay of turbulence. Furthermore, the spectrum shows flattening in the lower energy regime owing to the energization of low-energy micro-particles to higher energy by STA.

#### 4.3.2.2 Effect of turbulent acceleration on particle population

This section focuses on the effects of turbulent acceleration on the entire macro-particle population in the lobe. In particular, we compute the effect of the STA with turbulence decay on the cutoff energy ($\gamma_{\rm max}$) for the macro-particle population. To compute the cutoff energy of a macro-particle we consider a generic form of its energy spectrum

$$\gamma^{-m} \exp\left(-\frac{\gamma}{\gamma_{\rm max}}\right), \tag{4.17}$$

where $m$ can be positive or negative depending on the macro-particle and $\gamma_{\rm max}$ is the cutoff energy. The exponential decay term takes care of the effects on the spectrum due to various radiative losses (see section 4.3.2.1). The value of $\gamma_{\rm max}$ is calculated by multiplying Eq. (4.17) by a power-law profile, $\gamma^{10}$, and calculating the maximum point of the resultant curve.

In Fig. 4.4 we show the probability distribution function (PDF) of the maximum (or cutoff) energy ($\gamma_{\max}$) attained by individual macro-particles for cases (a) (left panel), (b) (middle panel), and (c) (right panel). For case (a) the distribution peaks around $\gamma_{\max} \approx 10^2$, followed by a broken power-law-like tail beyond that. The origin of this peak can be attributed to the presence of various radiative losses in the system. The peak is also observed to gradually move toward lower values of $\gamma_{\max}$ with time. To support this argument, we undertake the following exercise: for a particle undergoing synchrotron cooling only, the initial Lorentz factor $\gamma^{'}$ after a time period of $t^{'}$ becomes

$$\gamma^{*} = \frac{1}{C_0 B^2 t' + \frac{1}{\gamma'}}, \tag{4.18}$$

where $C_0 = 1.28 \times 10^{-9}$ is the synchrotron constant for the electron and $B$ is the magnetic field. For our case, considering an averaged magnetic field of $B = 19.70\,\mu$G and $t^{'} = 117\,$Myr, we obtain $\gamma^{*} \approx 5.4 \times 10^2$ for a range of $\gamma^{'}$ values, which correlates with the position of the peak. The break in the power law around $\gamma_{\max} \sim 10^5$ is attributed to the continuous injection of the macro-particles in the computational domain with $\gamma_{\max} = 10^5$ (see section 4.2.2). The presence of an additional smaller peak around $\gamma_{\max} \sim 10^9$ can also be observed. This smaller peak is a transient feature, which arises from recently shocked macro-particles and is a manifestation of the continuous injection of jet material along with the Lagrangian macro-particles inside the computational domain. The presence of this transient peak has been reported in earlier works as well (see, e.g., Borse, Nikhil et al., 2021). Furthermore, the power-law trend of the tail of the PDF is typically ascribed to the interplay between the continuous injection of macro-particles in the computational domain and the shock acceleration of these freshly injected particles. This power-law-like behavior of the distribution in an AGN jet cocoon is also reported in Mukherjee et al. (2021).

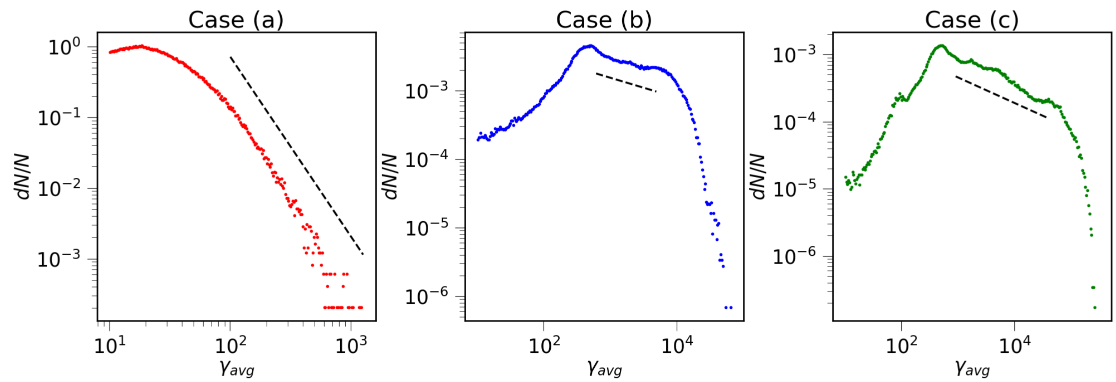


Figure 4.5: PDF of the $\gamma_{\rm avg}$ (see Eq. 4.19) for the entire macro-particle population. The **left, middle,** and **right panel** shows the PDF for case (a), (b), and (c) respectively.

The PDFs for cases (b) and (c) show some additional peaks compared to case (a). The origin of the peak at $\gamma_{\rm max} \sim 10^2$ is similar to case (a), while the high-energy peak ($\gamma_{\rm max} \sim 10^9$) is again due to recently shocked macro-particles. In addition, humps are observed at $\gamma_{\rm max} \sim 10^4$ (for case b) and at $\gamma_{\rm max} \sim 10^5$ (for case c). Their presence is caused by particles undergoing turbulent acceleration downstream of the shock, resulting in freezing the evolution of the cutoff at $\gamma_{\rm max} \approx \alpha$ for some time, due to the competition between STA and radiative losses, and afterward, due to the decay of turbulence, the cutoff continues to decrease toward lower energy, as dictated by loss processes.

To understand the distribution of electron energy within macro-particles, we also estimate the average value of $\gamma$ (at the final simulation time, $t = 117$ Myr) denoted by $\gamma_{\rm avg}$ as

$$\gamma_{\rm avg}(t) = \frac{\int_{\gamma_{min}}^{\gamma_{\rm max}} \gamma N(\gamma, t) d\gamma}{\int_{\gamma_{min}}^{\gamma_{\rm max}} N(\gamma, t) d\gamma}\,, \tag{4.19}$$

where $\gamma_{\rm max}$ and $\gamma_{\rm min}$ are given in section 4.2.2. In Fig. 4.5, we plot the PDF of $\gamma_{\rm avg}$ for the entire macro-particle population. In the left panel of the figure we show the PDF for $\gamma_{\rm avg}$ for case (a). The distribution exhibits a power-law tail ($\propto \gamma_{\rm avg}^{-q}$, with $q \approx 2.54$) beyond $\gamma_{\rm avg} \sim 10^2$. For cases (b) and (c) in the middle and right panels of

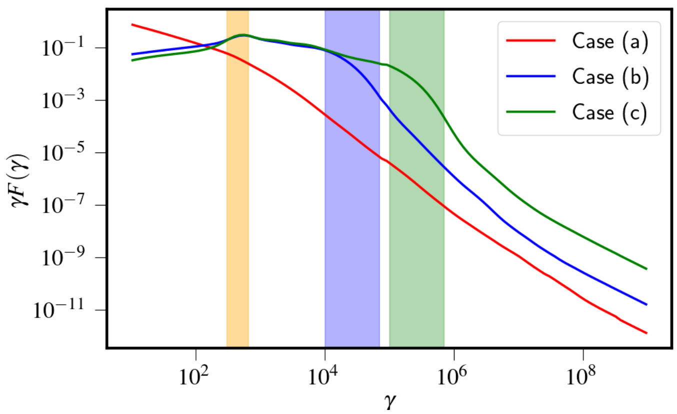


Figure 4.6: Integrated spectrum of the entire macro-particle population for the three cases. The portion of the spectrum highlighted in orange corresponds to the low-energy break. The highlighted portions of the spectrum in blue and green correspond to the high-energy cutoff for case (b) and (c), respectively.

the figure the PDFs exhibit a power-law distribution starting from $\gamma_{\rm avg} \sim 10^3$ with a small hump and an exponential cutoff. The hump feature arises due to competition between STA and radiative losses (see above). It is interesting to note that the slope of the power law for cases (b) and (c) ($q = 0.29$, $0.38$, respectively) are both flatter than for case (a). This is a consequence of the fact that STA continuously supplies energy to the macro-particles by accelerating the low-energy micro-particles to the higher energy, thus compensating for the radiative losses, as opposed to the case with only DSA. Finally, in the presence of both DSA and STA, the $\gamma_{\rm avg}$ PDFs exhibit a low-energy break around $\gamma_{\rm avg} \sim 10^3$ because STA boosts low-energy particles to higher energies. This process is absent if only DSA is present since there is no selective mechanism to accelerate only the low-energy particles during shock acceleration (which involves convolution of the entire upstream spectrum of each macro-particles to downstream; Mukherjee et al. 2021), and hence $\gamma_{\rm avg}$ PDF cannot form a low-energy break.

In Fig. 4.6 we present the integrated particle spectrum considering the whole macro-particle population for each of the three case scenarios. The integrated particle spectrum is calculated as

$$F(\gamma) = \sum_i \frac{\chi_p^i(\gamma)}{\mathcal{N}_i(\gamma) \int \chi_p^i(\gamma')d\gamma'}\,, \tag{4.20}$$

where $i$ corresponds to individual macro-particles inside the computational domain,

$\chi_p^i(\gamma)$ is the distribution function of the $i$-th macro-particle, and $\mathcal{N}_i(\gamma)$ represents the number of macro-particles with Lorentz factor $\gamma$. The DSA spectrum (case (a)) is in the form of a broken power law with the break at $\gamma \approx 5 \times 10^2$ (region highlighted in orange in the figure). This behavior is expected when computing a resultant distribution comprising all the macro-particles, where the spectral evolution is mediated by shock acceleration and radiative losses (Heavens & Meisenheimer, 1987). The position of the break has a direct correspondence with the peak in the $\gamma_{\max}$ PDF for case (a) and can be explained by the same reasoning (see Eq. 4.18). When STA is taken into account (cases (b) and (c)), the spectrum exhibits an inverse power-law behavior for $\gamma \lesssim 4 \times 10^2$, followed by a low-energy break and a power-law trend with a high-energy cutoff (highlighted in blue and green for cases (b) and (c), respectively). The spectral behavior in the region $\gamma \lesssim 4 \times 10^2$ is a manifestation of the low-energy flattening in the individual macro-particle spectrum (see section 4.3.2.1) due to turbulent acceleration. The origin of the low-energy break bears a similar explanation to case (a). However, for cases where STA is taken into account the cutoff is accompanied by piled up micro-particles (see case (c) in Fig. 4.3) as opposed to case (a), which is why the break appears more prominent in cases (b) and (c). The high-energy cutoff in the integrated particle spectrum (at $\gamma \approx 10^4$ for case (b) and $\approx 10^5$ for case (c)) is governed by the formation of the quasi-stationary cutoff in the individual macro-particle spectrum due to the interplay of DSA and STA. As a result, the position of these high-energy cutoffs has an exact correspondence with the peaks observed in Fig. 4.4 for the cases where STA is taken into account. The power-law trend beyond $\gamma \gtrsim 10^6$ for all the case scenarios is a consequence of the continuous macro-particle injection in the computational domain and a fraction of them subsequently undergoing shock acceleration.

In summary, turbulent acceleration with exponential decay modifies the macro-particles' maximum energy ($\gamma_{\max}$) distribution by presenting an additional hump

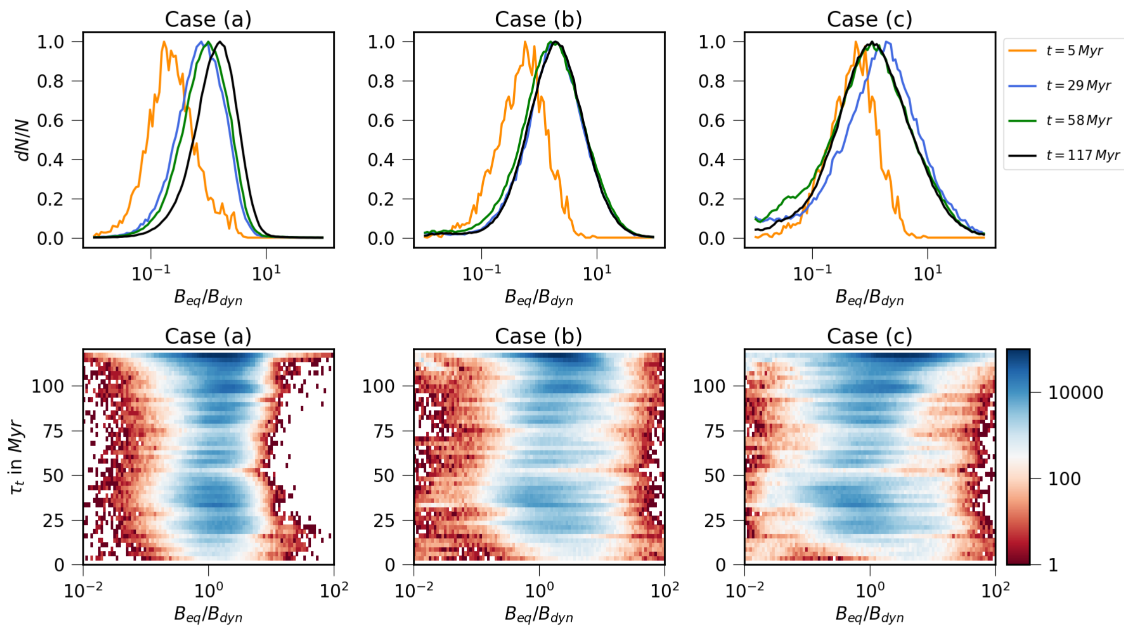


Figure 4.7: Histogram of macro-particles with respect to $B_{\rm eq}/B_{\rm dyn}$ to further study the effect of STA on the macro-particle population. The histograms are normalized and then scaled with the maximum value. **Top panel:** Histograms for three different cases at four different times (color-coded, see inset at right). The **top left, middle,** and **right panel** shows the histogram for case (a), (b), and (c), respectively. **Bottom panel:** Two-dimensional histograms showing $\tau_t$ vs. $B_{\rm eq}/B_{\rm dyn}$ at the final time $t = 117\,$Myr for three cases. The **bottom left, middle,** and **right panel** shows the histogram for case (a), (b), and (c), respectively. The color bar at the bottom panel shows the number of macro-particles.

to the PDFs. The location of the each hump is closely connected to the $\gamma$ of individual macro-particles, where $\tau_c = t_A$. The PDF of $\gamma_{\rm avg}$ for cases (b) and (c) exhibits a power-law trend with an exponential cutoff and a low-energy break. The integrated spectrum with only DSA exhibits a low-energy break, whereas with STA an additional cutoff at high energy is also seen.

#### 4.3.2.3 Turbulent acceleration as a sustained acceleration process

In this section we examine how STA supports the macro-particles to sustain their energy from extreme radiative losses. To properly characterize this behavior we consider an equivalent magnetic field for each macro-particle and compare it with the dynamical magnetic field at the position of the macro-particle. This is computed from the instantaneous single macro-particle energy distribution as

$$\frac{B_{\rm eq}^2}{8\pi} = m_0 c^2 \int_{\gamma_{min}}^{\gamma_{\rm max}} \gamma N(\gamma, t) d\gamma, \tag{4.21}$$

where $B_{\rm eq}$ is the corresponding equivalent magnetic field.

Following Eq. (4.21), we compute $B_{\rm eq}$ for cases (a), (b), and (c) and compare it with the corresponding dynamical magnetic field $B_{\rm dyn}$ computed at the local macro-particle position at each instant. We plot the time evolution of the histogram of the quantity $B_{\rm eq}/B_{\rm dyn}$ on a logarithmic scale for all three cases in the top panel of Fig. 4.7, where orange, blue, green, and black curves in each panel depict the histogram at times 5 Myr, 29 Myr, 58 Myr, and 117 Myr, respectively. All the histograms are normalized so that the maximum peak value is unity.

As shown in the top left panel, for case (a) the histogram gradually shifts toward a state with $B_{\rm dyn} \sim B_{\rm eq}$ as time progresses. Cases (b) and (c) exhibit a similar pattern, and a broadening of the histogram is observed as well. For case (a) the shape of the PDF can be observed to evolve to a negatively skewed distribution on a logarithmic scale. To analyze the reason for this evolution, we show a 2D histogram (bottom left panel) depicting the value of $\tau_t$ with respect to the magnetic field ratio, which indicates that the macro-particle population with a larger magnetic field ratio has recently been shocked. This should not be surprising since the shock acceleration energizes particles, thereby increasing $B_{\rm eq}$. The 2D histogram also shows that a relatively small fraction of macro-particles has magnetic field ratios higher than unity, due to the absence of any further acceleration process. As a result these particles undergo strong cooling and quickly lose their energy, hence featuring an exponential fall in the histogram beyond $B_{\rm eq} \sim B_{\rm dyn}$ (top left plot of Fig. 4.7).

On the contrary, for cases (b) and (c) (top middle and right panels) the 1D histogram evolves to a more extended structure, which closely resembles the log-normal shape.

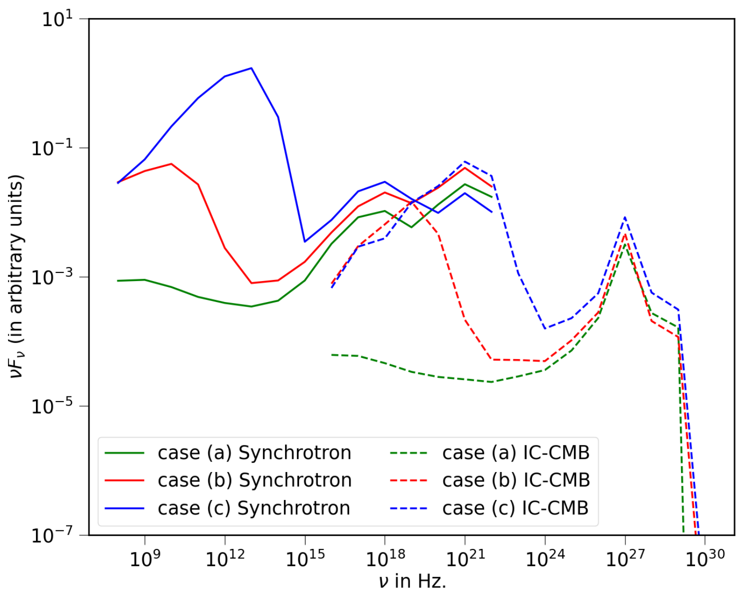


Figure 4.8: Synthetic spectral energy distribution for case (a) (in green), case (b) (in red), and case (c) (in blue). The SED due to the synchrotron mechanism is shown in solid lines and the IC-CMB part is shown in dashed lines. The vertical axis shows the value of $\nu F_\nu$ in arbitrary units.

This extended form of the histograms is ascribed to the presence of STA which provides a continuous acceleration to the macro-particles and helps them maintain their energy even in the presence of radiative cooling. This is further confirmed by observing the corresponding 2D histograms in the bottom panels (middle and right, respectively). In contrast to case (a), both figures show more macro-particles in the region $B_{\rm eq}/B_{\rm dyn} \gtrsim 1$. We can also infer that even macro-particles that were shocked earlier (smaller $\tau_t$) feature a higher value of $B_{\rm eq}/B_{\rm dyn}$ as a result of the fact that with STA macro-particles can sustain their energy for a longer amount of time.

In summary, for all the cases, we observe that the distribution gradually evolves toward a state where $B_{\rm eq} \sim B_{\rm dyn}$. Furthermore, due to the presence of STA, compared to only DSA, the histogram manifests a more extended structure that is evenly spread due to the macro-particles that were shocked at earlier time, but could sustain their energy from radiative losses because of STA.

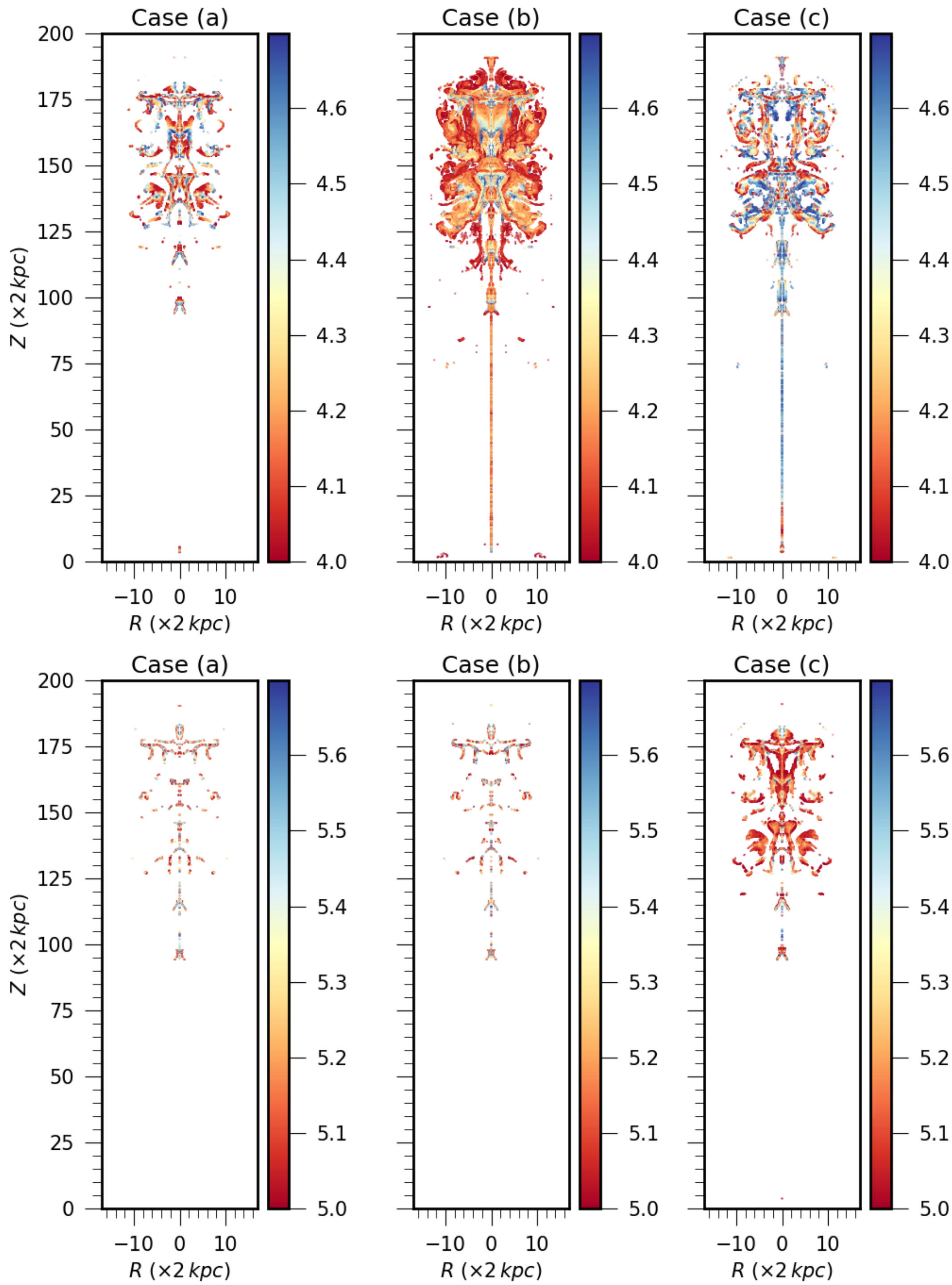


Figure 4.9: Spatial distribution of the particles responsible for the peaks in SED. **Top panel:** Position of the particle population with $\gamma_{\rm max} \sim 10^4$ for case (a) (**left**), case (b) (**middle**), and case (c) (**right**). **Bottom panel:** Position of the particle population with $\gamma_{\rm max} \sim 10^5$ for case (a) (**left**), case (b) (**middle**), and case (c) (**right**).

#### 4.3.2.4 Synthetic spectral energy distribution of radio lobe

In Fig. 4.8 we present the spectral energy distribution (SED) for cases (a), (b), and (c). The SED is calculated by integrating the emissivity (Eq. 4.16) along the line of sight (Vaidya et al., 2018) with two different radiation mechanisms: synchrotron and IC-CMB. The synchrotron SED shows, for case (a), enhanced emission in the X-ray band with multiple peaks at $\nu \sim 10^{18}$ and $\nu \sim 10^{21}$ Hz. These peaks originate from freshly shocked macro-particles (Borse, Nikhil et al., 2021; Mukherjee et al., 2021). This can be further verified analytically using the relation between the critical (or cutoff) frequency ($\nu_c$) of synchrotron radiation and the corresponding $\gamma$ (see, e.g., Eqs. (5.80) from Condon & Ransom, 2016):

$$\nu_c \approx \frac{\gamma^2 eB}{2\pi m_e c}. \tag{4.22}$$

For instance, with an averaged magnetic field of the lobe $B = 19.70\,\mu$G and $\nu_c \sim 10^{21}$ Hz, we obtain a corresponding value for $\gamma \sim 10^9$, which is consistent with the peak in the PDF of $\gamma_{\max}$ seen in Fig. 4.4.

For case (b), in addition to similar shock-induced transient signatures, the synchrotron emission shows a distinct peak in the low-energy GHz radio band ($\nu \sim 10^{10}$ Hz). The origin of such a low-energy peak is direct evidence of turbulent acceleration, and corresponds to the hump in the PDF at $\gamma_{\max} \sim 10^4$ (see middle panel of Fig. 4.4). Likewise, the synchrotron peak can also be observed for case (c) at a slightly higher energy, $\nu \sim 10^{13}$ Hz. The macro-particles that are accelerated via STA and give rise to the peak in PDF around $\gamma_{\max} \sim 10^5$ (right panel of Fig. 4.4) are mainly contributing to the emission at this frequency band. The macro-particle population that is stochastically accelerated in cases (b) and (c) is not only responsible for synchroton emission, but also contributes to the distinct peaks in the IC-CMB spectral energy distribution ($\nu \sim 10^{19}$ Hz for case b, $\nu \sim 10^{21}$ Hz for case c). We verified that these values correspond to the frequency of the photons scattered of a population of electrons with energy $\gamma_{\max} \sim 10^4$ and $\gamma_{\max} \sim 10^5$ for case (b) and (c), respectively. The post-scattering frequency of the photons $\nu_s$ is related to the electron energy as

$$\nu_s \approx \gamma_{\rm max}^2 \nu_0 \,, \tag{4.23}$$

where $\nu_0$ is the frequency at which the cosmic microwave background (CMB) radiates. Using $\nu_0 = 160\,\mathrm{GHz}$ in Eq. (4.23), we find that an electron population at $\gamma_{\rm max} \sim 10^4$ would scatter the CMB photons at a frequency of $\sim 10^{19}\,\mathrm{Hz}$. A similar inference can be drawn for the origin of the IC-CMB peak around $\sim 10^{21}\,\mathrm{Hz}$ for case (c). Additionally, the peaks in the $\gamma$-ray band ($\nu \sim 10^{27}\,\mathrm{Hz}$) for all cases corresponds to the particles with $\gamma_{\rm max} \sim 10^9$.

After observing the SED and identifying the particle populations responsible for the various peaks, we proceed to show the spatial distributions of these particle populations in order to understand the resulting emission structure. In Fig. 4.9 we show the spatial distribution of the particle populations responsible for these peaks. The top panels depict the particle distributions with $\gamma_{\rm max} \sim 10^4$ for case (a) (left plot), case (b) (middle plot), and case (c) (right plot). These particles are correlated to the peak in the SED caused by IC-CMB at $\nu \sim 10^{19}\,\mathrm{Hz}$, as explained earlier in this section. The macro-particles in case (a) can be seen to be more confined around the shocks in the beam and, to a lesser extent, to the cocoon region. The reason is that, after the shock acceleration, the macro-particles' energy evolution is governed by loss mechanisms alone, and as a result they lose a considerable amount of energy in a short distance. On the contrary, when turbulent acceleration is included, the particle distribution corresponding to $\gamma_{\rm max} \sim 10^4$ stretches over a wider area (see the upper middle and right plot) since macro-particles can be reaccelerated via turbulence, sustaining high energy for a longer distance before losing a substantial portion of their energy. In comparison to case (a), this extended spatial distribution implies a more diffuse structure of X-ray radiation attributable to IC-CMB. In the lower panel of Fig. 4.9 we show the spatial distribution of the macro-particles with

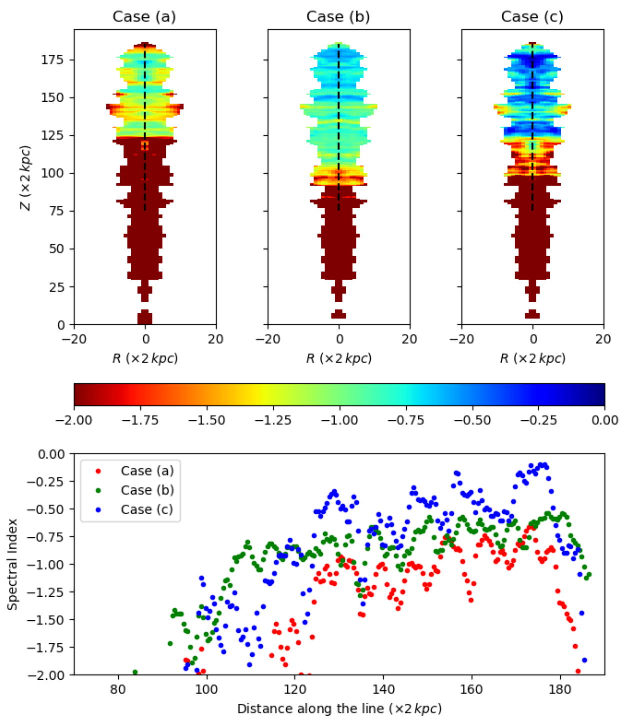


Figure 4.10: Spectral index map and spectral index distribution of the radio lobe for cases (a), (b), and (c). The spectral index maps are drawn considering two radio frequencies, 1.5 GHz and 15 GHz. **Top left panel:** Spectral index map for case (a), **Top middle panel:** for case (b), and **Top right panel:** for case (c). **Bottom panel:** Spectral index distribution for all three cases.

$\gamma_{\rm max} \sim 10^5$, responsible for the peak in the IC-CMB SED at $\sim 10^{21}$ Hz. Similar to the former scenario, the particle distribution shows an extended morphology for case (c) compared to the other two cases for the same reasons discussed before. Interestingly, the spatial distributions for case (a) (left panel) and case (b) (middle panel) have a very similar structure. The reason for this can be investigated by comparing the $\gamma_{\rm max}$ histograms for case (a) and (b) (left and middle panels in Fig. 4.4), showing a similar behavior (after the peak at $\gamma_{\rm max} \sim 10^4$ for the latter).

In summary, we showed that in the presence of stochastic acceleration the emission from the radio lobe changes significantly compared to the case where STA is neglected. With the inclusion of STA, the spatial distribution of the X-ray emitting particles through IC-CMB exhibit a wider extent (see Fig. 4.9) compared to the DSA-only case, indicating an emission structure that is diffusive.

#### 4.3.2.5 Spectral index distribution

In this section we focus on the effect of STA on the radio frequency regime ($\leq$ 15 GHz). With the advent of several high-resolution low-frequency telescope arrays it is possible to quantify the distribution of the spectral index in extended lobes (Alexander & Leahy, 1987; Harwood et al., 2013). In this regime the emission from astrophysical systems are dominated by synchrotron radiation, which follows a power-law relation with the frequency $I_\nu \propto \nu^{-\delta}$, with $\delta$ being the spectral index. In our simulation we compute the intensity from the macro-particle energy distribution (see section 4.2.2) and further calculate the spectral index $\delta$ using the equation

$$\delta = \frac{\log(I_{\nu_2}) - \log(I_{\nu_1})}{\log(\nu_1) - \log(\nu_2)}. \tag{4.24}$$

In the top panel of Fig. 4.10 we show the Gaussian-filtered spectral index maps of the radio lobe considering two frequencies, $\nu_1 = 1.5\,GHz$ and $\nu_2 = 15\,GHz$, for cases (a), (b), and (c). All the spectral maps show signs of spectral steepening from the outer regions of the lobe (near the bow-shock) toward the inner part. This spatial distribution can be further analyzed by observing the bottom panel of the figure, where we plot the vertical distribution of the spectral index value on the path depicted by the black dashed line shown in the corresponding top panel, from the inner region of the lobe to the outer region. The spectral index distribution behaves similarly for all three cases, showing a rapid increase followed by a softer (or almost constant) increase. By analyzing the slope of this second part, we obtain an average value for case (a) of $-1.01$, while for cases (b) and (c) it is $-0.80$ and $-0.49$, respectively. This implies that the radiation spectrum becomes harder with increasing $\alpha$ in the lobe. The spatial extent of the region with constant spectral index is larger for case (b) compared to cases (a) and (c). For case (a) this directly follows from the absence of any continuous acceleration mechanism other than shocks, and the ensuing radiative cooling of the macro-particles in the back flow over a short timescale. In contrast, for cases (b) and (c), STA provides additional continuous acceleration to the macro-particles. For this reason, the macro-particles could radiate for a longer amount of time and the value of the spectral index could be maintained for a longer distance. Additionally, due to faster turbulence decay, case (c) maintains the spectral index for a shorter spatial extent compared to case (b).

Our results have shown that the signature of the continuous acceleration of particles is due to the stochastic turbulence impact on several observables, including the spectral index variation along the lobe. We also observed that while with increasing $\alpha$ the spectral index value inside the lobe increases owing to the shorter acceleration timescale, the extent of the region with constant spectral index decreases due to turbulence decay. We discuss the implications of the synthetic measures quantified in section 4.3 with multiwavelength observational signatures in the next section.

## 4.4 Summary and discussion

In this work we presented 2D axisymmetric large-scale numerical simulations of AGN jets using a fluid-particle hybrid approach, in order to focus on particle acceleration processes and emissions from radio lobes. In spite of their limitations, and owing to the prohibitive cost of 3D computations, 2D models still provide fundamental insights into the interplay between different acceleration mechanisms and their influence on emission signatures.

Owing to the multiscale nature of the system, the underlying turbulence is considered in a sub-grid manner and its effect on the cosmic ray transport is modeled with a phenomenologically motivated ansatz for the turbulent acceleration timescale that can mimic the turbulence decay process usually observed in various astrophysical sources. By introducing this timescale, we solve the cosmic ray transport equation to evolve their energy distribution, accounting for diffusive shock acceleration (DSA), stochastic turbulent acceleration (STA), and for radiative losses (synchrotron and inverse-Compton), as implemented in the PLUTO code by Vaidya et al. (2018). We explore different scenarios by selectively including or excluding these acceleration mechanisms, and study their effects on the emission signatures of the radio lobes.

We summarize the primary results from this work as follows:

- We observe significant modification of the energy spectra of macro-particles when turbulent acceleration is included in addition to DSA compared to the shock acceleration-only case. The interplay of DSA, STA, and turbulent decay results in features such as flattening of the spectrum in the low-energy region and a dynamically evolving high-energy cutoff. These features produce curvature in the particle spectrum which can further manifest in the emission properties of the radio lobe (Duffy & Blundell, 2012).

- The analysis of the maximum attainable energy results in a unimodal PDF with a broken power-law tail when only shock acceleration is accounted for; instead, when both DSA and STA are included the PDF exhibits a bimodal structure. Furthermore, the PDF of the average energy ($\gamma_{\rm avg}$) for each macro-particle shows a power-law profile with an exponential cutoff on inclusion of STA. These distributions closely resemble the case in which STA is mediated by continuous particle injection and escape (see Fig. 2b of Katarzyński et al., 2006). Here particle injection due to shocks act as a source, while the escape is due to turbulence decay. The lobe integrated spectrum exhibits a broken power-law structure for DSA, whereas with STA it displays a high-energy cutoff in addition to the low-energy break. The position of the low-energy break corresponds to the $\gamma$ where radiative loss time becomes equal to the dynamical time. The integrated spectrum generated by including STA can be utilized as a consistent input for one-zone radio lobe modeling that accounts for particle acceleration due to turbulence.

- Further analysis of STA and its effect on sustaining the particle's energy against radiative cooling is performed through the evolution of $B_{\rm eq}/B_{\rm dyn}$ histograms, showing for all three cases that the system evolves to a state where $B_{\rm eq} \sim B_{\rm dyn}$. However, with STA the corresponding distributions become wider when compared to the shock-only scenario as a result of the additional energization.

- The study of the synthetic SED of the simulated source demonstrates the existence of additional peaks in the radio band due to synchrotron emission, and in the X-ray band through the IC-CMB mechanism when STA is taken into account. Further analysis of the spatial distribution of the macro-particles corresponding to these additional peaks implies a more extended and diffuse emission in the X-ray band owing to the interplay of the two acceleration mechanisms. The extent of the spatial distribution is further observed to be modulated by changing the value of $\alpha$ (see Eq. 4.13). This implies that with an appropriate choice of $\alpha$ one might achieve diffuse emission around localized regions inside the radio lobe (e.g., diffuse synchrotron emission around the hotspot of 3C445, see Prieto et al., 2002).

- The radio frequency spectral maps along with the spectral index profile inside the lobe indicate a harder emission spectrum due to STA compared to the DSA case. The spectral index is observed to remain constant over a distance inside the radio lobe whose length is modulated with the efficiency of the turbulent acceleration. The value of the spectral index in this region is $\sim -0.49$ for case (c), for case (b) it is $\sim -0.8$, and for case (a) it is $\sim -1.01$. This behavior has also been found in various observations of radio lobes (Parma et al., 1999). Radio lobes of parsec-scale AGN jets have been observed to exhibit similar characteristics (Hovatta et al., 2014). However, it should be noted that from observation of radio lobes there is no evidence of a spectral index $\approx -0.5$ or higher. This, consequently, may impose a limit to the extent and the effectiveness of STA in the actual radio lobes.

### Present limitations and future extension

The results shown in the present study represent a first step toward a more realistic description of the complex interaction between the turbulent radio lobe material and the nonthermal particles, and it is certainly limited by a number of considerations.

Two-dimensional axisymmetric models, for instance, are similar to 3D models only in the case of stable jets and homogeneous media. Time-dependent jet propagation is known to be prone to 3D instabilities (e.g., KelvinHelmholtz and current-driven modes) that cannot be captured by axisymmetric models (see, e.g., Bodo et al., 2013, 2016; Mignone et al., 2010). These instabilities are known to have an effect on the jet emission (Acharya et al., 2021; Borse, Nikhil et al., 2021) and can induce a range of non-axisymmetric structures, such as filaments and shocks along jets and in the back-flowing zone (see, e.g., Matthews et al., 2019; Tregillis et al., 2001). These non-axisymmetric structures are known to enhance the turbulence inside the back-flowing region, and hence would strongly influence particle mixing (Jones et al., 1999).

Another potential issue with 2D axisymmetric simulations is that, because of the $\partial_\phi = 0$ condition, the induction equation (Eq. 4.4) does not allow conversion of a toroidal magnetic field ($B_\phi$) to a poloidal field (Porth, 2013). This leads to the continuous amplification of the injected $B_\phi$ component in the computational domain over time, eventually affecting the jet dynamics. However, for this work we consider a very small $B_\phi$ value to lessen any substantial impact on the dynamics. Nevertheless, 2D computations still allow our method to be tested with finer grid spacing providing better resolution across shocked structures. This would be computationally expensive in the fully 3D case. Additionally, we also consider an un-magnetized ambient medium in the expectation that the magnetic field in the ambient medium will have minimal impact on the nonthermal particle transport within the lobe.

Our simulations describe the interaction between cosmic ray particles and jet materials although the former behave essentially as passive scalars without back-reaction on the fluid. A future extension of our work will consider more exhaustive two-fluid approaches by also taking into account energy and momentum transfer between the two components in a self-consistent way (Girichidis et al., 2020; Ogrodnik et al., 2021). It should be emphasized that the employment of parameters in our model is an unwanted, albeit necessary, consequence of the fact that large-scale simulations cannot possibly resolve (and therefore sample) the small-scale turbulence regions. Sub-scale micro-physical processes (such as turbulent acceleration timescales or MHD turbulence damping rates) must therefore be encoded through a sub-grid recipe. In this work, in fact, we consider a one-parameter exponentially decaying hard-sphere turbulence as a model of STA inside the radio lobe, with certain values for the parameter ($\alpha = 10^4, 10^5$) and compute the emission signatures from the radio lobes via synchrotron and IC-CMB processes.

Future extensions of this work will hopefully consider fully 3D investigations, where the impact of non-axisymmetric plasma instabilities may deeply affect the morphology. Additionally, the sub-grid prescription of turbulence decay plays a crucial role in governing some of the essential properties of emission.

# Chapter 5

# Cosmic ray acceleration due to small-scale MHD turbulence

*This chapter is adopted from Kundu et al. (2023)*[0]*, and discusses the effect of small-scale turbulence on the stochastic acceleration of non-thermal charged particles. This chapter illustrates the behaviour of the momentum diffusion coefficients in such a turbulent environment using a quasi-linear calculation with an isotropic turbulence spectrum taking into account no power in the resonant scale. Additionally, it investigates the interplay of stochastic acceleration due to small-scale turbulence with the synchrotron cooling process.*

---

## 5.1 Introduction

The transport of non-thermal charged particles dictates the emission properties of various highly energetic astrophysical sources. Usually, this transport phenomenon is mediated by a turbulent magnetic field, which subsequently leads the particles to exhibit diffusive behaviour in both space and energy domains. Such a diffusive behaviour in energy is a crucial component in accelerating the particles via the Fermi

[0]Kundu, S., Singh, N. K., & Vaidya, B. (2023). Acceleration of cosmic rays in presence of magnetohydrodynamic fluctuations at small scales. MNRAS, 524(4), 4950-4972, doi:10.1093/mnras/stad2098

mechanism since the efficiency and the rate of particle acceleration directly depend on the scattering due to the random magnetic fields. This turbulent acceleration is speculated to occur in different astrophysical sources with a diverse set of physical conditions, from the solar atmosphere (Bian et al., 2012; Petrosian & Liu, 2004; Selkowitz & Blackman, 2004) up to more exotic objects, e.g. blazars, gamma-ray bursts and other relativistic outflows (Asano & Hayashida, 2018; Asano & Mészáros, 2016; Bykov & Meszaros, 1996; Lemoine, 2016; Tramacere et al., 2011; Xu et al., 2019; Xu & Zhang, 2017). The magnetic turbulence also dictates the confinement of these charged particles in various astrophysical systems (Shalchi, 2009; Vukcevic & Schlickeiser, 2007).

An analytical quasilinear model of diffusion (Jokipii, 1966, 1973) has often been used to estimate diffusion coefficients when the turbulent field is weaker than the background magnetic field. Such analytical approach has been invoked to study the acceleration of particles via various MHD modes [by Alfvén modes (Chandran, 2000; Cho & Lazarian, 2006; Schlickeiser, 1989); by compressive modes (Chandran, 2003; Schlickeiser & Miller, 1998; Yan & Lazarian, 2002)]. For strong turbulence, on the other hand, several studies have employed numerical simulations to examine the transport properties of charged particles (Candia & Roulet, 2004; Casse et al., 2001; Fatuzzo et al., 2010; Giacalone & Jokipii, 1999). Most of these studies have focused their attention on the situation in which large-scale turbulence cascades toward smaller dissipative scales and the interaction between turbulent waves and charged particles is mediated by particular resonance conditions. Further, in such studies, it is also implicitly assumed that the particles gyro-radius is smaller than the maximum scale of the turbulence spectrum.

However, in certain astrophysical scenarios, the particle's gyro-radius can exceed the maximum coherence length of the turbulence. One example is the transport of supra-thermal particles near a relativistic shock, where sub-gyroscale turbulence is essential in scattering cosmic rays (CRs) and enabling them to complete enough Fermi cycles for efficient acceleration (Lemoine et al., 2006). Additionally, such situations can also arise when the gyro-radius of highly energetic charged particles become comparable to albeit less than the Hillas limit of the system exceeding any length scale where fluctuations can occur in the system (Reichherzer et al., 2022a). Despite the wide application of this regime in several astrophysical systems, it has gained little attention to date. Although some recent research has been devoted to studying this under-explored field, it has primarily focused on the problem of spatial transport (Casse et al., 2001). For example, Plotnikov et al. (2011) developed an analytical formulation of the spatial transport coefficients compatible with the numerical results for an intense small-scale random magnetic field. Furthermore, the work by Subedi et al. (2017) is worth noting, which studies the spatial diffusion of the charged particle in three-dimensional isotropic turbulent magnetic fields without a mean field. Dundovic et al. (2020) studied the transport of energetic particles in a synthetic magnetostatic turbulence, which in a way extended the work by (Subedi et al., 2017).

In this work, we examine the momentum diffusive transport of charged particles in high-energy (or rigidity) regime with $R_l/l_c >> 1$, where $R_l$ is the gyro-radius of the particle and $l_c$ is the highest correlation length of the turbulence. A possible scenario that illustrates this concept involves a particle undergoing acceleration through turbulent processes in a large-scale turbulent environment. As the particle continues to accelerate, it will eventually reach a point where its gyro-radius exceeds the correlation length of the turbulence that is accelerating it. This work seeks to address the question of whether the particle's motion will continue to be influenced by the turbulence, despite having surpassed its correlation length. To investigate this question, we focus on a turbulence spectrum that exhibits power at scales smaller than the gyro-radius of the particle, but not at the scale of the gyro-radius itself.

Using an asymptotic analysis of the quasilinear diffusion coefficient, we estimate the transport coefficients corresponding to this regime. We also demonstrate the impact of the interplay between stochastic Fermi acceleration due to small-scale turbulence and synchrotron loss on the spectrum of non-thermal particles.

The chapter is organised in the following way: in section 5.2 we show the calculations for the momentum transport coefficient for small-scale turbulence and the results are shown in sections 5.3.1, 5.3.2 and 5.3.3. In section 5.3.4, we show the results from solving the cosmic ray Fokker-Planck equation using the calculated transport coefficient. Subsequently, in section 5.4, we discuss possible astrophysical situations where the phenomena of small-scale turbulence can become potentially impactful on the energy distribution of the non-thermal particles. We discuss and summarize our findings in section 5.5, and in the appendix, we lay out all the required derivations.

## 5.2 Calculation of the transport coefficients due to small-scale turbulence

In this section, we provide the derivation of the momentum transport coefficients $D_{pp}$, $D_{\mu\mu}$ and $D_{\mu p}$ due to sub-gyroscale perturbations in the presence of a mean magnetic field, where $p$ and $\mu$ are the momentum and pitch-angle of the non-thermal particles, respectively. We begin with the following form of the diffusive transport coefficients in momentum space (Schlickeiser & Achatz, 1993):

$$\begin{bmatrix} D_{\mu\mu} \\ D_{\mu p} \\ D_{pp} \end{bmatrix} = \frac{\Omega^2(1-\mu^2)}{2B_0^2} \begin{bmatrix} 1 \\ mc \\ m^2c^2 \end{bmatrix} \mathcal{R}e \sum_{n=-\infty}^{n=\infty} \int_{k_{\min}}^{k_{\max}} d^3\boldsymbol{k} \int_0^\infty dt e^{-\iota(k_\parallel v_\parallel - \omega + n\Omega)t}$$
$$\left\{ J_{n+1}^2\left(\frac{k_\perp v_\perp}{\Omega}\right) \begin{bmatrix} P_{\mathcal{RR}}(\boldsymbol{k}) \\ T_{\mathcal{RR}}(\boldsymbol{k}) \\ R_{\mathcal{RR}}(\boldsymbol{k}) \end{bmatrix} + J_{n-1}^2\left(\frac{k_\perp v_\perp}{\Omega}\right) \begin{bmatrix} P_{\mathcal{LL}}(\boldsymbol{k}) \\ -T_{\mathcal{LL}}(\boldsymbol{k}) \\ R_{\mathcal{LL}}(\boldsymbol{k}) \end{bmatrix} \right.$$
$$\left. + J_{n+1}\left(\frac{k_\perp v_\perp}{\Omega}\right) J_{n-1}\left(\frac{k_\perp v_\perp}{\Omega}\right) \left[ e^{\iota 2\phi} \begin{bmatrix} -P_{\mathcal{RL}}(\boldsymbol{k}) \\ T_{\mathcal{RL}}(\boldsymbol{k}) \\ R_{\mathcal{RL}}(\boldsymbol{k}) \end{bmatrix} + e^{-\iota 2\phi} \begin{bmatrix} -P_{\mathcal{LR}}(\boldsymbol{k}) \\ -T_{\mathcal{LR}}(\boldsymbol{k}) \\ R_{\mathcal{LR}}(\boldsymbol{k}) \end{bmatrix} \right] \right\} \tag{5.1}$$

where $\Omega = \Omega_{NR}/\gamma$ and $m = \gamma m_e$ are the gyro-frequency and mass of the relativistic non-thermal particle (electron for our case), respectively; $\Omega_{NR}$ denotes the non-relativistic gyro-frequency and $\gamma$ is the Lorentz factor; wave number $k_{\min}$ corresponds to the inverse of some maximal length scale L as $k_{\min} = 2\pi L^{-1}$, and $k_{\max}$ corresponds to the dissipation scale; $v_\perp$ and $k_\perp$ are the particle's velocity and the wave vector components perpendicular to the mean magnetic field $\boldsymbol{B}_0 = B_0\hat{z}$; $\phi$ represents the phase angle between the Cartesian components of the wave vector in a plane perpendicular to the mean magnetic field, i.e., $\phi = \tan^{-1}(k_y/k_x)$; $\mathcal{L}$ and $\mathcal{R}$ represent left and right hand polarizations, given by $\mathcal{L}, \mathcal{R} = (x \pm \iota y)/\sqrt{2}$, with $x$ and $y$ being the Cartesian coordinates, and $\iota = \sqrt{-1}$ is the imaginary number; $J_n(:)$ is the Bessel function of first kind with integer order $n$. Note that the diffusive transport coefficients in Eq. (5.1) corresponds to the lowest order in $V_A/c$ with $V_A$ being the Alfvén velocity. The above transport coefficients are only valid for Alfvén modes, whereas for other compressible modes, additional terms are needed to be considered in the equation for $D_{\mu p}$. Here we focus only on Alfvén waves because of their damping free nature in fully ionised medium (Ginzburg, 1970; Kulsrud & Pearce, 1969; Yan & Lazarian, 2002). Further, the terms $P_{ij}$, $T_{ij}$, $Q_{ij}$ and $R_{ij}$ are defined using two point correlations at scales $\boldsymbol{k}$ and $\boldsymbol{k'}$ as follows,

$$\left\langle B_i(\boldsymbol{k})B_j^*(\boldsymbol{k'})\right\rangle = \delta(\boldsymbol{k}-\boldsymbol{k'})P_{ij}(\boldsymbol{k}), \qquad \left\langle B_i(\boldsymbol{k})E_j^*(\boldsymbol{k'})\right\rangle = \delta(\boldsymbol{k}-\boldsymbol{k'})T_{ij}(\boldsymbol{k}),$$
$$\left\langle E_i(\boldsymbol{k})B_j^*(\boldsymbol{k'})\right\rangle = \delta(\boldsymbol{k}-\boldsymbol{k'})Q_{ij}(\boldsymbol{k}), \qquad \left\langle E_i(\boldsymbol{k})E_j^*(\boldsymbol{k'})\right\rangle = \delta(\boldsymbol{k}-\boldsymbol{k'})R_{ij}(\boldsymbol{k}). \tag{5.2}$$

where $B_i$ and $E_i$ are the magnetic and electric field fluctuations. We also define terms $C_{ij}$ and $Y_{ij}$ that relate the magnetic field and velocity correlations as follows:

$$\left\langle u_i(\boldsymbol{k})B_j^*(\boldsymbol{k'})\right\rangle /V_A B_0 = \delta(\boldsymbol{k}-\boldsymbol{k'})C_{ij}(\boldsymbol{k}),$$
$$\left\langle u_i(\boldsymbol{k})u_j^*(\boldsymbol{k'})\right\rangle /V_A^2 = \delta(\boldsymbol{k}-\boldsymbol{k'})Y_{ij}(\boldsymbol{k}), \tag{5.3}$$

Further considering MHD turbulence, the Ohm's Law implies $\mathbf{E}(\boldsymbol{k}) = -\frac{\mathbf{u}(\boldsymbol{k})}{c} \times \mathbf{B}_0$ with $\mathbf{u}(\boldsymbol{k})$ being the Fourier component of the velocity fluctuation of the underlying MHD flow. Adopting this expression of electric field in Eq (5.2) and using the definitions provided in Eq. (5.3) we obtain,

$$T_{ij}(\boldsymbol{k}) = -\frac{B_0^2 V_A}{c}\epsilon_{jpz}C_{ip}\left(\boldsymbol{k}\right),$$
$$Q_{ij}(\boldsymbol{k}) = -\frac{B_0^2 V_A}{c}\epsilon_{imz}C_{mj}\left(\boldsymbol{k}\right),$$
$$R_{ij}(\boldsymbol{k}) = \frac{B_0^2 V_A^2}{c^2}\left[\delta_{ij}Y_{pp}\left(\boldsymbol{k}\right) - Y_{ji}\left(\boldsymbol{k}\right)\right] \tag{5.4}$$

where, $z$ is the Cartesian coordinate along the mean magnetic field (see appendix A.3 for detailed derivation). To explore the effect of sub-gyroscale fluctuations threaded by a coherent magnetic field on the momentum transport of the charged particles, we consider both the isotropic and anisotropic turbulence spectra. In the isotropic scenario we consider Alfvèn and fast wave turbulence, whereas for the anisotropic case we only consider Alfvèn wave turbulence. Such considerations are motivated by the fact that in wave-turbulence framework fast wave turbulence is known to follow an isotropic spectrum and the Alfvèn wave turbulence follows a highly anisotropic spectrum (Cho & Lazarian, 2002; Yan & Lazarian, 2002). However in literature isotropic Alfvènic turbulence is also considered (see for example, Brose et al., 2016). Moreover from solar wind data, the turbulence is found to become isotropic at and below electron gyro-scale range and the wave-wave interaction is found out to have resemblance with kinetic Alfvén waves (Kiyani et al., 2012). In the following sections first we calculate the momentum diffusion coefficients following an isotropic single scale injection spectrum and subsequently we carry out the calculation with a more realistic anisotropic turbulence.

### 5.2.1 Isotropic turbulence

In this section we focus on an isotropic single scale turbulence injection spectrum to compute the momentum transport coefficient for high-energy charged particles. In particular we consider the following spectrum,

$$Y_{ij}\left(\boldsymbol{k}\right) = \left(\delta_{ij} - \frac{k_i k_j}{k^2}\right) P_{iso} \delta \left(\frac{k}{m' k_g} - 1\right) k^{-2} \tag{5.5}$$

where, $k_g$ is the inverse of the non-relativistic gyro-radius of a charged particle, $k_g = \Omega_{NR}/v$, and $m'$ is a parameter which dictates the scale of the turbulent energy injection. The choice of such a monochromatic injection spectrum is driven by the expectation that the energy present in the outer scale of the turbulence would maximally impact the high rigidity particles. Additionally, it has already been observed that the behavior of these particles is only marginally influenced by the specific form of the turbulence spectrum (Subedi et al., 2017). An estimation of $P_{iso}$ in the definition of turbulent spectrum can be computed following the equipartion between the total magnetic energy and kinetic energy (Yan & Lazarian, 2002),

$$\int d^3\boldsymbol{k} Y_{ii} \frac{\rho V_A^2}{2} \sim \frac{B_0^2}{8\pi} \tag{5.6}$$

with $\rho$ being the density and $V_A = B_0^2/(4\pi\rho)$ is the Alfvén velocity. Comparing the value of the integration on the left side to the right side results in $P_{iso} \sim (8\pi m' k_g)^{-1}$. On substituting the correlation coefficients for MHD turbulence (Eqs. 5.2 and 5.4) in Eq. (5.1), we obtain the expression of $D_{pp}$ as follows (see appendix A.4)

$$D_{pp} = \frac{\Omega^2\left(1-\mu^2\right)}{2} m^2 c^2 \frac{V_A^2}{c^2} P_0 \mathcal{R}e\left[\sum_{n=-\infty}^{\infty}\int_{k_{min}}^{k_{max}} \delta\left(\frac{k}{m' k_g}-1\right) k^{-2} d^3\boldsymbol{k}\right.$$
$$\int_0^{\infty} dt\; e^{-\iota\left(k_{||}v_{||}-\omega+n\Omega\right)t}\left\{\left(J_{n+1}^2\left(\frac{k_\perp v_\perp}{\Omega}\right)+J_{n-1}^2\left(\frac{k_\perp v_\perp}{\Omega}\right)\right)\left(1+\frac{k_\perp^2}{2k^2}\right)\right.$$
$$\left.\left.+J_{n+1}\left(\frac{k_\perp v_\perp}{\Omega}\right)J_{n-1}\left(\frac{k_\perp v_\perp}{\Omega}\right)\frac{k_\perp^2}{k^2}\right\}\right] \tag{5.7}$$

On performing the integration, $D_{pp}$ simplifies to (see appendix A.5),

$$D_{pp} \simeq \Omega\left(1-\mu^2\right) m^2 c^2 \frac{V_A^2}{c^2}\pi^2 m' k_g P_0 \mathcal{R}e\left[\int_{-1}^{1} dx\left\{\left(J^2_{\frac{\omega}{\Omega}-\frac{m' k_g x v\mu}{\Omega}+1}\right.\right.\right.$$
$$\left(\frac{m' k_g v}{\Omega}\sqrt{1-x^2}\sqrt{1-\mu^2}\right)+J^2_{\frac{\omega}{\Omega}-\frac{m' k_g x v\mu}{\Omega}-1}\left.\left(\frac{m' k_g v}{\Omega}\sqrt{1-x^2}\sqrt{1-\mu^2}\right)\right)\left(\frac{3-x^2}{2}\right)$$
$$+\left(1-x^2\right)J_{\frac{\omega}{\Omega}-\frac{m' k_g x v\mu}{\Omega}+1}\left(\frac{m' k_g v}{\Omega}\sqrt{1-x^2}\sqrt{1-\mu^2}\right)$$
$$\left.\left.J_{\frac{\omega}{\Omega}-\frac{m' k_g x v\mu}{\Omega}-1}\left(\frac{m' k_g v}{\Omega}\sqrt{1-x^2}\sqrt{1-\mu^2}\right)\right\}\right]. \tag{5.8}$$

The above expression for $D_{pp}$ consists of several integrations involving the Bessel function within the limits of $\pm1$, and analytical solutions of such integrations are very challenging. We, therefore, consider integrating the above expression numerically to obtain the functional form of $D_{pp}$. For that we further simplify Eq.(5.8) by noting that the The bessel function $J_x(y)$ contributes most significantly when $x \approx y$, i.e., when the order of the Bessel function is approximately equal to its argument. This gives,

$$\frac{\omega}{\Omega}-\frac{m' k_g x v\mu}{\Omega}\pm 1 \simeq \frac{m' k_g v}{\Omega}\sqrt{1-x^2}\sqrt{1-\mu^2} \gg 1 \tag{5.9}$$

which implies an analogous resonance condition of the following form:

$$\omega - m'\boldsymbol{k}_g\cdot\boldsymbol{v} \simeq \mp\Omega. \tag{5.10}$$

Furthermore, note that the presence of $\simeq$ in the above equation indicates that this condition has to be weakly satisfied. Therefore, we introduce a parameter to modulate the value of $(\omega - m'\boldsymbol{k}_g\cdot\boldsymbol{v}\pm\Omega)$ to broaden the resonance condition of Eq. (5.10). Furthermore, it is important to highlight that the resonance condition mentioned in

Eq. (5.10) is different from the quasilinear resonance expressed as,

$$k_{||}v_{||} - \omega \mp n\Omega = 0.$$

Such a quasilinear resonance dictates the interaction between plasma waves and CR particles. The origin of Eq. (5.10) lies in the mathematical nature of the Bessel functions. In this context, we consider a broadening parameter that modulates the difference between the left and right-hand sides of Eq. (5.10). Hereafter, when referring to resonance broadening, we specifically refer to this type of broadening. Additionally, it should be noted that the literature extensively discusses the broadening of the quasilinear resonance (see Schlickeiser, 2002b; Yan & Lazarian, 2008, for example), but this work does not consider it. The presence of this resonance condition constrains the limit of the $x$ integral in Eq. (5.8). To identify the limits for Alfvén waves, we undertake the following exercise: The resonance condition due to the shear Alfvén wave, ($\omega = k_{||}V_A = kxV_A$), becomes,

$$\frac{\gamma m' k_g V_A x}{\Omega_{NR}} - \frac{m' k_g c\sqrt{1-\frac{1}{\gamma^2}}\mu x}{\Omega_{NR}}\gamma - \frac{m' k_g c\sqrt{1-\frac{1}{\gamma^2}}}{\Omega_{NR}}\gamma\sqrt{1-x^2}\sqrt{1-\mu^2} \simeq \mp 1$$
$$\implies Ax - Bx - G\sqrt{1-x^2} = Q, \tag{5.11}$$

where the form of $A$, $B$ and $G$ are as follows,

$$A = \frac{\gamma m' \Omega_{NR} V_A}{\Omega_{NR} v} = \frac{\gamma \beta_A m'}{\sqrt{1-\frac{1}{\gamma^2}}}; \quad B = \frac{m' \Omega_{NR} c \gamma \mu}{\Omega_{NR} v}\sqrt{1-\frac{1}{\gamma^2}} = \gamma \mu m';$$

$$G = \frac{m' \Omega_{NR} c \gamma}{\Omega_{NR} v}\sqrt{1-\frac{1}{\gamma^2}}\sqrt{1-\mu^2} = m'\gamma\sqrt{1-\mu^2},$$

with $\beta_A$ being the Alfvén velocity normalized to $c$, $\beta_A = V_A/c$. Note that we have used the definition of $k_g$, while defining $A$, $B$ and $G$. Further with the presence of $Q$, the resonance broadening effect can also be considered. Our interest is to find the range of $x$ such that the following equation is satisfied,

$$Q_{min} \le \frac{\gamma m' k_g V_A x}{\Omega_{NR}} - \frac{m' k_g c\sqrt{1-\frac{1}{\gamma^2}}\mu x}{\Omega_{NR}}\gamma - \frac{m' k_g c\sqrt{1-\frac{1}{\gamma^2}}}{\Omega_{NR}}\gamma\sqrt{1-x^2}\sqrt{1-\mu^2} \le Q_{max} \tag{5.12}$$

Following the range of $x$ through solving Eq. (5.12), we write the form for $D_{pp}$ in the following way,

$$\frac{D_{pp}}{m_e^2c^2} = D_{\gamma\gamma} \simeq \Omega_{NR}\left(1-\mu^2\right)\gamma\beta_A^2\pi^2 m' k_g P_0 \mathcal{R}e \left[\int_{\mathcal{F}^+} dy \left(\frac{3-y^2}{2}\right) J^2_{(A-B)y+1}\left(G\sqrt{1-y^2}\right) + \int_{\mathcal{F}^-} dy \left(\frac{3-y^2}{2}\right) J^2_{(A-B)y-1}\left(G\sqrt{1-y^2}\right) + \int_{\mathcal{F}^+\cap\mathcal{F}^-} dy \left(1-y^2\right) J_{(A-B)y+1}\left(G\sqrt{1-y^2}\right) J_{(A-B)y-1}\left(G\sqrt{1-y^2}\right)\right]. \tag{5.13}$$

where $\mathcal{F}^+$ corresponds to the range of $x$ when Eq. (5.12) is solved considering $Q_{max} = 1+\sigma$ and $Q_{min} = 1-\sigma$ with $\sigma$ being the broadening parameter. Similarly $\mathcal{F}^-$ considers the range of $x$ for the solution of Eq. (5.12) with $Q_{max} = -1+\sigma$ and $Q_{min} = -1-\sigma$. We solve Eq. (5.13) for different values of $m'$, $\beta_A$ and $\sigma$ and the result of the numerical integration is discussed in section 5.3.1.

Now we proceed to compute the form of $D_{\mu\mu}$ considering the correlation tensor $P_{ij} = B_0^2 Y_{ij}$. Such an assumption for the correlation function is typically used for Alfvén waves (see for example Yan & Lazarian, 2002). With this correlation function and an exactly similar kind of calculation as shown in appendix A.4 & A.5 leads to the following form for $D_{\mu\mu}$,

$$D_{\mu\mu} \simeq \frac{\Omega_{NR}}{\gamma}\left(1-\mu^2\right)\pi^2 m' k_g P_0 \mathcal{R}e \left[\int_{\mathcal{F}^+} dy \left(\frac{1+y^2}{2}\right) J^2_{(A-B)y+1}\left(G\sqrt{1-y^2}\right) + \int_{\mathcal{F}^-} dy \left(\frac{1+y^2}{2}\right) J^2_{(A-B)y-1}\left(G\sqrt{1-y^2}\right) + \int_{\mathcal{F}^+\cap\mathcal{F}^-} dy \left(1-y^2\right) J_{(A-B)y+1}\left(G\sqrt{1-y^2}\right) J_{(A-B)y-1}\left(G\sqrt{1-y^2}\right)\right] \tag{5.14}$$

Here also, due to the presence of the Bessel function, we consider numerical integration. Interestingly, owing to the isotropic nature of the turbulence, all the components of the correlation function for $D_{\mu p}$ come out to be imaginary (see appendix A.4). Therefore, $D_{\mu\gamma} = D_{\mu p}/(m_e c)$ does not make any contribution toward the transport of these non-thermal particles.

### 5.2.2 Anisotropic turbulence

In this section we calculate the momentum transport coefficient considering a realistic power law like turbulence spectrum for Alfvèn waves. We further consider the maximum turbulence correlation length to be smaller than the gyro-radius of the charged particle by considering unit step function. In particular we choose the following form for the anisotropic turbulence spectrum,

$$Y_{ij}(k) = P_{aniso}\left(\delta_{ij} - \frac{k_i k_j}{k_\perp^2}\right)\Theta\left(k_\perp - m' k_g\right)\delta\left(\frac{k_{||}}{m'' k_g} - 1\right) k_\perp^{-\alpha}, \tag{5.15}$$

where $\Theta$ corresponds to Heaviside Theta function and $P_{aniso}$ being the injected turbulent power; $m'k_g$ and $m''k_g$ are the respective scales of $k_\perp$ and $k_{||}$ where the turbulence energy is being injected, with $k_g = \Omega_{NR}/v$; $k_i$ and $k_j$ corresponds to the components of wave vector $k$, in the perpendicular direction of the magnetic field. The motivation behind choosing such a spectral form for the anisotropic turbulence spectrum stems from the observation that, at the largest length scale, MHD turbulence tends to exhibit a weak turbulent behaviour. In this regime, the energy cascade primarily occurs in the direction perpendicular to the mean magnetic field ($k_\perp$), while the parallel wavenumber ($k_{||}$) remains unchanged. In particular, the interaction between waves in weak turbulence leads to alterations in the perpendicular wavenumber while leaving the parallel wavenumber unaffected. Therefore, considering that the maximum impact on high rigidity cosmic rays is influenced by the turbulence properties at the largest scale, we consider an anisotropic spectrum of the turbulence as Eq. (5.15).

With such a spectrum the equipartition of energy implies the form of $P_{aniso}$ as the following,

$$P_{aniso} \simeq \frac{\alpha - 2}{2\pi m'' k_g (m' k_g)^{2-\alpha}}. \tag{5.16}$$

The positivity constraint of the power implies $\alpha > 2$. With such turbulence spectrum the momentum diffusion coefficients $D_{\gamma\gamma}$ becomes,

$$D_{\gamma\gamma} = \frac{D_{pp}}{m_e^2 c^2} = \frac{\gamma \Omega_{NR}\left(1-\mu^2\right)}{4} 2\pi^2 \beta_A^2 m'' k_g P_{aniso} \mathcal{R}e \left[ \int_{m' k_g}^{\infty} k_\perp^{-\alpha+1} dk_\perp \left\{ J^2_{\frac{\omega}{\Omega} - \frac{m'' k_g v_{||}}{\Omega} + 1} \left(\frac{k_\perp v_\perp}{\Omega}\right) + J^2_{\frac{\omega}{\Omega} - \frac{m'' k_g v_{||}}{\Omega} - 1} \left(\frac{k_\perp v_\perp}{\Omega}\right) + 2 J_{\frac{\omega}{\Omega} - \frac{m'' k_g v_{||}}{\Omega} + 1} \left(\frac{k_\perp v_\perp}{\Omega}\right) J_{\frac{\omega}{\Omega} - \frac{m'' k_g v_{||}}{\Omega} - 1} \left(\frac{k_\perp v_\perp}{\Omega}\right) \right\} \right] \tag{5.17}$$

Although we have considered the upper limit of the integral to be $\infty$, note that the value of $k_\perp$ cannot take an arbitrarily large value owing to the following constraint,

$$m'' k_g V_A - m'' k_g v \mu \pm \Omega \approx k_\perp v \sqrt{1-\mu^2} \tag{5.18}$$

Following a similar kind of analysis described in the previous section, we introduce a parameter $Q$ and after some algebraic manipulations we write the above equation in the following way,

$$\frac{m'' \beta_A}{\sqrt{1-\frac{1}{\gamma^2}}} - m'' \mu + \frac{Q_{max}}{\gamma} \geq m' \sqrt{1-\mu^2} \tag{5.19}$$

Note that while writing the above equation we consider $k_g = \Omega_{NR} / \left(c\sqrt{1-1/\gamma^2}\right)$ and $k_\perp \geq m' k_g$. From Eq. (5.19) we compute the range of $\mu$ such that the inequality is satisfied. Subsequently for each value of $\mu$ in that range we compute the value of upper limit of the $k_\perp$ integral through the following equation,

$$k_\perp(Q) = \frac{\Omega_{NR}}{v\sqrt{1-\mu^2}\gamma} \left( \frac{\gamma m'' \beta_A}{\sqrt{1-\frac{1}{\gamma^2}}} - \gamma m'' \mu + Q \right). \tag{5.20}$$

$k_\perp(Q_{max})$ being the upper limit of the $k_\perp$ integral and the maximum between $k_\perp(Q_{min})$ and $m' k_g$ is considered as the lower limit of the integral. Following the limit of the integration we compute the integral in Eq. (5.17) numerically.

## 5.3 Transport coefficients $D_{\gamma\gamma}$ and $D_{\mu\mu}$

First, we present our results on the transport coefficients by numerically evaluating the integrals that appear in the expressions for $D_{\gamma\gamma}$ and $D_{\mu\mu}$ as presented above in section 5.2. Subsequently, we solve the cosmic ray transport equation with the

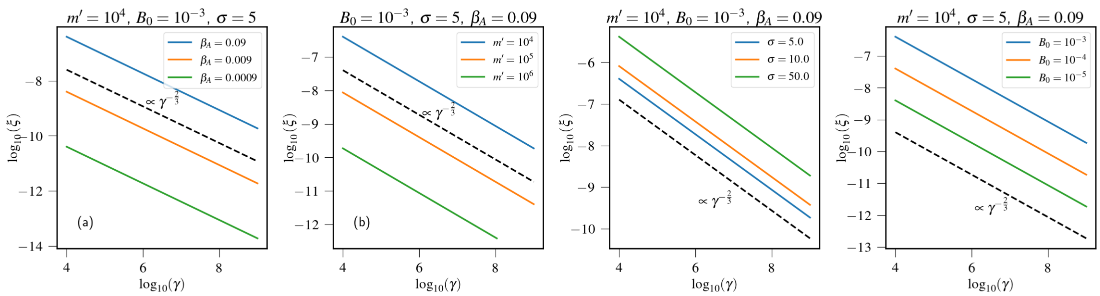


Figure 5.1: Plot (isotropic case) showing the dependence of pitch-angle-averaged momentum diffusion coefficient on $\gamma$ for different values of Alfvèn velocity ($\beta_A$), turbulent injection scale ($m'$), broadening ($\sigma$) and magnetic field ($B_0$). All the plots show the same trend of $\xi \propto \gamma^{-2/3}$.

calculated diffusion coefficients in addition to the synchrotron loss process and study their interplay.

### 5.3.1 Momentum diffusion Coefficient ($D_{\gamma\gamma}$)

We are interested here in the average diffusion which is obtained by integrating $D_{\gamma\gamma}$ over the distribution of the pitch angle $\mu \in [-1, 1]$ as the following,

$$\xi = \int_{-1}^{1} D_{\gamma\gamma}\, d\mu \tag{5.21}$$

In Fig. 5.1 we show the dependence of pitch-angle-averaged momentum diffusion coefficient ($\xi$) on $\gamma$ for different values of the parameters $\beta_A$, $m'$, $\sigma$ and $B_0$, which are all defined above in section 5.2. For all the plots shown in the figure, $\xi$ exhibits a power-law trend following the same exponent with the Lorentz factor $\gamma$ of the non-thermal particles, $\xi \propto \gamma^{-2/3}$. In panel (a), one can observe the increase in $\xi$ with increasing $\beta_A$ for a constant value of $m' = 10^4, B_0 = 10^{-3}\,\mathrm{G}$ and $\sigma = 5$. This indicates that the higher the velocity of the Alfvén wave is, the quicker the non-thermal particles will diffuse in $\gamma$ space. In panel (b) we show the dependence of $\xi$ on $\gamma$ for different values of $m'$. We observe that with increasing $m'$, $\xi$ decreases for a fixed $\gamma$ value. Such behaviour of $\xi$ is expected as $m'$ parameterizes the scale of the turbulent energy injection, and higher values of $m'$ indicate that the energy is getting

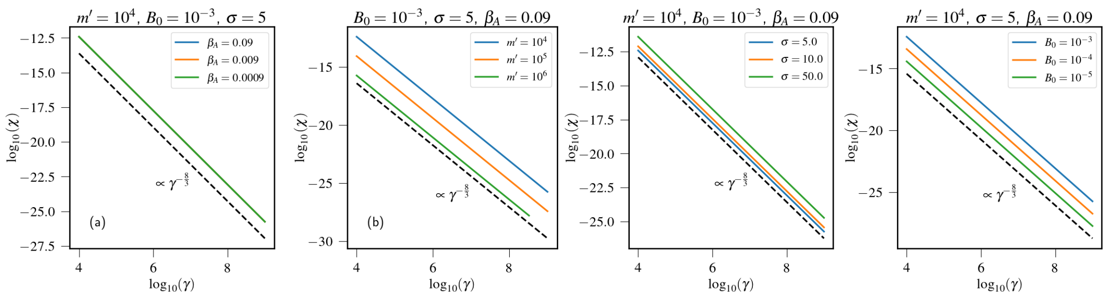


Figure 5.2: Plot (isotropic case) showing the dependence of pitch-angle-averaged pitch angle diffusion coefficient on $\gamma$ for different values of Alfvèn velocity ($\beta_A$), Turbulence injection scale ($m'$), broadening ($\sigma$) and magnetic field ($B_0$). All the plots show the same trend of $\chi \propto \gamma^{-8/3}$.

injected at a lower scale. The behaviour shown in panel (b) of the figure implies that such an energy injection at smaller scales reduces the momentum diffusion, resulting in the reduced acceleration of particles with large gyro-radii.

In panel (c) the right panel of the figure we show the functional dependence of $\xi$ on $\gamma$ for fixed $\beta_A$, $B_0$ and $m'$ but varying $\sigma$. We observe with increasing $\sigma$ values the value of $\xi$ increases for a fixed $\gamma$ which is expected as with increasing $\sigma$, more and more Alfvén waves would interact with the particles resulting in higher momentum diffusion $\xi$. Finally, in panel (d) we show the variation of the $\xi$ with the Lorentz factor $\gamma$ for different values of the magnetic field $B_0$. From the trend it can be observed that with increasing $B_0$ value the diffusion coefficient increases which implies that with higher magnetic field the diffusion enhances.

### 5.3.2 Pitch-angle diffusion coefficient $(D_{\mu\mu})$

Similar to Eq. (5.21), we define another dimensionless pitch-angle averaged diffusion coefficient $\chi$ as:

$$\chi = \int_{-1}^{1} D_{\mu\mu}\, d\mu \,, \tag{5.22}$$

with $D_{\mu\mu}$ being calculated by numerically integrating Eq. (5.14) for the region of $x$ satisfying Eq. (5.12). In Fig. 5.2, we plot $\chi$ for different values of $m'$, $\beta_A$, $B_0$ and $\sigma$

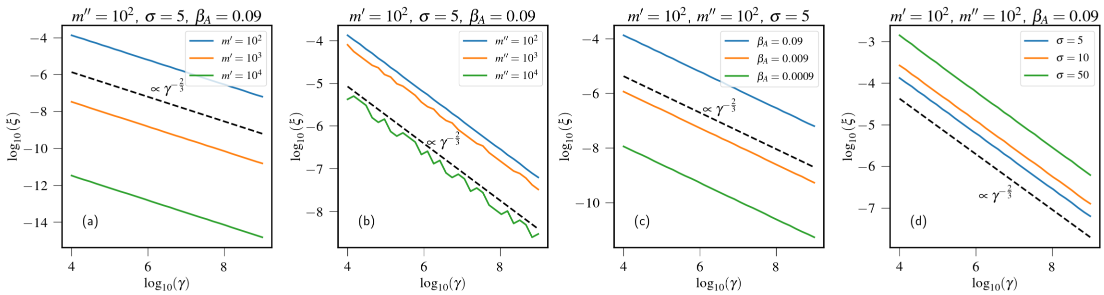


Figure 5.3: Figure showcasing the dependence of the pitch-angle-averaged momentum diffusion coefficient ($\xi$) on particle Lorentz factor $\gamma$ for different parameter values when the underlying turbulence is anisotropic. Similar to the isotropic case, the diffusion coefficient can be observed to behave as a power-law with the particle Lorentz factor and with a similar index of $-2/3$. A black dashed curve of similar power-law trend is shown in all of the panel of the figure for the reference.

All the plots exhibit an inverse power-law trend with Lorentz factor $\gamma$ of the cosmic rays. For all the cases in the figure, we find the same power-law index of $-8/3$. In panel (a) of the figure, the plots are shown for constant $m'$, $B_0$ and $\sigma$ but varying $\beta_A$. The curves can be observed to almost overlap for different $\beta_A$, indicating that $\chi$ has a very weak dependency on the velocity of the Alfvén waves. In panel (b), the form of $\chi$ has been shown for different $m'$ values while $B_0$, $\beta_A$ and $\sigma$ are kept constant. Similar to $\xi$, here also we observe decrease in $\chi$ with increasing $m'$. In panel (c) of the figure we show the plots for different values of $\sigma$. We find that $\chi$ increases with $\sigma$, which is expected as larger $\sigma$ consequently implies that more number of waves are interacting with the charged particles. This results in more efficient diffusion. In the rightmost panel, we plot the variation of $\chi$ with the Lorentz factor $\gamma$ for different magnetic field values, $B_0$. Similar to $\xi$, we can observe the increase in the diffusion coefficient with increasing magnetic field.

### 5.3.3 Momentum diffusion coefficient due to anisotropic small-scale turbulence

Fig. 5.3 presents the pitch-angle averaged momentum diffusion coefficient $\int_{-1}^{1} D_{\gamma\gamma}\, d\mu$

as a function of the particle Lorentz factor $\gamma$, for different parameter values. In all the simulations, the magnetic field value is fixed at $10^{-3}$ G and we consider $\alpha = 3$. The diffusion coefficient follows a power law behavior with an index of $-2/3$, which is consistent with the isotropic case. Panel (a) shows the variation of the diffusion coefficient with different values of $m'$, which correspond to different scales of energy injection along the direction of $k_\perp$. It can be observed that for larger values of $m'$, the diffusion coefficient decreases. This trend is expected as a larger value of $m'$ corresponds to a smaller energy injection scale, resulting in a weaker effect of turbulence on the charged particles. In panel (b), we modulate the value of $m''$ and observe its effect on the diffusion coefficient. Similar to panel (a), the diffusion coefficient exhibits a decreasing trend with an increasing $m''$ value. Additionally, as we increase the value of $m''$, we notice that the diffusion coefficient becomes highly responsive, resulting in a fluctuating pattern. Nevertheless, the general tendency is apparent, and it conforms to a power-law distribution with an exponent of $-2/3$. This behavior indicates that the injection of turbulence power at the coherent magnetic field's length scale has a more significant qualitative impact than the length scale perpendicular to $B_0$. Next, in panel (c), we modulate the Alfvèn velocity of the small-scale Alfvèn waves and show the trend of the diffusion coefficient. It is observed that with decreasing Alfvèn speed of the underlying fluctuations, the momentum diffusion decreases. Finally, in panel (d), we investigate the effect of the parameter $\sigma$ on the momentum diffusion coefficient. As expected, with an increasing $\sigma$ value, the momentum diffusion coefficient increases. This trend is due to the fact that particles interact with more waves as the value of $\sigma$ increases.

In summary, we have observed that the pitch-angle averaged momentum diffusion coefficient exhibits a power-law like behaviour with an index of $-2/3$ for both isotropic and anisotropic turbulence spectrum. This is consistent with theoretical expectations, as cosmic ray particles with high rigidity are expected to be weakly dependent on the specific form of the turbulence spectrum.

Note that, during all the above calculations of the diffusion coefficients, it was ensured that the values of both the order and argument of the Bessel functions remained sufficiently large to satisfy Eq. (5.9). In the majority of cases, the values of the argument and order were observed to be greater than 100, while in one case, it remained greater than 70. Moreover, our analysis indicates that the parameters $m'$ and $m''$ have a significant impact on modulating the values of the argument and order. Increasing their values leads to larger values of the argument and order. This behavior is expected, as $m'$ and $m''$ determine the scale difference between the gyro-radius and turbulence injection scale. A decrease in their values implies a reduction in the rigidity of the non-thermal particle and eventually leading to the case of large-scale turbulence. Hence, for large-scale turbulence, the order of the Bessel function is typically considered in the range of 0, $\pm 1$, $\pm 2$ (Berezinskii et al., 1990).

Furthermore, we anticipate that for anisotropic turbulence, the pitch angle diffusion coefficient will follow a similar trend to that of the isotropic case (see Fig. 5.2). This expectation is based on the comparable behavioral patterns displayed by the momentum diffusion coefficient for both isotropic and anisotropic turbulence. Additionally, in quasilinear theory, the momentum diffusion coefficient is related to the spatial diffusion coefficient along the direction of the coherent magnetic field through the constraint given by (Thornbury & Drury, 2014):

$$\mathcal{K} D_{\gamma\gamma} = \frac{1}{9}\gamma^2 V_A^2, \tag{5.23}$$

where $\mathcal{K}$ represents the spatial diffusion coefficient along the direction of the coherent magnetic field $B_0$. The spatial diffusion coefficient is related to the pitch-angle diffusion coefficient (Shalchi, 2009). Thus, once the behaviour of the momentum diffusion coefficient is known, the behaviour of the pitch angle diffusion coefficient can be constrained by the above equation. Therefore, we abstain from explicitly

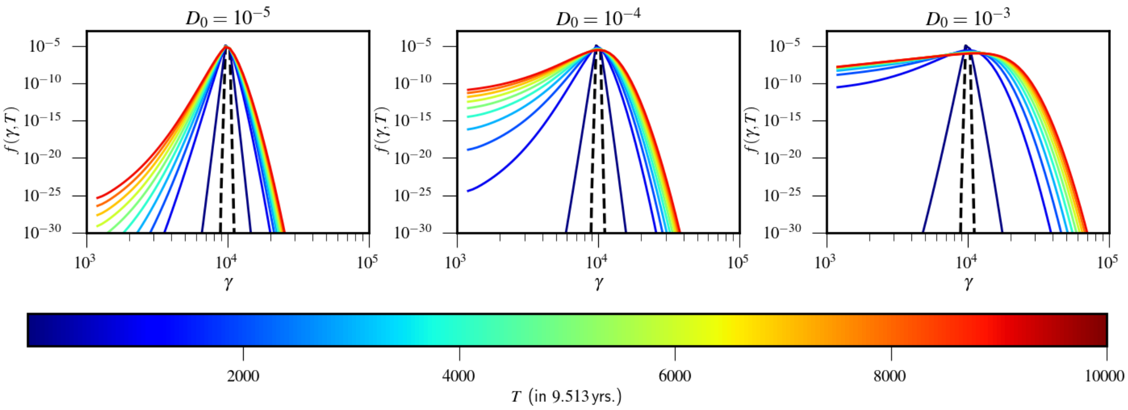


Figure 5.4: Evolution of an initial Gaussian (with mean $10^4$ and standard deviation $10^2$) for stochastic acceleration due to small-scale turbulence with different values of $D_0$ and following Eq. (5.27). The initial function is shown with a black dashed curve.

calculating the behavioural trend of the pitch-angle-averaged pitch angle diffusion coefficient due to the anisotropic turbulence spectrum.

### 5.3.4 Solutions of the Fokker-Planck equation

In this section we demonstrate the effect of the small-scale turbulence on the non-thermal particle spectrum by numerically solving the cosmic ray transport equation with the coefficients calculated in the earlier sections. Note that all the numerical simulations are performed with a conservative, second order accurate IMEX scheme (Kundu et al., 2021) and considering a discretization of the the particle Lorentz factor $\gamma$ from $\gamma_{\min} = 10^3$ to $\gamma_{\max} = 10^7$ with 128 logarithmically spaced bins to provide equal resolution per decade.

In a turbulent medium with a guided field, the transport of cosmic rays is governed by a Fokker-Planck equation of the following type (Kirk et al., 1988; Schlickeiser &

Miller, 1998),

$$\frac{\partial F}{\partial t} = \frac{\partial}{\partial z}\left(\mathcal{K}\frac{\partial F}{\partial z}\right) - \left(U + \frac{1}{4p^2}\left(\frac{\partial}{\partial p}p^2 v a_1\right)\right)\frac{\partial F}{\partial z} + \left(\frac{p}{3}\frac{\partial U}{\partial z} + \frac{v}{4}\frac{\partial a_1}{\partial z}\right)\frac{\partial F}{\partial p} + \frac{1}{p^2}\frac{\partial}{\partial p}\left(p^2 a_2 \frac{\partial F}{\partial p}\right) + S_0 \quad (5.24)$$

where $F$ is the pitch angle averaged cosmic ray distribution function, $U$ is the non-relativistic fluid velocity, $v$ is the velocity of the cosmic ray particle and $p$ is the momentum of the cosmic rays and

$$\mathcal{K} = \frac{v^2}{8}\int_{-1}^{1} d\mu\, \frac{(1-\mu^2)^2}{D_{\mu\mu}},\;\; a_1 = \int_{-1}^{1} d\mu\,(1-\mu^2)\frac{D_{\mu p}}{D_{\mu\mu}},\;\; a_2 = \frac{1}{2}\int_{-1}^{1} d\mu\,\left(D_{pp} - \frac{D_{\mu p}^2}{D_{\mu\mu}}\right). \quad (5.25)$$

Note that while deriving Eq. (5.24) the background flow and the guided magnetic field are considered to be in the same spatial direction, $z$, and the timescale of pitch-angle scattering is assumed to be minimum among all the timescales present in the system. The latter assumption introduces the spatial diffusion term parallel to the guided magnetic field in the right hand side of the equation (Shalchi, 2020). A term consisting diffusion of cosmic rays in the direction perpendicular to the guided field also arises in the Fokker-Planck equation due to the stochasticity in the magnetic field line structure (Shalchi, 2021). For the current work such term due to perpendicular diffusion is neglected as quasilinear theory is unable to address such diffusive transport (Shalchi, 2020). As noted in the end of section 5.2, $D_{\mu p} = 0$ which gives $a_1 = 0$ and $a_2$ is simply the pitch-angle averaged $D_{pp}$. For this work we consider averaging out the spatial coordinates and following the leaky-box approximation (Lerche & Schlickeiser, 1985) we replace the spatial diffusion and convection term by a momentum dependent escape term (Rieger & Duffy, 2019) with an escape timescale defined as $T_{\rm esc} \sim \mathcal{K}^{-1} \propto \gamma^{-8/3}$. Further considering the calculated forms for pitch-angle averaged diffusion coefficients (see section 5.3.2) in addition to synchrotron cooling and neglecting adiabatic loss/gain process, Eq. (5.24) takes the following form (see appendix A.6 for a derivation),

$$\frac{\partial f}{\partial T} + \frac{\partial}{\partial \gamma}\left(2a\gamma^{-\frac{5}{3}} - \gamma^2\right) f = \frac{\partial}{\partial \gamma}\left(a\gamma^{-\frac{2}{3}}\frac{\partial f}{\partial \gamma}\right) - b\gamma^{\frac{8}{3}} f + S, \tag{5.26}$$

where $a$, $b$ and $S$ are defined via Eq. (A.42).

Before considering the interplay of various micro-physical processes, we first analyze the effect of the acceleration due to small-scale turbulence only. For that, we numerically solve the following equation which is similar to Eq. (5.26) but without the synchrotron loss, particle escape, and injection,

$$\frac{\partial f}{\partial T} + \frac{\partial}{\partial \gamma}\left(2D_0\gamma^{-\frac{5}{3}}\right) f = \frac{\partial}{\partial \gamma}\left(D_0\gamma^{-\frac{2}{3}}\frac{\partial f}{\partial \gamma}\right), \tag{5.27}$$

with $D_0$ being a parameter with which the efficiency of acceleration can be tuned , $\int_{-1}^{1} D_{\gamma\gamma}\, d\mu = D_0\gamma^{-2/3}$. The value of $D_0$ can be determined from the dependence of the momentum diffusion coefficients on $\gamma$ as shown in Figs. 5.1, 5.3, and observed to vary between $10^{-2} - 10^{-5}$ for various parameter values typically observed in astrophysical systems.

The numerical solution of Eq. (5.27) for different times and different $D_0$ values are shown in Fig. 5.4. An arbitrary Gaussian with $10^4$ and $10^2$ as mean and standard deviation respectively, has been considered as the initial distribution (shown by a black dashed curve). Owing to the lower efficiency of the turbulent acceleration process due to small-scale fluctuations, we choose a larger final time ($\sim 100\,\mathrm{kyr}$) to demonstrate sufficient acceleration of the initial Gaussian profile. With time all the plots show the spreading of the initial distribution owing to the momentum diffusion and acceleration due to small-scale turbulence. However, the spreading of the initial distribution function is not uniform, the low energy part spreads faster than the high energy. Such an acceleration can be analyzed by observing the dependency of the acceleration timescale, $\tau_{acc}$, on $\gamma$, which is $\tau_{acc} \sim \gamma^2/D \propto \gamma^{8/3}/D_0$ from Eq. (5.27). It clearly shows that the timescale of acceleration is smaller for smaller $\gamma$, which explains the faster acceleration in the low energy part. The acceleration timescale also inversely depends on the choice of $D_0$, which is why we observe faster

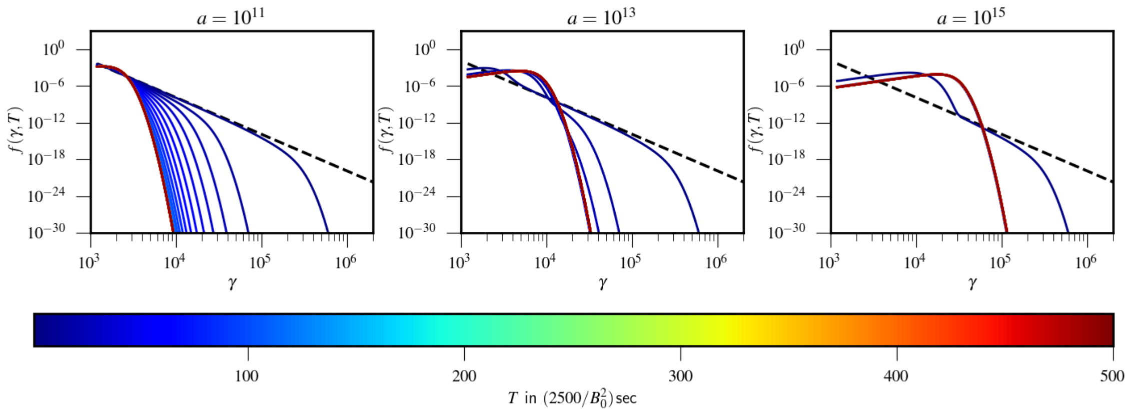


Figure 5.5: Evolution of an initial power-law energy distribution of the form $\gamma^{-6}$ following Eq. (5.26) considering synchrotron loss process and different values for $a$ for electrons. The values for $b$ and $S$ are considered zero. The initial distribution is shown with the black dashed curve. Different color of the distribution function corresponds to different time of evolution, as illustrated by the colorbar. To account for the varying magnetic field values observed in different astrophysical systems and the resulting variation in temporal units, the unit time is specified in terms of a variable magnetic field.

acceleration for higher values of $D_0$.

After analyzing various aspects and features of stochastic acceleration due to small-scale turbulence we now proceed to analyze the interplay of different micro-physical processes with this acceleration. To explore the combined effect of different processes on the distribution function, we numerically solve Eq. (5.26) with the above-mentioned algorithm by incorporating different processes gradually.

In Fig. 5.5 we show the effect of the interplay of synchrotron loss process and particle acceleration due to small-scale turbulence on the particle distribution function. We solve Eq. (5.26) with an initial power-law type particle distribution of the form, $f(\gamma, 0) \propto \gamma^{-6}$. As has been shown in the previous section 5.3.1, the transport coefficients are dependent on the choice of the broadening $\sigma$ and injected power $P_0$, which could be different for different astrophysical systems. As an illustration, therefore, we solve Eq. (5.26) to demonstrate the effects induced by the interplay of various micro-physical processes on the distribution function by varying $a$ and $b$, which are treated as arbitrary parameters in this work. Nonetheless, we make some estimates for the parameter $a$ considering some generic values for the magnetic field and Alfvèn velocity in different astrophysical situations. Noting $a = D_0 {\gamma_s}^{-11/3}/(c_0 B^2)$, in Table 5.1 we give some quantitative estimate for the values of both $D_0$ and $a$ for different astrophysical environments. The quantitative estimations are shown for both electrons and protons. Note that all estimates of the momentum diffusion coefficient presented in the table are computed from the isotropic turbulence case due to fewer parameter specifications. It is important to emphasize that the quantitative presentation of diffusion coefficients for various astrophysical systems aims to provide an estimate and more importantly demonstrate the variation in diffusion values between electrons and protons. However, it is crucial to acknowledge that the specific parameter values chosen for the calculations can influence the resulting diffusion coefficients. If alternative parameter values were selected, the diffusion coefficients would differ, while the qualitative concept and trends would remain unchanged.

The value of $c_0$ is calculated to be $1.2 \times 10^{-9}$ for electron and $2.08 \times 10^{-19}$ for proton and also the value $m'$ for all the calculations is considered to be fixed at $10^5$. Moreover, it can be noticed that the length scale for turbulence injection is not in the same order of scales typically where the injection of turbulence happens in those astrophysical systems. Additionally, one can observe that the values of the momentum diffusion coefficient are smaller for the proton compared to that of the electron of the same Lorentz factor. Such kind of difference in the momentum diffusion value results in a longer acceleration time for the former as compared to the latter one. Further implication of such behaviour is explored in the following part of this section.

In the left panel of Fig. 5.5 we show the evolution of the energy distribution function for electrons without the source and escape terms (considering $b = 0$ and $S = 0$ in

| Environment | Particle Nature | Magnetic field ($B_0$) | $\beta_A$ | $D_0$ | $a = \frac{D_0}{c_0 B_0^2}$ | Relativistic gyro-radius ($k_g^{-1}$ cm) |
|---|---|---|---|---|---|---|
| Galaxy Cluster | Electron | $10\,\mu$G | $9 \times 10^{-4}$ (Petrosian, 2001) | $1.12 \times 10^{-5}$ | $9.3 \times 10^{13}$ | $1.7 \times 10^{8}\,\gamma$ |
| | Proton | | | $4.29 \times 10^{-7}$ | $2.06 \times 10^{22}$ | $3.13 \times 10^{11}\,\gamma$ |
| Relativistic shock downstream | Electron | 1 mG (Virtanen & Vainio, 2005) | $9 \times 10^{-2}$ | $4.54 \times 10^{-3}$ | $3.78 \times 10^{12}$ | $1.7 \times 10^{6}\,\gamma$ |
| | Proton | | | $1.73 \times 10^{-4}$ | $8.32 \times 10^{20}$ | $3.13 \times 10^{9}\,\gamma$ |
| Interstellar Medium | Electron | $3\,\mu$G (Farmer & Goldreich, 2004) | $6.6 \times 10^{-4}$ (Farmer & Goldreich, 2004) | $5.09 \times 10^{-6}$ | $4.7 \times 10^{14}$ | $5.69 \times 10^{8}\,\gamma$ |
| | Proton | | | $1.94 \times 10^{-7}$ | $1.04 \times 10^{23}$ | $1.04 \times 10^{12}\,\gamma$ |

Table 5.1: Quantitative estimate for the values of $D_0$ and $a$ for different astrophysical systems. Column 1 depicts the name of the astrophysical system, column 2 represents the nature of particle for which the values of $D_0$ and $a$ are calculated. Columns 3 and 4 represent typical values for the magnetic field and Alfvèn velocity in such astrophysical environments. Column 5, 6 and 7 shows the numerical values for $D_0$, $a$ and relativistic gyro-radius considered for the calculations.

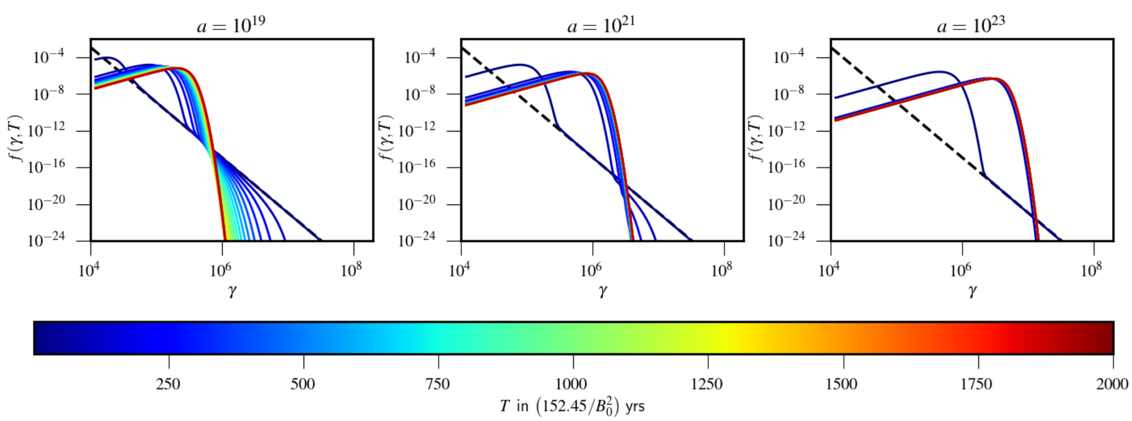


Figure 5.6: Evolution of an initial power-law energy distribution of the form $\gamma^{-6}$ following Eq. (5.26) considering synchrotron loss process and different values for $a$ which typically occurs for protons. The values for $b$ and $S$ are considered zero. Different color of the distribution function corresponds to different time of evolution, as illustrated by the colorbar. To account for the varying magnetic field values observed in different astrophysical systems and the resulting variation in temporal units, the unit time is specified in terms of a variable magnetic field.

Eq. 5.26) and considering $a = 10^{11}$. A color-coded representation is utilized to illustrate the evolutionary trend of the distribution function over time. Different colors correspond to different points in time, as shown on the color bar located at the bottom of the figure. The unit time is specified based on a variable magnetic field ($B_0$). Such a choice of temporal unit is motivated by the fact that the synchrotron cooling time varies in different astrophysical environments due to differences in the magnetic field values. Therefore use of such temporal unit allows for the consideration of different synchrotron cooling times, depending on the magnetic field values present in different astrophysical systems. The use of this representation allows for a better understanding of the evolution of the distribution function in different astrophysical systems. To aid in the comprehension of the results, the unified temporal unit is used in all subsequent figures. The distribution function can be observed to develop an exponential cut-off at higher $\gamma$, which moves towards lower energy as time progresses, due to synchrotron cooling. Additionally a hump like structure can be observed to develop at the low energy regime due to the acceleration of low energy particles owing to the turbulent acceleration. The overall distribution function attains a steady state as a result of the competition between stochastic acceleration and synchrotron loss. The form of the steady state distribution can be computed analytically from Eq. (5.26) considering $b = 0$ and $S = 0$ and is $\propto \gamma^2 \exp\{-\Lambda(\gamma)\}$, where $\Lambda(\gamma) = 3\left(\gamma^{11/3} - 1\right)/11a$ (see Eq. (A1) of Kundu et al., 2021). Further, with such a steady state distribution function it can be observed that the maximum of the distribution occurs at $(2a)^{3/11}$ and it increases with $a$ which can be observed from the middle and the right panel of the figure where the evolution of the distribution is shown form $a = 10^{13}$ and $a = 10^{15}$ respectively.

Fig. 5.6 illustrates the evolution of the distribution function for protons. All the panels of the figure show that the steady state distribution function for protons is morphologically very similar to that of electrons, although with variations in the peak positions. However, the time taken for protons to attain the steady state distribution function is longer than that for electrons as can be observed comparing the temporal unit and final time of both the figures. This difference is attributed to the fact that the synchrotron cooling time for protons is higher due to their higher rest mass, and the momentum diffusion coefficient for protons is lower than that for electrons of similar energy, which can be inferred from the Column 5 of Table 5.1. This implies that it takes more time to accelerate a proton compared to an electron of the same Lorentz factor. As a result, the value of the parameter $a$ is larger for protons, leading to a longer time to reach the steady state.

Further observation reveals that the value of $\gamma$ at which the distribution function is maximum for protons is higher than that for electrons. This indicates that small-scale MHD fluctuations can sustain the energy of higher energy protons for a longer period of time than electrons from the catastrophic synchrotron cooling. Therefore, it can be concluded that the effect of small-scale turbulence would be more prominent for higher energy protons than for electrons.

It is important to note that the evolution of the distribution function show a similar trend for both electrons and protons, and the steady state distribution functions are morphologically similar. Therefore, we focus on the electron distribution for all the subsequent analyses, but the results can be extended to the proton distribution in a similar manner.

In Fig. 5.7, we show the evolution of the distribution function including particle escape and acceleration along with synchrotron loss. The escape time is controlled by the parameter $b = 10^{-6}$ which is kept fixed for the curves shown with different $a$ values in three different panels. For all the plots the high-energy cut-off show a rapid decrement towards lower $\gamma$ as compared to Fig. 5.5 owing to the particle escape in addition to the synchrotron loss process. One interesting observation is that due to escape, the evolution of the distribution begins with the movement of the

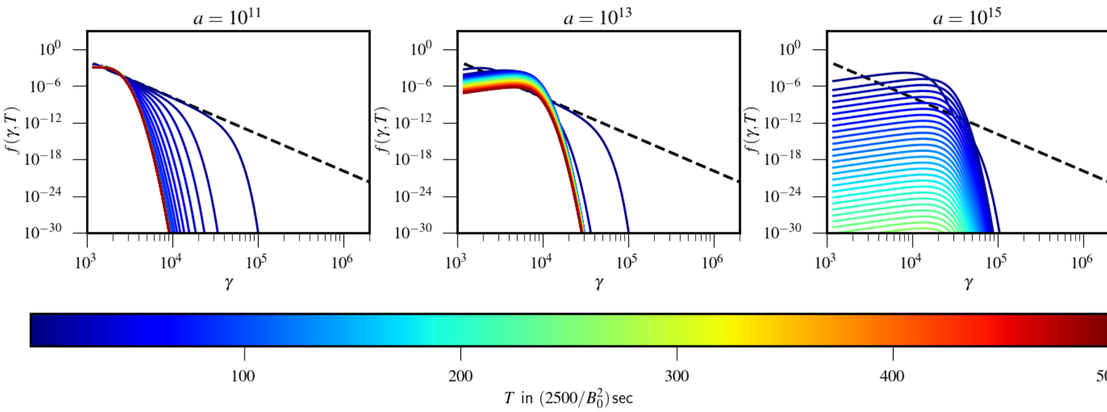


Figure 5.7: Evolution of an initial power-law energy distribution of the form $\gamma^{-6}$ following Eq. (5.26) considering synchrotron loss process with different values for $a$ and $b = 10^{-6}$. The values for $S$ is considered as zero. The initial distribution is shown with the black dashed curve. Different color of the distribution function corresponds to different time of evolution, as illustrated by the colorbar. To account for the varying magnetic field values observed in different astrophysical systems and the resulting variation in temporal units, the unit time is specified in terms of a variable magnetic field.

high-energy cut-off to lower $\gamma$ and increasing the rate of the evolution towards the steady state. After attaining the steady state the movement of the cut-off towards lower $\gamma$ ceases and the height of the distribution starts to decrease as a result of the particle escape. Such kind of evolution is a manifestation of the escape time-scale which follows $\gamma^{-8/3}$ implying that the high-energy particles have lower escape time and therefore they leaks out of the system faster than the low energy particles. We further show the evolution of the distribution function for $b = 10^{-4}$ and $10^{-5}$ with different $a$ values in Figs. A.2, A.3 which exhibit an almost similar evolutionary dynamics. However, due to lesser escape timescale than with $b = 10^{-6}$ the particles leaks out much faster for the cases presented in Figs. A.2, A.3.

In summary, we investigate the impact of small-scale magnetohydrodynamic (MHD) fluctuations on the acceleration of high-energy particles in astrophysical environments. We find that the acceleration of high-energy protons is significantly enhanced by small-scale MHD fluctuations compared to electrons. Turbulent acceleration mediated by these fluctuations enables protons to maintain their energy levels in the presence of radiative synchrotron cooling. Additionally, the inclusion of the spatial escape term, which arises from the parallel diffusion coefficient along the mean magnetic field, demonstrates a relatively dominant escape of higher energy particles from the system.

## 5.4 Astrophysical applications

### 5.4.1 Particle transport in the vicinity of relativistic shocks

Small-scale turbulence has been identified as the primary scattering agent of non-thermal cosmic ray (CR) particles in the vicinity of relativistic shock waves, which is crucial for efficient Fermi acceleration (Lemoine et al., 2006). The downstream medium experiences intense small-scale turbulence due to weakly magnetized upstream regions, providing efficient scattering of CR particles and aiding in the completion of enough Fermi-cycles to facilitate acceleration (Plotnikov et al., 2011). The resulting scenario leads to a power-law-like particle spectrum at the shock front, while small-scale turbulence in the downstream region could act as an agent to energize CR particles via stochastic turbulent acceleration as they move further downstream.

Resonant scattering of particles with turbulent waves in the downstream region, which is typical for low rigidity particles ($R_l < l_c$), has been examined as a second-order turbulent acceleration mechanism in parallel relativistic shock (Virtanen & Vainio, 2005) considering the quasilinear condition. It has been concluded that this mechanism could have a significant impact on the evolution of the particle spectrum. However, as observed by Chang et al. (2008); Plotnikov et al. (2011), for a certain period of time, the downstream turbulence is expected to be mediated by intense ($\delta B \gg B_0$) small-scale magnetic turbulence, which decays with a damping rate $\propto k^3$

suggesting a comparative quick decay of the power available at small-scales. Whereas larger modes show a damping rate of $\propto k^2$ indicating that the power on scales exceeding the Larmor radius of the bulk plasma decays on long, MHD scales (Keshet et al., 2009; Sironi et al., 2015). This observation implies that turbulent acceleration at the low rigidity regime with longer magnetohydrodynamic (MHD) modes could be dominant at later stages, but initially, charged particles will experience acceleration through small-scale turbulence. This argument is in consonance with the theory that small-scale turbulence leads to large-scale turbulence through an inverse cascade (Katz et al., 2007; Medvedev et al., 2004), although further research is needed in this area.

Moreover, evidence of microturbulence generated through Weibel instability has been observed in the precursor region of relativistic shocks, where the upstream medium shows elongated filamentary structures (Plotnikov et al., 2013). This region provides a scenario where turbulent acceleration of charged particles could take place through small-scale turbulence.

This study focuses on the effect of stochastic turbulent acceleration on non-thermal CRs in the presence of small-scale turbulence, where no power is available at the scale of the gyro-radius of the particle. However, the present study relies on quasilinear theory, and the intense small-scale microturbulence needed in relativistic shocks both upstream and downstream requires a larger turbulence intensity $\delta B \gg B_0$, which is not possible to achieve through the present analytical framework. This study can be considered as an initial step to explore the turbulent acceleration mechanism in such intense turbulence scenarios. Although the study cannot provide a realistic quantification of the turbulent acceleration taking place in such microturbulence, the universality in the momentum diffusion coefficient gives a hint of the enriched physics, which would be interesting to explore and would be taken up in future works.

### 5.4.2 Ballistic transport of cosmic ray in Blazars

The regime under investigation in this work is commonly also referred to as the "Ballistic Regime" (Reichherzer et al., 2022b), in which the parallel transport of charged particles is minimally affected. The Ballistic Regime is especially suitable for modeling the transportation of particles with extremely high energies, near the Hillas limit. It is also effective during the initial stages of particle acceleration, before the particle has spent enough time in the acceleration region for its transport to become diffusive (Reichherzer et al., 2022a). Recent studies have attributed the transport of particles in the Ballistic Regime to explaining the spectral energy distributions and light curves of high-energy emission from Blazars (Becker Tjus et al., 2022; Reichherzer et al., 2022a; Tjus, 2022). These works mainly focused on the spatial transport of high energetic particles in AGN-plasmoids, which are often speculated to be responsible for the observed temporal variability in the Blazar sources.

Recent studies have shown that cosmic ray particles with energies above a certain threshold are expected to follow Ballistic transport. Specifically, it has been suggested by Becker Tjus et al. (2022) that cosmic ray particles with energies above $E \gtrsim 5l_c cqB_0/2\pi$ are expected to exhibit Ballistic transport. For AGN-plasmoids, it has been found that the transport of protons with energies $\gtrsim 10^{15}$,eV should also be considered under the Ballistic regime. Such protons typically possess a Lorentz factor of the order of $10^6$.

In Fig. 5.6, it has been shown that small-scale turbulence can effectively provide continuous acceleration to such high-energy protons, enabling them to maintain their energy levels despite catastrophic radiative cooling. However, it is important to note that a more precise quantitative analysis is necessary to fully comprehend the transport of such particles in the context of AGN-plasmoids. We believe that our work will be relevant in studying the effect of turbulent acceleration on cosmic ray particles in Ballistic transport regimes. In particular, it would be interesting to investigate the interplay between turbulent acceleration due to small-scale fluctuations and synchrotron loss in the context of AGN-plasmoids and Blazar variability.

## 5.5 Summary and outlook

In this work we consider the effect of small-scale turbulence with a guided magnetic field on the acceleration of very high-energy charged particles. This study is motivated primarily by an academic interest where our emphasis is towards understanding the nature of interaction between the cosmic rays and the stochastic magnetic fields at scales smaller than the particles' gyro-radius corresponding to the uniform guided magnetic field. It is likely that such kind of situations occur in various astrophysical scenarios, for example in the vicinity of relativistic shocks. We carry out a semi-analytic study based on the quasilinear theory of plasma and determine the momentum transport coefficients for scenarios involving both isotropic and anisotropic turbulence at small scales. For Alfvènic turbulence, we consider isotropic single-scale turbulence injection spectrum and anisotropic turbulence with cascade along $k_\perp$ direction. Our calculation indicates that in both the turbulence scenarios the transport coefficients follow an inverse power-law trend with the energy, or in other words, the Lorentz factor $\gamma$, of the charged particles. In the present work, we obtain the following power law scaling relations for the turbulent transport coefficients: $D_{\gamma\gamma} \propto \gamma^{-2/3}$, $D_{\mu\mu} \propto \gamma^{-8/3}$, and $D_{\mu\gamma} = 0$. The earlier work by Tsytovich & Burdick (1977) reports a power law behaviour of $D_{\gamma\gamma} \propto \gamma^{-1}$ which is different from what we observe here. Additionally, a similar trend for the transport coefficient $D_{\gamma\gamma}$ is found for fast magnetosonic wave turbulence with an isotropic single-scale injection spectrum, as described in detail in Appendix A.10. The similarity in the behavior of $D_{\gamma\gamma}$ for isotropic Alfvèn, anisotropic Alfvén, and isotropic fast wave turbulence suggests that the behavior of the momentum diffusion coefficient becomes universal when turbulent fluctuations occur in the sub-gyro scale regime. Such universality of the diffusion coefficient has also been reported for spatial diffusion of charged particles in small-scale turbulent environment[1]. Moreover, Pezzi et al. (2022) also observed that the impact of anisotropy in MHD turbulence spectrum on the particle diffusion coefficient is weak, which we also observe for the momentum diffusion coefficient. Therefore it appears that for particles with larger gyro-radius or greater energy, the specific details of the small-scale turbulence may not significantly affect particle distribution, though the presence of power at these scales can still impact the overall distribution. The calculated form for $D_{\mu\mu}$ leads to a parallel spatial diffusion coefficient which scales with $\gamma$ as $\sim \gamma^{8/3}$; see Eq. (5.25) for $\mathcal{K}$. Such a trend is compatible with the QLT constraint defined in Eq. (5.23). Moreover, the parallel diffusion that we find is similar to that of obtained from numerical simulation by Casse et al. (2001). Their result showed that the parallel diffusion in quasilinear regime scales with rigidity (or $\gamma$) with an exponent of 7/3 which is close to the result that we obtain from asymptotic expansion of the quasilinear diffusion coefficients.

Having observed the trend of the transport coefficients, we then solve the transport equation for the cosmic rays, i.e., the Fokker-Planck equation. When we ignore the synchrotron loss and diffusive escape mechanisms, we find that the small-scale turbulence leads to the energization of particles in such a way that the low energy particles are accelarated faster compared to the particles with higher $\gamma$, which is typical for Fermi type stochastic acceleration. Thus resulting in a non-uniform acceleration of the cosmic ray particles. A qualitative comparison with the case where the gyro-radius of particle is smaller than the turbulence correlation length reveals that the acceleration due to small-scale turbulence is relatively less efficient.

[1]See Plotnikov et al. (2011) for small-scale magnetic field following white noise and parallel diffusion scaling as rigidity squared. Also, see Subedi et al. (2017) and Dundovic et al. (2020) for similar scaling in isotropic spatial diffusion in synthetically constructed turbulence fields. Pezzi et al. (2022) showed the same trend for MHD turbulence.

We further demonstrate the interplay of various micro-physical processes, such as acceleration, synchrotron loss and diffusive particle escape, on the particle spectrum in various regimes of the parameters $a$ and $b$ in Eq. (5.26). The particle spectrum is observed to attain a steady-state as a result of the competition between acceleration and synchrotron loss. Additionally, with the particle escape process included, the distribution function evolves in such a way that the high-energy particles leak out of the system faster than the low-energy ones.

Our study indicates that in a situation where small-scale turbulence is mediated by a mean magnetic field, acceleration of high energy particles would be small in presence of other more dominant competing micro-physical processes, such as the synchrotron loss and diffusive escape. However, such an acceleration is found to be significant for lower energy particles. The hump like structure that develops in the distribution function signifies the acceleration of low-$\gamma$ particles. Additionally, while investigating such interplay with electron and proton distributions individually, we observe that small-scale turbulence can accelerate protons to higher energies than electrons, and this acceleration may assist high-energy proton particles in maintaining their energy from synchrotron loss effects. Therefore, we envisage that in some cases with appropriate values for the dynamical quantities this acceleration could become significant and it may help the non-thermal particles to sustain their energy against the radiative cooling mechanisms. Finally we discuss about adequate astrophysical systems that could provide suitable conditions for small-scale turbulence to potentially influence the energy distribution of non-thermal particles.

This work is the first step towards studying a more complex interplay of various micro-physical processes and their impact on the energy spectrum of the cosmic ray. Other acceleration scenarios where resonant interaction between turbulent waves and high energy cosmic ray particles is not included, for example, adiabatic acceleration due to random velocity of the MHD fluid (Lemoine, 2019; Ptuskin, 1988) could also provide significant acceleration to the non-thermal particles with high rigidity. Such acceleration configurations along with various energy loss processes will be considered in future works. As an extension to this present work, it would be interesting to see the effects of small-scale turbulence on the high energy non-thermal particles in a non-linear framework of wave-particle interaction (Beresnyak et al., 2011; Yan & Lazarian, 2008).

# Chapter 6

# Conclusion and outlook

Astrophysical plasma is known to be of a turbulent nature. The turbulence in the astrophysical sources plays a fundamental role in governing the behaviour of these systems. Due to the multi-scale nature of astrophysical systems, the impact of turbulence shows different manifestations at different scales. At the micro-physical scale, turbulence significantly impacts the dynamics of the charged particles residing in astrophysical systems. Such an effect of turbulence is expected to be observed through the emission these particles emit by interacting with the local magnetic field or surrounding photon distribution. The work presented here aims to investigate the impact of the underlying turbulence on the emission from astrophysical sources. The investigation focuses on the particle acceleration processes driven by the turbulent astrophysical plasma. In typical astrophysical sources, these acceleration processes occur in tandem with various other micro-physical processes, and we observe the collective action of all these processes.

This thesis studies the impact of different particle acceleration processes along with different loss processes typically expected to be operating in a weakly magnetised plasma environment. The actual micro-physical processes in these astrophysical systems are still unknown and cannot be probed with current observational facilities. In these circumstances, the developed framework offers a connection between the theoretical models and realistic observations. Below we reiterate the conclusive points that came out of the works presented in this thesis.

## Numerical implementation of STA

- Here, we present a novel second-order accurate conservative numerical approach designed to investigate the microphysical interplay between the stochastic turbulent acceleration (STA) process and various loss mechanisms. This framework contributes to a comprehensive understanding of the evolution of non-thermal particle distributions in the presence of turbulence.

- By integrating the newly developed numerical methodology into the existing particle module of the PLUTO code, we explore the effects of different acceleration processes on emission. Through a series of test case scenarios, we examine how different acceleration mechanisms influence emission signatures.

- Finally, we showcase the emission maps of a toy axisymmetric RMHD jet considering all the acceleration and loss processes are working in tandem. A distinct contrast emerges when comparing the outcomes with and without STA in addition to shock acceleration. This difference becomes evident in the evolving particle distribution and subsequent emission patterns. Notably, the presence of STA plays a significant role in shaping the emission, particularly manifesting as diffuse X-ray emission originating from the turbulent back-flow region of the RMHD jet. This finding highlights the distinctive contribution of STA compared to the sole influence of shock acceleration.

## Emission properties of radio lobes of FR-II AGN jets

- Here, we investigate the interplay of multiple particle acceleration and loss mechanisms on the emission from the turbulent radio lobe of the FR-II AGN jet by adopting a phenomenologically motivated ansatz for STA, via numerical simulations.

- Stochastic acceleration introduces distinctive characteristics into the spectra of non-thermal particles within the lobe. In comparison to scenarios without STA, the resulting particle spectrum showcases a distinct morphology.

- The presence of STA leads to the emergence of both low- and high-energy cut-offs in the resultant particle spectrum. The lower cut-off correlates with the system's radiative age, while the upper cut-off is a consequence of the interplay between stochastic acceleration and radiative loss processes.

- The spectral energy distribution of the simulated source shows evidence of different emission peaks emerging due to the presence of turbulent acceleration. Observation of the spatial distribution of the particles responsible for the SED peaks at X-ray frequencies indicates a diffuse nature of the emission arising due to the complementary nature of the interplay of both the particle acceleration processes.

### Particle acceleration due to small-scale turbulence

- Here we study the effect of sub-gyroscale MHD turbulence threaded by a mean magnetic field on the transport of non-thermal charged particles via quasi-linear theory.

- The investigation has provided insights into the behaviour of the momentum diffusion coefficient within the framework of both isotropic and anisotropic small-scale turbulence. Our semi-analytical calculations have revealed a remarkable universal power-law-like trend, linking the coefficient to the particle Lorentz factor with a relationship of $\gamma^{-2/3}$.

- We find that such small-scale turbulence could produce a steady-state particle spectrum due to the competition with the synchrotron loss process, indicating that such turbulence can provide continuous energization to non-thermal particles, with which particles can keep their energy for a longer amount of time. Additionally, our observations highlight a marked distinction between protons and electrons. The steady-state peak occurs at substantially higher energy levels for protons in comparison to electrons.

## 6.1 Outlook

The work presented in this thesis demonstrates the importance of a distributed turbulent acceleration process and its interplay with other acceleration and loss processes in astrophysical sources. This thesis focuses on the turbulent radio lobes of FR-II jets and studies the particle acceleration processes in such systems and their manifestations on the systems' emission characteristics. For the turbulent acceleration, we consider a phenomenological ansatz to mimic the effect of the turbulence happening in realistic radio lobe systems.

The framework developed here can be used to study the effect of the interplay of different particle acceleration processes in other astrophysical sources. For example the radio halos of galaxy cluster is known to be highly turbulent and the radio emission is attributed to originate due STA (Ohno et al., 2002). In such scenarios, the developed framework can be utilised to simulate the emission from such turbulent radio halos considering turbulent acceleration and can be further compared with observations to understand the actual turbulent transport. In the downstream of radio relics of galaxy clusters, stochastic acceleration is known to play a significant role in providing continuous acceleration to the already shock accelerated non-thermal particles (Fujita et al., 2015). Such a scenario can also be synthetically reproduced using the framework developed in this thesis. These numerical reproductions can then be compared with actual observations to constrain the microphysical processes occurring at those extragalactic sites.

Another application of this framework can be devised at the Inter-Stellar Medium (ISM). Compared to the turbulence in cluster of galaxies, ISM turbulence is known to be weak ($\delta b/B < 1$) and highly supersonic. Such supersonic magnetised turbulence is capable of driving shocks in the ISM, and the current framework can easily be applied to understand the relative contributions of shock and turbulence on the particle acceleration in such a system (Falceta-Gonçalves et al., 2014).

The framework that has been developed as a part of this thesis can be extended in future to work for a strong turbulent medium. Such turbulence is observable in the solar wind and is capable of driving the magnetic reconnection process (Vlahos & Isliker, 2018). The reconnection process contributes to the direct acceleration of non-thermal particles, and the FP-like evolution equation for non-thermal energy distribution cannot be employed in such a scenario. In addition to random acceleration, it is speculated that this type of direct acceleration causes particles to follow a Levy flight-like process in the energy space. By incorporating the microphysics of such an anomalous process, the simulations of particle transport under intense magnetised turbulence would become more realistic.

The work presented in this thesis has set the stage for developing more realistic multifrequency emission models of the FR-II radio galaxies, which can be further tested by several future telescopes, such as the SKA facility for the low-energy radio domain or ATHENA for keV energy range.

# Appendix A

# Appendix

## A.1 Transport of charged particles in turbulent plasma

Relativistic Vlasov Equation reads,

$$\frac{\partial f}{\partial t} + (\boldsymbol{v} \cdot \nabla) f + q(\boldsymbol{E} + \frac{\boldsymbol{v}}{c} \times \boldsymbol{B}) \cdot \frac{\partial f}{\partial \boldsymbol{p}} = 0 \tag{A.1}$$

To perturbatively solve the Vlasov equation we consider a multi-time-scale perturbation of various quantities in the following way,

$$\begin{aligned} \frac{\partial}{\partial t} &= \frac{\partial}{\partial T_0} + \epsilon^1 \frac{\partial}{\partial T_1} + \epsilon^2 \frac{\partial}{\partial T_2} + \dots \\ f &= f_0 + \epsilon^1 f_1 + \epsilon^2 f_2 + \dots \\ \boldsymbol{E} &= \epsilon^1 \boldsymbol{E_1} + \epsilon^2 \boldsymbol{E_2} + \dots \\ \boldsymbol{B} &= B_0 + \epsilon^1 \boldsymbol{B_1} + \epsilon^2 \boldsymbol{B_2} + \dots \end{aligned} \tag{A.2}$$

where $\epsilon^1$, $\epsilon^2$, ... describes the order of perturbation. Note that we have not considered the zeroth order electric field, which is validated by the fact that Cosmic Rays get transported through a medium where ideal MHD approximation works. So, the presence of a mean electric field can be neglected and $\boldsymbol{E}$ field can only be generated through random fluctuations. In the following, we will also assume $f_0$ to be homogeneous, so $\nabla f_0 = 0$.

Upon substituting the perturbed quantities, as described in Eq. (A.2), in Eq. (A.1) and collecting all the terms containing $\epsilon_0$ both from left and right side of the equation, we obtain the following equation,

$$\frac{\partial f_0}{\partial T_0} + q\left(\frac{\boldsymbol{v}}{c} \times \boldsymbol{B_0}\right) \cdot \frac{\partial f_0}{\partial \boldsymbol{p}} = 0 \tag{A.3}$$

To proceed further we assume $f_0$ is steady during the timescale $T_0$. Further, Noting $\boldsymbol{p} = m_q \gamma \boldsymbol{v}$ and $\boldsymbol{B_0} = B_0 \hat{z}$, Eq. (A.3) becomes the following,

$$\frac{q}{m_q \gamma c}(\boldsymbol{p} \times \boldsymbol{B_0}) \cdot \frac{\partial f_0}{\partial \boldsymbol{p}} = 0 \tag{A.4}$$

Considering $p$ in cylindrical coordinates as $p_x = p_\perp \cos\phi$, $p_y = p_\perp \sin\phi$ and after substituting it, the above equation takes the following form (see Eq. 10.1.4 - 10.1.8 in Gurnett & Bhattacharjee, 2017),

$$-\frac{\partial f_0}{\partial \phi} B_0 = 0 \tag{A.5}$$

Note that while deriving the above equation we consider $p_z$ to be independent of $\phi$. Eq. (A.5) shows that $f_0$ is independent of $\phi$, the gyro-phase. Further, remember that it assumes $f_0$ is homogeneous and steady. So this proves $f_0$ is independent of $\phi$, the gyro-phase. Note that this independence comes from the fact that $f_0$ is homogeneous and steady.

Further, equating the terms containing $\epsilon_1$ in in Eq. (A.1) after perturbation, we obtain the following equation,

$$\frac{\partial f_1}{\partial T_0} + \frac{\partial f_0}{\partial T_1} + \boldsymbol{v} \cdot \nabla f_1 + q\left(\boldsymbol{E_1} + \frac{\boldsymbol{v}}{c} \times \boldsymbol{B_1}\right) \cdot \nabla_p f_0 + \frac{q}{c}(\boldsymbol{v} \times \boldsymbol{B_0}) \cdot \nabla_p f_1 = 0 \tag{A.6}$$

We assume all the mean field quantities, described with subscript "0", to be non-random and the perturbations are random fluctuations. Therefore, performing ensemble averaging over Eq. A.6 and noting that $f_1$ is a fluctuation on $f_0$, we obtain,

$$\frac{\partial f_0}{\partial T_1} = 0 \tag{A.7}$$

While deriving above equation we consider, $\langle f_0 \rangle = f_0$, $\langle \boldsymbol{B}_0 \rangle = \boldsymbol{B}_0$, $\langle f_1 \rangle = 0$, $\langle \boldsymbol{E}_1 \rangle = 0$ and $\langle \boldsymbol{B}_1 \rangle = 0$. Eq. (A.7) implies that $f_0$ does not change over the timescale $T_1$. Substituting Eq. (A.7) back into Eq. (A.6), we obtain the following evolution equation for $f_1$ over a timescale $T_0$,

$$\frac{\partial f_1}{\partial T_0} + \boldsymbol{v} \cdot \nabla f_1 + q\left(\boldsymbol{E_1} + \frac{\boldsymbol{v}}{c} \times \boldsymbol{B_1}\right) \cdot \nabla_p f_0 + q\left(\frac{\boldsymbol{v}}{c} \times \boldsymbol{B_0}\right) \cdot \nabla_p f_1 = 0 \tag{A.8}$$

The above equation indicates, that $f_1$, the linear perturbation on Eq. (A.1), evolves as a function of the zeroth order distribution function, the zeroth order magnetic field and first order electric and magnetic fluctuations. One gets various kinds of waves which are possible in Vlasov system, by solving such equation. To understand the emergence of linearized waves and their consequences in Vlasov system, the readers are encouraged to look chapter 19 of Bittencourt (2013).

Following the terms containing $\epsilon^2$ after substituting Eq. (A.2) in Eq. (A.1), we obtain,

$$\begin{aligned} \frac{\partial f_2}{\partial T_0} + \frac{\partial f_0}{\partial T_2} + \boldsymbol{v} \cdot \nabla f_2 + q\left(\boldsymbol{E_1} + \frac{\boldsymbol{v}}{c} \times \boldsymbol{B_1}\right) \cdot \nabla_p f_1 + q\left(\frac{\boldsymbol{v}}{c} \times \boldsymbol{B_0}\right) \cdot \nabla_p f_2 \\ + q\left(\boldsymbol{E_2} + \frac{\boldsymbol{v}}{c} \times \boldsymbol{B_2}\right) \cdot \nabla_p f_0 = 0 \end{aligned} \tag{A.9}$$

Upon employing the similar strategy of taking the ensemble average of the above equation and considering $\langle f_2 \rangle, \langle E_2 \rangle, \langle B_2 \rangle = 0$, we obtains,

$$\frac{\partial f_0}{\partial T_2} + q\left\langle \left(\boldsymbol{E_1} + \frac{\boldsymbol{v}}{c} \times \boldsymbol{B_1}\right) \cdot \nabla_p f_1 \right\rangle = 0 \tag{A.10}$$

The above equation is very important for our analysis and it implies that the evolution of $f_0$ will occur at a timescale of $T_2$ due to the linear perturbations of Eq. (A.1).

We are interested to solve Eq. (A.10). Such a solution will be obtained by substituting the value of $f_1$ from Eq. (A.8) in Eq. (A.10).

For solving Eq. (A.8), we do all the analysis in Fourier domain. Therefore, performing a Fourier transformation of Eq. (A.8), we obtain,

$$\left(-i\omega_k + i\boldsymbol{k}\cdot\boldsymbol{v}\right)\tilde{f}_1 - \Omega\frac{\partial \tilde{f}_1}{\partial\phi} + q\left(\tilde{\boldsymbol{E}}_1 + \frac{\boldsymbol{v}}{c}\times\tilde{\boldsymbol{B}}_1\right)\cdot\frac{\partial f_0}{\partial\boldsymbol{p}} = 0 \tag{A.11}$$

where $\Omega$ is the relativistic gyro-frequency, $\Omega = qB_0/m_q\gamma c$ while deriving the above equation we consider $f_0$ to be independent of spatial variables due to homogeneity due to which convolution did not arise in the last term on the left-hand side, while Fourier transforming. We also consider the following relation (Gurnett & Bhattacharjee, 2017),

$$q\left(\frac{\boldsymbol{v}}{c}\times\boldsymbol{B_0}\right)\cdot\nabla_p f_1 = -\frac{qB_0}{m\gamma c}\frac{\partial f_1}{\partial\phi} = -\Omega\frac{\partial f_1}{\partial\phi} \tag{A.12}$$

Further, we consider Amperes' law to transform $\tilde{\boldsymbol{B}}_1$ to $\tilde{\boldsymbol{E}}_1$ in Eq. (A.11). After a simple but long calculation, we obtain the form for $f_1$ in the Fourier space as follows (see section 9.3.1 in Gurnett & Bhattacharjee, 2017),

$$\tilde{f}_1 = \iota q\sum_{n=-\infty}^{\infty}\sum_{m=-\infty}^{\infty}\frac{J_n(\beta)e^{i(n-m)(\phi-\psi)}}{m\Omega + k_{||}v_{||} - \omega}\left[\frac{P_\perp}{2}\left\{\tilde{E_+}e^{i\psi}J_{m+1}(\beta) + \tilde{E_-}e^{-i\psi}J_{m-1}(\beta)\right\} + \tilde{E}_{||}P_{||}J_m(\beta)\right] \tag{A.13}$$

Eq. (A.13) has various terms which are explained below,

$$
\begin{aligned}
P_{||} &= \frac{\partial f_0}{\partial p_{||}} + \frac{\Omega m}{\omega v_\perp} T, \\
T &= \left( v_{||} \frac{\partial f_0}{\partial p_\perp} - v_\perp \frac{\partial f_0}{\partial p_{||}} \right), \\
P_\perp &= \left( 1 - \frac{k_{||} v_{||}}{\omega} \right) \frac{\partial f_0}{\partial p_\perp} + \frac{v_\perp k_{||}}{\omega} \frac{\partial f_0}{\partial p_{||}}, \\
\beta &= \frac{k_\perp v_\perp}{\Omega}, \\
\alpha &= \frac{k_{||} v_{||} - \omega}{\Omega}, \\
\tilde{E}_\pm &= \tilde{E}_x \mp \iota \tilde{E}_y, \\
\tilde{E}_{||} &= \frac{\tilde{\boldsymbol{E}}_1 \cdot \boldsymbol{B}_0}{|\boldsymbol{B}_0|}
\end{aligned}
\tag{A.14}
$$

Upon substituting Eq. (A.13) back in Eq. (A.8), we obtain our required equation. Before proceeding we note that, Eq. (A.8) is defined in real space while Eq. (A.13) is in Fourier space so we transform Eq. (A.8) in the following way,

$$
\int \frac{\partial f_0}{\partial T_2} e^{-i\boldsymbol{g}\cdot\boldsymbol{r}} d^3\boldsymbol{r} = -q \left\langle \int \left( \tilde{\boldsymbol{E}}_1{}^{(\boldsymbol{g}-\boldsymbol{k})} + \frac{\boldsymbol{v}}{c} \times \tilde{\boldsymbol{B}}_1{}^{(\boldsymbol{g}-\boldsymbol{k})} \right) \cdot \nabla_p f_1^{\boldsymbol{k}} d^3\boldsymbol{k} \right\rangle \tag{A.15}
$$

The superscripts of $\tilde{\boldsymbol{E}}_1$, $\tilde{\boldsymbol{B}}_1$ and $\tilde{f}_1$ represents the dependencies of these quantities on the Fourier variables $\boldsymbol{g}$ and $\boldsymbol{k}$. Further a convolution operation is performed, which is implied through the dependency of $\tilde{\boldsymbol{E}}_1$ and $\tilde{\boldsymbol{B}}_1$ on $\boldsymbol{g}-\boldsymbol{k}$.

Note that in Eq. (A.15) if we make $\boldsymbol{g} = 0$ the left-hand side becomes ordinary average of the temporal evolution of $f_0$, which through commutativity between the integration and ensemble averaging implies an average of $f_0$. Due to the definition of $f_0$, such an averaging will not change its value, hence considering $\boldsymbol{g} = 0$ in Eq. (A.15) we obtain the following,

$$
\frac{\partial f_0}{\partial T_2} = -q \left\langle \int d^3k \left( \tilde{\boldsymbol{E}}_1{}^{-\boldsymbol{k}} + \frac{\boldsymbol{v}}{c} \times \tilde{\boldsymbol{B}}_1{}^{-\boldsymbol{k}} \right) \cdot \nabla_p f_1^{\boldsymbol{k}} \right\rangle \tag{A.16}
$$

Further due to the fact that all the field variables are real, their Fourier transforms obey the following identity (see page 462 of Bellan, 2008),

$$\begin{aligned}\left(\tilde{\boldsymbol{E}}_1{}^{\boldsymbol{k}}\right)^* &= \tilde{\boldsymbol{E}}_1{}^{-\boldsymbol{k}},\\ \left(\tilde{\boldsymbol{B}}_1{}^{\boldsymbol{k}}\right)^* &= \tilde{\boldsymbol{B}}_1{}^{-\boldsymbol{k}},\\ \left(\omega^{\boldsymbol{k}}\right)^* &= -\omega^{-\boldsymbol{k}}\end{aligned} \tag{A.17}$$

where, $\omega^{\boldsymbol{k}}$ is the $\boldsymbol{k}-$dependent circular frequency of the wave which we consider to be imaginary in our calculation for the sake of generality. After considering the above condition, we obtain the Fourier transformation of Eq.(A.13) as the following,

$$\frac{\partial f_0}{\partial T_2} = -q\left\langle \int \left(\tilde{\boldsymbol{E}}_1{}^{\boldsymbol{k}} + \frac{\boldsymbol{v}}{c} \times \tilde{\boldsymbol{B}}_1{}^{\boldsymbol{k}}\right)^* \cdot \nabla_p f_1^{\boldsymbol{k}} d^3\boldsymbol{k} \right\rangle \tag{A.18}$$

After performing some simple but lengthy algebra and considering some identities of the Bessel function we finally obtain the following equation,

$$\begin{aligned}\frac{\partial f_0}{\partial T_2} = -q^2 \int d^3\boldsymbol{k} \Bigg\langle &\left[L_{||}^* (\tilde{E_{||}}^{\boldsymbol{k}})^* J_m(\beta) + \left(L_\perp^* - \frac{1}{p_\perp}\left(\frac{k_{||}v_{||}}{(\omega^{\boldsymbol{k}})^*} - 1\right)\right)(\tilde{E_\perp}^{\boldsymbol{k}})^*\right] \\ &i\frac{1}{m\Omega + k_{||}v_{||} - \omega^{\boldsymbol{k}}}\left(L_{||}\tilde{E_{||}}^{\boldsymbol{k}} J_m(\beta) + L_\perp \tilde{E_\perp}^{\boldsymbol{k}}\right) f_0 \Bigg\rangle\end{aligned} \tag{A.19}$$

where $L||$ and $L_\perp$ are differential operators which are defined as $P|| = L_{||}f_0$ and $P_\perp = L_\perp f_0$ respectively.

## A.2 Analytical solution of Fokker-Planck Equation

Eq. (4.12) is very hard to solve for a proper general analytic solution. Various work has been devoted to solve Eq. (4.12) for various transport coefficients (e.g., Chang & Cooper, 1970; Kardashev, 1962; Katarzyński et al., 2006; Park & Petrosian, 1995). Chang & Cooper (1970) solved Eq. (4.12) for the steady-state solution and the solution could be written as,

$$\chi_{\rm steady}(\gamma) = \chi_0 \exp\Big\{ -\int_1^{\gamma} \Big(\frac{S(\gamma',\tau) - D_{\rm A}(\gamma',\tau)}{D_{\gamma\gamma}(\gamma',\tau)}\Big) d\gamma' \Big\}. \tag{A.20}$$

Katarzyński et al. (2006) solved Eq. (A.20) for $D_{\gamma\gamma}(\gamma,\tau) = D_{\gamma 0}\gamma^2/2$ with $D_{\gamma 0} = 1/t_{\rm A}$, $D_{\rm A}(\gamma,\tau) = \gamma/t_{\rm A}$ and $S(\gamma,\tau) = S_0\gamma^2$. These form of the parameters are typical for particles in plasma. The loss term $S(\gamma,\tau)$ gets a similar form if Inverse-Compton radiation is taken in the Thompson limit with Synchrotron radiation and the form for the diffusion coefficient $D_{\gamma\gamma}$ which also matches the form from typical particle in cell simulation as discussed above. The solution to Eq. (A.20) with the above mentioned parameters is,

$$\chi_{\rm steady}(\gamma) = \chi_0 \gamma^2 \exp\{-2S_0 t_{\rm A}(\gamma - 1)\}. \tag{A.21}$$

Kardashev (1962) got a time-dependent solution for Eq. (4.12) without the loss terms and showed the acceleration leads to a log-normal particle distribution (similar to Eq. (4.17)).

So, if the particles only accelerate via STA the particle distribution follows a log-normal form due to the fact that the STA process is a multiplicative acceleration process (Tramacere et al., 2011). But if those particles loose their energy via radiative means along with the acceleration the particle distribution starts to follow an ultra-relativistic Maxwellian (Eq. (A.21)), which looks like a thermal or quasi-thermal spectrum with a scaled temperature of $1/S_0 t_{\rm A}$ which is also the value of $\gamma$ where, $t_{\rm A} = t_{\rm L}$.

## A.3 Calculation of correlation terms for MHD turbulence

Here we show the derivations pertaining to the calculations of $T_{ij}$, $Q_{ij}$ and $R_{ij}$ for MHD turbulence. The Ohm's Law for MHD regime can be written in the following way,

$$\boldsymbol{E}(\boldsymbol{k}) = -\left(\frac{1}{c}\right)\boldsymbol{u}(\boldsymbol{k}) \times \boldsymbol{B}_0 \implies E_i(\boldsymbol{k}) = -\left(\frac{1}{c}\right)\epsilon_{imn}u_m(\boldsymbol{k}) \times B_{0n}$$

Therefore, the electric field correlations can be written as follows,

$$\left\langle E_i(\boldsymbol{k})\, E_j^*(\boldsymbol{k}')\right\rangle = \frac{1}{c^2}\left\langle \epsilon_{imn}\epsilon_{jpq}u_m(\boldsymbol{k})\, B_{0n}u_p^*(\boldsymbol{k}')\, B_{0q}\right\rangle$$

As mean B-field is only directed along z direction, the correlation becomes,

$$\left\langle E_i(\boldsymbol{k})\, E_j^*(\boldsymbol{k}')\right\rangle = \frac{B_0^2}{c^2}\left\langle \epsilon_{imz}\epsilon_{jpz}u_m(\boldsymbol{k})\, u_p^*(\boldsymbol{k}')\right\rangle$$

Employing the identity $\epsilon_{imn}\epsilon_{jpq} = (\delta_{ij}\delta_{mp} - \delta_{ip}\delta_{jm})$ the correlation function simplifies to,

$$\left\langle E_i(\boldsymbol{k})\, E_j^*(\boldsymbol{k}')\right\rangle = \frac{B_0^2}{c^2}[\delta_{ij}\left\langle u_p(\boldsymbol{k})\, u_p^*(\boldsymbol{k}')\right\rangle - \langle u_j(\boldsymbol{k})\, u_i^*(\boldsymbol{k}')\rangle] \tag{A.22}$$

Similarly, the electric field magnetic field correlation becomes,

$$\left\langle E_i(\boldsymbol{k})\, B_j^*(\boldsymbol{k}')\right\rangle = -\frac{1}{c}\left\langle \epsilon_{imn}u_m(\boldsymbol{k})\, B_{0n}B_j^*(\boldsymbol{k}')\right\rangle = -\frac{B_{0z}}{c}\left\langle \epsilon_{imz}u_m(\boldsymbol{k})\, B_j^*(\boldsymbol{k}')\right\rangle \tag{A.23}$$

and,

$$\left\langle B_i(\boldsymbol{k})\, E_j^*(\boldsymbol{k}')\right\rangle = -\frac{B_{0z}}{c}\left\langle B_i(\boldsymbol{k})\, \epsilon_{ipz}u_p^*(\boldsymbol{k}')\right\rangle = -\frac{B_{0z}}{c}\epsilon_{ipz}\left\langle B_i(\boldsymbol{k})\, u_p^*(\boldsymbol{k}')\right\rangle$$

Following the definitions given in Eq. (5.3) we get,

1. $\left\langle E_i(\boldsymbol{k})\, E_j^*(\boldsymbol{k}')\right\rangle = \dfrac{B_0^2}{c^2}\left[\delta_{ij}V_A^2\delta(\boldsymbol{k}-\boldsymbol{k}')\, Y_{pp}(k) - V_A^2\delta(\boldsymbol{k}-\boldsymbol{k}')\, Y_{ji}(\boldsymbol{k})\right]$
   $= \dfrac{B_0^2V_A^2}{c^2}[\delta_{ij}Y_{pp}(\boldsymbol{k}) - Y_{ji}(\boldsymbol{k})]$

2. $\left\langle E_i(\boldsymbol{k})\, B_j^*(\boldsymbol{k}')\right\rangle = -\dfrac{B_0}{c}\epsilon_{imz}\left\langle u_m(\boldsymbol{k})\, B_j^*(\boldsymbol{k}')\right\rangle = -\dfrac{B_0^2V_A}{c}\epsilon_{imz}\delta(\boldsymbol{k}-\boldsymbol{k}')\, C_{mj}(\boldsymbol{k})$

3. $\left\langle B_i(\boldsymbol{k})\, E_j^*(\boldsymbol{k}')\right\rangle = -\dfrac{B_0}{c}\epsilon_{jpz}\left\langle B_i(\boldsymbol{k})\, u_p^*(\boldsymbol{k}')\right\rangle = -\dfrac{B_0^2V_A}{c}\epsilon_{jpz}\delta(\boldsymbol{k}-\boldsymbol{k}')\, C_{ip}(\boldsymbol{k})$

## A.4 Calculation of correlation functions

In this appendix, we derive the transformation laws for various turbulent spectra, from Cartesian space to polarization space.

$$\begin{aligned} R_{11}\delta(k-k') &= \langle E_1(k)E_1^*(k')\rangle = \left\langle \frac{E_{\mathcal{R}}(k)+E_{\mathcal{L}}(k)}{\sqrt{2}} \cdot \frac{E_{\mathcal{R}}^*(k')+E_{\mathcal{L}}^*(k')}{\sqrt{2}} \right\rangle \\ &= \frac{1}{2}\left[\langle E_{\mathcal{R}}(k)E_{\mathcal{R}}^*(k')\rangle + \langle E_{\mathcal{R}}(k)E_{\mathcal{L}}^*(k')\rangle + \langle E_{\mathcal{L}}(k)E_{\mathcal{R}}^*(k')\rangle \right. \\ &\quad \left. + \langle E_{\mathcal{L}}(k)E_{\mathcal{L}}^*(k')\rangle\right] \end{aligned} \tag{A.24}$$

Where, $E_{\mathcal{R}}$ and $E_{\mathcal{L}}$ are known as Jones vectors and they are defined as,

$$E_{\mathcal{R}} = \frac{E_1 - \iota E_2}{\sqrt{2}}, \qquad E_{\mathcal{L}} = \frac{E_1 + \iota E_2}{\sqrt{2}}$$

.

$$\implies E_1 = \frac{E_{\mathcal{R}} + E_{\mathcal{L}}}{\sqrt{2}}, \qquad E_2 = \frac{E_{\mathcal{L}} - E_{\mathcal{R}}}{\iota\sqrt{2}} = \frac{\iota(E_{\mathcal{R}} - E_{\mathcal{L}})}{\sqrt{2}}$$

. Further with the following definitions of the correlation tensor in the polarization space $R_{11}$ becomes,

- $R_{\mathcal{R}\mathcal{R}}\delta(k-k') = \langle E_{\mathcal{R}}(k)E_{\mathcal{R}}^*(k')\rangle$;
- $R_{\mathcal{R}\mathcal{L}}\delta(k-k') = \langle E_{\mathcal{R}}(k)E_{\mathcal{L}}^*(k')\rangle$;
- $R_{\mathcal{L}\mathcal{R}}\delta(k-k') = \langle E_{\mathcal{L}}(k)E_{\mathcal{R}}^*(k')\rangle$;
- $R_{\mathcal{L}\mathcal{L}}\delta(k-k') = \langle E_{\mathcal{L}}(k)E_{\mathcal{L}}^*(k')\rangle$;

$$R_{11} = \frac{1}{2}\left(R_{\mathcal{R}\mathcal{R}} + R_{\mathcal{R}\mathcal{L}} + R_{\mathcal{L}\mathcal{R}} + R_{\mathcal{L}\mathcal{L}}\right)$$

Similarly $R_{22}$, $R_{12}$ and $R_{21}$ can be written as,

$$\begin{aligned} R_{22}\delta(k-k') = \langle E_2(k)E_2^*(k')\rangle &= \frac{1}{2}\left[\langle E_{\mathcal{R}}(k)E_{\mathcal{R}}^*(k')\rangle + \langle E_{\mathcal{L}}(k)E_{\mathcal{L}}^*(k')\rangle \right. \\ &\quad \left. - \langle E_{\mathcal{R}}(k)E_{\mathcal{L}}^*(k')\rangle - \langle E_{\mathcal{L}}(k)E_{\mathcal{R}}^*(k')\rangle\right] \\ &= -\frac{1}{2}\left(R_{\mathcal{R}\mathcal{R}} + R_{\mathcal{L}\mathcal{L}} - R_{\mathcal{L}\mathcal{R}} - R_{\mathcal{R}\mathcal{L}}\right)\delta(k-k'). \end{aligned} \tag{A.25}$$

$$
\begin{aligned}
R_{12}\delta(k-k') = \langle E_1(k)E_2^*(k')\rangle &= \left\langle \frac{E_{\mathcal{R}}(k)+E_{\mathcal{L}}(k)}{\sqrt{2}} - \iota\frac{(E_{\mathcal{R}}^*(k')-E_{\mathcal{L}}^*(k'))}{\sqrt{2}} \right\rangle \\
= -\frac{\iota}{2}\left[\langle E_{\mathcal{R}}(k)E_{\mathcal{R}}^*(k')\rangle - \langle E_{\mathcal{R}}(k)E_{\mathcal{L}}^*(k')\rangle + \langle E_{\mathcal{L}}(k)E_{\mathcal{R}}^*(k')\rangle - \langle E_{\mathcal{L}}(k)E_{\mathcal{L}}^*(k')\rangle\right] \\
&= -\frac{\iota}{2}\left(R_{\mathcal{RR}} - R_{\mathcal{RL}} + R_{\mathcal{LR}} - R_{\mathcal{LL}}\right)\delta(k-k').
\end{aligned}
\tag{A.26}
$$

$$
\begin{aligned}
R_{21}\delta(k-k') = \langle E_2(k)E_1^*(k')\rangle &= \frac{\iota}{2}\left[\langle E_{\mathcal{R}}(k)E_{\mathcal{R}}^*(k')\rangle + \langle E_{\mathcal{R}}(k)E_{\mathcal{L}}^*(k')\rangle\right. \\
&\quad \left. - \langle E_{\mathcal{L}}(k)E_{\mathcal{R}}^*(k')\rangle - \langle E_{\mathcal{L}}(k)E_{\mathcal{L}}^*(k')\rangle\right] \\
&= \frac{\iota}{2}\left(R_{\mathcal{RR}} + R_{\mathcal{RL}} - R_{\mathcal{LR}} - R_{\mathcal{LL}}\right)\delta(k-k').
\end{aligned}
\tag{A.27}
$$

Therefore, we can write,

$$
\begin{pmatrix} R_{11} \\ R_{12} \\ R_{21} \\ R_{22} \end{pmatrix} = \frac{1}{2}\begin{pmatrix} 1 & 1 & 1 & 1 \\ -\iota & \iota & -\iota & \iota \\ \iota & \iota & -\iota & -\iota \\ 1 & -1 & -1 & 1 \end{pmatrix}\begin{pmatrix} R_{\mathcal{RR}} \\ R_{\mathcal{RL}} \\ R_{\mathcal{LR}} \\ R_{\mathcal{LL}} \end{pmatrix}
\tag{A.28}
$$

The matrix upon inversion gives,

- $R_{\mathcal{RR}} = \frac{1}{2}\left(R_{11} + R_{22} + \iota(R_{12} - R_{21})\right)$;
- $R_{\mathcal{LL}} = \frac{1}{2}\left(R_{11} + R_{22} - \iota(R_{12} - R_{21})\right)$;
- $R_{\mathcal{LR}} = \frac{1}{2}\left(R_{11} - R_{22} + \iota(R_{12} + R_{21})\right)$;
- $R_{\mathcal{RL}} = \frac{1}{2}\left(R_{11} - R_{22} - \iota(R_{12} + R_{21})\right)$;

By definition (see Eq. 5.2),

$$
\begin{aligned}
R_{ij}(k)\delta(k-k') = \left\langle E_i(k)E_j^*(k')\right\rangle &= \frac{B_0^2}{c^2}\left(\delta_{ij}\left\langle u_p(k)u_p^*(k')\right\rangle - \langle u_j(k)u_i^*(k')\rangle\right) \\
\implies R_{ij} = \frac{B_0^2V_A^2}{c^2}\left(\delta_{ij}Y_{pp}(k) - Y_{ji}(k)\right) &= \frac{B_0^2V_A^2}{c^2}\left(\delta_{ij}Y_{pp} - Y_{ij}\right) \\
&= \frac{B_0^2V_A^2}{c^2k^2}\left(\delta_{ij} + \frac{k_ik_j}{k^2}\right)P_0\delta\left(\frac{k}{m'k_g} - 1\right)
\end{aligned}
\tag{A.29}
$$

where we have used Eq. (A.22) for the electric field correlation term, Eq. (5.5) for the small-scale turbulence spectrum and utilized its symmetry property ($Y_{ij} = Y_{ji}$). We further use the following identity for $Y_{pp}$,

$$Y_{pp}(\boldsymbol{k}) = k^{-2}(\delta_{pp} - 1) P_0 \delta\left(\frac{k}{m' k_g} - 1\right) = \frac{2P_0}{k^2}\delta\left(\frac{k}{m' k_g} - 1\right).$$

Therefore, with the definition of $\boldsymbol{k} = \{k_\perp \cos\psi, k_\perp \sin\psi, k_{||}\}$ the correlations in the polarization space takes the following form,

- $$R_{\mathcal{RR}} = \frac{1}{2}\frac{B_0^2 V_A^2}{c^2 k^2} P_0 \delta\left(\frac{k}{m' k_g} - 1\right)\left[1 + \frac{k_\perp^2 \cos\psi^2}{k^2} + 1 + \frac{k_\perp^2 \sin\psi^2}{k^2}\right.$$
$$\left. + \iota\left(\tfrac{k_\perp^2}{k^2}\cos\psi\sin\psi - \tfrac{k_\perp^2}{k^2}\cos\psi\sin\psi\right)\right]$$
$$= \frac{B_0^2 V_A^2}{c^2 k^2} P_0 \left(1 + \frac{k_\perp^2}{2k^2}\right)\delta\left(\frac{k}{m' k_g} - 1\right);$$

- $$R_{\mathcal{LL}} = \frac{B_0^2 V_A^2}{c^2 k^2} P_0 \left(1 + \frac{k_\perp^2}{2k^2}\right)\delta\left(\frac{k}{m' k_g} - 1\right);$$

- $$R_{\mathcal{LR}} = \frac{1}{2}\left(1 + \frac{k_\perp^2 \cos\psi^2}{k^2} - 1 - \frac{k_\perp^2 \sin\psi^2}{k^2} + \iota\left(2\frac{k_\perp^2}{k^2}\cos\psi\sin\psi\right)\right)$$
$$\tfrac{B_0^2 V_A^2}{c^2 k^2} P_0 \delta\left(\tfrac{k}{m' k_g} - 1\right) = \tfrac{1}{2}\tfrac{B_0^2 V_A^2}{c^2 k^2} P_0 \delta\left(\tfrac{k}{m' k_g} - 1\right)\tfrac{k_\perp^2}{k^2} e^{2\iota\psi}$$

- $$R_{\mathcal{RL}} = \frac{1}{2}\frac{B_0^2 V_A^2}{c^2 k^2} P_0 \delta\left(\frac{k}{m' k_g} - 1\right)\frac{k_\perp^2}{k^2} e^{-2\iota\psi}$$

where we have used the following,

$$\delta_{ij} + \frac{k_i k_j}{k^2} = \begin{bmatrix} 1 & 0 & 0 \\ 0 & 1 & 0 \\ 0 & 0 & 1 \end{bmatrix} + \frac{1}{k^2}\begin{bmatrix} k_\perp^2 \cos^2\psi & k_\perp^2 \cos\psi\sin\psi & k_\perp k_{||}\cos\psi \\ k_\perp^2 \cos\psi\sin\psi & k_\perp^2 \sin^2\psi & k_\perp k_{||}\sin\psi \\ k_{||}k_\perp \cos\psi & k_{||}k_\perp \sin\psi & k_{||}^2 \end{bmatrix} \quad \text{(A.30)}$$

Similarly considering $P_{ij} = B_0^2 Y_{ij}$ we get,

- $$P_{\mathcal{RR}} = B_0^2 Y_{\mathcal{RR}} = \frac{B_0^2}{k^2}\left(1 - \frac{k_\perp^2}{2k^2}\right) P_0 \delta\left(\frac{k}{m' k_g} - 1\right);$$

- $$P_{\mathcal{LL}} = B_0^2 Y_{\mathcal{LL}} = \frac{B_0^2}{k^2}\left(1 - \frac{k_\perp^2}{2k^2}\right) P_0 \delta\left(\frac{k}{m' k_g} - 1\right);$$

- $$P_{\mathcal{LR}} = B_0^2 Y_{\mathcal{LR}} = \frac{-B_0^2}{2}\frac{k_\perp^2}{k^4} e^{2\iota\psi} P_0 \delta\left(\frac{k}{m' k_g} - 1\right);$$

- $P_{\mathcal{RL}} = B_0^2 Y_{\mathcal{RL}} = \dfrac{-B_0^2}{2}\dfrac{k_\perp^2}{k^4} e^{-2\iota\psi} P_0 \delta\left(\dfrac{k}{m' k_g} - 1\right).$

Further, following the definition of $T_{ij}$ and $C_{ij}$ while noting the fact that $C_{ij} = \sigma Y_{ij}$ and $Y_{ij}$ is real, the velocity-magnetic field correlation function becomes,

- $T_{11} = -\dfrac{B_0^2 V_A}{c}\epsilon_{1m3} C_{m1}^* = -\dfrac{B_0^2 V_A}{c}\epsilon_{123} C_{21}^* = -\dfrac{B_0^2 V_A}{c} C_{21}^*$
  $= \frac{B_0^2 V_A}{c}\sigma \frac{k_\perp^2}{k^4}\cos\psi \sin\psi P_0 \delta\left(\frac{k}{m' k_g} - 1\right);$

- $T_{22} = -\dfrac{B_0^2 V_A}{c}\epsilon_{2m3} C_{m2}^* = \dfrac{B_0^2 V_A}{c} C_{12}^* = -\dfrac{B_0^2 V_A}{c}\sigma \dfrac{k_\perp^2}{k^4}\cos\psi \sin\psi P_0 \delta\left(\dfrac{k}{m' k_g} - 1\right);$

- $T_{12} = -\dfrac{B_0^2 V_A}{c}\epsilon_{2m3} C_{m1}^* = -\dfrac{B_0^2 V_A}{c}\epsilon_{213} C_{11}^* = \dfrac{B_0^2 V_A}{c} C_{11}^*$
  $= \frac{B_0^2 V_A}{ck^2}\sigma\left(1 - \frac{k_\perp^2 \cos\psi^2}{k^2}\right) P_0 \delta\left(\frac{k}{m' k_g} - 1\right)$

- $T_{21} = -\dfrac{B_0^2 V_A}{c}\epsilon_{1m3} C_{m2}^* = -\dfrac{B_0^2 V_A}{c} C_{22}^* = -\dfrac{B_0^2 V_A}{ck^2}\sigma\left(1 - \dfrac{k_\perp^2 \sin\psi^2}{k^2}\right)$
  $P_0 \delta\left(\frac{k}{m' k_g} - 1\right)$

where $\epsilon_{ijk}$ is the Levi-Civita symbol and we have further used the fact that $C_{ij} = C_{ij}^*$. Following these the correlation in the polarization space takes the form,

- $T_{\mathcal{RR}} = \dfrac{P_0}{2k^2}\left(\iota \dfrac{B_0^2 V_A \sigma}{c}\left(1 - \dfrac{k_\perp^2 \cos\psi^2}{k^2} + 1 - \dfrac{k_\perp^2 \sin\psi^2}{k^2}\right)\right)\delta\left(\dfrac{k}{m' k_g} - 1\right)$
  $= \iota \frac{B_0^2 V_A \sigma}{2ck^2}\left(2 - \frac{k_\perp^2}{k^2}\right) P_0 \delta\left(\frac{k}{m' k_g} - 1\right);$

- $T_{\mathcal{LL}} = -\iota \dfrac{B_0^2 V_A \sigma}{2ck^2}\left(2 - \dfrac{k_\perp^2}{k^2}\right) P_0 \delta\left(\dfrac{k}{m' k_g} - 1\right);$

- $T_{\mathcal{LR}} = \dfrac{P_0}{k^2}\left[\dfrac{B_0^2 V_A \sigma}{2c}\left(\dfrac{k_\perp^2 \cos\psi \sin\psi}{k^2} + \dfrac{k_\perp^2 \cos\psi \sin\psi}{k^2}\right)\right.$
  $\left. + \iota\left(1 - \frac{k_\perp^2 \cos\psi^2}{k^2} - 1 + \frac{k_\perp^2 \sin\psi^2}{k^2}\right)\right]\delta\left(\frac{k}{m' k_g} - 1\right)$
  $= -\iota \dfrac{B_0^2 V_A \sigma}{2c}\dfrac{k_\perp^2}{k^4} e^{2\iota\psi} P_0 \delta\left(\dfrac{k}{m' k_g} - 1\right);$

- $T_{\mathcal{RL}} = \iota \frac{B_0^2 V_A \sigma}{2c} \frac{k_\perp^2}{k^4} e^{-2\iota\psi} P_0 \delta\left(\frac{k}{m' k_g} - 1\right)$.

Note that all the velocity-magnetic field correlations becomes imaginary in the polarization space.

## A.5 Derivation of $D_{pp}$

From Eq. (5.7) we get,

$$\begin{aligned} D_{pp} = \frac{\Omega^2\left(1-\mu^2\right)}{2} m^2 c^2 \frac{V_A^2}{c^2} P_0 \mathcal{R}e \Bigg[ \sum_{n=-\infty}^{\infty} \int_{k_{min}}^{k_{max}} \delta\left(\frac{k}{m' k_g} - 1\right) k^{-2}\, d^3\boldsymbol{k} \\ \int_0^\infty dt\, e^{-\iota\left(k_{||} v_{||} - \omega + n\Omega\right)t} \\ \left\{ \left( J_{n+1}^2\left(\frac{k_\perp v_\perp}{\Omega}\right) + J_{n-1}^2\left(\frac{k_\perp v_\perp}{\Omega}\right)\right)\left(1 + \frac{k_\perp^2}{2k^2}\right) \right. \\ \left. + J_{n+1}\left(\frac{k_\perp v_\perp}{\Omega}\right) J_{n-1}\left(\frac{k_\perp v_\perp}{\Omega}\right) \frac{k_\perp^2}{k^2} \right\} \Bigg] \end{aligned} \tag{A.31}$$

Time integration leads,

$$\begin{aligned} D_{pp} = \frac{\Omega^2\left(1-\mu^2\right)}{2} m^2 c^2 \frac{V_A^2}{c^2} \pi P_0 \mathcal{R}e \Bigg[ \sum_{n=-\infty}^{\infty} \int_{k_{min}}^{k_{max}} \delta\left(\frac{k}{m' k_g} - 1\right) dk \\ \int_0^\pi \sin\theta d\theta \int_0^{2\pi} d\phi\, \delta(k\cos\theta v_{||} - \omega + n\Omega) \\ \left\{ \left( J_{n+1}^2\left(\frac{k_\perp v_\perp}{\Omega}\right) + J_{n-1}^2\left(\frac{k_\perp v_\perp}{\Omega}\right)\right)\left(1 + \frac{k_\perp^2}{2k^2}\right) \right. \\ \left. + J_{n+1}\left(\frac{k_\perp v_\perp}{\Omega}\right) J_{n-1}\left(\frac{k_\perp v_\perp}{\Omega}\right) \frac{k_\perp^2}{k^2} \right\} \Bigg] \end{aligned} \tag{A.32}$$

The presence of the $\delta$ function inside the $\phi$ integration, gives rise to a resonance condition which the plasma waves and the charged particles have to satisfy in order for interaction to happen between them. In this work, we consider the resonance to be exact with no broadening. Additional modifications regarding the resonance condition is also considered in literature which results from modifications of the quasilinear approach (see Yan & Lazarian, 2008, for example). Upon performing the $\phi$ integration we get,

$$D_{pp} = \Omega^2 \left(1-\mu^2\right) m^2 c^2 \frac{V_A^2}{c^2} \pi^2 P_0 \mathcal{R}e \left[ \sum_{n=-\infty}^{\infty} \int_{k_{min}}^{k_{max}} \delta \left( \frac{k}{m' k_g} - 1 \right) dk \int_0^{\pi} \sin\theta d\theta \right.$$
$$\delta(k\cos\theta v_{||} - \omega + n\Omega) \left\{ \left( J_{n+1}^2 \left( \frac{k_\perp v_\perp}{\Omega} \right) + J_{n-1}^2 \left( \frac{k_\perp v_\perp}{\Omega} \right) \right) \right.$$
$$\left. \left. \left( 1 + \frac{k_\perp^2}{2k^2} \right) + J_{n+1} \left( \frac{k_\perp v_\perp}{\Omega} \right) J_{n-1} \left( \frac{k_\perp v_\perp}{\Omega} \right) \frac{k_\perp^2}{k^2} \right\} \right]. \tag{A.33}$$

Further, we note that $k_\perp = k\sin\theta = k\sqrt{1-x^2}$ with $x$ being the cosine of the angle between $\boldsymbol{k}$ and the direction of the mean magnetic field, $x = \cos\theta$. Owing to the small scale limit, $\frac{k_\perp v_\perp}{\Omega} >> 1$, the summation on 'n' becomes integration and integration over delta function with resonance condition leads (Tsytovich & Burdick, 1977),

$$D_{pp} \simeq \Omega \left(1-\mu^2\right) m^2 c^2 \frac{V_A^2}{c^2} \pi^2 P_0 \mathcal{R}e \left[ \int_0^{\infty} \delta \left( \frac{k}{m' k_g} - 1 \right) dk \right.$$
$$\int_{-1}^{1} dx \left\{ \left( J^2_{\frac{\omega}{\Omega} - \frac{kxv\mu}{\Omega} + 1} \left( \frac{kv}{\Omega} \sqrt{1-x^2}\sqrt{1-\mu^2} \right) \right. \right.$$
$$\left. + J^2_{\frac{\omega}{\Omega} - \frac{kxv\mu}{\Omega} - 1} \left( \frac{kv}{\Omega} \sqrt{1-x^2}\sqrt{1-\mu^2} \right) \right) \left( \frac{3-x^2}{2} \right)$$
$$\left. \left. + \left(1-x^2\right) J_{\frac{\omega}{\Omega} - \frac{kxv\mu}{\Omega} + 1} \left( \frac{kv}{\Omega} \sqrt{1-x^2}\sqrt{1-\mu^2} \right) J_{\frac{\omega}{\Omega} - \frac{kxv\mu}{\Omega} - 1} \left( \frac{kv}{\Omega} \sqrt{1-x^2}\sqrt{1-\mu^2} \right) \right\} \right], \tag{A.34}$$

where we consider $v_\perp = v\sqrt{1-\mu^2}$ with $\mu$ being the pitch-angle and the limit of the $k$ integration to be 0 to $\infty$. Performing the $k$ integration leads,

$$D_{pp} \simeq \Omega \left(1-\mu^2\right) m^2 c^2 \frac{V_A^2}{c^2} \pi^2 m' k_g P_0 \mathcal{R}e \left[ \int_{-1}^{1} dx \left\{ \left( J^2_{\frac{\omega}{\Omega} - \frac{m' k_g xv\mu}{\Omega} + 1} \right. \right. \right.$$
$$\left( \frac{m' k_g v}{\Omega} \sqrt{1-x^2}\sqrt{1-\mu^2} \right) + J^2_{\frac{\omega}{\Omega} - \frac{m' k_g xv\mu}{\Omega} - 1} \left. \left( \frac{m' k_g v}{\Omega} \sqrt{1-x^2}\sqrt{1-\mu^2} \right) \right) \left( \frac{3-x^2}{2} \right)$$
$$+ \left(1-x^2\right) J_{\frac{\omega}{\Omega} - \frac{m' k_g xv\mu}{\Omega} + 1} \left( \frac{m' k_g v}{\Omega} \sqrt{1-x^2}\sqrt{1-\mu^2} \right)$$
$$\left. \left. J_{\frac{\omega}{\Omega} - \frac{m' k_g xv\mu}{\Omega} - 1} \left( \frac{m' k_g v}{\Omega} \sqrt{1-x^2}\sqrt{1-\mu^2} \right) \right\} \right], \tag{A.35}$$

## A.6 Transport Equation

From Eq. (5.24) following $a_1 = 0$, due to the fact that $D_{\mu p} = 0$, leads to

$$\frac{\partial F}{\partial t} = \frac{\partial}{\partial z}\left(\mathcal{K}\frac{\partial F}{\partial z}\right) - U\frac{\partial F}{\partial z} + \frac{p}{3}\frac{\partial U}{\partial z}\frac{\partial F}{\partial p} + \frac{1}{p^2}\frac{\partial}{\partial p}\left(p^2 a_2 \frac{\partial F}{\partial p}\right) + S_0 \tag{A.36}$$

Substituting $F = \frac{f}{p^2}$, $f$ follows the following equation,

$$\frac{\partial f}{\partial t} = \frac{\partial}{\partial z}\left(\mathcal{K}\frac{\partial f}{\partial z}\right) - U\frac{\partial f}{\partial z} + \frac{p^3}{3}\frac{\partial U}{\partial z}\frac{\partial}{\partial p}\left(\frac{f}{p^2}\right) + \frac{\partial}{\partial p}\left(p^2 a_2 \frac{\partial}{\partial p}\left(\frac{f}{p^2}\right)\right) + S_0 p^2 \tag{A.37}$$

which upon simplification gets the following form,

$$\frac{\partial f}{\partial t} = \frac{\partial}{\partial z}\left(\mathcal{K}\frac{\partial f}{\partial z}\right) - \frac{\partial (Uf)}{\partial z} + \frac{\partial}{\partial p}\left(\frac{\partial U}{\partial z}\frac{p}{3}f\right) + \frac{\partial}{\partial p}\left(a_2 \frac{\partial f}{\partial p}\right) - \frac{\partial}{\partial p}\left(\frac{2a_2 f}{p}\right) + S_0 p^2. \tag{A.38}$$

For the present work, we neglect the $3^{rd}$ term on the right-hand side, which corresponds to adiabatic loss/gain, and introduce a radiative loss term due to synchrotron process. We further employ the leaky-box approximation (Lerche & Schlickeiser, 1985), following which we replace the spatial advection and diffusion terms by a momentum dependent escape term. Such an approximation leads the transport equation to take the following form,

$$\frac{\partial f}{\partial t} + \frac{\partial}{\partial \gamma}\left(\frac{2Df}{\gamma} - c_0 B^2 \gamma^2 f\right) = \frac{\partial}{\partial \gamma}\left(D\frac{\partial f}{\partial \gamma}\right) - \frac{f}{T_{esc}} + S_0 \gamma^2. \tag{A.39}$$

Note that, the above equation is written in terms of particle's Lorentz factor $\gamma$ instead of momentum $p$ and the corresponding conversion factor is encapsulated within the constant factors of the transport coefficients. Further, following the forms of the transport coefficients for small-scale turbulence as discussed in sections 5.3.1 and 5.3.2, we find $1/T_{esc} = \alpha\gamma^{8/3}$, $D = D_0\gamma^{-2/3}$, with $\alpha$ and $\beta$ being the constants whose values depends on $\beta_A$, $m'$ and $\sigma$. Upon substitution of the transport coefficients, the transport equation takes the following form,

$$\frac{\partial f}{\partial(T_sT)}+\frac{\partial}{\partial(\gamma_s\Gamma)}\left(\frac{2D_0(\gamma_s\Gamma)^{-\frac{2}{3}}f}{\gamma_s\Gamma}-c_0B^2(\gamma_s\Gamma)^2f\right)=\frac{\partial}{\partial(\gamma_s\Gamma)}\left(D_0(\gamma_s\Gamma)^{-\frac{2}{3}}\frac{\partial f}{\partial(\gamma_s\Gamma)}\right)-f\alpha(\gamma_s\Gamma)^{\frac{8}{3}}+S_0(\gamma_s\Gamma)^2. \tag{A.40}$$

Note that the substitution of the transport coefficients is done considering $t = T_sT$ and $\gamma = \gamma_s\Gamma$ with $T_s$ and $\gamma_s$ being the scaled time and Lorentz factor respectively. The above transport equation when written in the scaled units, simplifies to,

$$\frac{\partial f}{\partial T}+T_s\frac{\partial}{\partial\Gamma}\left\{\frac{2D_0(\gamma_s\Gamma)^{-\frac{5}{3}}f}{\gamma_s}-\frac{c_0B^2}{\gamma_s}(\gamma_s\Gamma)^2f\right\}=T_s\frac{\partial}{\partial\Gamma}\left(\frac{D_0}{\gamma_s^2}(\gamma_s\Gamma)^{-\frac{2}{3}}\frac{\partial f}{\partial\Gamma}\right)-T_sf\alpha(\gamma_s\Gamma)^{\frac{8}{3}}+T_sS_0(\gamma_s\Gamma)^2.$$

Next, we consider $T_s$ to be the synchrotron cooling time for $\gamma_s$, $T_s = T_{cool}(\gamma_s) = 1/(c_0B^2\gamma_s)$ and with such choice of $T_s$ the transport equation further simplifies to,

$$\frac{\partial f}{\partial T}+\frac{\partial}{\partial\Gamma}\left\{\frac{2D_0\gamma_s^{-\frac{5}{3}}\Gamma^{-\frac{5}{3}}}{\gamma_sc_0B^2\gamma_s}f-\frac{c_0B^2(\gamma_s\Gamma)^2f}{\gamma_sc_0B^2\gamma_s}\right\}=\frac{\partial}{\partial\Gamma}\left(\frac{D_0\gamma_s^{-\frac{2}{3}}\Gamma^{-\frac{2}{3}}}{\gamma_s^2c_0B^2\gamma_s}\frac{\partial f}{\partial\Gamma}\right)-f\frac{\gamma_s^{\frac{8}{3}}\alpha\Gamma^{\frac{8}{3}}}{c_0B^2\gamma_s}+S_0\frac{\gamma_s^2\Gamma^2}{c_0B^2\gamma_s},$$

which finally takes the following form,

$$\frac{\partial f}{\partial T}+\frac{\partial}{\partial\Gamma}\left(2a\Gamma^{-\frac{5}{3}}f-\Gamma^2f\right)=\frac{\partial}{\partial\Gamma}\left(a\Gamma^{-\frac{2}{3}}\frac{\partial f}{\partial\Gamma}\right)-b\Gamma^{\frac{8}{3}}f+S. \tag{A.41}$$

where $a$ and $b$ are the ratios of the synchrotron cooling time to diffusion timescale and escape timescale at $\gamma = \gamma_s$, respectively; $S$ is the scaled source term. They can be defined in the following way,

$$a=\frac{D_0\gamma_s^{-\frac{11}{3}}}{c_0B^2},\quad b=\frac{\gamma_s^{\frac{5}{3}}\alpha}{c_0B^2},\quad S=S_0\frac{\gamma_s}{c_0B^2}\Gamma^2. \tag{A.42}$$

## A.7 Comparison with Hard-sphere turbulence

In this appendix we show a comparative analysis between the acceleration efficiency of the small-scale turbulence and hard-sphere turbulence. For this purpose we solve the following Fokker-Planck equation considering different forms for the diffusion

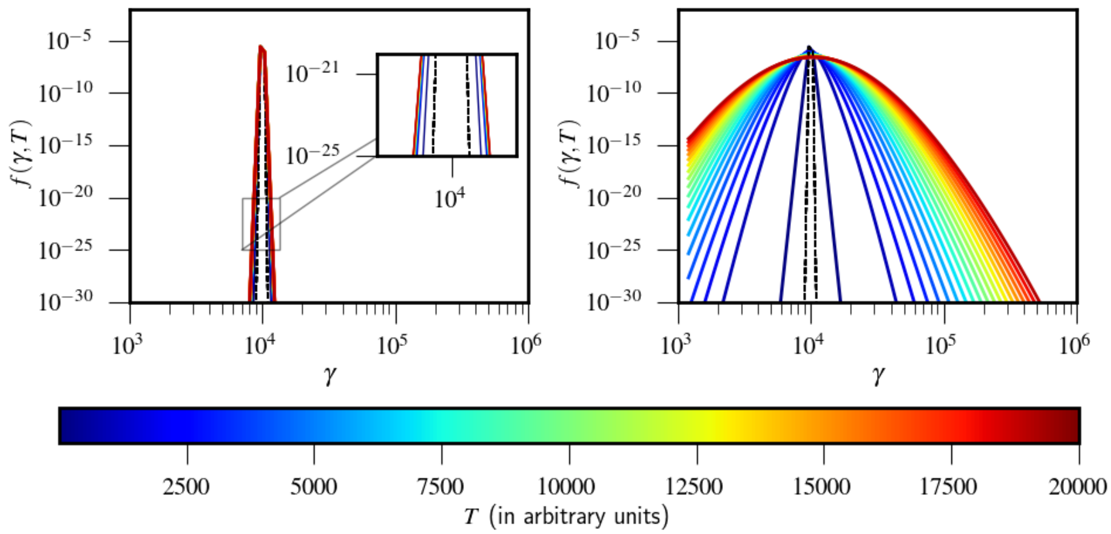


Figure A.1: Evolution of an initial Gaussian with mean $10^4$ and standard deviation 100 (shown by a black dashed curve) for two different cases, following Eq. (A.43). **Left:** Due to small-scale turbulence ($D = \gamma^{-2/3}$), **Right:** due to hard-sphere turbulence ($D = \gamma^2$). The temporal value is depicted by the colorbar.

coefficient.

$$\frac{\partial f}{\partial T} + \frac{\partial}{\partial \gamma}\left(\frac{2D}{\gamma}\right) f = \frac{\partial}{\partial \gamma}\left(D\frac{\partial f}{\partial \gamma}\right), \tag{A.43}$$

We consider $D = D_0\gamma^{-2/3}$ for the stochastic acceleration due to small-scale turbulence (see section 5.3.1) and $D = D_{hs}\gamma^2$ for the case of hard-sphere turbulence with both $D_0 = D_{hs} = 1$.

In Fig. A.1 we show the temporal evolution of the initial distribution function for both the case scenarios. In the left plot, due to small-scale turbulence, the spread of the initial distribution function increases owing to the acceleration of particles. However, the spreading of the distribution function happens slowly compared to the plot shown in the right panel. Such an evolution is due to the larger acceleration time ($\tau_{acc} \sim \gamma^2/D \propto \gamma^{8/3}$) for the small-scale turbulence as compared to the right one where $\tau_{acc}$ is constant. This exercise clearly shows that the acceleration due to the small-scale turbulence is less efficient as compared to the hard-sphere case,

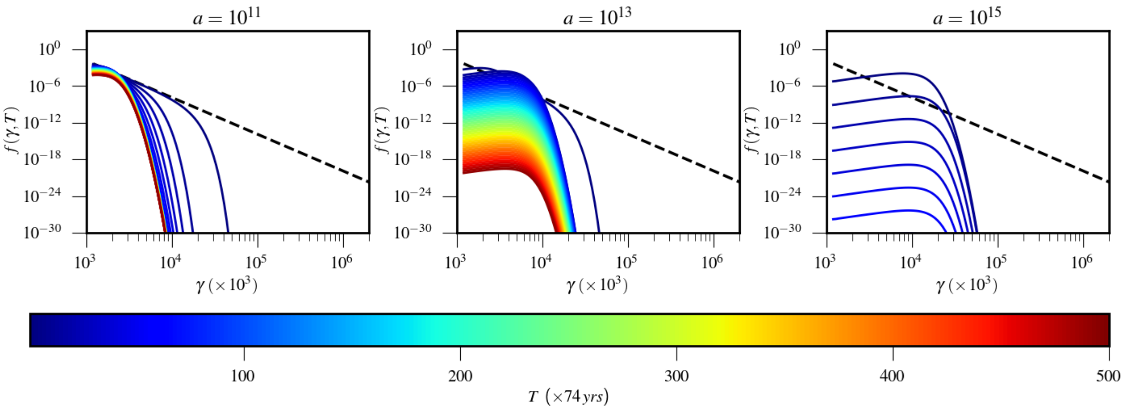


Figure A.2: Evolution of an initial power-law energy distribution of the form $\gamma^{-6}$ following Eq. (5.26) considering synchrotron loss process with different values for $a$ and $b = 10^{-5}$. The values for $S$ is considered as zero. The initial distribution is shown with the black dashed curve.

however one should keep in mind that the result is largely dependent on the choice of $D_0$ and $D_{hs}$ (see Fig. 5.4). The purpose of this analysis is to compare the evolution of the distribution function for two mathematically different form of $D$.

## A.8 Evolution of the distribution function with different escape timescale

In this appendix we show additional figures (figs. A.3 and A.2) for the evolution of the distribution function by solving Eq. (5.26) with $b = 10^{-4}$ and $10^{-5}$. The evolution is computed for different values of $a$ and $S = 0$.

## A.9 Computation of transport coefficients for small-scale anisotropic Alfvèn wave turbulence spectrum

For computing the transport coefficients for small-scale anisotropic turbulence, we consider the form of the turbulence spectrum such that it can mimic the behaviour of realistic Alfvènic turbulence upto a certain degree (Yan & Lazarian, 2002). In particular, we consider the turbulence spectrum of the following form,

$$Y_{ij}(k) = P_{aniso}\left(\delta_{ij} - \frac{k_i k_j}{k_\perp^2}\right)\Theta\left(k_\perp - m' k_g\right)\delta\left(\frac{k_{||}}{m'' k_g} - 1\right)k_\perp^{-\alpha}, \qquad \text{(A.44)}$$

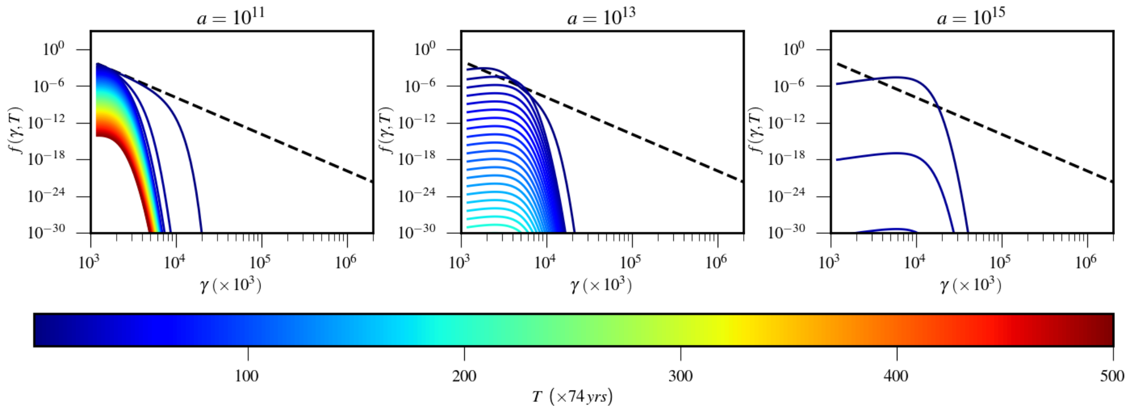


Figure A.3: Evolution of an initial power-law energy distribution of the form $\gamma^{-6}$ following Eq. (5.26) considering synchrotron loss process with different values for $a$ and $b = 10^{-4}$. The values for $S$ is considered as zero. The initial distribution is shown with the black dashed curve.

where $\Theta$ corresponds to Heaviside theta function and $P_{aniso}$ being the injected turbulent power; $k_\perp$ and $k_{||}$ are the perpendicular and parallel wave vector components; $m'k_g$ and $m''k_g$ are the respective scales where power corresponding to $k_\perp$ and $k_{||}$ are injected. Note the difference between the above spectrum with the isotropic one given by Eq. (5.5), the isotropic part here corresponds to the isotropy in the plane perpendicular to $k_{||}$ and unlike the earlier one the injection of energy is happening at different scales for $k_\perp$ and $k_{||}$ separately, which is governed by the value of $m'$ and $m''$ respectively. Moreover the above spectrum allows for the energy to cascade along $k_\perp$ direction, while a single scale injection is considered along $k_{||}$. With such a spectrum the equipartition of energy implies the form of $P_{aniso}$ as the following,

$$P_{aniso} \simeq \frac{\alpha - 2}{2\pi m'k_g (m''k_g)^{2-\alpha}}. \tag{A.45}$$

The positivity constraint of the power implies $\alpha > 2$. Such a turbulence spectrum takes the following form in the polarisation space,

- $R_{\mathcal{RR}} = \dfrac{1}{2}\dfrac{B_0^2 V_A^2}{c^2} P_{aniso} \Theta\left(k_\perp - m'k_g\right)\delta\left(\dfrac{k_{||}}{m''k_g} - 1\right) k_\perp^{-\alpha}$;
- $R_{\mathcal{LL}} = \dfrac{1}{2}\dfrac{B_0^2 V_A^2}{c^2} P_{aniso} \Theta\left(k_\perp - m'k_g\right)\delta\left(\dfrac{k_{||}}{m''k_g} - 1\right) k_\perp^{-\alpha}$;

- $R_{\mathcal{LR}} = \frac{1}{2}\frac{B_0^2 V_A^2}{c^2} P_{aniso}\Theta\left(k_\perp - m' k_g\right)\delta\left(\frac{k_{||}}{m'' k_g} - 1\right) k_\perp^{-\alpha} e^{2\iota\psi};$

- $R_{\mathcal{RL}} = \frac{1}{2}\frac{B_0^2 V_A^2}{c^2} P_{aniso}\Theta\left(k_\perp - m' k_g\right)\delta\left(\frac{k_{||}}{m'' k_g} - 1\right) k_\perp^{-\alpha} e^{-2\iota\psi};$

With such turbulent spectrum, $D_{pp}$ takes the following form,

$$\begin{aligned} D_{pp} = \frac{\Omega\left(1-\mu^2\right)}{4} 2\pi^2 m^2 c^2 \frac{V_A^2}{c^2} m'' k_g P_{aniso} \mathcal{R}e \Bigg[ \int_{m' k_g}^{\infty} k_\perp^{-\alpha+1} dk_\perp \\ \left\{ J^2_{\frac{\omega}{\Omega} - \frac{m'' k_g v_{||}}{\Omega} + 1}\left(\frac{k_\perp v_\perp}{\Omega}\right) + J^2_{\frac{\omega}{\Omega} - \frac{m'' k_g v_{||}}{\Omega} - 1}\left(\frac{k_\perp v_\perp}{\Omega}\right) \right. \\ \left. + 2 J_{\frac{\omega}{\Omega} - \frac{m'' k_g v_{||}}{\Omega} + 1}\left(\frac{k_\perp v_\perp}{\Omega}\right) J_{\frac{\omega}{\Omega} - \frac{m'' k_g v_{||}}{\Omega} - 1}\left(\frac{k_\perp v_\perp}{\Omega}\right) \right\} \Bigg] \end{aligned} \tag{A.46}$$

Note that the integral over $k_\perp$ resembles a variation of the Weber-Schafheitlin type integral and the integration is performed by bounding the upper limit of the integral due to the constraint given in Eq. (5.18).

## A.10 Transport coefficient for fast magnetosonic wave

We show the calculation of the momentum transport coefficient for the scenario when the small-scale turbulence is mediated via compressional fast waves. For simplicity we consider the dispersion relation of the fast wave in a cold plasma medium, which takes the following form (see Eq. 13.3.1 in Schlickeiser, 2002b),

$$\omega = V_A k \tag{A.47}$$

where $V_A$ is the Alfvèn velocity and $k = |\boldsymbol{k}|$. With such dispersion relation Eq. (5.10) becomes the following,

$$\frac{\gamma m' k_g V_A}{\Omega_{NR}} - \frac{m' k_g c\sqrt{1-\frac{1}{\gamma^2}}\mu x}{\Omega_{NR}}\gamma - \frac{m' k_g c\sqrt{1-\frac{1}{\gamma^2}}}{\Omega_{NR}}\gamma\sqrt{1-x^2}\sqrt{1-\mu^2} = Q,$$

With such a condition, we compute the region of validity for $x$ from the following equation,

$$Q_{min} \leq \frac{\gamma m' k_g V_A}{\Omega_{NR}} - \frac{m' k_g c\sqrt{1-\frac{1}{\gamma^2}}\mu x}{\Omega_{NR}}\gamma - \frac{m' k_g c\sqrt{1-\frac{1}{\gamma^2}}}{\Omega_{NR}}\gamma\sqrt{1-x^2}\sqrt{1-\mu^2} \leq Q_{max}, \tag{A.48}$$

for fast waves and thereby calculate the momentum diffusion coefficient following Eq. (5.8).

Below we investigate the impact of various parameter values on the pitch-angle-averaged momentum diffusion coefficient for isotropic fast wave turbulence. The results are presented in Fig. A.4, which comprises of four panels displaying the impact of different parameters on the diffusion coefficient. The diffusion coefficient can be observed to follow a power-law like trend with an index of $-2/3$ with the particle Lorentz factor $\gamma$ in all of the panels, similar to that of the Alfvènic turbulence as shown in section 5.3.1.

Panel (a) of the figure investigates the influence of different values of the mean magnetic field $B$ on the diffusion coefficient. It can be observed that the diffusion coefficient increases with the magnetic field strength. In panel (b), the effect of the parameter $m'$ on the diffusion coefficient is examined. It is observed that a smaller energy injection scale, corresponds to larger values of $m'$, results in a reduced influence of turbulence on the charged particles, causing the diffusion coefficient to decrease. Panel (c) investigates the effect of the Alfvén velocity on the momentum diffusion coefficient. The results indicate that a decrease in the Alfvén velocity of the underlying fluctuations leads to a reduction in momentum diffusion. In addition, panel (d) examines the effect of the parameter $\sigma$ on the momentum diffusion coefficient. The results indicate that the momentum diffusion coefficient increases as $\sigma$ increases, due to particles interacting with an increasing number of waves as $\sigma$ increases.

Moreover, comparing the value of the diffusion coefficients by modulating various parameters with the one observed for the Alfvèn waves (as discussed in section 5.3.1, see also Fig. 5.1), we find the values to be of the same order which ultimately resonate with the fact that the nature of the turbulence becomes degenerate to the non-thermal particles whose gyro-radius is higher that the turbulence correlation

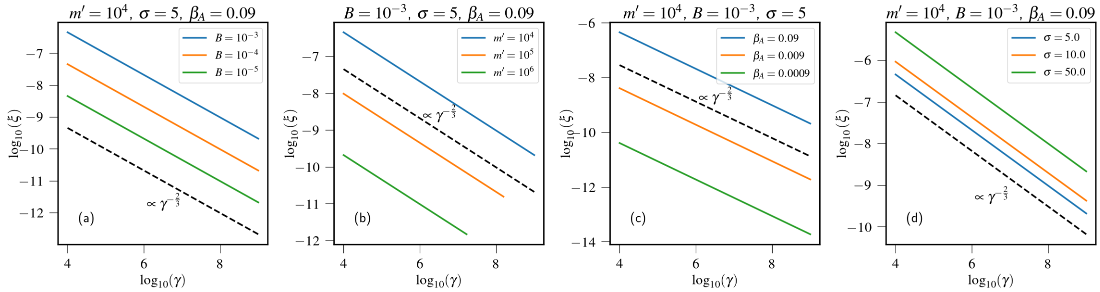


Figure A.4: Figure demonstrating the dependence of the pitch-angle-averaged momentum diffusion coefficient ($\xi$) on particle Lorentz factor $\gamma$ considering an isotropic single-scale turbulence injection spectrum for fast magnetosonic waves in cold plasma.

length.

# Bibliography


Acharya, S., Borse, N. S., & Vaidya, B. 2021, Monthly Notices of the Royal Astronomical Society, 506, 1862

Achterberg, A., & Krulls, W. M. 1992, A&A, 265, L13

Alexander, P., & Leahy, J. P. 1987, MNRAS, 225, 1

Alfvén, H. 1942, Nature, 150, 405

Alfven, H. 1950, Cosmical electrodynamics

Araudo, A. T., Bell, A. R., & Blundell, K. M. 2018, Nuclear and Particle Physics Proceedings, 297-299, 242, cosmic Ray Origin - Beyond the Standard Models

Asano, K., & Hayashida, M. 2018, The Astrophysical Journal, 861, 31

Asano, K., & Mészáros, P. 2016, Phys. Rev. D, 94, 023005

Ascher, U. M., Ruuth, S. J., & Spiteri, R. J. 1997, Applied Numerical Mathematics, 25, 151, special Issue on Time Integration

Bai, X.-N., Caprioli, D., Sironi, L., & Spitkovsky, A. 2015, ApJ, 809, 55

Baring, M. G. 2004, Nuclear Physics B - Proceedings Supplements, 136, 198, cRIS 2004 Proceedings of the Cosmic Ray International Seminars: GZK and Surroundings

Baring, M. G., Böttcher, M., & Summerlin, E. J. 2016, Monthly Notices of the Royal Astronomical Society, 464, 4875

Baring, M. G., Ellison, D. C., & Jones, F. C. 1994, International Astronomical Union Colloquium, 142, 547552

Barkhudarov, E. 2014, $$d$$-Dimensional Coulomb Gas (Cham: Springer International Publishing), 17–26

Bartelmann, M. 2013, Theoretical Astrophysics: An Introduction, EBL-Schweitzer (Wiley)

Becker Tjus, J., Hörbe, M., Jaroschewski, I., et al. 2022, Physics, 4, 473

Bell, A. R. 1978, MNRAS, 182, 147

Bell, A. R. 2014, Brazilian Journal of Physics, 44, 415

Bellan, P. 2008, Fundamentals of Plasma Physics (Cambridge University Press)

Belmont, R., Malzac, J., & Marcowith, A. 2008, A&A, 491, 617

Beresnyak, A., & Lazarian, A. 2019, in Turbulence in Magnetohydrodynamics (de Gruyter)

Beresnyak, A., Yan, H., & Lazarian, A. 2011, ApJ, 728, 60

Berezinskii, V. S., Bulanov, S. V., Dogiel, V. A., & Ptuskin, V. S. 1990, Astrophysics of cosmic rays

Bian, N., Emslie, A. G., & Kontar, E. P. 2012, ApJ, 754, 103

Bittencourt, J. 2013, Fundamentals of Plasma Physics (Springer New York)

Blandford, R., & Eichler, D. 1987, Physics Reports, 154, 1

Blandford, R., Meier, D., & Readhead, A. 2019, ARA&A, 57, 467

Blandford, R. D. 1994, ApJS, 90, 515

Blundell, K. M., Fabian, A. C., Crawford, C. S., Erlund, M. C., & Celotti, A. 2006, ApJ, 644, L13

Bodo, G., Mamatsashvili, G., Rossi, P., & Mignone, A. 2013, Monthly Notices of the Royal Astronomical Society, 434, 3030

—. 2016, Monthly Notices of the Royal Astronomical Society, 462, 3031

Borse, Nikhil, Acharya, Sriyasriti, Vaidya, Bhargav, et al. 2021, A&A, 649, A150

Böttcher, M., & Dermer, C. D. 2010, ApJ, 711, 445

Bridle, A. H., Hough, D. H., Lonsdale, C. J., Burns, J. O., & Laing, R. A. 1994, The Astronomical Journal, 108, 766

Brose, R., Telezhinsky, I., & Pohl, M. 2016, A&A, 593, A20

Brunetti, G., Bondi, M., Comastri, A., et al. 2001, ApJ, 561, L157

Brunetti, G., & Lazarian, A. 2007, MNRAS, 378, 245

Brydges, D. C., & Federbush, P. 1981, Debye Screening in Classical Coulomb Systems, ed. G. Velo & A. S. Wightman (Boston, MA: Springer US), 371–439

Bykov, A. M., & Fleishman, G. D. 1992, Monthly Notices of the Royal Astronomical Society, 255, 269

Bykov, A. M., & Meszaros, P. 1996, ApJ, 461, L37

Candia, J., & Roulet, E. 2004, Journal of Cosmology and Astroparticle Physics, 2004, 007

Carilli, C. L., Perley, R. A., Dreher, J. W., & Leahy, J. P. 1991, ApJ, 383, 554

Casse, F., Lemoine, M., & Pelletier, G. 2001, Phys. Rev. D, 65, 023002

Celotti, A., Ghisellini, G., & Chiaberge, M. 2001, MNRAS, 321, L1

Chandran, B. D. G. 2000, Phys. Rev. Lett., 85, 4656

—. 2003, ApJ, 599, 1426

Chang, J., & Cooper, G. 1970, Journal of Computational Physics, 6, 1

Chang, P., Spitkovsky, A., & Arons, J. 2008, The Astrophysical Journal, 674, 378

Cheung, C., Wardle, J., & Chen, T. 2005, The Astrophysical Journal, 628, 104

Cho, J., & Lazarian, A. 2002, Phys. Rev. Lett., 88, 245001

Cho, J., & Lazarian, A. 2006, ApJ, 638, 811

Cielo, S., Antonuccio-Delogu, V., Macciò, A. V., Romeo, A. D., & Silk, J. 2014, Monthly Notices of the Royal Astronomical Society, 439, 2903

Comisso, L., & Sironi, L. 2018, Phys. Rev. Lett., 121, 255101

Condon, J. J., & Ransom, S. M. 2016, Essential Radio Astronomy

Croston, J. H., Hardcastle, M. J., Harris, D. E., et al. 2005, ApJ, 626, 733

Croston, J. H., Hardcastle, M. J., Harris, D. E., et al. 2005, The Astrophysical Journal, 626, 733

Crumley, P., Caprioli, D., Markoff, S., & Spitkovsky, A. 2019, Monthly Notices of the Royal Astronomical Society, 485, 5105

de Vries, M. N., Wise, M. W., Huppenkothen, D., et al. 2018, MNRAS, 478, 4010

Dedner, A., Kemm, F., Kröner, D., et al. 2002, Journal of Computational Physics, 175, 645

Dermer, C. D., Miller, J. A., & Li, H. 1996, ApJ, 456, 106

Donnert, J., & Brunetti, G. 2014, Monthly Notices of the Royal Astronomical Society, 443, 3564

Drury, L. O. 1983, Reports on Progress in Physics, 46, 973

Duffy, P., & Blundell, K. M. 2012, MNRAS, 421, 108

Dundovic, A., Pezzi, O., Blasi, P., Evoli, C., & Matthaeus, W. H. 2020, Physical Review D, 102, 103016

Ellison, D. C., & Double, G. P. 2002, Astroparticle Physics, 18, 213

Ellison, D. C., Jones, F. C., & Reynolds, S. P. 1990, ApJ, 360, 702

Ellison, D. C., Warren, D. C., & Bykov, A. M. 2013, The Astrophysical Journal, 776, 46

Englert, B. 2014, Lectures On Classical Electrodynamics (World Scientific Publishing Company)

English, W., Hardcastle, M. J., & Krause, M. G. H. 2016, MNRAS, 461, 2025

Falceta-Gonçalves, D., Kowal, G., Falgarone, E., & Chian, A.-L. 2014, Nonlinear Processes in Geophysics, 21, 587

Fan, Z.-H., Liu, S., Wang, J.-M., Fryer, C. L., & Li, H. 2008, The Astrophysical Journal, 673, L139

Fanaroff, B. L., & Riley, J. M. 1974, MNRAS, 167, 31P

Farmer, A. J., & Goldreich, P. 2004, The Astrophysical Journal, 604, 671

Fatuzzo, M., Melia, F., Todd, E., & Adams, F. C. 2010, ApJ, 725, 515

Fermi, E. 1949, Phys. Rev., 75, 1169

Ferrand, G., & Marcowith, A. 2010, A&A, 510, A101

Fitzpatrick, R. 2020, Thermodynamics And Statistical Mechanics (World Scientific Publishing Company)

Frisch, U. 1995, Turbulence: The Legacy of A. N. Kolmogorov (Cambridge University Press), doi:10.1017/CBO9781139170666

Fujita, Y., Takizawa, M., Yamazaki, R., Akamatsu, H., & Ohno, H. 2015, ApJ, 815, 116

Galtier, S. 2022, Physics of Wave Turbulence (Cambridge University Press), doi:10.1017/9781009275880

Galtier, S., Nazarenko, S., Newell, A. C., & Pouquet, A. 2000, Journal of plasma physics, 63, 447

Ghisellini, G., Tavecchio, F., & Chiaberge, M. 2005, A&A, 432, 401

Giacalone, J., & Ellison, D. C. 2000, Journal of Geophysical Research: Space Physics, 105, 12541

Giacalone, J., & Jokipii, J. R. 1999, ApJ, 520, 204

Gill, A., Boyce, M. M., O'Dea, C. P., et al. 2021, ApJ, 912, 88

Ginzburg, V. L. 1970, International Series of Monographs in Electromagnetic Waves

Giri, G., Vaidya, B., Rossi, P., et al. 2022, A&A, 662, A5

Girichidis, P., Pfrommer, C., Hanasz, M., & Naab, T. 2020, MNRAS, 491, 993

Gurnett, D., & Bhattacharjee, A. 2017, Introduction to Plasma Physics: With Space, Laboratory and Astrophysical Applications (Cambridge University Press)

Hardcastle, M. J., Birkinshaw, M., Cameron, R. A., et al. 2002, The Astrophysical Journal, 581, 948

Hardcastle, M. J., Cheung, C. C., Feain, I. J., & Stawarz, Ł. 2009, MNRAS, 393, 1041

Hardcastle, M. J., & Croston, J. H. 2020, New Astron. Rev., 88, 101539

Hardcastle, M. J., Croston, J. H., & Kraft, R. P. 2007a, ApJ, 669, 893

Hardcastle, M. J., Harris, D. E., Worrall, D. M., & Birkinshaw, M. 2004, The Astrophysical Journal, 612, 729

Hardcastle, M. J., & Krause, M. G. H. 2013, MNRAS, 430, 174

Hardcastle, M. J., Kraft, R. P., Sivakoff, G. R., et al. 2007b, ApJ, 670, L81

Harris, D., & Krawczynski, H. 2006, Annual Review of Astronomy and Astrophysics, 44, 463

Harris, D. E., Moldón, J., Oonk, J. R. R., et al. 2019, ApJ, 873, 21

Harwood, J. J., Hardcastle, M. J., Croston, J. H., & Goodger, J. L. 2013, Monthly Notices of the Royal Astronomical Society, 435, 3353

Heavens, A. F., & Meisenheimer, K. 1987, MNRAS, 225, 335

Hervet, O., Meliani, Z., Zech, A., et al. 2017, A&A, 606, A103

Hovatta, T., Aller, M. F., Aller, H. D., et al. 2014, AJ, 147, 143

Huarte-Espinosa, M., Krause, M., & Alexander, P. 2011, MNRAS, 417, 382

Iroshnikov, P. S. 1964, Soviet Ast., 7, 566

Jokipii, J., Giacalone, J., & Kóta, J. 2007, Planetary and Space Science, 55, 2267, dynamical Processes in Space Plasmas

Jokipii, J. R. 1966, ApJ, 143, 961

—. 1973, ApJ, 183, 1029

Jones, T. W., Ryu, D., & Engel, A. 1999, The Astrophysical Journal, 512, 105

Kang, H., Ryu, D., & Jones, T. W. 2017, The Astrophysical Journal, 840, 42

Kardashev, N. S. 1962, Soviet Ast., 6, 317

Kataoka, J., Stawarz, Ł., Aharonian, F., et al. 2006, ApJ, 641, 158

Katarzyński, K., Ghisellini, G., Mastichiadis, A., Tavecchio, F., & Maraschi, L. 2006, A&A, 453, 47

Katz, B., Keshet, U., & Waxman, E. 2007, The Astrophysical Journal, 655, 375

Kembhavi, A., & Narlikar, J. 1999, Quasars and Active Galactic Nuclei: An Introduction, Quasars and Active Galactic Nuclei: An Introduction (Cambridge University Press)

Keshet, U., Katz, B., Spitkovsky, A., & Waxman, E. 2009, The Astrophysical Journal, 693, L127

King, I. R. 1972, ApJ, 174, L123

Kirk, J. G., Duffy, P., & Gallant, Y. A. 1996, A&A, 314, 1010

Kirk, J. G., Melrose, D. B., & Priest, E. R. 1994, Plasma Astrophysics, ed. A. O. Benz, , & T. J.-L. Courvoisier (Springer Berlin Heidelberg), doi:10.1007/3-540-31627-2

Kirk, J. G., Schlickeiser, R., & Schneider, P. 1988, ApJ, 328, 269

Kiyani, K. H., Chapman, S. C., Sahraoui, F., et al. 2012, The Astrophysical Journal, 763, 10

Kolmogorov, A. N. 1941, Cr Acad. Sci. URSS, 30, 301

Komissarov, S. S., Barkov, M. V., Vlahakis, N., & Königl, A. 2007, MNRAS, 380, 51

Kraichnan, R. H. 1965, Physics of Fluids, 8, 1385

Krause, M. 2005, Astronomy & Astrophysics, 431, 45

Kulsrud, R., & Pearce, W. P. 1969, ApJ, 156, 445

Kulsrud, R. M., & Ferrari, A. 1971, Ap&SS, 12, 302

Kundu, S., Singh, N. K., & Vaidya, B. 2023, MNRAS, 524, 4950

Kundu, S., & Vaidya, B. 2022, to appear in ”Proceedings of the International Astronomical Union (IAU)”

Kundu, S., Vaidya, B., & Mignone, A. 2021, The Astrophysical Journal, 921, 74

Kundu, S., Vaidya, B., Mignone, A., & Hardcastle, M. J. 2022, Astronomy & Astrophysics, 667, A138

Lähteenmäki, A., & Valtaoja, E. 1999, The Astronomical Journal, 117, 1168

Laing, R. A., & Bridle, A. H. 1987, MNRAS, 228, 557

Lemoine, M. 2016, Journal of Plasma Physics, 82, 635820401

Lemoine, M. 2019, Phys. Rev. D, 99, 083006

Lemoine, M., & Pelletier, G. 2003, The Astrophysical Journal, 589, L73

Lemoine, M., Pelletier, G., & Revenu, B. 2006, The Astrophysical Journal, 645, L129

Lerche, I. 1968, Physics of Fluids, 11, 1720

Lerche, I., & Schlickeiser, R. 1985, A&A, 151, 408

Lind, K. R., Payne, D. G., Meier, D. L., & Blandford, R. D. 1989, ApJ, 344, 89

Liu, S., Petrosian, V., & Melia, F. 2004, ApJ, 611, L101

Longair, M. 1992, High Energy Astrophysics: Volume 1, Particles, Photons and Their Detection, High Energy Astrophysics (Cambridge University Press)

Longair, M. S., Ryle, M., & Scheuer, P. A. G. 1973, MNRAS, 164, 243

Mahatma, V. H., Hardcastle, M. J., Croston, J. H., et al. 2019, Monthly Notices of the Royal Astronomical Society, 491, 5015

Malkov, M. A., & Drury, L. O. 2001, Reports on Progress in Physics, 64, 429

Marcowith, A., & Casse, F. 2010, A&A, 515, A90

Marcowith, A., Ferrand, G., Grech, M., et al. 2020, Living Reviews in Computational Astrophysics, 6, 1

Marcowith, A., & Kirk, J. G. 1999, A&A, 347, 391

Massaglia, S., Bodo, G., Rossi, P., Capetti, S., & Mignone, A. 2016, A&A, 596, A12

Massaro, E., Tramacere, A., Perri, M., Giommi, P., & Tosti, G. 2006, A&A, 448, 861

Massaro, F., & Ajello, M. 2011, The Astrophysical Journal Letters, 729, L12

Massaro, F., Missaglia, V., Stuardi, C., et al. 2018, The Astrophysical Journal Supplement Series, 234, 7

Massaro, E., Perri, M., Giommi, P., & Nesci, R. 2004, A&A, 413, 489

Matthews, J. H., Bell, A. R., Blundell, K. M., & Araudo, A. T. 2019, Monthly Notices of the Royal Astronomical Society, 482, 4303

Medvedev, M. V., Fiore, M., Fonseca, R. A., Silva, L. O., & Mori, W. B. 2004, The Astrophysical Journal, 618, L75

Meisenheimer, K. 2003, New Astronomy Reviews, 47, 495, the physics of relativistic jets in the CHANDRA and XMM era

Meli, A., & Biermann, P. L. 2013, A&A, 556, A88

Melrose, D. B. 1996, Astrophysics and Space Science, 242, 209

Mertsch, P., & Petrosian, V. 2019, A&A, 622, A203

Meyer, D. M. A., Pohl, M., Petrov, M., & Oskinova, L. 2021, MNRAS, 502, 5340

Mignone, A., Bodo, G., Massaglia, S., et al. 2007, The Astrophysical Journal Supplement Series, 170, 228

Mignone, A., Bodo, G., Vaidya, B., & Mattia, G. 2018, The Astrophysical Journal, 859, 13

Mignone, A., Rossi, P., Bodo, G., Ferrari, A., & Massaglia, S. 2010, Monthly Notices of the Royal Astronomical Society, 402, 7

Mignone, A., Zanni, C., Tzeferacos, P., et al. 2012, ApJS, 198, 7

Mimica, P., & Aloy, M. A. 2012, Monthly Notices of the Royal Astronomical Society, 421, 2635

Miniati, F. 2001, Computer Physics Communications, 141, 17

Miniati, F. 2003, MNRAS, 342, 1009

Miniati, F., Ryu, D., Kang, H., & Jones, T. W. 2001, The Astrophysical Journal, 559, 59

Mukherjee, D., Bodo, G., Rossi, P., Mignone, A., & Vaidya, B. 2021, MNRAS, 505, 2267

Mullin, L. M., Riley, J. M., & Hardcastle, M. J. 2008, MNRAS, 390, 595

Niemiec, J., & Ostrowski, M. 2006, The Astrophysical Journal, 641, 984

Nishikawa, K.-I., Hededal, C. B., Hardee, P. E., et al. 2007, Astrophysics and Space Science, 307, 319

Ogrodnik, M. A., Hanasz, M., & Wóltański, D. 2021, ApJS, 253, 18

Ohno, H., Takizawa, M., & Shibata, S. 2002, The Astrophysical Journal, 577, 658

Orienti, M., Prieto, M. A., Brunetti, G., et al. 2012, Monthly Notices of the Royal Astronomical Society, 419, 2338

Ostrowski, M. 1988, Monthly Notices of the Royal Astronomical Society, 233, 257

O'Sullivan, S., Reville, B., & Taylor, A. M. 2009, Monthly Notices of the Royal Astronomical Society, 400, 248

Palmroth, M., Ganse, U., Pfau-Kempf, Y., et al. 2018, Living Reviews in Computational Astrophysics, 4, 1

Pareschi, L., & Russo, G. 2005, Journal of Scientific Computing, 25, 129

Park, B. T., & Petrosian, V. 1995, ApJ, 446, 699

—. 1996, ApJS, 103, 255

Parker, E. N. 1955, Physical Review, 99, 241

Parma, P., Murgia, M., Morganti, R., et al. 1999, A&A, 344, 7

Perlman, E. S., Clautice, D., Avachat, S., et al. 2020, Galaxies, 8, doi:10.3390/galaxies8040071

Perri, S., & Zimbardo, G. 2015, ApJ, 815, 75

Peterson, B. M. 1997, An Introduction to Active Galactic Nuclei

Petrosian, V. 2001, ApJ, 557, 560

—. 2012, Space Sci. Rev., 173, 535

Petrosian, V., & Liu, S. 2004, ApJ, 610, 550

Pezzi, O., Blasi, P., & Matthaeus, W. H. 2022, The Astrophysical Journal, 928, 25

Plotnikov, I., Pelletier, G., & Lemoine, M. 2011, Astronomy & Astrophysics, 532, A68

—. 2013, Monthly Notices of the Royal Astronomical Society, 430, 1280

Pope, S., & Pope, S. 2000, Turbulent Flows (Cambridge University Press)

Porth, O. 2013, MNRAS, 429, 2482

Press, W. H., Teukolsky, S. A., Vetterling, W. T., & Flannery, B. P. 1992, Numerical recipes in C. The art of scientific computing

Prieto, M. A., Brunetti, G., & Mack, K.-H. 2002, Science, 298, 193

Prieto, M. A., & Kotilainen, J. K. 1997, The Astrophysical Journal, 491, L77

Ptuskin, V. S. 1988, Soviet Astronomy Letters, 14, 255

Rajpurohit, K., Hoeft, M., Vazza, F., et al. 2020, A&A, 636, A30

Rangelov, B., Montmerle, T., Federman, S. R., Boissé, P., & Gabici, S. 2019, The Astrophysical Journal, 885, 105

Reichherzer, P., Becker Tjus, J., Hörbe, M., et al. 2022a, in 37th International Cosmic Ray Conference, 468

Reichherzer, P., Merten, L., Dörner, J., et al. 2022b, SN Applied Sciences, 4, 15

Richardson, L., & Lynch, P. 2007, Weather Prediction by Numerical Process, Cambridge Mathematical Library (Cambridge University Press)

Rieger, F. M., & Duffy, P. 2019, The Astrophysical Journal, 886, L26

Rogachevskii, I. 2021, Introduction to Turbulent Transport of Particles, Temperature and Magnetic Fields: Analytical Methods for Physicists and Engineers (Cambridge University Press), doi:10.1017/9781009000918

Sarazin, C. L. 1999, The Astrophysical Journal, 520, 529

Schekochihin, A. A. 2022, Journal of Plasma Physics, 88, 155880501

Schlickeiser, R. 1989, ApJ, 336, 243

—. 2002a, Cosmic Ray Astrophysics

—. 2002b, Cosmic Ray Astrophysics

Schlickeiser, R., & Achatz, U. 1993, Journal of Plasma Physics, 49, 6377

Schlickeiser, R., & Dermer, C. D. 2000, A&A, 360, 789

Schlickeiser, R., & Miller, J. A. 1998, The Astrophysical Journal, 492, 352

Selkowitz, R., & Blackman, E. G. 2004, MNRAS, 354, 870

Sengupta, P. 2007, Classical Electrodynamics (New Age International (P) Limited)

Shalchi, A. 2009, Nonlinear Cosmic Ray Diffusion Theories, Vol. 362, doi:10.1007/978-3-642-00309-7

—. 2020, Space Sci. Rev., 216, 23

—. 2021, ApJ, 923, 209

Sironi, L., Keshet, U., & Lemoine, M. 2015, Space Science Reviews, 191, 519

Sironi, L., & Spitkovsky, A. 2011, ApJ, 726, 75

Spitkovsky, A. 2008, The Astrophysical Journal, 682, L5

Sturrock, P. A. 1966, Phys. Rev., 141, 186

Subedi, P., Sonsrettee, W., Blasi, P., et al. 2017, The Astrophysical Journal, 837, 140

Swanson, D. 2008, Plasma Kinetic Theory, Series in Plasma Physics and Fluid Dynamics (Taylor & Francis)

Tavecchio, F., Costa, A., & Sciaccaluga, A. 2022, Monthly Notices of the Royal Astronomical Society: Letters

Tavecchio, F., Maraschi, L., Sambruna, R. M., & Urry, C. M. 2000, The Astrophysical Journal, 544, L23

Teraki, Y., & Asano, K. 2019, The Astrophysical Journal, 877, 71

Thomson, R., Crane, P., & Mackay, C. 1995, arXiv preprint astro-ph/9505122

Thornbury, A., & Drury, L. O. 2014, MNRAS, 442, 3010

Tjus, J. B. 2022, Plasma Physics and Controlled Fusion, 64, 044013

Tramacere, A., Massaro, E., & Taylor, A. M. 2011, The Astrophysical Journal, 739, 66

Tregillis, I. L., Jones, T. W., & Ryu, D. 2001, ApJ, 557, 475

Tsytovich, V. N., & Burdick, D. L. 1977, Theory of turbulent plasma (Springer)

Tverskoǐ, B. A. 1967, Soviet Journal of Experimental and Theoretical Physics, 25, 317

Urry, C. M., & Padovani, P. 1995, PASP, 107, 803

Vaidya, B., Mignone, A., Bodo, G., Rossi, P., & Massaglia, S. 2018, The Astrophysical Journal, 865, 144

Vaidya, B., Prasad, D., Mignone, A., Sharma, P., & Rickler, L. 2017, Monthly Notices of the Royal Astronomical Society, 472, 3147

Van Leer, B. 1977, Journal of Computational Physics, 23, 276

van Weeren, R. J., Andrade-Santos, F., Dawson, W. A., et al. 2017, Nature Astronomy, 1, 0005

Vazza, F., Wittor, D., Brunetti, G., & Brüggen, M. 2021, arXiv e-prints, arXiv:2102.04193

Verma, M. 2019, Energy Transfers in Fluid Flows (Cambridge University Press)

Verma, M. K. 2004, Physics Reports, 401, 229

Virtanen, J. J. P., & Vainio, R. 2005, ApJ, 621, 313

Vlahos, L., & Isliker, H. 2018, Plasma Physics and Controlled Fusion, 61, 014020

Vukcevic, M., & Schlickeiser, R. 2007, A&A, 467, 15

Vurm, I., & Poutanen, J. 2009, The Astrophysical Journal, 698, 293

Wang, J.-S., Reville, B., Liu, R.-Y., Rieger, F. M., & Aharonian, F. A. 2021, MNRAS, 505, 1334

Webb, G. M. 1989, ApJ, 340, 1112

Winner, G., Pfrommer, C., Girichidis, P., & Pakmor, R. 2019, MNRAS, 488, 2235

Wolff, M., & Tautz, R. C. 2015, A&A, 580, A58

Wong, K., Zhdankin, V., Uzdensky, D. A., Werner, G. R., & Begelman, M. C. 2019, arXiv e-prints, arXiv:1901.03439

Worrall, D. M. 2009, A&ARv, 17, 1

Worrall, D. M., Birkinshaw, M., Kraft, R. P., et al. 2008, ApJ, 673, L135

Xu, S., Klingler, N., Kargaltsev, O., & Zhang, B. 2019, ApJ, 872, 10

Xu, S., & Zhang, B. 2017, ApJ, 846, L28

Yan, H., & Lazarian, A. 2002, Phys. Rev. Lett., 89, 281102

Yan, H., & Lazarian, A. 2008, ApJ, 673, 942

Zank, G. 2013, Transport Processes in Space Physics and Astrophysics, Lecture Notes in Physics (Springer New York)

Zimbardo, G., & Perri, S. 2017, Nature Astronomy, 1, 0163